

Microkinetic modeling of CO₂ hydrogenation to methanol on Ni-In₂O₃ catalysts

Citation for published version (APA):

Cannizzaro, F. (2023). *Microkinetic modeling of CO₂ hydrogenation to methanol on Ni-In₂O₃ catalysts*. [Phd Thesis 1 (Research TU/e / Graduation TU/e), Chemical Engineering and Chemistry]. Eindhoven University of Technology.

Document status and date:

Published: 25/05/2023

Document Version:

Publisher's PDF, also known as Version of Record (includes final page, issue and volume numbers)

Please check the document version of this publication:

- A submitted manuscript is the version of the article upon submission and before peer-review. There can be important differences between the submitted version and the official published version of record. People interested in the research are advised to contact the author for the final version of the publication, or visit the DOI to the publisher's website.
- The final author version and the galley proof are versions of the publication after peer review.
- The final published version features the final layout of the paper including the volume, issue and page numbers.

[Link to publication](#)

General rights

Copyright and moral rights for the publications made accessible in the public portal are retained by the authors and/or other copyright owners and it is a condition of accessing publications that users recognise and abide by the legal requirements associated with these rights.

- Users may download and print one copy of any publication from the public portal for the purpose of private study or research.
- You may not further distribute the material or use it for any profit-making activity or commercial gain
- You may freely distribute the URL identifying the publication in the public portal.

If the publication is distributed under the terms of Article 25fa of the Dutch Copyright Act, indicated by the "Taverne" license above, please follow below link for the End User Agreement:

www.tue.nl/taverne

Take down policy

If you believe that this document breaches copyright please contact us at:

openaccess@tue.nl

providing details and we will investigate your claim.

Microkinetic modeling of CO₂ hydrogenation to methanol on Ni-In₂O₃ catalysts

PROEFSCHRIFT

ter verkrijging van de graad van doctor aan de Technische Universiteit Eindhoven, op
gezag van de rector magnificus prof.dr.ir. S.K. Lenaerts, voor een commissie aangewezen
door het College voor Promoties, in het openbaar te verdedigen op donderdag 25 mei 2023
om 13:30 uur

door

Francesco Cannizzaro

geboren te Palermo, Italië

Dit proefschrift is goedgekeurd door de promotoren en de samenstelling van de promotiecommissie is als volgt:

Voorzitter: prof.dr.ir. R. A. J. Janssen
Promotor: prof.dr.ir. E. J. M. Hensen
Copromotor: dr.ir. I. A. W. Filot
Leden: prof.dr. M. Maestri (Politecnico di Milano)
prof.dr. N. Lopez (Institut Català d'Investigació Química)
prof.dr.ir. M. van Sint Annaland
prof.dr.ir. J. van der Schaaf

Het onderzoek of ontwerp dat in dit proefschrift wordt beschreven is uitgevoerd in overeenstemming met de TU/e Gedragscode Wetenschapsbeoefening.

*To the scientists,
innovators,
and activists
who are leading the way.*

Francesco Cannizzaro

Microkinetic modeling of CO₂ hydrogenation to methanol on Ni-In₂O₃ catalysts

A catalogue record is available from the Eindhoven University of Technology Library

ISBN: 978-90-386-5737-0

Copyright © 2023 by Francesco Cannizzaro



INORGANIC MATERIALS & CATALYSIS



The work described in this thesis has been carried out at the Laboratory of Inorganic Materials & Catalysis, Eindhoven University of Technology, the Netherlands. We acknowledge NWO and SurfSARA for providing access to computational resources used to carry out the DFT calculations reported in this work. This work was supported by the Netherlands Center for Multiscale Catalytic Energy Conversion (MCEC), an NWO Gravitation program funded by the Ministry of Education, Culture and Science of the government of the Netherlands. This project has received funding from the European Union's Horizon 2020 research and innovation program under the Marie Skłodowska-Curie grant agreement No 801359.

Cover layout: Laura Donk and Francesco Cannizzaro

Cover picture: By changing the composition and size of Ni metal phases in contact with the In₂O₃ surface, we can steer the selectivity to either CH₃OH or CO.

Printed by: proefschriftspecialist.nl

Contents

CHAPTER 1	
Introduction and scope	6
CHAPTER 2	
Computational methods	20
CHAPTER 3	
A computational study of CO₂ hydrogenation on single atoms of Pt, Pd, Ni and Rh on In₂O₃(111)	41
Appendix A	71
CHAPTER 4	
The promoting role of Ni on In₂O₃ for CO₂ hydrogenation to methanol	91
Appendix B	125
CHAPTER 5	
First-principles microkinetic modeling of the rWGS reaction on NiIn alloys	149
Appendix C	172
CHAPTER 6	
On the role of Ni-In clusters on In₂O₃ during CO₂ hydrogenation to methanol	181
Appendix D	210
Summary and Outlook	236
Acknowledgments	242

CHAPTER 1

Introduction and scope

1.1 The energy transition

The current energy and chemical sectors are largely dependent on the availability of fossil resources. The widespread availability of coal, oil and gas has fueled the industrialization of our society and formed the basis of the high levels of prosperity of a significant fraction of the world population.¹ Besides providing energy, especially crude oil is a primary feedstock for the manufacture of intermediate chemicals relevant for the production of many different end products such as polymers, solvents and pharmaceuticals. The combustion of such fossil fuels generates useful energy but transforms carbon into carbon dioxide (CO₂), which accumulates in the Earth's atmosphere. These emissions are a threat to our society, because they are the main cause of global warming which in turns leads to climate change, sea level rise and ocean acidification.² Therefore, despite their key role in the progress of human civilization, the widespread use of fossil fuels causes serious environmental concerns. Thus, if we want to avoid a climate disaster, transitioning to sustainable and renewable energy sources is necessary.

CO₂ emissions come from many human-related activities. Figure 1.1 shows a breakdown of global anthropogenic emissions of CO₂ by sector. More than 50% of global emissions comes from the energy and industrial sector; almost one-fifth from agriculture (19%) and transportation (16%) and the remaining 7% from heating and cooling. Reducing our dependence on fossil-based energy and reducing CO₂ emissions has become a crucial societal challenge.³⁻⁵ Currently, much effort is directed towards decarbonizing the energy sector by developing renewable energy sources such as solar, wind and tidal which have experienced a significant growth in global energy production in the past years.^{6,7} These developments are necessary as the energy sector is responsible for most of the CO₂ emissions. In the near future, a mix of renewable energy sources will increasingly contribute to satisfy the global energy demand.⁸ However, the intermittent nature of electricity generated by solar panels and wind turbines poses some serious challenges. Currently, there is a mismatch between the electricity grid systems and the intermittent availability of renewable sources. It has been reported that a substantial integration of intermittent renewable energy can cause serious disruptions to the current grid system.⁸ At present, pumped hydroelectric energy storage is the main way to store energy, but it has limited capacity and is geographically constrained.⁸ Thus, scalable and efficient energy storage technologies are pivotal to enable the sustainable energy transition. Large-scale energy storage is important also for transportation purposes to cover the energy demand for mobility. Such storage technologies require high energy density in relatively small volumes. Batteries serve already as a storage medium for electric vehicles, but their energy density remains 1-2 orders of magnitude lower than

conventional liquid fuels. Furthermore, other sectors such as heavy-duty transport and aviation will remain dependent on energy-dense fuels in the foreseeable future.

Innovation in large-scale energy storage technologies necessary for the sustainable energy transition and electric mobility can come from chemistry. Storing surplus renewable energy in chemical bonds of liquid carriers is considered a promising approach to energy storage, which is also compatible with the existing energy infrastructure. As most of the current energy carriers and nearly all chemicals are based on carbon, considering CO₂ waste as a carbon source and its conversion to chemical compounds are attractive, the more as it would also reduce atmospheric CO₂ levels when performed at a very large scale.⁹ CO₂ streams can come from irreducible point sources such as the cement industry, from the upgrading of renewables (e.g., biomass), or from direct capture of CO₂ from the air. The latter option is considered as the preferred solution, because it would allow to use carbon in a circular manner.¹⁰ Nevertheless, this method is also the most challenging. Renewable energy can be used to generate hydrogen (H₂), which in turn can be used to hydrogenate CO₂ to hydrocarbon products.¹¹ CO₂ hydrogenation technologies are therefore an attractive solution to mitigate global warming and enable large-scale use of renewable energy sources. Both factors are key to the sustainable energy transition.

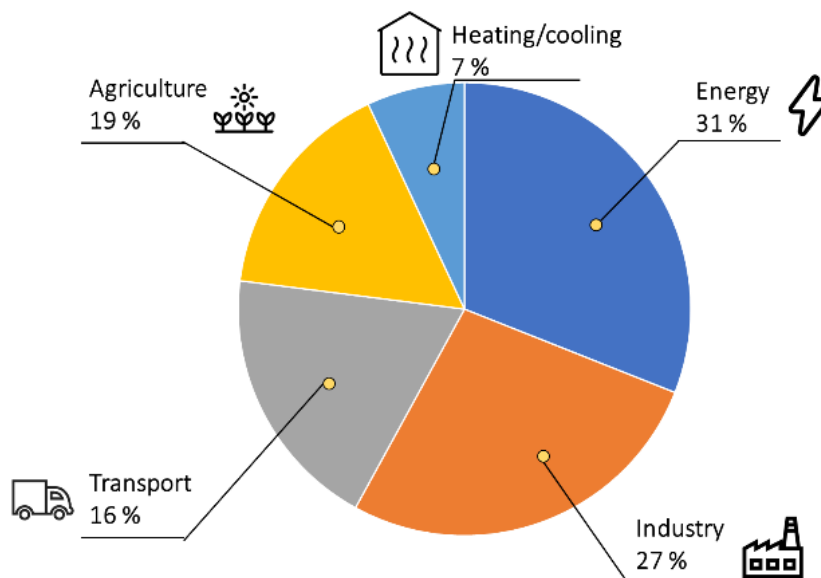


Figure 1.1: Global CO₂ emissions by sector. Adapted from ref[¹²]

1.2 Methanol economy

With the highest oxidized state (+4) and high heat of formation ($\Delta H^{\circ}_f = -393.5$ kJ/mol at 25 °C), CO₂ is a thermodynamically stable form of carbon ($\Delta G^{\circ}_f = -394.4$ kJ/mol at 25 °C). As its C-O bonds are very strong (799 kJ/mol), converting CO₂ back to more useful forms requires relatively high temperatures or a

catalytic process. A common way is to reduce CO₂ to useful chemical intermediates via either (i) electrocatalytic reduction using electricity or (ii) thermocatalytic reduction of CO₂ with hydrogen. The field of electrocatalytic CO₂ reduction is rapidly developing and has been reviewed recently.^{13,14} Thermocatalytic CO₂ hydrogenation can be performed in various ways, i.e. via the reverse water-gas shift reaction (rWGS, CO₂+H₂⇌CO+H₂O), methanation (CO₂+4H₂⇌CH₄+2H₂O) or methanol synthesis (CO₂+3H₂⇌CH₃OH+H₂O).^{3,7-11} The topic of thermocatalytic CO₂ hydrogenation to C₁ products has also been reviewed recently.²⁰⁻²⁴ Methanation allows obtaining synthetic natural gas, which can be directly injected into existing gas grids.^{25,26} CO₂ can be directly transformed into longer hydrocarbon chains and aromatics.^{15,27} Indirect conversion of CO₂ to hydrocarbons via synthesis gas (CO + H₂) is also possible via known commercial methanol and Fischer-Tropsch processes.

Methanol is a particularly interesting product of CO₂ hydrogenation, because it is useful as a fuel and a chemical intermediate. As such, it is considered a “platform chemical” on which a sustainable chemical industry can be built. Given its high energy density and ease of transport, methanol could be an important energy carrier and storage chemical. Therefore, the catalytic synthesis of methanol directly from CO₂ and hydrogen is currently of great interest. Large-scale methanol synthesis from CO₂ and H₂ could lead to a chemical industry in which methanol would be a starting chemical instead of hydrocarbons in fossil resources.^{28,29} This was already realized by Olah in the 1990s, when he introduced the term “methanol economy”.²⁹ The concept of the methanol economy is illustrated in Figure 1.2. Methanol can serve as a clean burning fuel, a convenient storage material for renewable energy and a versatile raw material. Methanol can for instance be converted to olefins such as ethylene and propylene as well as gasoline using methanol-to-olefin (MTO) and methanol-to-gasoline (MTG) technologies.³⁰ Various other important chemicals can be obtained from methanol such as formaldehyde, methyl methacrylate, acetic acid and methyl chloride. In addition, owing to its high octane rating, methanol can be used as an additive or substitute for gasoline in internal combustion engines. Another advantage of the methanol economy lies in its potential contribution to global warming mitigation, because atmospheric CO₂ can be used as feedstock for methanol production. Hydrogen could also be used directly as commercial fuel to fulfill a substantial fraction of the global energy demand (hence the term “hydrogen economy”). However, transportation and storage of hydrogen is challenging. In contrast, methanol is a liquid that can be more easily and safely transported and stored.

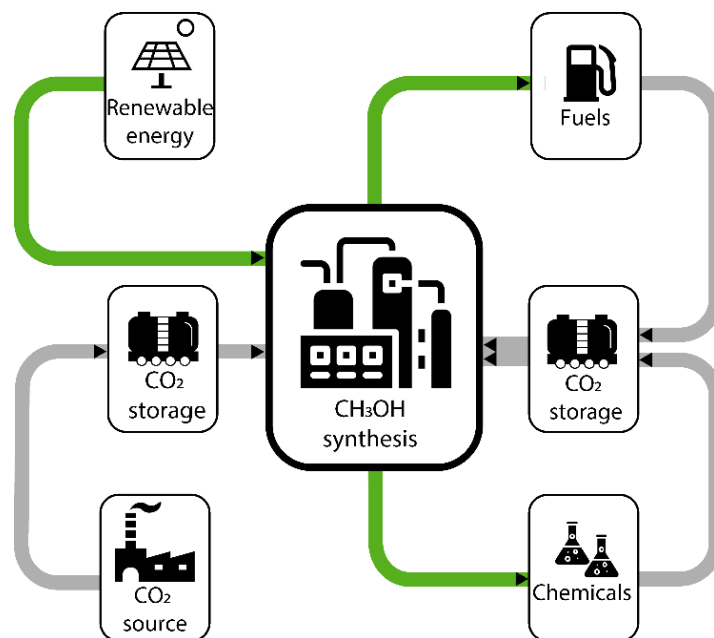


Figure 1.2: Schematic overview of CO₂-based methanol economy.

1.3 Catalysis

1.3.1 The catalytic process

Modern chemical industry, including methanol production, strongly relies on catalysis. It is estimated that 85-90% of all the chemical products meet a catalyst during their life.³¹ Other important large-scale catalytic chemical processes rely on the use of catalysts, for instance, ammonia synthesis, Fischer–Tropsch synthesis, methane steam reforming, fluid catalytic cracking (FCC), hydrodesulfurization, etc. Furthermore, catalysis also plays a critical role in environmental protection and pollution control. The most prominent example is probably the three-way catalyst (TWC), which simultaneously converts CO, unburned hydrocarbon (C_xH_y) and NO_x from the car exhaust into less harmful CO₂, N₂ and H₂O.³²

A catalyst is a substance that accelerates a chemical reaction, where chemical bonds are being broken or formed. This effect is achieved by establishing a multistep catalytic cycle, offering a lower overall activation barrier as compared to the non-catalytic pathway. To illustrate this, Figure 1.3 shows the potential energy diagrams of catalytic and non-catalytic pathways for a hypothetical association reaction ($A + B \rightarrow AB$). For the non-catalytic pathway, the reaction proceeds in the gas phase when A and B collide with sufficient energy to overcome the high activation energy barrier. The presence of a catalyst offers an alternative reaction pathway: A and B first adsorb on the catalyst surface, where they react to form AB, after which AB desorbs from the surface, thereby closing the catalytic cycle. Notably, the activation of the adsorbates by adsorption on the catalyst leads to lower barriers for the association reaction, thereby contributing to a decreased overall barrier for the reaction of interest as compared to the non-catalytic

reaction pathway. Besides increasing the reaction rate, catalysts can influence the product selectivity in complex reactions schemes by promoting desired reactions and/or inhibiting undesired ones. Despite the changes in reaction kinetics (i.e., activity and selectivity), it should be mentioned that the overall changes in reaction Gibbs free energy are the same for catalytic and non-catalytic reactions, meaning that catalysts do not affect reaction thermodynamics.

Although the formal definition states that a catalyst is not being altered or consumed during the reaction, catalysts tend to deactivate for different reasons. Therefore, they must be frequently regenerated or removed from the process. The interaction of a catalyst with the reactants in terms of catalytic activity follows the Goldilocks' principle: if the bond between the catalyst and the reactants is too weak, the reactant is insufficiently activated and there will be little to no conversion. If the interaction is too strong, the product will not desorb from the surface and the catalyst will be poisoned. This requirement for an optimal catalyst is known as the Sabatier's principle.

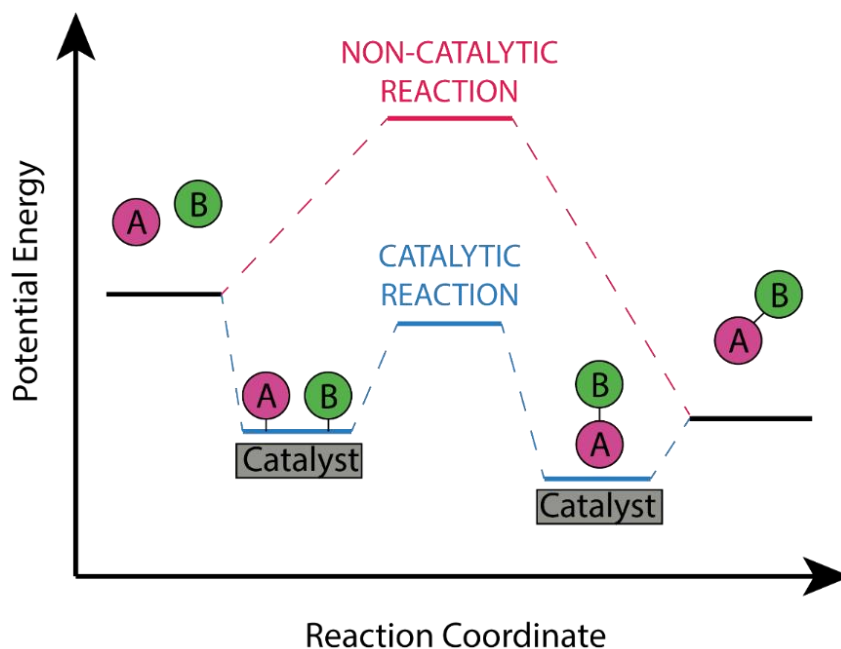


Figure 1.3: Energy profile of a non-catalytic reaction (red) and a catalytic reaction (blue).

1.4 Methanol synthesis from CO₂

Hydrogenation of CO₂ to methanol and water is exothermic at room temperature and it competes with the reverse water-gas shift reaction:



$$\Delta H_{\text{r}}^{298\text{K}} = -49.5 \text{ kJ/mol}$$



$$\Delta H_{\text{r}}^{298\text{K}} = 41.2 \text{ kJ/mol}$$

The synthesis of methanol from CO₂ is thus an equilibrium-limited reaction at high temperature. However, finding a catalysts able to activate CO₂ without breaking both C-O bonds is challenging.³³ Several types of materials have been tested as catalysts for CO₂ hydrogenation to CH₃OH, including commercial Cu/ZnO catalysts, noble metal-based catalysts and transition metal-oxides. Several reviews are available that discuss catalysts for CO₂ hydrogenation to methanol.^{27,34–37} The Cu/ZnO/Al₂O₃ catalyst used industrially for CO hydrogenation to methanol has been investigated in CO₂ hydrogenation extensively.^{38–40} Operating with feeds containing high concentrations of CO₂, such materials exhibit low methanol selectivity, resulting from significant activity in the parasitic reverse water–gas shift (rWGS) reaction and insufficient stability due to the water-induced sintering of the active phase. By comparison, due to the high resistance to sintering and poisoning, noble metal-based catalysts have been proposed as alternatives to Cu-based catalysts.^{41,42} However, these catalysts suffer from low CH₃OH selectivity and high cost. Transition metal oxides such as Zn–Zr–Ox are emerging as active, cost-effective catalysts for methanol synthesis.⁴³ It has been reported that the interfacial synergetic effect between Zn and Zr sites plays a crucial role in enhancing the activity and stability, even in the presence of sulfur species H₂S and SO₂. However, ZnO-based catalysts are also limited by the low activity and the mobility of ZnO.^{44,45}

Recently, indium oxide (In₂O₃) has emerged as a highly selective catalyst for CO₂ hydrogenation to methanol. Oxygen vacancies on the surface of In₂O₃ play a critical role in determining the high selectivity and activity toward CH₃OH.^{46–48} In₂O₃ exhibits both higher methanol selectivity than Cu, Co, or noble metal catalysts and higher catalytic activity than ZnO catalyst. In addition, In₂O₃ can be easily supported and modified to facilitate the activation of both CO₂ and H₂ and stabilize key intermediates.^{49–51, 52–54} However, the CO₂ conversion and methanol yield over the In₂O₃ remain low. A key limiting factor is the low rate of H₂ activation necessary to produce oxygen vacancies and perform hydrogenation reactions. H₂ can be easily activated on the surface of noble and transition metals, among which Pd has been found to play an important role in the improvement of the catalytic performance of In₂O₃. Ye et al.⁵³ found by DFT calculations that the addition of a Pd₄ improved the catalytic performance by providing metal sites for H₂ dissociative

adsorption and interfacial sites for CO₂ adsorption and hydrogenation. Rui et al. prepared a Pd-In₂O₃ catalyst containing highly dispersed Pd nanoparticles and confirmed the DFT predictions of Ye et al.⁵⁵ Similar results have been reported for Pt-promoted In₂O₃.⁵⁶⁻⁵⁸ Due to the mobility of In, often bimetallic phases are formed between In and the metal promoter. Frei et al. proposed that single atom (SA) Pd doped inside the In₂O₃ lattice can stabilize clusters of a few Pd atoms on the In₂O₃ surface, enhancing H₂ activation and, therefore, CH₃OH productivity.⁵⁹ Snider et al. reported by experiments and DFT calculations that the active phase of Pd-In catalysts during CO₂ hydrogenation arises from a synergy between the indium oxide phase and a bimetallic In-Pd particle.⁶⁰ Wu et al. reported by combined DFT and microkinetic study that CH₃OH formation occurs mainly via hydrogenation of formates on Pd-In model surfaces.²⁴ Dostagir et al. have shown by experiments and DFT calculations that Rh atoms encapsulated in In₂O₃ can promote formation of oxygen vacancies and methanol formation via formates.^{61,62} Given their price, it would be advantageous to replace noble metals by Earth-abundant metals like first-row transition metals. Earlier investigations have shown that adding Co⁶³ and Cu⁶⁴ to In₂O₃ can enhance the activity of In₂O₃ for methanol synthesis. More recently, Jia et al. prepared a highly dispersed Ni-In₂O₃ catalyst with significantly enhanced CO₂ conversion compared to the unpromoted oxide while preserving high methanol selectivity.⁶⁵ In nearly all these studies, the formation of atomically dispersed active sites, clusters or single atoms was effective in shifting the selectivity towards the desired product. However, differentiating the catalytic role of single metal atoms and small clusters was challenging, meaning that the exact nature of metal species in the active sites of metal-promoted In₂O₃ catalysts remains unclear. To unravel these aspects, a combination of theoretical models can be employed (*vide infra*).

1.5 Modeling catalysts from first principles

Understanding the mechanism and active phase of catalytic reactions is key to design better catalysts and industrial catalytic processes. The behavior of a catalyst strongly depends on its structure.^{66,67} Factors such as size of metal nanoparticles,⁶⁸ chemical composition,⁶⁹ shape⁷⁰ can impact the performance of a heterogeneous catalyst significantly.⁷¹ For instance, strong metal-support interactions between catalysts and their supports can affect the performance of the active metal phase, leading to the formation of unique electronic structures.⁷²⁻⁷³ Furthermore, the metal-support interaction results in a redistribution of electrons within both the metal and the support that may significantly affect the catalytic activity by enhancing the formation of oxygen vacancies on reducible oxides supports.⁷⁴ Structure-activity relationships and metal-support interactions on supported metal catalysts can be studied with a wide arrange of experimental techniques. However, understanding the reaction mechanism and the active phase of a catalyst relying only on these techniques is difficult. To unravel these aspects, catalyst models based on quantum chemical calculations can be successfully employed. Examples of models for supported metal catalysts are shown in Figure 1.4. Herein, different models are displayed featuring (i) a metal nanoparticle, (ii) a small metal

cluster and a single metal atom either (iii) adsorbed on the surface or (iv) doped in the lattice. Using these models, one can study the catalytic properties of the interface and provide fundamental understanding of the reaction mechanisms.

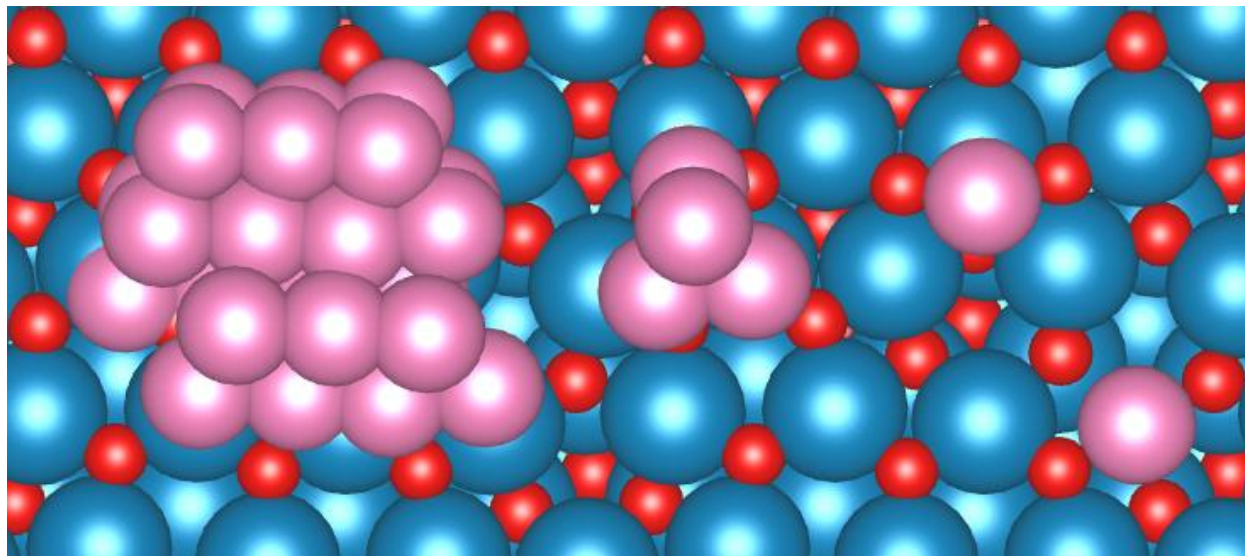


Figure 1.4: Catalyst models of a metal oxide support on which (from left to right) a nanoparticle, a 4-atom cluster, a single atom adsorbed on the surface or doped in the lattice are placed.

1.6 Scope of the thesis

The successful implementation of catalytic processes relies on understanding of the reaction mechanism and its relation to the catalyst structure at the molecular scale. Unraveling these aspects with atomic-level precision remains very challenging when solely based on experimental techniques, making the use of computational methods crucial. In this thesis, we employ density functional theory calculations, genetic algorithms and microkinetic simulations to elucidate the nature of the active phase and mechanism of the methanol synthesis reaction from CO_2 and H_2 . We have chosen indium oxide (In_2O_3) as the support on which nanoclusters and single atoms of transition metals are placed. We mainly focus on Ni as a promoter given its abundance and compare it in some cases to the more noble metals Pd, Pt and Rh. Our work explores the catalytic properties of metal-support interfaces and oxygen vacancies providing new approaches to guide the design of efficient catalytic systems.

Chapter 2 describes the computational approaches and the models used in this study. Density functional theory calculations are performed to obtain adsorption energies and activation barriers of elementary reaction steps. Such energetics are used as input to microkinetic modelling to detail the kinetic properties of the catalysts in CO_2 hydrogenation. The basic concepts of microkinetic simulations are introduced.

Chapter 3 clarifies the role of single atoms (SA) on the $\text{In}_2\text{O}_3(111)$ surface during CO_2 hydrogenation. We investigate four representative SA- In_2O_3 models: (i) Ni- In_2O_3 , (ii) Pd- In_2O_3 (iii) Pt- In_2O_3 and (iv) Rh- In_2O_3 . We study different pathways of CO_2 hydrogenation to CH_3OH and CO and compare trends among the different models.

Chapter 4 investigates the promotional effect of finely dispersed Ni species on In_2O_3 catalyst with a combination of computational methods. The model catalysts included are (i) a single-atom Ni doped inside the In_2O_3 lattice, (ii) a Ni single atom adsorbed on top of the In_2O_3 and (iii) a cluster of 8 Ni atom on top of In_2O_3 . Genetic algorithms are used to identify optimum structures of the Ni clusters on the In_2O_3 surface. By comparing different models, we find the most likely active phase for CO_2 hydrogenation to methanol on Ni- In_2O_3 catalysts.

Chapter 5 discusses the role of bimetallic Ni-In alloys for CO_2 hydrogenation based on DFT and microkinetic study about the mechanism and active phase of CO_2 hydrogenation on bimetallic NiIn catalysts. Herein, we show the effect of isolated Ni sites in activating and hydrogenating CO_2 to either CO , CH_3OH or CH_4 . Furthermore, we compare NiIn surface models with Ni ones to highlight the effect of alloy formation on CO_2 hydrogenation.

Chapter 6 provides insights into the role of Ni-In clusters on In_2O_3 during CO_2 hydrogenation to methanol. From a database of many 8-atom NiIn clusters on the $\text{In}_2\text{O}_3(111)$ surface optimized by a combination of DFT and artificial neural networks, we selected two clusters, a Ni-rich one (Ni_6In_2) and an In-rich one (Ni_2In_6). We employ microkinetic simulations to reveal the effect of the formation of highly dispersed NiIn alloys with different compositions in the activity and selectivity of CO_2 hydrogenation to methanol on Ni- In_2O_3 catalysts.

1.7 References

- (1) Bithas, K.; Kalimeris, P. A Brief History of Energy Use in Human Societies. **2016**, SpringerBriefs in Economics, in: Revisiting the Energy-Development Link, chapter 0, pages 5-10, Springer. ISBN: 9783319207315.
- (2) Kondratenko, E. V.; Mul, G.; Baltrusaitis, J.; Larrazábal, G. O.; Pérez-Ramírez, J. Status and Perspectives of CO_2 Conversion into Fuels and Chemicals by Catalytic, Photocatalytic and Electrocatalytic Processes. *Energy Environ. Sci.* **2013**, 6 (11), 3112–3135.
- (3) González-Garay, A.; Frei, M. S.; Al-Qahtani, A.; Mondelli, C.; Guillén-Gosálbez, G.; Pérez-Ramírez, J. Plant-to-Planet Analysis of CO_2 -Based Methanol Processes. *Energy Environ. Sci.* **2019**, 12 (12), 3425–3436.
- (4) Kondratenko, E. V.; Mul, G.; Baltrusaitis, J.; Larrazábal, G. O.; Pérez-Ramírez, J. Status and Perspectives of CO_2 Conversion into Fuels and Chemicals by Catalytic, Photocatalytic and Electrocatalytic Processes. *Energy Environ. Sci.* **2013**, 6 (11), 3112.

- (5) Dias, V.; Pochet, M.; Contino, F.; Jeanmart, H. Energy and Economic Costs of Chemical Storage. *Front. Mech. Eng.* **2020**, *6*, 21.
- (6) Varone, A.; Ferrari, M. Power to Liquid and Power to Gas: An Option for the German Energiewende. *Renew. Sustain. Energy Rev.* **2015**, *45*, 207–218.
- (7) Chu, S.; Majumdar, A. Opportunities and Challenges for a Sustainable Energy Future. *Nat.* **2012**, *488*7411, 488 (7411), 294–303.
- (8) Gür, T. M. Review of Electrical Energy Storage Technologies, Materials and Systems: Challenges and Prospects for Large-Scale Grid Storage. *Energy Environ. Sci.* **2018**, *11* (10), 2696–2767.
- (9) Dimitriou, I.; García-Gutiérrez, P.; Elder, R. H.; Cuéllar-Franca, R. M.; Azapagic, A.; Allen, R. W. K. Carbon Dioxide Utilisation for Production of Transport Fuels: Process and Economic Analysis. *Energy Environ. Sci.* **2015**, *8* (6), 1775–1789.
- (10) Brunetti, A.; Scura, F.; Barbieri, G.; Drioli, E. Membrane Technologies for CO₂ Separation. *J. Membr. Sci.* **2010**, *359* (1–2), 115–125.
- (11) Centi, G.; Quadrelli, E. A.; Perathoner, S. Catalysis for CO₂ Conversion: A Key Technology for Rapid Introduction of Renewable Energy in the Value Chain of Chemical Industries. *Energy Environ. Sci.* **2013**, *6* (6), 1711–1731..
- (12) Bill Gates. *How to Avoid a Climate Disaster*; **2021**, Allen Lane, ISBN: 059321577X.
- (13) Tian Z.; Priest C.; Chen L.; Recent Progress in the Theoretical Investigation of Electrocatalytic Reduction of CO₂, *Adv. Theory Simul.* **2018**, *1*, 1800004.
- (14) Pei, Y.; Zhong, H.; Jin, F. A Brief Review of Electrocatalytic Reduction of CO₂—Materials, Reaction Conditions, and Devices. *Energy Sci. Eng.* **2021**, *9* (7), 1012–1032.
- (15) Gao, P.; Li, S.; Bu, X.; Dang, S.; Liu, Z.; Wang, H.; Zhong, L.; Qiu, M.; Yang, C.; Cai, J.; Wei, W.; Sun, Y. Direct Conversion of CO₂ into Liquid Fuels with High Selectivity over a Bifunctional Catalyst. *Nat. Chem.* **2017**, *9* (10), 1019–1024.
- (16) Porosoff, M. D.; Yan, B.; Chen, J. G. Catalytic Reduction of CO₂ by H₂ for Synthesis of CO, Methanol and Hydrocarbons: Challenges and Opportunities. *Energy Environ. Sci.* **2016**, *9* (1), 62–73.
- (17) Dang, S.; Yang, H.; Gao, P.; Wang, H.; Li, X.; Wei, W.; Sun, Y. A Review of Research Progress on Heterogeneous Catalysts for Methanol Synthesis from Carbon Dioxide Hydrogenation. *Catal. Today* **2018**, *330* (March 2018), 61–75.
- (18) Guan, H.; Chen, Y.; Ruan, C.; Lin, J.; Su, Y.; Wang, X.; Qu, L. Versatile Application of Wet-Oxidation for Ambient CO Abatement over Fe(OH)_x Supported Sub-nanometer Platinum Group Metal Catalysts. *Chin. J. Catal.* **2020**, *41* (4), 613–621.
- (19) Gong, J.; Chu, M.; Guan, W.; Liu, Y.; Zhong, Q.; Cao, M.; Xu, Y. Regulating the Interfacial Synergy of Ni/Ga₂O₃ for CO₂ Hydrogenation toward the Reverse Water–Gas Shift Reaction. **2021**.
- (20) Alam, M. I.; Cheula, R.; Moroni, G.; Nardi, L.; Maestri, M. Mechanistic and Multiscale Aspects of Thermo-Catalytic CO₂ Conversion to C₁ Products. *Catal. Sci. Technol.* **2021**, *11* (20), 6601–6629.

- (21) Barbera, M; Mantoan F.; Bertucco, A.; Bezzo, F.; Hydrogenation to convert CO₂ to C₁ chemicals: Technical comparison of different alternatives by process simulation. *Can J Chem Eng.*, **2020**; 98:1893–1906.
- (22) Zhang, Y.; Zhang, T.; Das, S. Catalytic Transformation of CO₂ into C₁ Chemicals Using Hydrosilanes as a Reducing Agent. *Green Chem.* **2020**, 22 (6), 1800–1820.
- (23) Jangam, A.; Das, S.; Dewangan, N.; Hongmanorom, P.; Hui, W. M.; Kawi, S. Conversion of CO₂ to C₁ Chemicals: Catalyst Design, Kinetics and Mechanism Aspects of the Reactions. *Catal. Today* **2020**, 358, 3–29.
- (24) Li, Y.; Cui, X.; Dong, K.; Junge, K.; Beller, M. Utilization of CO₂ as a C₁ Building Block for Catalytic Methylation Reactions. *ACS Catal.* **2017**, 7 (2), 1077–1086.
- (25) Götz, M.; Lefebvre, J.; Mörs, F.; McDaniel Koch, A.; Graf, F.; Bajohr, S.; Reimert, R.; Kolb, T. Renewable Power-to-Gas: A Technological and Economic Review. *Renew. Energy* **2016**, 85, 1371–1390.
- (26) Ghaib, K.; Nitz, K.; Ben-Fares, F. Z. Chemical Methanation of CO₂: A Review. *ChemBioEng Rev.* **2016**, 3 (6), 266–275.
- (27) Wang, Y.; Gao, X.; Wu, M.; Tsubaki, N. Thermocatalytic Hydrogenation of CO₂ into Aromatics by Tailor-Made Catalysts: Recent Advancements and Perspectives. *EcoMat* **2021**, 3 (1).
- (28) Goepfert, A.; Czaun, M.; Jones, J.-P.; Surya Prakash, G. K.; Olah, G. A. Recycling of Carbon Dioxide to Methanol and Derived Products – Closing the Loop. *Chem.Soc.Rev.* **2014**, 43 (23), 7995–8048.
- (29) Olah, G. A. Beyond Oil and Gas: The Methanol Economy. *Angew. Chem. - Int. Ed.* **2005**, 44 (18), 2636–2639..
- (30) Tian, P.; Wei, Y.; Ye, M.; Liu, Z. Methanol to Olefins (MTO): From Fundamentals to Commercialization. *ACS Catal.* **2015**, 5 (3), 1922–1938.
- (31) Chorkendorff, I.; Niemantsverdriet, J. W. Chapter 5 - Solid Catalysts. *Concepts Mod. Catal. Kinet.* **2013**, 206–210.
- (32) Matsumoto, S. Recent Advances in Automobile Exhaust Catalysts. *Catal. Today* **2004**, 90 (3–4), 183–190.
- (33) Rodriguez, J. A.; Liu, P.; Stacchiola, D. J.; Senanayake, S. D.; White, M. G.; Chen, J. G. Hydrogenation of CO₂ to Methanol: Importance of Metal-Oxide and Metal-Carbide Interfaces in the Activation of CO₂. *ACS Catal.* **2015**, 5 (11), 6696–6706.
- (34) Ren, M.; Zhang, Y.; Wang, X.; Qiu, H. Catalytic Hydrogenation of CO₂ to Methanol: A Review. *Catalysts* **2022**, 12, 403.
- (35) Bowker, M. Methanol Synthesis from CO₂ Hydrogenation. *ChemCatChem* **2019**, 11 (17), 4238–4246.
- (36) Jadhav, S. G.; Vaidya, P. D.; Bhanage, B. M.; Joshi, J. B. Catalytic Carbon Dioxide Hydrogenation to Methanol: A Review of Recent Studies. *Chem. Eng. Res. Des.* **2014**, 92 (11), 2557–2567.
- (37) Wang, W.-H.; Himeda, Y.; Muckerman, J. T.; Manbeck, G. F.; Fujita, E. CO₂ Hydrogenation to Formate and Methanol as an Alternative to Photo- and Electrochemical CO₂ Reduction. *Chem. Rev.* **2015**, 115 (23), 12936–12973.
- (38) Zhong, Z.; Etim, U.; Song, Y. Improving the Cu/ZnO-Based Catalysts for Carbon Dioxide Hydrogenation to Methanol, and the Use of Methanol As a Renewable Energy Storage Media. *Front. Energy Res.* **2020**, 8.

-
- (39) Niu, J.; Liu, H.; Jin, Y.; Fan, B.; Qi, W.; Ran, J. Comprehensive Review of Cu-Based CO₂ Hydrogenation to CH₃OH: Insights from Experimental Work and Theoretical Analysis. *Int. J. Hydrog. Energy* **2022**, *47* (15), 9183–9200.
- (40) Kanuri, S.; Roy, S.; Chakraborty, C.; Datta, S. P.; Singh, S. A.; Dinda, S. An Insight of CO₂ Hydrogenation to Methanol Synthesis: Thermodynamics, Catalysts, Operating Parameters, and Reaction Mechanism. *Int. J. Energy Res.* **2022**, *46* (5), 5503–5522.
- (41) Schwiderowski, P.; Ruland, H.; Muhler, M. Current Developments in CO₂ Hydrogenation towards Methanol: A Review Related to Industrial Application. *Curr. Opin. Green Sustain. Chem.* **2022**, *38*, 100688.
- (42) Zhong, J.; Yang, X.; Wu, Z.; Liang, B.; Huang, Y.; Zhang, T. State of the Art and Perspectives in Heterogeneous Catalysis of CO₂ Hydrogenation to Methanol. *Chem. Soc. Rev.* **2020**, *49* (5), 1385–1413.
- (43) Li, K.; Chen, J. G. CO₂ Hydrogenation to Methanol over ZrO₂-Containing Catalysts: Insights into ZrO₂ Induced Synergy. *ACS Catal.* **2019**, *9* (9), 7840–7861.
- (44) Wang, J.; Li, G.; Li, Z.; Tang, C.; Feng, Z.; An, H.; Liu, H.; Liu, T.; Li, C. A Highly Selective and Stable ZnO-ZrO₂ Solid Solution Catalyst for CO₂ Hydrogenation to Methanol. *Sci. Adv.* **2017**, *3* (10).
- (45) Lunkenbein, T.; Schumann, J.; Behrens, M.; Schlögl, R.; Willinger, M. G. Formation of a ZnO Overlayer in Industrial Cu/ZnO/Al₂O₃ Catalysts Induced by Strong Metal-Support Interactions. *Angew. Chem. - Int. Ed.* **2015**, *54* (15), 4544–4548.
- (46) Frei, M. S.; Capdevila-Cortada, M.; García-Muelas, R.; Mondelli, C.; López, N.; Stewart, J. A.; Curulla Ferré, D.; Pérez-Ramírez, J. Mechanism and Microkinetics of Methanol Synthesis via CO₂ Hydrogenation on Indium Oxide. *J. Catal.* **2018**, *361*, 313–321.
- (47) Ye, J.; Liu, C.; Ge, Q. DFT Study of CO₂ Adsorption and Hydrogenation on the In₂O₃ Surface. *J. Phys. Chem. C* **2012**, *116* (14), 7817–7825.
- (48) Ye, J.; Liu, C.; Mei, D.; Ge, Q. Active Oxygen Vacancy Site for Methanol Synthesis from CO₂ Hydrogenation on In₂O₃(110): A DFT Study. *ACS Catal.* **2013**, *3* (6), 1296–1306.
- (49) Dou, M.; Zhang, M.; Chen, Y.; Yu, Y. Theoretical Study of Methanol Synthesis from CO₂ and CO Hydrogenation on the Surface of ZrO₂ Supported In₂O₃ Catalyst. *Surf. Sci.* **2018**.
- (50) Wu, P.; Yang, B. Intermetallic PdIn Catalyst for CO₂ Hydrogenation to Methanol: Mechanistic Studies with a Combined DFT and Microkinetic Modeling Method. *Catal. Sci. Technol.* **2019**, *9* (21), 6102–6113.
- (51) Dou, M.; Zhang, M.; Chen, Y.; Yu, Y. DFT Study of In₂O₃-Catalyzed Methanol Synthesis from CO₂ and CO Hydrogenation on the Defective Site. *New J. Chem.* **2018**, *42* (5), 3293–3300.
- (52) Rui, N.; Wang, Z.; Sun, K.; Ye, J.; Ge, Q.; Liu, C. jun. CO₂ Hydrogenation to Methanol over Pd/In₂O₃: Effects of Pd and Oxygen Vacancy. *Appl. Catal. B Environ.* **2017**, *218*, 488–497.
- (53) Ye, J.; Liu, C. J.; Mei, D.; Ge, Q. Methanol Synthesis from CO₂ Hydrogenation over a Pd₄/In₂O₃ Model Catalyst: A Combined DFT and Kinetic Study. *J. Catal.* **2014**, *317*, 44–53.
- (54) Ye, J.; Ge, Q.; Liu, C. Effect of PdIn Bimetallic Particle Formation on CO₂ Reduction over the Pd–In/SiO₂ Catalyst. *Chem. Eng. Sci.* **2015**, *135*, 193–201.
-

- (55) Rui, N.; Wang, Z.; Sun, K.; Ye, J.; Ge, Q.; Liu, C. jun. CO₂ Hydrogenation to Methanol over Pd/In₂O₃: Effects of Pd and Oxygen Vacancy. *Appl. Catal. B Environ.* **2017**, *218*, 488–497.
- (56) Sun, K.; Rui, N.; Zhang, Z.; Sun, Z.; Ge, Q.; Liu, C. J. A Highly Active Pt/In₂O₃ catalyst for CO₂ hydrogenation to Methanol with Enhanced Stability. *Green Chem.* **2020**, *22* (15), 5059–5066.
- (57) Sun, K.; Rui, N.; Shen, C.; Liu, C. J. Theoretical Study of Selective Hydrogenation of CO₂ to Methanol over Pt₄/In₂O₃ Model Catalyst. *J. Phys. Chem. C* **2021**, *125* (20), 10926–10936.
- (58) Han, Z.; Tang, C.; Wang, J.; Li, L.; Li, C. Atomically Dispersed Ptⁿ⁺ Species as Highly Active Sites in Pt/In₂O₃ Catalysts for Methanol Synthesis from CO₂ Hydrogenation. *J. Catal.* **2020**.
- (59) Frei, M. S.; Mondelli, C.; García-Muelas, R.; Kley, K. S.; Puértolas, B.; López, N.; Safonova, O. V.; Stewart, J. A.; Curulla Ferré, D.; Pérez-Ramírez, J. Atomic-Scale Engineering of Indium Oxide Promotion by Palladium for Methanol Production via CO₂ Hydrogenation. *Nat. Commun.* **2019**, *10* (1), 1–11.
- (60) Snider, J. L.; Streibel, V.; Hubert, M. A.; Choksi, T. S.; Valle, E.; Upham, D. C.; Schumann, J.; Duyar, M. S.; Gallo, A.; Abild-Pedersen, F.; Jaramillo, T. F. Revealing the Synergy between Oxide and Alloy Phases on the Performance of Bimetallic In-Pd Catalysts for CO₂ Hydrogenation to Methanol. *ACS Catal.* **2019**, *9* (4), 3399–3412.
- (61) Dostagir, N. H. M.; Thompson, C.; Kobayashi, H.; Karim, A. M.; Fukuoka, A.; Shrotri, A. Rh Promoted In₂O₃ as a Highly Active Catalyst for CO₂ hydrogenation to Methanol. *Catal. Sci. Technol.* **2020**, *10* (24), 8196–8202.
- (62) Wang, J.; Sun, K.; Jia, X.; Liu, C. jun. CO₂ Hydrogenation to Methanol over Rh/In₂O₃ Catalyst. *Catal. Today* **2021**, *365*, 341–347.
- (63) Bavykina, A.; Yarulina, I.; Al Abdulghani, A. J.; Gevers, L.; Hedhili, M. N.; Miao, X.; Galilea, A. R.; Pustovarenko, A.; Dikhtiarenko, A.; Cadiou, A.; Aguilar-Tapia, A.; Hazemann, J.-L.; Kozlov, S. M.; Oud-Chikh, S.; Cavallo, L.; Gascon, J. Turning a Methanation Co Catalyst into an In-Co Methanol Producer. *ACS Catal.* **2019**, *9*, 6910–6918.
- (64) Shi, Z.; Tan, Q.; Tian, C.; Pan, Y.; Sun, X.; Zhang, J.; Wu, D. CO₂ Hydrogenation to Methanol over Cu-In Intermetallic Catalysts: Effect of Reduction Temperature. *J. Catal.* **2019**, *379*, 78–89.
- (65) Jia, X.; Sun, K.; Wang, J.; Shen, C.; Liu, C. jun. Selective Hydrogenation of CO₂ to Methanol over Ni/In₂O₃ Catalyst. *J. Energy Chem.* **2020**, *50*, 409–415.
- (66) Sun, G.; Alexandrova, A. N.; Sautet, P.; *ACS Catal.* **2020**, *10*, 5309–5317.
- (67) Liu, J. X.; Su, Y.; Filot, I. A. W.; Hensen, E. J. M. A Linear Scaling Relation for CO Oxidation on CeO₂-Supported Pd. *J. Am. Chem. Soc.* **2018**, *140* (13), 4580–4587.
- (68) Leendert Bezemer, G.; Bitter, J. H.; Kuipers, H. P. C. E.; Oosterbeek, H.; Holewijn, J. E.; Xu, X.; Kapteijn, F.; Jos Van Dillen, A.; De Jong, K. P. Cobalt Particle Size Effects in the Fischer-Tropsch Reaction Studied with Carbon Nanofiber Supported Catalysts. **2006**.
- (69) Zhang, L.; Su, Y. Q.; Chang, M. W.; Filot, I. A. W.; Hensen, E. J. M. Linear Activation Energy-Reaction Energy Relations for LaBO₃ (B = Mn, Fe, Co, Ni) Supported Single-Atom Platinum Group Metal Catalysts for CO Oxidation. *J. Phys. Chem. C* **2019**, *123* (51), 31130–31141.

- (70) Spezzati, G.; Benavidez, A. D.; DeLaRiva, A. T.; Su, Y.; Hofmann, J. P.; Asahina, S.; Olivier, E. J.; Neethling, J. H.; Miller, J. T.; Datye, A. K.; Hensen, E. J. M. CO Oxidation by Pd Supported on CeO₂(100) and CeO₂(111) Facets. *Appl. Catal. B Environ.* **2019**, *243*, 36–46.
- (71) Zhou, J.; Gao, Z.; Xiang, G.; Zhai, T.; Liu, Z.; Zhao, W.; Liang, X.; Wang, L. Interfacial Compatibility Critically Controls Ru/TiO₂ Metal-Support Interaction Modes in CO₂ Hydrogenation. *Nat. Commun.* **2022**, *13* (1), 1–10.
- (72) Slavinskaya, E. M.; Kardash, T. Y.; Stonkus, O. A.; Gulyaev, R. V.; Lapin, I. N.; Svetlichnyi, V. A.; Boronin, A. I. Metal-Support Interaction in Pd/CeO₂ Model Catalysts for CO Oxidation: From Pulsed Laser-Ablated Nanoparticles to Highly Active State of the Catalyst †. *Cite This Catal Sci Technol* **2014**, *6*, 6650.
- (73) Hansen, P. L.; Wagner, J. B.; Helveg, S.; Rostrup-Nielsen, J. R.; Clausen, B. S.; Topsøe, H. Atom-Resolved Imaging of Dynamic Shape Changes in Supported Copper Nanocrystals. *Science* **2002**, *295* (5562), 2053–2055.
- (74) Lin, F.; Hoang, D. T.; Tsung, C. K.; Huang, W.; Lo, S. H. Y.; Wood, J. B.; Wang, H.; Tang, J.; Yang, P. Catalytic Properties of Pt Cluster-Decorated CeO₂ Nanostructures. *Nano Res.* **2010**, *4* (1), 61–71.

CHAPTER 2

Computational Methods

2.1 Introduction

The macroscopic rate of a catalytic reaction is the result of the interplay of events occurring at different length and time scales¹ and as such the observed catalyst functionality is a multiscale property of the system (Figure 2.1). To model chemical reactivity, detailed understanding of its underlying processes at the various scales involved is thus of crucial importance. At the nanoscale, the kinetic parameters of the elementary reaction steps that make up the overall rate are related to the making and breaking of chemical bonds and ultimately to the behavior of the electrons and the interactions between the active site and molecules. At the mesoscale the rates of the possible reaction steps and their interplay give rise to the prevalent catalytic mechanism. Transport phenomena occurring under the specific conditions of pressure, temperature and composition result in the observed catalytic behavior at the macroscale. To investigate catalytic reactions, a wide range of computational modeling techniques covering different time and length scales are used in a complementary manner. Combining methods at different length and time scales is termed *multi-scale* modelling. An important prerequisite is that the rate constants of the elementary reaction steps that make up the mechanism of a catalytic reaction can be accurately predicted. This can be achieved by employing electronic structure calculations. A comprehensive introduction to electronic structure theory can be found in the book by Szabo and Ostlund.² Detailed description about DFT methods can be found in the books from Parr and Weitao and Parr and Yang.^{3,4} The information gathered at this level of theory can be used to construct kinetic models such as a microkinetic model to ultimately arrive at a macroscopic rate equation for a catalytic reaction. The combination of electronic structure calculations and microkinetic simulations is termed first-principles microkinetic modeling.

In this thesis, we make use of multiscale analysis based on microkinetic modeling to predict chemical reactivity of reducible oxides under CO₂ reduction to methanol and carbon monoxide. These properties are directly related to the electronic properties of the chemical system and can only be described when such electronic structure is taken in account. First, *ab initio* modeling using Density Functional Theory (DFT) is employed to calculate the electronic structure of the chemical system and construct the reaction energy surface for calculating rate constants and energetics. Second, this dataset is used to construct a chemical reaction network, which serves as the parameters for a microkinetic model (MKM) that is made up of all relevant elementary reaction steps in the mechanism of the reaction under study. With this, we can predict surface coverages, reaction rates of individual steps and, also, the overall macroscopic reaction rate. Such understanding is essential to interpret spectroscopic and catalytic data.

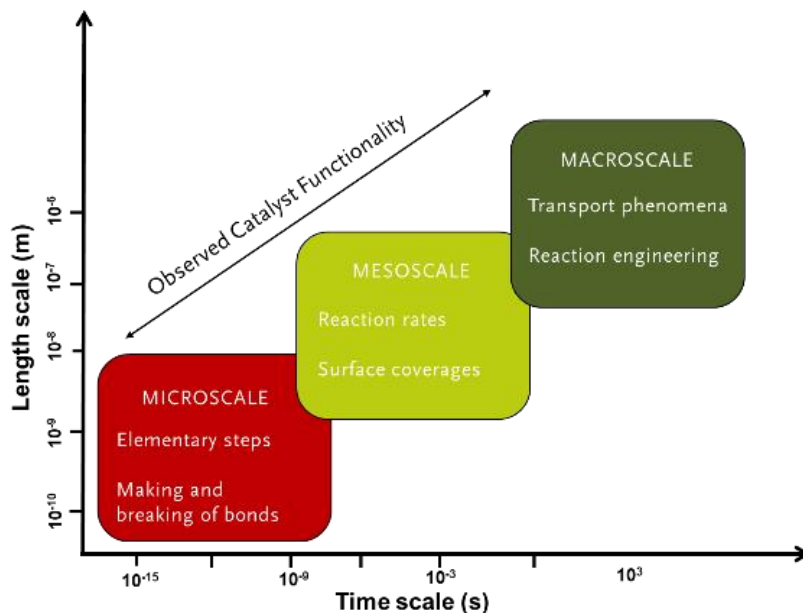


Figure 2.1: Schematic representation of the time and length scales involved in a catalytic process.

In the upcoming sections, a description of the electronic structure methods and the microkinetic modelling procedure will be given. An overview of commonly used analysis techniques within this work, e.g. crystal orbital Hamiltonian population and degree of rate control, are provided as well.

2.2 Quantum chemical methods

2.2.1 The electronic structure problem

Questions about the electronic structure of chemical systems can be resolved by means of quantum mechanics. Herein, the goal is to find solutions to the non-relativistic time-independent Schrödinger equation as given by

$$\hat{H} |\Psi\rangle = E |\Psi\rangle \quad (2.1)$$

Herein, \hat{H} is the Hamiltonian operator for a system of nuclei and electrons described by position vectors \mathbf{R}_j and \mathbf{r}_i respectively. Ψ is the wave function and E refers to the energy of the system.

In atomic units, the Hamiltonian can be expressed as follows:⁵

$$\hat{H} = -\frac{1}{2} \sum_{i=1}^N \nabla_i^2 - \frac{1}{2} \sum_{j=1}^M \frac{1}{M_j} \nabla_j^2 - \sum_{i=1}^N \sum_{j=1}^M \frac{Z_j}{r_{i,j}} + \sum_{i=1}^N \sum_{k>i}^N \frac{1}{r_{i,k}} + \sum_{j=1}^M \sum_{l>j}^M \frac{Z_j Z_l}{R_{j,l}} \quad (2.2)$$

M_j is here the ratio of the mass of the nucleus j to the mass of an electron and Z is the atomic number of nucleus j . The five terms in the above equation correspond, in order, to the kinetic energy of the electrons,

the kinetic energy of the nuclei, the interaction energy between each electron and the collection of atomic nuclei, the interaction between different electrons and finally the repulsion between the nuclei.

Central to many electronic structure calculations is the Born-Oppenheimer approximation.⁶ Within this approximation, since the nuclei are much heavier than the electrons, we can assume that the electrons will spontaneously adjust their position under any perturbation of the nuclei. Furthermore, the repulsion between the nuclei is considered constant. The result is the decoupling of the electronic degrees of freedom from the nuclear degrees of freedom wherein the electron motion can be described by its motion in an electrostatic field produced by the nuclei. The remaining terms are collected in the so-called electronic Hamiltonian (\hat{H}_{elec}) describing the motion of N electrons in the field of M point charges:

$$\hat{H}_{\text{elec}} = -\frac{1}{2} \sum_{i=1}^N \nabla_i^2 - \sum_{i=1}^N \sum_{j=1}^M \frac{Z_j}{r_{i,j}} + \sum_{i=1}^N \sum_{k>i}^N \frac{1}{r_{i,k}} \quad (2.3)$$

This form of the Hamiltonian is called the electronic Hamiltonian, which acts on the many-electron wavefunction Ψ to produce the energy E . Because of the decoupling of the nuclear from the electronic degrees of freedom the electronic energy due to the repulsion between the nuclei (i.e. the fifth term in equation 2.2) becomes a constant which is added to the electronic energy to obtain the total energy of the electronic problem. The solution of the corresponding Schrödinger equation involving the electronic Hamiltonian is the electronic wave function. Obtaining a solution to such equation is the main focus in electronic structure calculations.

The electronic Hamiltonian depends only on the spatial coordinates of the electrons. To completely describe an electron it is necessary, however, to also specify its *spin*. Within the context of the non-relativistic Schrödinger equation, there is no term in the Hamiltonian that acts directly upon the spin of the electrons, however, the spin state is indirectly accounted for by the form of the wave function as will be shown below.

We introduce two spin functions corresponding to spin up and spin down respectively. These are functions of an unspecified spin variable. We then collect the three spatial coordinates \mathbf{r} with the spin variable ω into a four-variable electron coordinate \mathbf{x} :

$$\mathbf{x} = \{\mathbf{r}, \omega\} \quad (2.4)$$

In this formalism, an electron is described not only by the three spatial coordinates but also by one spin coordinate. The wave function for a single electron that describes both its spatial distribution as well as its spin is called a *spin-orbital*.

When considering a collection of electrons, as in a molecule, one could take the product of a set of single electron wave-functions to give equation (2.5):

$$\Psi^{\text{HP}} = \prod_{i=1}^N \chi_i(\mathbf{x}_i) \quad (2.5)$$

Where $\chi(\mathbf{x})$ is the so-called spin-orbital. Such a wavefunction is termed a Hartree product and assumes independent non-interacting electrons. This approach has a basic deficiency: it takes no account of the indistinguishability of electrons and thus does not satisfy the antisymmetry principle. To comply with this principle, a wave function needs to be built that is antisymmetric upon exchange of the coordinates \mathbf{x} (both space and spin) of any two electrons. This can be accomplished by using a Slater determinant which basically takes a series of linear combinations of all possible Hartree products and is given by

$$\Psi(\mathbf{x}_1, \mathbf{x}_2, \dots, \mathbf{x}_N) = (N!)^{-\frac{1}{2}} \begin{bmatrix} \chi_i(\mathbf{x}_1) & \cdots & \chi_k(\mathbf{x}_1) \\ \vdots & \ddots & \vdots \\ \chi_i(\mathbf{x}_N) & \cdots & \chi_k(\mathbf{x}_N) \end{bmatrix}. \quad (2.6)$$

Herein, the factor $(N!)^{-\frac{1}{2}}$ acts as a normalization factor. Note that the rows of an N -electron Slater determinant are labeled by electrons, while the columns are labeled by spin orbitals. Interchanging the coordinates of two electrons corresponds to interchanging two rows of the Slater determinant, which changes the sign of the determinant, satisfying the antisymmetry principle. Furthermore, note that expansion of the determinant in equation (2.6) yields a large set of terms ($N!$ to be precise) of all possible combinations between the electrons and the spin-orbitals. Clearly, in such an expansion one is unable to distinguish between individual electrons and hence this feature properly represents the indistinguishable nature of the electrons. Conclusively, the Slater determinants meets all the necessary requirements.

2.2.2 The Hartree-Fock approximation

Finding and explaining approximate solutions to the Schrödinger equation has been a key challenge in quantum chemistry. The Hartree-Fock approximation is one of the main ones and usually constitutes a first step towards more accurate approximations. The basic idea underlying the Hartree-Fock method is that a single Slater determinant can be used to describe the ground state of an N -electron system, as given by:

$$|\Psi_0\rangle = |\chi_1, \chi_2, \dots, \chi_N\rangle \quad (2.7)$$

The best approximate wave function can be found by applying the variational principle stating that the best wave function of this functional form is the one which gives the lowest possible energy

$$E_0 = \langle \Psi_0 | \hat{H} | \Psi_0 \rangle \quad (2.8)$$

Where H is the full electronic Hamiltonian and Ψ_0 the ground state wave function. The variational flexibility in the wave function (2.7) lies in the linear coefficients that build molecular orbitals from the basis functions. By minimizing E_0 with respect to the choice of spin orbitals, one can derive an equation, called the Hartree-Fock equation which determines the optimal spin orbitals:

$$f_i \chi(\mathbf{x}_i) = \epsilon \chi(\mathbf{x}_i) \quad (2.9)$$

where f_i is an effective one-electron operator, called the Fock operator. The essence of the Hartree-Fock approximation is to replace the complicated many-electron problem by a one-electron problem in which electron-electron repulsion is treated in an average way.

The major drawback in the Hartree-Fock approximation is that the correlation of the movement of the electrons is neglected. The exchange is however treated in an exact manner. Thus, the method fails to describe the instantaneous electron-electron repulsion, hence also dispersion and van der Waals interactions are poorly represented within this theory.

Many post-Hartree-Fock methods have been developed to incorporate the electron-electron correlation. Relevant examples include the Configuration interaction (CI) method⁷ which uses a linear combination of Slater determinants instead of a single one. Møller-Plesset⁸ perturbation theory treats electron correlation using perturbation theory. In the Coupled Cluster method,⁹ the electron correlation is handled through use of a so-called cluster operations.

Although all these methods provide chemically accurate descriptions of the electronic structure, their application is limited because of their scaling with the number of electrons. Whereas Hartree-Fock scales by N^4 where N is the number of atoms, second-order Møller-Plesset perturbation theory scales by N^5 , coupled cluster using single and doubles scales by N^6 , and finally configuration interaction can have a scaling as high as N^9 . Generally, given the scaling behavior with respect to the number of atoms, these approaches are only applicable to calculations involving relatively small systems. In practice they find applications to systems with less than 50 atoms. As the majority of the systems of interest in heterogeneous catalysis are in the order of 100-200 atoms, these methods are not suitable for engineering applications.

2.2.3 Density Functional Theory

In contrast with the Hartree-Fock and post-Hartree-Fock methods, density functional theory (DFT) uses electron density as the central quantity. Specifically, only for the coulombic interaction, the exchange and the correlation interaction the electron density is used. The kinetic energy of the electrons is still being calculated from the wave function. By substituting the many-body wave function with the electron density, the dimensionality of the problem is reduced because the electron density is always three-dimensional regardless of the number of electrons. As a result, DFT can effectively treat significantly larger systems. For these reasons, DFT has become a standard method in electronic structure calculations, particularly in the field of computational catalysis. Comprehensive discussions on DFT can be found in excellent reviews.^{4,10}

2.2.3.1 Hohenberg-Kohn theorems

An important step in the development of DFT was done thanks to the paper of Hohenberg and Kohn.¹¹ Herein, two fundamental theorems were postulated. The first theorem states: “*The ground state of any interacting many-particle system with a given fixed inter-particle interaction is a unique functional of the electron density.*” The first theorem entails that there exists a one-to-one mapping between the ground-state external potential (from the nuclei) and the ground-state electron density. Thus, the ground-state electron density uniquely determines the electronic properties of the system, such as the total energy and wave function of the ground state.

We can thus write the energy E explicitly as a functional of the electron density:

$$E[\rho] = T[\rho] + V[\rho] + U[\rho] \quad (2.10)$$

Where $T[\rho]$, $V[\rho]$ and $U[\rho]$ are the kinetic energy, the external potential and the electron interaction energy respectively. It should also be noticed that, although the theory states that the kinetic energy can be evaluated based on the electron density, the functional dependence is unknown and in practice it is evaluated from the (independent particle) wave function.

Herein, the electron density is defined as:

$$\rho(\mathbf{r}) = \sum_{i=1}^N |\Psi_i(\mathbf{r})|^2 \quad (2.11)$$

Although the first Hohenberg-Kohn theorem shows that it is possible to employ a functional of the electron density to solve the electronic problem, it does not provide additional information on the form of this functional which is still unknown. The second Hohenberg-Kohn theorem states that: “*The electron density that minimizes the energy of the overall functional is the true electron density corresponding to the full solution of the Schrodinger equation*”. The second Hohenberg-Kohn theorem demonstrates that the ground state energy can be obtained using the variational principle, where the density that gives the lowest energy is the exact ground state density. This gives us a detailed prescription for finding the wave function and the electron density in the ground state.

Given an external potential $v(\mathbf{r})$, equation (2.10) can be rewritten as follows:

$$E[\rho(\mathbf{r})] = \int v(\mathbf{r})_{\text{XC}} \rho(\mathbf{r}) d\mathbf{r} + F[\rho(\mathbf{r})] \quad (2.12)$$

Note that $F\rho(\mathbf{r})$ is a universal functional of the electron density valid for any number of particles and any external potential which integrates the kinetic and electron-electron interaction energy:

$$F[\rho] = T[\rho] + \frac{1}{2} \int \int \frac{\rho(\mathbf{r})\rho(\mathbf{r}')}{|\mathbf{r} - \mathbf{r}'|} d\mathbf{r}d\mathbf{r}' + E_{XC}[\rho] \quad (2.13)$$

Plugging the above equation into the expression for the energy we obtain:

$$E[\rho] = T[\rho] + \int v_{XC}(\mathbf{r})\rho(\mathbf{r})d\mathbf{r} + \frac{1}{2} \int \int \frac{\rho(\mathbf{r})\rho(\mathbf{r}')}{|\mathbf{r} - \mathbf{r}'|} d\mathbf{r}d\mathbf{r}' + E_{XC}[\rho] \quad (2.14)$$

The four terms in this equation are, in order, the kinetic energy, the potential energy, the electron-electron interaction energy, and the exchange correlation functional. $T[\rho]$ can be exactly calculated but not on the basis of ρ but on the basis of the underlying wave function while the fourth term, corresponding to the exchange correlation functional is unknown.

Since exact expressions are known for the first three terms, we can collect these in a so-called “known” energetic term. The term $E_{XC}[\rho]$ includes the non-classical aspects of the electron-electron interaction along with the component of the kinetic energy of the real system different from the fictitious non-interacting system.

2.2.3.3 Kohn-Sham equations

The Hohenberg-Kohn theorems previously discussed point out a way to obtain the ground state energy. However, it is still difficult to find the ground energy state solution from the total energy functional because the exchange-correlation functional is yet undefined.

To solve this problem, Kohn and Sham demonstrated that the electron density can be written in a way that involves solving a set of single-electron equations. They employed the non-interacting single-electron kinetic energy functional $T_s[\rho(\mathbf{r})]$ to replace the actual kinetic energy functional $T[\rho(\mathbf{r})]$.

The kinetic energy for this system would be

$$T_s[\rho] = \sum_i^N \langle \chi_i | -\frac{1}{2} \nabla^2 | \chi_i \rangle \quad (2.15)$$

Furthermore, the $E_{XC}[\rho]$ as shown in eq. 2.13 is now defined as the exchange and correlation energy of an *interacting* system and it also includes all the differences between the real kinetic energy term and non-interacting single electron kinetic energy term.

This gives the following expression for the total energy:

$$E[\rho] = T_s[\rho] + \int v(\mathbf{r})\rho(\mathbf{r})d\mathbf{r} + \frac{1}{2} \int \int \frac{\rho(\mathbf{r})\rho(\mathbf{r}')}{|\mathbf{r} - \mathbf{r}'|} d\mathbf{r}d\mathbf{r}' + E_{XC}[\rho] \quad (2.16)$$

The Kohn–Sham equations are found by varying the total energy expression with respect to a set of orbitals, subject to constraints on those orbitals, to yield the Kohn–Sham potential as

To derive the non-interacting kinetic term $T_s[\rho]$, the set Kohn-Sham equations reported below needs to be solved:

$$\left\{ -\frac{\nabla^2}{2} + v_{KS}[\rho(\mathbf{r})] \right\} \Psi_i(\mathbf{r}) = \epsilon_i \Psi_i(\mathbf{r}) \quad (2.17)$$

$$v_{KS}[\rho(\mathbf{r})] = v(\mathbf{r}) + \int \frac{\rho(\mathbf{r}')}{|\mathbf{r} - \mathbf{r}'|} d\mathbf{r}' + \frac{\delta E_{XC}[\rho]}{\delta \rho(\mathbf{r})} \quad (2.18)$$

Where ϵ_i represents the lowest eigenvalues of a Kohn-Sham single-electron equation. We remark a fundamental difference between the Kohn-Sham equations and the full Schrödinger equation: the solution of the Kohn-Sham equations are single-electron wave functions that depend only on three spatial variables. In equation (2.17), V_{KS} is the full Kohn-Sham potential which includes a term for the interaction between an electron and the collection of atomic nuclei, $V(\mathbf{r})$. The second term of the Kohn-Sham potential is the Hartree potential which describes the Coulomb repulsion between the electrons. The third term refers to the potential for the exchange and correlation contributions to the single-electron equations. The second and third term both depend on the total electron density $\rho(\mathbf{r})$ resulting from all electrons in the system in an averaged way. The Kohn-Sham equations are a set of integro-differential equations. The solutions are found by starting with some carefully chosen set of linear coefficients. Next, all the properties are calculated resulting a new set of linear coefficients. This happens iteratively using the self-consistent field procedure shown in Figure 2.2.

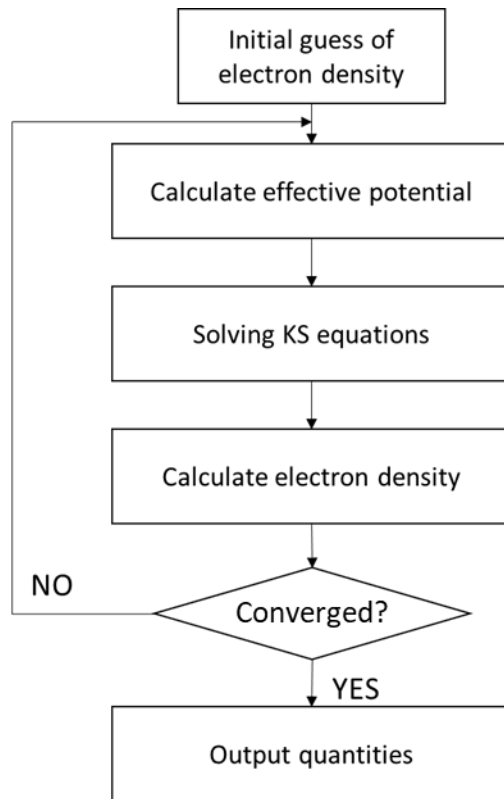


Figure 2.2: Schematic representation of the self-consistent loop for solving the Kohn-Sham equations.

2.2.4 Exchange and correlation functionals

Local density approximation (LDA)

In the previous paragraph we showed that we can obtain the ground state energy by solving the Kohn-Sham equations in a self-consistent way instead of solving the full Schrödinger equation. In order to use the Kohn-Sham equations, the form of the exchange correlation functional has to be known. Although an exact expression for this term is unknown, some approximations have been proposed. The simplest approach to approximate the exchange-correlation is the local density approximation (LDA).

Within LDA, we assume that the exchange-correlation energy is calculated based on an idealized situation of the homogeneous electron gas. Herein, the total exchange-correlation energy is calculated from the following integral:

$$E_{XC}^{LDA}(n) = \int \rho(\mathbf{r}) \epsilon_{XC}(\rho(\mathbf{r})) d\mathbf{r} \quad (2.19)$$

where $\epsilon_{XC}(\rho(\mathbf{r}))$ is a constant corresponding to the exchange-correlation energy per particle of the homogeneous electron gas of density $\rho(\mathbf{r})$.

LDA is an oversimplification of the actual density distribution and generally leads to overestimation of bond energies. Strictly, the LDA is only valid for slowly varying densities, which is not the case for many chemical systems. Nevertheless, this approximation works relatively well on systems such as metals and semiconductors and has helped increasing fundamental understanding about these materials.

Generalized gradient approximation (GGA)

In the previous paragraph we discussed that LDA is not suitable for describing chemical reactions where the electron density rapidly varies. To overcome this limitation, a relatively straightforward extension of the LDA has been introduced that also includes the gradient of the electron density. This is the so-called generalized gradient approximation (GGA) method. The general expression is written as:

$$E_{XC}^{GGA}(n) = \int \rho(\mathbf{r}) \epsilon_{XC}(\rho(\mathbf{r}), \nabla \rho(\mathbf{r})) d\mathbf{r} \quad (2.20)$$

Several GGA functionals are available based on the different ways of implementing the gradient information of the electron density in the exchange-correlation term. This gave birth to many distinct GGA functionals. In this thesis, the Perdew-Burke-Ernzerhof (PBE)¹² functional is used because of its outstanding performances in describing electronic structures of metal and oxides.¹³ The level of accuracy that we can obtain at this level of theory is of about ± 15 kJ/mol.¹⁰

2.2.3.5 Pseudopotentials and plane-waves method

In the previous paragraph we showed that DFT provides a feasible approach to obtain the electron density of the system in the ground state. To solve the Kohn-Sham equations, a self-consistent field (SCF) procedure is applied which gradually improves the electron density at each iteration until the ground state solution is obtained. In order to perform the SCF procedure, the electronic wave function is expanded by a set of functions called a basis set.

In practice, the choice for a basis set depends on many aspects, such as the size of the system, the accuracy required for the simulations and the boundary conditions of the system. In this thesis, we investigate catalytic reactions on large periodic surfaces. Hence, planewaves are used as our basis-set as this basis functions readily encompass the periodic nature of the electronic systems.

This is demonstrated in Bloch's theorem¹⁴ which implies that the eigenstates of the one-electron Hamiltonian can be written as

$$\Psi(\mathbf{r} + \mathbf{R}_n) = \exp(i\mathbf{k} \cdot \mathbf{R}_n) \Psi(\mathbf{r}) \quad (2.21)$$

Where \mathbf{R}_n refers to an arbitrary translation vector of the crystallographic lattice and \mathbf{k} represents the wave vector in reciprocal space. Using this theorem, the Kohn-Sham equation for a periodic system can be solved

by expanding electronic wavefunctions at each k -point in the reduced reciprocal space. The size or number of planewaves employed is typically described by the highest energy among the planewaves in the basis set; this is termed the cut-off energy.

In chemistry, valence electrons play a more important role than the core electrons as they are the only ones involved in the making and breaking of bonds. Furthermore, core electrons require a large amount of basis functions because they exhibit rapid oscillations close to the nuclear core. This leads to the absurd situation that the least important part of the electron density requires the largest amount of computational effort. A solution to this problem is to describe the core electrons using a so-called frozen core approximation. Herein, we make use of pseudopotentials in which core electrons and nuclei are described by a smooth effective potential. In such method however, all the information about the real wave function close to the nuclei is lost. A more general approach is the Projector-Augmented-Wave method (PAW) introduced by Blöchl.¹⁵ This approach is divided in two parts: a partial expansion within an atom-centered sphere and an envelope function outside. The two parts are then matched smoothly at the sphere edge. The wavefunction within the sphere is linked onto a local basis of auxiliary functions. This linkage ensures that the kinks and strong oscillations near the nucleus are attached to a numerically smooth auxiliary wave function, which is expanded into planewaves. This methodology describes the core electrons is one of the key features that is implemented in the VASP simulation package.¹⁶ All electronic structure calculations conducted in this thesis have made use of this package.

2.2.5 Density of states and Crystal Orbital Hamilton Population

The electronic structure of molecules is described by molecular orbital (MO) theory wherein the energy levels of electrons and is given by a molecular orbital. For small molecules, these orbitals have distinct energy levels. The simplest and most iconic representative of that is the H_2 molecule with its bonding (σ_g stabilizing) and antibonding (σ_u^* destabilizing)orbital interactions.¹⁷

In larger systems, such as the ones encountered in heterogeneous catalysis, several atomic orbitals contribute to the formation of several molecular orbitals. In principle, these orbitals are still distinguishable, however, because their energy levels lie so close to each other they result in a continuous band of energy levels.

The electronic density of states (DOS) quantifies the distribution of the energy levels that can be occupied by electrons in a quasiparticle picture, and is central to modern electronic structure theory.¹⁸ The DOS is defined as the amount of occupied states within a specific slice ($E + dE$) of the total range of possible energies for a specific volume.

The partial DOS (pDOS, given throughout in units of states/eV per cell), with respect to the Fermi level, is defined as:

$$\text{pDOS}_i = \sum_n \langle \phi_i | \Psi_n \rangle \delta(E - E_n) \langle \Psi_n | \phi_i \rangle \quad (2.22)$$

where Ψ_n is the molecular orbital defined as the following sum of atomic orbitals ϕ_i with coefficients c_i :

$$\Psi_n = \sum_i c_{in} \phi_i \quad (2.23)$$

If we normalize equation 2.22, then the pDOS is essentially the probability of finding an electron in an atomic orbital i as a function of the electron energy.

Furthermore, the position of the bands with respect to the Fermi level can give information about the bonding character of the interaction. This rationalization is done in tandem with the crystal orbital Hamilton population (COHP) of the bonds between the catalyst surface and the adsorbate. The COHP (given throughout in units of states/eV per cell), with respect to the Fermi level, is then defined as:

$$-\text{COHP}_{ij}(E) = H_{ij} \sum_i c_i^n c_j^n \delta(E - E_n) \quad (2.24)$$

where H_{ij} is the Hamiltonian matrix element between atomic orbitals $\{\phi_i\}$ and $\{\phi_j\}$. The COHP is interpreted as the magnitude of the ‘bond energy overlap’ and can be used to determine how many bonding and anti-bonding states there are as a function of electron energy. Integration of the COHP for all energies up to the Fermi level also gives us a relative estimate of the bond strength between two such atomic orbitals. The application of the COHP technique to compute the electronic structure of solid-state materials requires the use of crystal orbitals derived from local basis sets. The more popular and essentially delocalized plane-wave-based computations, however, are blind to for chemical bonding analysis, so one first needs to reconstruct both Hamilton and overlap matrix elements using auxiliary atomic orbitals. In other words, such information may be projected from plane waves by means of the projected Crystal Orbital Hamilton Population (pCOHP) technique, a modern descendant of the COHP method.¹⁹

Once the pDOS has been obtained we can calculate the average d -band energy for all energies up to the Fermi energy E_f (‘ d -band centre ϵ_d ’) as such:

$$\epsilon_d = \frac{\int_{-\infty}^{E_f} E \rho(E) dE}{\int_{-\infty}^{E_f} \rho(E) dE} \quad (2.25)$$

where $\rho(E)$ is the density of states.

To obtain the DOS and COHP data the Local Orbital Basis Suite Towards Electronic Structure Reconstruction (Lobster) package was used.^{17,20} This package constructs both the data for the DOS and COHP analysis by partitioning the band structure after a static VASP run.

2.4 Microkinetic modeling

Microkinetic modeling allows the description of complex chemo-kinetic networks by modeling them as a set of elementary reaction steps. To construct such a model, a detailed analysis of the reaction network is required. In practice, this information is retrieved either from experimental data or *ab initio* data, such as DFT calculations. The transient behavior of a chemical system is then studied by solving a series of ordinary differential equations (ODE) over time. In this section, we will first explain how microkinetic parameters can be established from first-principles calculations, next, we will show how a series of elementary reaction steps results in a set of ordinary differential equations and finally we close this section by explaining how such a set is solved and how a sensitivity analysis can be employed to obtain valuable insights from microkinetic simulations.

2.4.2 Parameter evaluation for microkinetic modeling

To construct a microkinetic model, the rate constants of all the elementary reaction steps need to be known. These can be calculated by DFT calculations. By optimizing the electronic structure of initial, transition and final state of all relevant elementary reaction steps, the absolute electronic energy is calculated. From these, the electronic activation energy in the forward and backward direction is obtained. By performing a frequency analysis on all these states, the vibrational degrees of freedom are collected from which the zero-point energy (ZPE) correction to the electronic activation energies is calculated. The ZPE correction to the electronic activation energy can be as large as 10-15 kJ/mol. Although this value might not seem significant, especially given that the accuracy of state-of-the-art DFT calculations is comparable, neglecting the ZPE correction yields incorrect results, especially when hydrogenation reaction are involved.

We use the Eyring equation to compute the rate constant of any elementary reaction step:²¹

$$k = \frac{k_b T}{h} \frac{Q_{\text{TS}}^\ddagger}{Q_{\text{IS}}} e^{\left(\frac{-\Delta E_{\text{act}}}{k_b T}\right)} \quad (2.26)$$

Where k is the reaction rate of a single elementary reaction step, k_b and h are the Boltzmann's constant and Planck's constant and T is the temperature in Kelvin, Q_{TS}^\ddagger and Q_{IS} are the total partition functions for the molecular degrees of freedom in the initial and transition state and finally ΔE_{act} is the zero-point energy corrected electronic activation energy. The underlying assumption leading to the Eyring equation are:

- 1) The transition state is in thermal equilibrium with the initial state.

- 2) Going from the transition state to the final state is an irreversible process.
- 3) Crossing the transition state is done with a particular velocity or frequency.

Typically, the molecular partition function Q is decomposed into translational, vibrational, and rotational contributions

$$Q = q_{\text{trans}} \cdot q_{\text{vib}} \cdot q_{\text{rot}} \quad (2.27)$$

When modeling chemical reactions occurring on a catalytic surface, three types of elementary reactions steps are typically considered: adsorption, surface reaction and desorption.

The initial state and transition state in a surface reaction are composed of the partition functions corresponding to $3N$ and $3N-1$ vibrational degrees of freedom, where N is the number of atoms in the reactant, respectively. In this analysis, the catalytic surface is assumed to provide a negligible contribution to the vibrational partition function as the mass of the metal atoms is much larger than the atoms of the adsorbent. The values for the partition function can be calculated using a frequency analysis employing equation (2.27):

$$q_{\text{vib}} = \frac{1}{1 - e^{\left(\frac{-hv}{k_b T}\right)}} \quad (2.28)$$

For surface reactions, there is no significant change in the entropy and consequently the pre-exponential factor of the rate constants is typically in the order of 10^{13} s^{-1} .

In contrast, during adsorption and desorption steps, there is a significant change in entropy. Typically, a gaseous compound has several rotational and translational degrees of freedom and most of them are lost upon adsorption. To model adsorption reactions, we assume that one translational mode corresponding to a translational degree of freedom (perpendicular to the direction of the surface) is converted to a vibrational mode. The translational partition function q_{trans} is given by the formula:

$$q_{\text{trans}} = \frac{L \sqrt{2\pi m k_b T}}{h} \quad (2.29)$$

Herein, L is the characteristic length of the translation and m is the mass of the particle. The rotational partition function for a diatomic molecule can be written as:

$$q_{\text{rot}} = \frac{8\pi^2 I k_b T}{h^2} \quad (2.30)$$

Where I stands for the total rotational moment of inertia.

To derive a rate for the adsorption processes, we assumed that the adsorbate loses one translational degree of freedom in the transition state with respect to the initial state. Furthermore, adsorption processes are

commonly assumed to be entropically activated, thus having zero activation energy. As a result, the exponential term in equation (2.21) is equal to unity. Insertion of the relevant partition functions in the Eyring equation and furthermore assuming that all vibrational partition functions can be set to unity, we obtain the following expression for the rate constant of an adsorption process.

$$k_{\text{ads}} = \frac{k_{\text{B}}T}{h} \frac{L^2(2\pi mk_{\text{B}}T)h^3}{L^3(2\pi mk_{\text{B}}T)^{3/2}h^2} \quad (2.31)$$

where A_{st} and m_i are the effective area of an adsorption site and the molar mass of the gas species, respectively. p refers to the partial pressure of the reactant in the gas phase and k_{B} is the Boltzmann constant. Using the general gas equation ($pV = nRT$), we obtain the rate constant for adsorption:

$$k_{\text{ads}} = \frac{p A_{\text{st}}}{\sqrt{2\pi m_i k_{\text{B}} T}} \quad (2.32)$$

The gas-phase entropy of the adsorbates was calculated using the thermochemical Shomate equation as given by:²²

$$S^0 = A \cdot \ln(T) + B \cdot T + \frac{C \cdot T^2}{2} + \frac{D \cdot T^3}{3} - \frac{E}{2 \cdot T^2} + G, \quad (2.33)$$

where S^0 is the standard molar entropy. The parameters A-G from equation (2.33) were obtained from the NIST Chemistry Webbook.²³

For desorption steps, we assume that the desorbing compound has two translational and three rotational degrees of freedom in the transition state. Furthermore, we assume that the initial state corresponds to a strongly adsorbed complex by which all molecular degrees of freedom are of a vibrational nature. Plugging the formulas for the translational degrees of freedom (2.29) and rotational (2.30) into the Eyring equation (2.26), we obtain the following expression of the constant for desorption (k_{des}):

$$k_{\text{des}} = \frac{k_{\text{B}}T^3}{h^3} \frac{A(2\pi mk_{\text{B}}T)}{\sigma \theta_{\text{rot}}} e^{-\frac{\Delta E_{\text{des}}}{k_{\text{B}}T}} \quad (2.34)$$

Here, σ is the symmetry number, θ_{rot} is the characteristic temperature of rotation and ΔE_{des} represents the zero-point energy corrected electronic desorption energy and h is the Planck constant.

Finally, we can construct the set of differential equation for all surface reaction intermediates. The rate expression for an elementary reaction step j is given by:

$$r_j = k_j \prod_i c_i^{v_i^j} \quad (2.35)$$

Wherein, k is the reaction rate constant as calculated by the Eyring equation, c_i the concentration of reactant i in the elementary reaction step j on the surface and ν the stoichiometric coefficient of reactant i in elementary reaction step j . It should be noticed that in equation (2.29), we only treat the elementary reaction step in one direction, thus for each elementary reaction step, two rate expressions are obtained.

2.4.3 Solving ODEs

The set of equations defined in (2.35) constitute an ensemble of ordinary differential equations (ODE) with respect to time. In order to construct such a set of ODEs, a series of elementary reaction steps and corresponding rate constants are constructed. This results in a set of $2R$ elementary reaction equations with N compounds. For each surface compound, its change with respect to time is given by the formula:

$$\frac{\partial \theta_i}{\partial t} = \sum_j^{2R} (\nu_{j,i} k_j \prod_q^{N_i} \theta_{q,j}^{\nu_{q,j}}) \quad (2.36)$$

Where θ refers to the concentration of species I on the surface, ν stands for the stoichiometric coefficient of compound j , k_j is the rate constant of reaction j , θ is the concentration of compound q in reaction j and $\nu_{q,j}$ is the stoichiometric coefficient of compound q in reaction j . By integrating these equations, we can calculate the kinetic properties of the reaction such as the overall reaction rate and steady-state coverages. The set of ODEs is solved until a steady-state solution is reached for all i . A simple way of solving this ODE set is to use the forward Euler method. It should be noted that this method should not be employed in practice because of its instability and thus only acts as a pedagogical tool. In the forward Euler method, the differential equation is time-integrated with a fixed step size of Δt by which a new value $y_i(t + \Delta t)$ can be found from a known value $y_i(t)$ by using the following recurrence equation:

$$y_i(t + \Delta t) \approx y_i(t) + \Delta t \cdot y'_i(t) \quad (2.37)$$

This forward Euler method shows that the error of the result increases with an increase of the step size.

An alternative method is the backward Euler method as given by:

$$y_i(t + \Delta t) \approx y_i(t) \cdot y'_i(t + \Delta t) \quad (2.38)$$

This method is termed implicit because the result of this equation depends on both the current state as well as the future state of the system as represented by an unknown term $y'_i(t + \Delta t)$. The advantage of using implicit methods over explicit ones is that they are more stable. This is especially important when solving stiff systems of ordinary differential equations such as the ones involved in microkinetic modeling. From a practical point of view, stiffness is the observation that extremely small time-steps are required to time-integrate the set of differential equations. It has been found that implicit integration methods allow for larger step sizes than explicit methods while retaining sufficient numerical stability. For these reasons, stiffness

is to be understood as a phenomenon observed for a particular set of ODEs and not as a property of the system. A very important consequence of the stiffness is that even small changes in the activation energy of an elementary reaction step result in large differences for the reaction rate constant due to the exponential dependency on the activation energy

In this work, we apply a multistep backward differentiation formula method as implemented in Sundials library²⁴ to solve such systems. This method allows for on-the-fly change of the order between 1 and 5, wherein the order is increased when the hyperdimensional surface is steep and more numerical accuracy is required and reducing the order when the hyperdimensional surface is relatively flat to save on computational time. In this method, the steepness is assessed by evaluation of the Jacobian matrix.

2.4.4 Kinetic sensitivity analysis

In microkinetic modeling, we aim at obtaining kinetic properties such as the reaction rates and surface coverages under transient and steady-state conditions. By performing a kinetic sensitivity analysis, we can calculate observables that can be related to experimental data, providing valuable insight towards the rational design of new catalysts or the interpretation of experimental results of existing catalytic materials.

2.4.4.1 Reaction orders

The reaction order probes the relative change in the reaction rate with respect to a relative change in the partial pressure of gas phase compounds (either reactants or products). It provides a way to investigate the influence of the reactants and products on the reaction rate.

To show this procedure, consider a generic bimolecular reaction $A + B \rightleftharpoons C$. We can express the rate of this reaction as:

$$r = k \cdot [A]^{n_A} \cdot [B]^{n_B} \cdot [C]^{n_C} \quad (2.39)$$

or

$$r = k \cdot p_A^{n_A} \cdot p_B^{n_B} \cdot p_C^{n_C} \quad (2.40)$$

Where n_A, n_B, n_C are the reaction orders of component A, B and C, respectively. The mathematical expression of the reaction order is given by the formula:

$$n_i = p_i \frac{\partial \ln r^+}{\partial p_i} \quad (2.41)$$

Where n_i is the reaction order in component i , r^+ is the rate in the forward direction and p_i the partial pressure of component i . The reaction orders can be found experimentally by changing the partial pressure of a reactant or product by a small amount and measuring the change in the reaction rate.

2.4.4.2 Apparent activation energy

The apparent activation energy can be used to probe the influence of temperature on the reaction rate, in other words, it represents kinetic sensitivity of analysis for temperature. The mathematical expression of the apparent activation energy is shown in the following formula:

$$\Delta E_{\text{act}}^{\text{app}} = RT^2 \frac{\partial \ln r^+}{\partial T} \quad (2.42)$$

A positive value of the $E_{\text{act}}^{\text{app}}$ suggests that the overall reaction rate increases with increasing temperature. In contrast, a negative value means that the overall reaction rate would be decreased with an increase in temperature. The apparent activation energy is an experimentally accessible value just like the reaction orders. Typically, it is measured by fitting the temperature dependence of the reaction rate or rate constant to the Arrhenius law.

2.4.4.3 Degree of rate and selectivity control

In analytical modeling of chemical kinetics, the so-called rate-determining step (RDS) assumption has proven very useful. Under this assumption, it is considered that a single elementary reaction step is so slow that is fully determining the overall reaction rate. In reality, multiple elementary reaction steps can potentially control the overall rate. In order to take this into account, in microkinetic simulations we conduct a sensitivity analysis on the activation energy for all elementary reaction steps. This approach is termed Degree of Rate Control (DRC) analysis. This method was developed by Kozuch and Shaik²⁵⁻²⁶ and popularized by Campbell.²⁷ Herein, we conduct a sensitivity analysis on the activation energy for all elementary reaction steps.

For each elementary reaction step, a DRC coefficient can be calculated by evaluating the following differential:

$$X_{\text{RC},i} = \frac{k_i}{r} \left(\frac{\partial r}{\partial \ln k_i} \right)_{k_{j \neq i}, K_i} = \left(\frac{\partial \ln r}{\partial \ln k_i} \right)_{k_{j \neq i}, K_i} \quad (2.43)$$

In equation (2.37), r is the overall reaction rate, k_i and K_i are the forward rate and the equilibrium constants for step i , respectively. The differential in equation (2.37) probes the relative effect on the reaction rate by changing the activation energy by an infinitesimal amount while keeping the rate constants of all other elementary reaction steps fixed as well as the overall thermodynamics of the reaction.

A positive value of $X_{\text{RC},i}$ implies that the overall reaction rate increases when the barrier of the elementary reaction step is decreased, i.e. the elementary reaction step is rate limiting. On the other hand, a negative coefficient indicates that by lowering the activation energy of such elementary step the overall rate would

decrease, i.e. the step under consideration is rate-inhibiting. In the case that only a single elementary reaction step has a DRC coefficient of 1, that step is termed the rate-determining step from the perspective of Langmuir-Hinshelwood-Hougen-Watson kinetics.

When operating at zero conversion (i.e., under kinetic conditions and infinitely far from equilibrium), the sum of DRC coefficient is conserved at one as given by:

$$\sum_i X_{RC,i} = 1 \quad (2.44)$$

Analogous to the degree of rate control, the degree of selectivity control (DSC) coefficient defined to determine the influence of a particular elementary reaction step on the selectivity of the overall reaction.

The DSC is evaluated from the following differential equation:

$$X_{DSC,i,c} = \left(\frac{\partial \eta_c}{\partial \ln k_i} \right)_{k_{j \neq i}, K_i} = \eta_c (X_{RC,i,c} - X_{RCi,r}) \quad (2.45)$$

where η_c is the selectivity to compound c with respect to some reference compound i , $X_{RC,i,c}$, is the DRC coefficient with respect to the rate of compound c , $X_{RCi,r}$ is the DRC coefficient with respect to the rate of a reactant r .

From equation (2.45), we can deduce that the sum of DSC coefficient is zero as given by:

$$\sum_i X_{DSC,i} = 0 \quad (2.46)$$

where $X_{SC,i,c}$ is the DSC of product C due to a change in the kinetics of elementary reaction step i , and η_c is the selectivity towards a key product (methanol or carbon monoxide in this work). Note that the relationship between DRC and DSC coefficient is given by

$$X_{SC,i,c} = \eta_c (X_{c,i} - X_{\text{reactant},i}). \quad (2.47)$$

2.5 References

- (1) Maestri, M. Escaping the Trap of Complication and Complexity in Multiscale Microkinetic Modelling of Heterogeneous Catalytic Processes. *Chem. Commun.* **2017**, 53 (74), 10244–10254.
- (2) Szabo, A.; Ostlund, N. S. Modern Quantum Chemistry: Introduction to Advanced Electronic Structure Theory. Revised. *McGraw-Hill, New York* **1989**, 141–147, ISBN: 9780486691862.
- (3) Parr, R. G.; Weitao, Y. Density-Functional Theory of Atoms and Molecules. *Density-Functional Theory Atoms Mol.* **1995**, ISBN: 0195092767.
- (4) R.G. Parr and W. Yang, Oxford University Press, New York, Oxford, 1989. *Int. J. Quantum Chem.* **1993**, 47 (1), 101–101.
- (5) Szabo, A.; Ostlund, N. S. Modern Quantum Chemistry: Introduction to Advanced Electronic Structure Theory. Revised. *McGraw-Hill, New York* **1989**, 141–147, ISBN: 9780486691862.
- (6) Born, M.; Oppenheimer, R. Zur Quantentheorie Der Molekeln. *Ann. Phys.* **1927**, 389 (20), 457–484.
- (7) Sherrill, C. D.; Schaefer, H. F. The Configuration Interaction Method: Advances in Highly Correlated Approaches. *Adv. Quantum Chem.* **1999**, 34 (C), 143–269.
- (8) Band, Y. B.; Avishai, Y. Electronic Structure of Multielectron Systems. *Quantum Mech. with Appl. to Nanotechnol. Inf. Sci.* **2013**, 545–578.
- (9) Lisoń, A.; Musiał, M.; Kucharski, S. A. Potential Energy Curves of the NaH Molecule and Its Cation with the Fock Space Coupled Cluster Method. *Adv. Quantum Chem.* **2019**, 79, 221–237.
- (10) Bogojeski, M., Vogt-Maranto, L., Tuckerman, M.E. *et al.* Quantum chemical accuracy from density functional approximations via machine learning. *Nat Commun* **11**, 5223 (2020).
- (11) Hohenberg, P.; Kohn, W. Inhomogeneous Electron Gas. *Phys. Rev.* **1964**, 136 (3B), B864.
- (12) Grimme, S. Semiempirical GGA-Type Density Functional Constructed with a Long-Range Dispersion Correction. *J. Comput. Chem.* **2006**, 27 (15), 1787–1799.
- (13) Carlotto, S.; Natile, M. M.; Glisenti, A.; Paul, J. F.; Blanck, D.; Vittadini, A. Energetics of CO Oxidation on Lanthanide-Free Perovskite Systems: The Case of Co-Doped SrTiO₃. *Phys. Chem. Chem. Phys.* **2016**, 18 (48), 33282–33286.
- (14) Kresse, G.; Joubert, D. From Ultrasoft Pseudopotentials to the Projector Augmented-Wave Method. *Phys. Rev. B* **1999**, 59 (3), 1758.
- (15) Blöchl, P. E. Projector Augmented-Wave Method. *Phys. Rev. B* **1994**, 50 (24), 17953.
- (16) Kresse, G.; Furthmüller, J. Efficient Iterative Schemes for Ab Initio Total-Energy Calculations Using a Plane-Wave Basis Set. *Phys. Rev. B - Condens. Matter Mater. Phys.* **1996**, 54 (16), 11169–11186.
- (17) Nelson, R.; Ertural, C.; George, J.; Deringer, V. L.; Hautier, G.; Dronskowski, R. LOBSTER: Local Orbital Projections, Atomic Charges, and Chemical-Bonding Analysis from Projector-Augmented-Wave-Based Density-Functional Theory. *J. Comput. Chem.* **2020**, 41 (21), 1931–1940.
- (18) Ben Mahmoud, C.; Anelli, A.; Csanyi, G.; Ceriotti, M. Learning the Electronic Density of States in Condensed Matter. *Phys. Rev. B* **2020**, 102 (23), 235130.

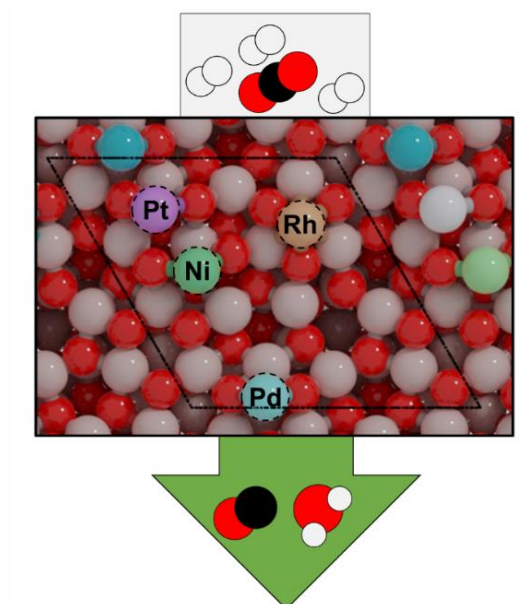
- (19) Deringer, V. L.; Tchougréeff, A. L.; Dronskowski, R. Crystal Orbital Hamilton Population (COHP) Analysis as Projected from Plane-Wave Basis Sets. *J. Phys. Chem. A* **2011**, *115* (21), 5461–5466.
- (20) Maintz, S.; Volker, L.; Deringer, L.; Tchougr, A. L.; Dronskowski, R.; LOBSTER: A Tool to Extract Chemical Bonding from Plane-Wave Based DFT. *J. Comput. Chem.*; **2016**, *37*, 11–12.
- (21) Gschneidner, K. A.; Eyring, L. Handbook on the Physics and Chemistry of Rare Earths, *Volume 26*; **1999**, ISBN: 9780444503466.
- (22) Shomate, C. H. A Method for Evaluating and Correlating Thermodynamic Data. *J. Phys. Chem.* **2002**, *58* (4), 368–372.
- (23) NIST Chemistry WebBook <https://webbook.nist.gov/chemistry/> (accessed Feb 1, 2022).
- (24) Hindmarsh, A. C.; Brown, P. N.; Grant, K. E.; Lee, S. L.; Serban, R.; Shumaker, D. E.; Woodward, C. S. SUNDIALS: Suite of Nonlinear and Differential/Algebraic Equation Solvers. *ACM Trans. Math. Softw.* **2005**, *31* (3), 363–396.
- (25) Kozuch, S.; Shaik, S. A Combined Kinetic-Quantum Mechanical Model for Assessment of Catalytic Cycles: Application to Cross-Coupling and Heck Reactions. *J. Am. Chem. Soc.* **2006**, *128* (10), 3355–3365.
- (26) Kozuch, S.; Shaik, S. Kinetic-Quantum Chemical Model for Catalytic Cycles: The Haber-Bosch Process and the Effect of Reagent Concentration. *J. Phys. Chem. A* **2008**, *112* (26), 6032–6041.
- (27) Campbell, C. T. The Degree of Rate Control: A Powerful Tool for Catalysis Research. *ACS Catalysis*. American Chemical Society April 7, **2017**, pp 2770–2779.
- (28) Minibaev, R. F.; Bagatur'yants, A. A.; Bazhanov, D. I.; Knizhnik, A. A.; Alifimov, M. V. First-Principles Investigation of the Electron Work Function for the (001) Surface of Indium Oxide In₂O₃ and Indium Tin Oxide (ITO) as a Function of the Surface Oxidation Level. *Nanotechnologies Russ.* **2010**, *5* (3), 185–190.
- (29) Walsh, A.; Catlow, C. R. A.; Sokol, A. A.; Woodley, S. M. Physical Properties, Intrinsic Defects, and Phase Stability of Indium Sesquioxide. *Chem. Mater.* **2009**, *21* (20), 4962–4969.
- (30) Karazhanov, S. Z.; Ravindran, P.; Vajeeston, P.; Ulyashin, A.; Finstad, T. G.; Fjellvåg, H. Phase Stability, Electronic Structure, and Optical Properties of Indium Oxide Polytypes. *Phys. Rev. B - Condens. Matter Mater. Phys.* **2007**, *76* (7).
- (31) Gurlo, A.; Kroll, P.; Riedel, R. Metastability of Corundum-Type In₂O₃. *Chem. - A Eur. J.* **2008**, *14* (11), 3306–3310.
- (32) Liu, D.; Lei, W. W.; Zou, B.; Yu, S. D.; Hao, J.; Wang, K.; Liu, B. B.; Cui, Q. L.; Zou, G. T. High-Pressure x-Ray Diffraction and Raman Spectra Study of Indium Oxide. *J. Appl. Phys.* **2008**, *104* (8).
- (33) Frei, M. S.; Capdevila-Cortada, M.; García-Muelas, R.; Mondelli, C.; López, N.; Stewart, J. A.; Curulla Ferré, D.; Pérez-Ramírez, J. Mechanism and Microkinetics of Methanol Synthesis via CO₂ Hydrogenation on Indium Oxide. *J. Catal.* **2018**, *361*, 313–321.
- (34) Walsh, A.; Catlow, C. R. A. Structure, Stability and Work Functions of the Low Index Surfaces of Pure Indium Oxide and Sn-Doped Indium Oxide (ITO) from Density Functional Theory. *J. Mater. Chem.* **2010**, *20* (46), 10438–10444.

CHAPTER 3

A computational study of CO₂ hydrogenation on single atoms of Pt, Pd, Ni and Rh on In₂O₃(111)

Abstract

Indium oxide (In₂O₃) promoted by metals are promising catalysts for CO₂ hydrogenation to products such as methanol and carbon monoxide. Although it is clear that a high dispersion of the promoting metal is important for obtaining selective catalysts, the exact role of atomically dispersed metal promoters remains debated. Herein, we used density functional theory calculations to compare the role of single atoms of Ni, Pd, Pt and Rh placed on the In₂O₃(111) surface to study CO₂ hydrogenation to CO and methanol. While single atoms of Pd, Pt and Rh do not change the overall barrier for oxygen vacancy formation compared to In₂O₃(111), the presence of Ni render oxygen vacancy formation more difficult. Microkinetic simulations show that all models mainly catalyze CO formation via a redox pathway involving oxygen vacancies where adsorbed CO₂ dissociates followed by CO desorption and water formation. Pd presents that highest reverse water-gas shift (rWGS) activity because it combines a low barrier for CO₂ dissociation with a relatively weak CO adsorption strength. The higher barriers for formate intermediate hydrogenation compared to the overall barrier for the rWGS reaction explains the negligible CH₃OH selectivity.



3.1 Introduction

Reducing CO₂ emissions has become a crucial technological challenge because of the negative impact on the climate.¹⁻³ Transforming CO₂ captured from combustion processes and in the future directly from air into liquid fuels and chemicals allows reducing such emissions and close the carbon cycle. A promising route to valuable products from CO₂ is through its hydrogenation, provided that hydrogen is obtained from renewable resources.⁴⁻⁶ While large-scale CO₂ hydrogenation to fuels can help decreasing our dependence on fossil fuels for energy, this technology can also be used to obtain chemical intermediates.⁷⁻¹⁰ In this context, methanol is particularly attractive, because it can be used as a fuel or chemical building block.¹¹⁻¹³

Currently, large-scale methanol production is achieved by converting synthesis gas (CO/CO₂/H₂) over a Cu/ZnO/Al₂O₃ catalyst at temperatures of 473–573 K and pressures of 50–100 bar.¹⁴ Challenges arise however when CO₂ is hydrogenated instead of CO. The Cu-based catalyst shows significant activity for the reverse water-gas-shift reaction (rWGS), leading to the formation of unwanted CO.¹⁵ Moreover, the catalyst suffers from sintering, resulting in slow deactivation.^{16,17} Many efforts have been made to identify new catalyst formulations with improved performance for the hydrogenation of CO₂ to CH₃OH.¹⁸ Recently, indium oxide (In₂O₃) has emerged as a promising catalyst for CO₂ hydrogenation to methanol.¹⁹⁻²⁰ Several density functional theory (DFT) studies emphasize the role of oxygen vacancies in the mechanism of CO₂ hydrogenation to methanol on In₂O₃.^{19,21,22,23-25} Although such catalysts enable high selectivity to methanol by suppressing the competitive rWGS reaction, CO₂ conversion is limited by the intrinsically low activity in H₂ activation. To improve this, the use of metal promoters has been investigated. Recently, we reported by microkinetic modeling that small Ni clusters on In₂O₃ mainly catalyze methanol formation, whereas single atoms of Ni either doped in or adsorbed on In₂O₃ mainly catalyze CO.^{26,27} In a recent study, Pinheiro Araújo et al. reported that, atomically dispersed metal atoms (Pd, Pt, Rh, Ni, Co, Au, Ir) on the In₂O₃ surface promote hydrogen activation and methanol production while hindering CO formation.²⁸ Frei et al. suggested by DFT calculations that single Ni atoms on In₂O₃ could catalyze the rWGS reaction but not methanol synthesis.²⁹ The same authors proposed that single atoms of Pd doped in In₂O₃ can stabilize clusters of a few Pd atoms on the In₂O₃ surface. These clusters can enhance H₂ activation and, therefore, CH₃OH productivity.³⁰ Han et al. suggested that single atom (SA) of Pt doped in In₂O₃ would result in high methanol selectivity, whereas Pt nanoparticles on In₂O₃ would improve the rWGS reaction.³¹ Sun et al. showed by DFT calculations that the energetically most favorable pathway for methanol synthesis on a Pt₄/In₂O₃ model occurs via hydrogenation of a CO intermediate.³² Wang et al. reported that highly dispersed Rh phases on In₂O₃ can enhance dissociative H₂ adsorption and oxygen vacancy formation.³³ Dostagir et al. found that Rh doped into In₂O₃ catalyzes CO₂ hydrogenation to formate species.³⁴ Furthermore, earlier DFT works pointed out that SAs on the In₂O₃ surface do not catalyze the formation of CH₄.^{28,29,30,35} In nearly all these studies, the formation of atomically dispersed active sites, clusters or single atoms was effective in shifting

the selectivity towards the desired product. Although the role of supported clusters in metal-promoted In₂O₃ catalysts has been clarified for many cases,^{32,36} generic understanding about the role of SAs is still lacking. To unravel the role of SAs on In₂O₃, detailed insights into the reaction pathways of methanol synthesis from CO₂ hydrogenation are required.

In the present work, we study the reaction mechanism of CO₂ hydrogenation to CH₃OH and CO on SA-In₂O₃ model catalysts. Based on the literature, we selected Ni, Pd, Pt and Rh as possible promoters. The reaction pathways explored in our DFT studies include a direct route for CO₂ hydrogenation to methanol (formate pathway), a pathway to methanol via CO hydrogenation and the competing rWGS reaction. We performed DFT calculations to determine the reaction energetics for all elementary reaction steps, which serve as input for microkinetic modeling. Microkinetic simulations show that the SA-In₂O₃ model surfaces produce CO as the main product with a very low methanol selectivity. The dominant pathway involves the formation of an oxygen vacancy followed by adsorption of CO₂ and direct C-O bond cleavage. Low rates of methanol formation are associated with high activation energies for the hydrogenation of formate intermediates.

3.2. Computational Methods

3.2.1 Density Functional Theory Calculations

All DFT calculations were conducted using the projector augmented wave (PAW) method³⁷ and the Perdew–Burke–Ernzerhof (PBE)³⁸ exchange-correlation functional as implemented in the Vienna Ab Initio Simulation Package (VASP) code.^{39,40} Solutions to the Kohn-Sham equations were calculated using a plane-wave basis set with a cut-off energy of 400 eV. The valence 5s and 5p states of In were treated explicitly as valence states within the scalar-relativistic PAW approach. All calculations were spin-polarized. The Brillouin zone was sampled using a 3x3x1 Monkhorst-Pack grid. Electron smearing was employed using Gaussian smearing with a smearing width (σ) of 0.1 eV. The stoichiometric In₂O₃(111) surface was modelled as a 2D slab with periodic boundary conditions. A 15.0 Å vacuum region was introduced in the *c*-direction to avoid the spurious interaction with neighbouring super cells. It was verified that the electron density approached zero at the edges of the periodic super cell in the *c*-direction. In all calculations, the bottom two layers were frozen, while the top two layers were allowed to perturb. The supercell has dimensions of 14.57 Å × 14.57 Å × 26.01 Å. The In₂O₃(111) slab consisted of 96 O atoms and 64 In atoms, distributed in four atomic layers on top of which the Ni species were placed. The electronic energies of gas-phase H₂, H₂O, CO, CO₂ and CH₃OH were calculated using a cubic unit cell with lattice vector of 8 Å. The Brillouin zone was sampled using a 1x1x1 Monkhorst-Pack grid (G-point only). Gaussian smearing was employed. Electronic energies were corrected for zero-point energies of adsorbates and gas-phase

molecules and finite-temperature contributions of the translational and rotational energies of gas-phase molecules.

The stable states of the elementary reaction steps pertaining to CO₂ hydrogenation were calculated using the conjugate-gradient algorithm. Adsorption energies of adsorbates (ΔE_X^{ads}) are defined as:

$$\Delta E_X^{\text{ads}} = E_{X+\text{In}_2\text{O}_3(111)} - E_{\text{In}_2\text{O}_3(111)} - E_X. \quad (3.1)$$

where $E_{X+\text{In}_2\text{O}_3(111)}$ is the electronic energy of the catalyst plus adsorbate system, $E_{\text{In}_2\text{O}_3(111)}$ is the reference energy of the In₂O₃(111) slab and E_X is the DFT-calculated energy of the adsorbate in the gas phase.

The influence of oxygen vacancies on the reaction energetics was investigated by removing oxygen atoms from the In₂O₃(111) lattice. The energy required to form an oxygen vacancy (ΔE_{Ov}) was calculated using either O₂ or H₂O as reference, according to the following two equations

$$\Delta E_{\text{Ov}} = E_{\text{defective slab}} - E_{\text{stoichiometric slab}} + E_{1/2\text{O}_2}, \quad (3.2)$$

$$\Delta E_{\text{Ov}} = E_{\text{defective slab}} - E_{\text{stoichiometric slab}} + E_{\text{H}_2\text{O}} - E_{\text{H}_2}, \quad (3.3)$$

where $E_{\text{defective slab}}$ is the electronic energy of the catalyst containing one oxygen vacancy, $E_{\text{stoichiometric slab}}$ is the reference energy of the stoichiometric slab. $E_{1/2\text{O}_2}$, $E_{\text{H}_2\text{O}}$ and E_{H_2} are the DFT-calculated energies of gas-phase O₂, H₂O and H₂, respectively. Herein, we include the electronic energy, the zero-point energy correction and a finite temperature correction of translational and rotational energy of each gas-phase molecule.

Transition states were determined using the climbing-image nudged elastic band (CI-NEB) method.⁴¹ A frequency analysis was performed to all states. It was verified that stable states have no imaginary frequencies and transition states have a single imaginary frequency in the direction of the reaction coordinate.⁴² The Hessian matrix in this frequency analysis was constructed using a finite difference approach with a step size of 0.015 Å for displacement of individual atoms along each Cartesian coordinate. The corresponding normal mode vibrations were used to calculate the zero-point energy (ZPE) correction and the vibrational partition functions.

Partial Density of State (pDOS) analysis are conducted to analyze the electronic structure of each SA-In₂O₃ model using the Lobster package.^{43,44} The atomic charges were calculated using the Bader charge method.⁴⁵

3.2.2 Microkinetic simulations

Microkinetic simulations were conducted based on the DFT-calculated activation barriers and reaction energies. The kinetic network was modelled using a set of ordinary differential equations involving rate constants, surface coverages and partial pressures of gas-phase species. Time-integration of the differential equations was conducted using the linear multistep backwards differential formula method with a relative and absolute tolerance of 10^{-8} .⁴⁶⁻⁴⁸

For the adsorption processes, the net rate of a gas-phase species i was calculated as:

$$r_i = k_{i,\text{ads}}\theta^*p_i - k_{i,\text{des}}\theta_i \quad (3.4)$$

where θ^* and θ_i are the fraction of free sites and the fraction of coverage species i , respectively. $k_{i,\text{ads/des}}$ is the rate constant for the adsorption/desorption process and p_i is the partial pressure of species i .

For the adsorption processes, we assumed that the adsorbate loses one translational degree of freedom in the transition state with respect to the initial state. Thus, the rate of adsorption derived from transition state theory is:

$$k_{i,\text{ads}} = \frac{p A_{st}}{\sqrt{2\pi m_i k_B T}}, \quad (3.5)$$

where A_{st} and m_i are the effective area of an adsorption site and the molar mass of the gas species, respectively. p and T are the total pressure and temperature, respectively, and k_B is the Boltzmann constant. The gas-phase entropy of the adsorbates was calculated using the thermochemical Shomate equation as given by

$$S^0 = A \cdot \ln(T) + B \cdot T + \frac{C \cdot T^2}{2} + \frac{D \cdot T^3}{3} - \frac{E}{2 \cdot T^2} + G, \quad (3.6)$$

where S^0 is the standard molar entropy.⁴⁹ The parameters A-G from equation (3.6) were obtained from the NIST Chemistry Webbook.⁵⁰ For the desorption processes, we assumed that the species gains two translational degrees of freedom and three rotational degrees of freedom in the transition state with respect to the initial state. Thus, the rate of desorption derived from transition state theory is:

$$k_{\text{des}} = \frac{k_B \cdot T^3}{h^3} \cdot \frac{A_{st}(2\pi m k_B)}{\sigma \theta_{\text{rot}}} \cdot e^{\frac{\Delta E_{\text{des}}}{k_B T}} \quad (3.7)$$

Herein, k_{des} is the rate constant for the desorption of the adsorbate, h is the Planck constant, σ is the symmetry number and corresponds to the number of rotational operations in the point group of each

molecule. θ_{rot} the rotational temperature, and ΔE_{ads} the desorption energy. The value of A_{st} is equal to $9 \cdot 10^{-19} \text{ m}^{-2}$.

Finally, the rate constant (k) of an elementary reaction step is given by

$$k = \frac{k_{\text{B}}T}{h} \frac{Q^{\ddagger}}{Q} e^{\left(\frac{-\Delta E_{\text{act}}}{k_{\text{B}}T}\right)}, \quad (3.8)$$

where Q^{\ddagger} and Q are the partition functions of the activated complex and its corresponding initial state, respectively, and ΔE_{act} is the ZPE-corrected activation energy.

To identify the steps that control the CO_2 consumption rate and the product distribution, we employed the concepts of the degree of rate control (DRC) developed by Kozuch and Shaik⁵¹⁻⁵² and popularized by Campbell⁵³ as well as the degree of selectivity control (DSC).⁵³⁻⁵⁵

Herein, the degree of rate control coefficient is defined as

$$X_{\text{RC},i} = \left(\frac{\partial \ln r_i}{\partial \ln k_i} \right)_{k_{j \neq i}, K_i} \quad (3.9)$$

A positive DRC coefficient indicates that the elementary reaction step is rate-controlling, whereas a negative coefficient suggests that the step is rate-inhibiting. When a single elementary reaction step has a DRC coefficient of 1, this step is identified as the rate-determining step.

3.3 Results and discussion

3.3.1 Indium Oxide support model

Indium oxide (In_2O_3) has been chosen as the reducible support on which single atoms and clusters of metal promoters are adsorbed (Chapters 3,4 and 6). In this section, we briefly mention details about models of In_2O_3 catalyst. In_2O_3 is an n-type semiconductor with diverse technological applications in nanoelectronics and optoelectronics.⁵⁶⁻⁵⁸ There are three crystal structures reported for In_2O_3 : the cubic bixbyite-type phase (c- In_2O_3), the hexagonal corundum-type phase (h- In_2O_3), and the orthorhombic Rh_2O_3 -type phase.^{59,60} All three phases have dominant ionic bonding with noticeable covalent interaction between indium and oxygen, where the coordination is 6-fold for In atoms and 4-fold for O atoms but differs in atomic arrangements and bond lengths. The c- In_2O_3 phase is thermodynamically the most stable phase and widely studied both theoretically and experimentally and it is used in this thesis (Figure 3.1a). We optimized the c- In_2O_3 bulk structure and calculated a lattice parameter of 10.284 Å that agrees well with the experimental one (10.117 Å).⁶¹ We calculated the surface energy for low-index surface In_2O_3 terminations based on a c- In_2O_3 bulk model. The calculated values for the, (110), and (111) facets correspond to 1.11 J/m², and 0.830 J/m²,

respectively. These results are in line with earlier calculations reported by Walsh et al. that also indicated that the stability of the three crystal facets follows the order of In₂O₃(111) > In₂O₃(110) > In₂O₃(100).⁶² This is moreover in line with experimental findings.⁶¹ The (110) and (111) facets of In₂O₃ are widely used in DFT calculations (Figure 3.1b-c). In this thesis, the most stable (111) surface termination is used for all calculations involving In₂O₃ as a support material.

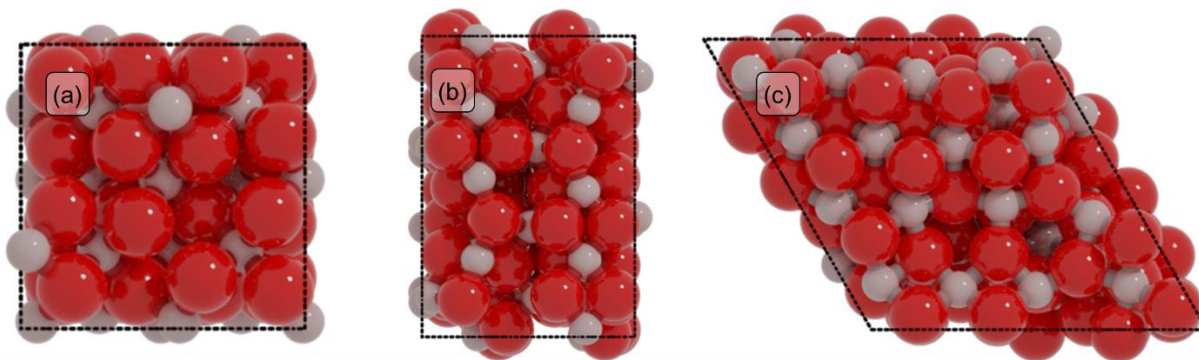


Figure 3.1. Optimized structures of (a) bulk In₂O₃, (b) In₂O₃(110) and (c) In₂O₃(111) surface. Red: O, brown: In.

3.3.2. Structure of SA-In₂O₃ models

To study the catalytic properties of single atoms (SAs) of Ni, Pd, Pt and Rh, we constructed four models in which the SA was placed on the In₂O₃(111) surface, which is the most stable termination of In₂O₃.⁶³ We first determined the most stable location of the SA on the In₂O₃(111) surface. For this, we calculated the adsorption energies of the SA in different positions (Table A1). The most stable adsorption sites are depicted in Figure 3.2. Single Ni, Pd and Pt atoms preferentially adsorb in bridge sites between two oxygen atoms, in agreement with previous theoretical studies (Figure 3.2a-c).^{30,64} The Rh SA prefers to coordinate to three oxygens (Figure 3.2d). A partial density of states (pDOS) analysis of the SA-In₂O₃ models shows that the bonding is mainly through interactions of the SA metal d orbitals and O 2p orbitals (Figure A2). The supported Ni, Pd, Pt and Rh SAs possess positive charges of +0.56, +0.35, +0.30 and +1.03, respectively. The energy needed to remove the SA atom to infinite distance from the surface is reported in Table A1. Ni is most strongly bound to the surface ($\Delta E_{\text{ads}} = -5.17$ eV), followed by Pt ($\Delta E_{\text{ads}} = -4.86$ eV), Rh ($\Delta E_{\text{ads}} = -4.31$ eV) and Pd ($\Delta E_{\text{ads}} = -3.44$ eV).

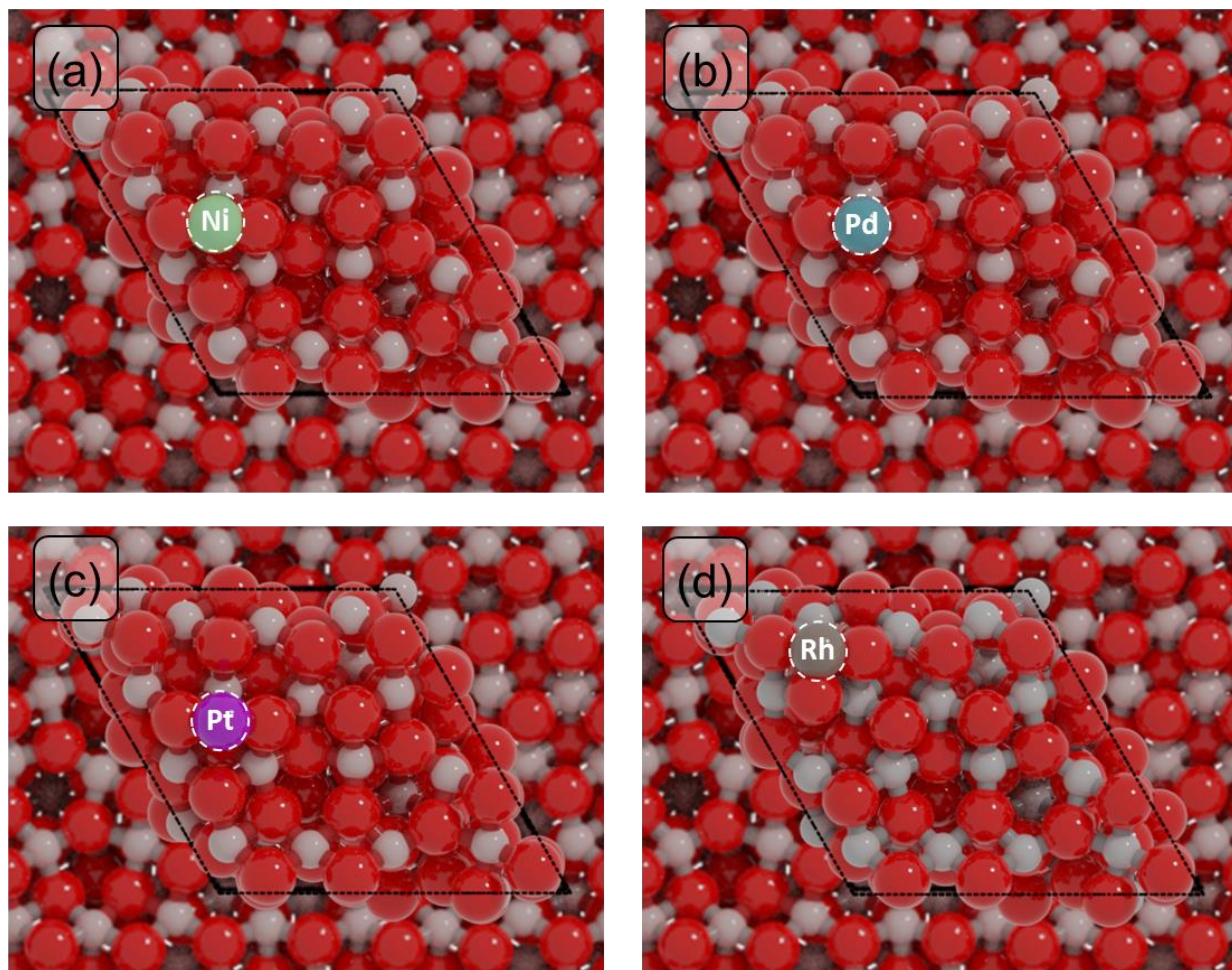


Figure 3.2. Structural models used in DFT calculations composed of single atoms on the $\text{In}_2\text{O}_3(111)$ surface. (a) Ni- In_2O_3 , (b) Pd- In_2O_3 , (c) Pt- In_2O_3 and (d) Rh- In_2O_3 . (green: Ni, light blue: Pd, purple: Pt ; brown: Rh; red: O; grey: In).

3.3.3. Oxygen vacancy formation

Oxygen vacancies (Ov) in the In_2O_3 surface have been identified as the active sites for CO_2 hydrogenation.^{19,21,22} Here, we determine the effect of surface SAs on the formation of such vacancies. To this purpose, we calculate the energy required to remove an oxygen atom on each SA- In_2O_3 model and compare the results with data for bare In_2O_3 (Figure 3.3, Table A2 and Figure A3). The computed energies are referenced to gaseous O_2 and H_2O . For the bare $\text{In}_2\text{O}_3(111)$ surface (Figure 3.3a), the energy needed to remove an oxygen atom (E_{Ov}) ranges between 1.94 and 2.76 eV, in line with previous theoretical calculations.⁶⁵ We also calculated the E_{Ov} with respect to H_2O , because oxygen vacancies are usually formed in the presence of H_2 . In this case, the E_{Ov} lies between -0.68 and 0.15 eV.

The presence of a Ni atom on In₂O₃ (Figure 3.3b) significantly increases the oxygen vacancy formation energy, resulting in E_{Ov} values between 3.42 and 4.41 eV referenced to O₂ and between 0.89 and 1.87 eV referenced to H₂O. The effect of a Pd SA is much less pronounced, resulting in values for E_{Ov} comparable to those for the bare In₂O₃(111) surface, namely between 1.75 and 3.36 eV referenced to O₂ and between -0.77 and 0.87 eV referenced to H₂O (Figure 3.3c). For the Pt- case (Figure 3.3d), E_{Ov} values range between 2.10 and 4.86 eV referenced to O₂ and between -0.41 and 2.22 eV referenced to H₂O. On the Rh-In₂O₃ model (Figure 3.3e), E_{Ov} values range between 2.95 and 4.29 eV referenced to O₂ and between 0.43 and 1.77 eV referenced to H₂O.

Further inspection of Figure 3.3b-d shows that, for each of the SA-promoted surfaces, formation of vacancies is easier for lattice oxygen atoms directly bonding to the SA than for O atoms bonding only to In atoms. Comparing the H₂O-referenced E_{Ov} values for O binding to the SA, we computed as lowest lowest E_{Ov} values of 1.46, -0.77, -0.41 and 0.43 eV for Ni-, Pd-, Pd- and Rh-In₂O₃, respectively (Table A3). On bare In₂O₃, the lowest E_{Ov} value is -0.68 eV. The relatively more endothermic E_{Ov} values for Ni-, Pt- and Rh-In₂O₃ are in line with the strong adsorption energy of the SA on the surface (Tables A1 and A8). Because Pd binds to the surface less strongly, E_{Ov} is relatively speaking more exothermic than for the other SAs. To understand whether oxygen vacancies will be formed on these models under reaction conditions and what role they play in CO₂ hydrogenation, we study the mechanism of oxygen vacancy formation via surface reduction by H₂ as well as the CO₂ hydrogenation reacton pathways by means of microkinetic simulations (*vide infra*).

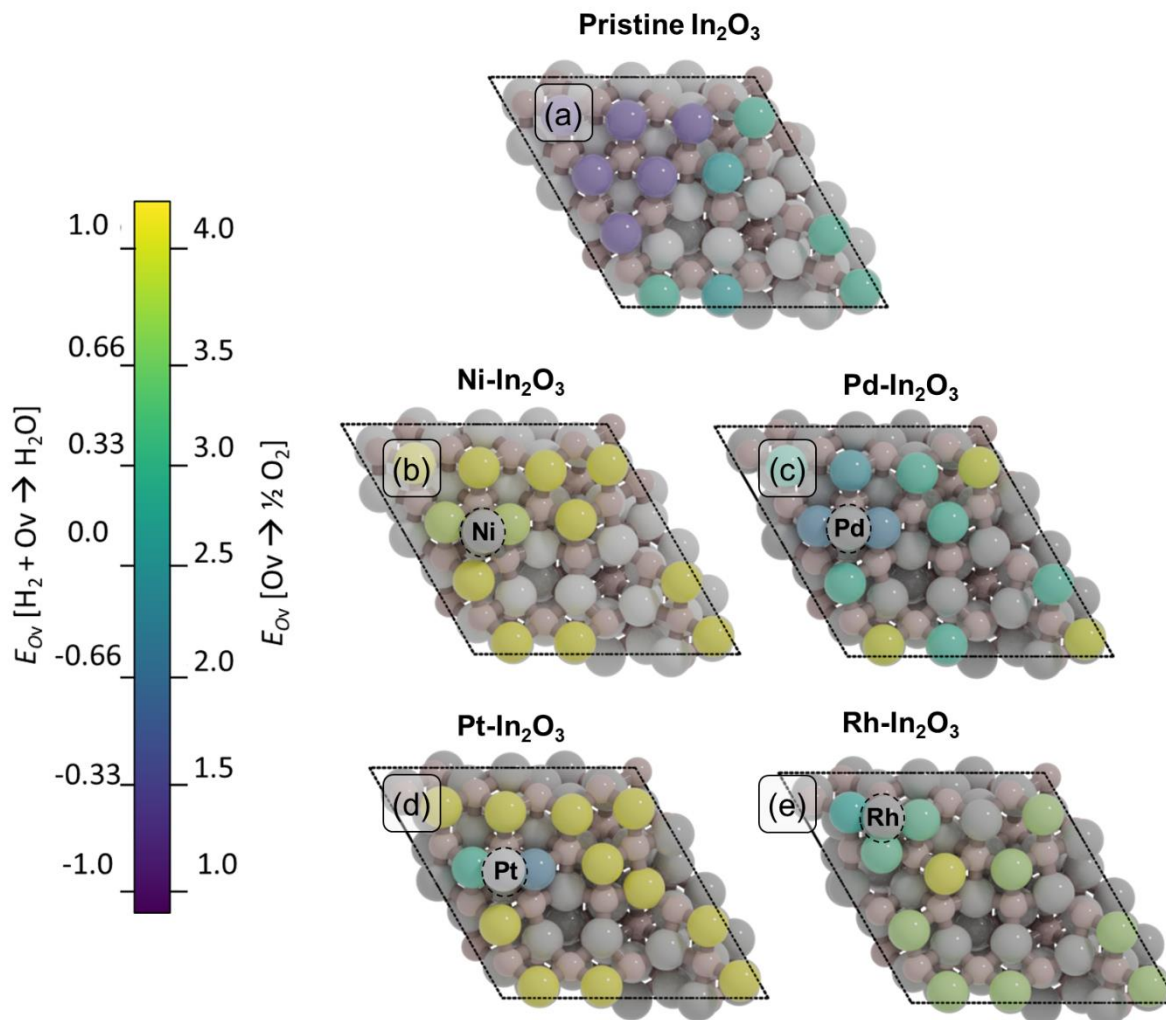


Figure 3.3: Oxygen vacancy formation energies (E_{Ov}) for the 12 surface oxygens on (a) bare In_2O_3 , (b) $\text{Ni-In}_2\text{O}_3$, (c) $\text{Pd-In}_2\text{O}_3$, (d) $\text{Pt-In}_2\text{O}_3$, and (e) $\text{Rh-In}_2\text{O}_3$. The coloring of the 12 surface oxygen atoms corresponds to their E_{Ov} indicated in the color bar. Vacancy formation energies are referenced to both O_2 and H_2O formation. All other atoms are colored in grey. The SAs are highlighted inside dashed circles.

3.3.4 Reaction mechanism

We performed DFT calculations to determine the reaction mechanism of CO_2 hydrogenation to methanol (CH_3OH), carbon monoxide (CO) and water (H_2O). Hydrogenation of CO_2 to methane (CH_4) was not included, because methane formation was not observed in experiments with low-loaded metal-promoted In_2O_3 catalysts.^{32,32,34,28} Furthermore, earlier DFT works pointed out that SAs on the In_2O_3 surface do not catalyze the formation of CH_4 .^{28,29,30,35} The mechanism is depicted in Figure 3.4 in the form of a reaction network diagram. Following previous computational studies, we investigated the pathways for (i) the formation of oxygen vacancies through H_2O formation, (ii) the formation of CH_3OH via formate, and (iii)

the reverse water-gas shift (rWGS) pathway leading to CO.^{32,63,68–70} The latter rWGS reaction can take place via either direct C-O bond cleavage in adsorbed CO or an H-assisted pathway involving COOH intermediate. In addition to methanol formation via formate, we considered the direct hydrogenation pathway of CO intermediate into CH₃OH. Figure 3.4 depicts the potential energy diagrams (PED) for each of these routes.

Next, we discuss the elementary reaction steps on each SA-In₂O₃ surface and highlight differences in activation energies and transition-state (TS) structures. The activation barriers are given with respect to the most stable adsorbed state for each intermediate. The geometries corresponding to initial, transition and final states can be found in Appendix A. The computed forward and backward barriers for all elementary reaction steps are given in Sections A4-7.

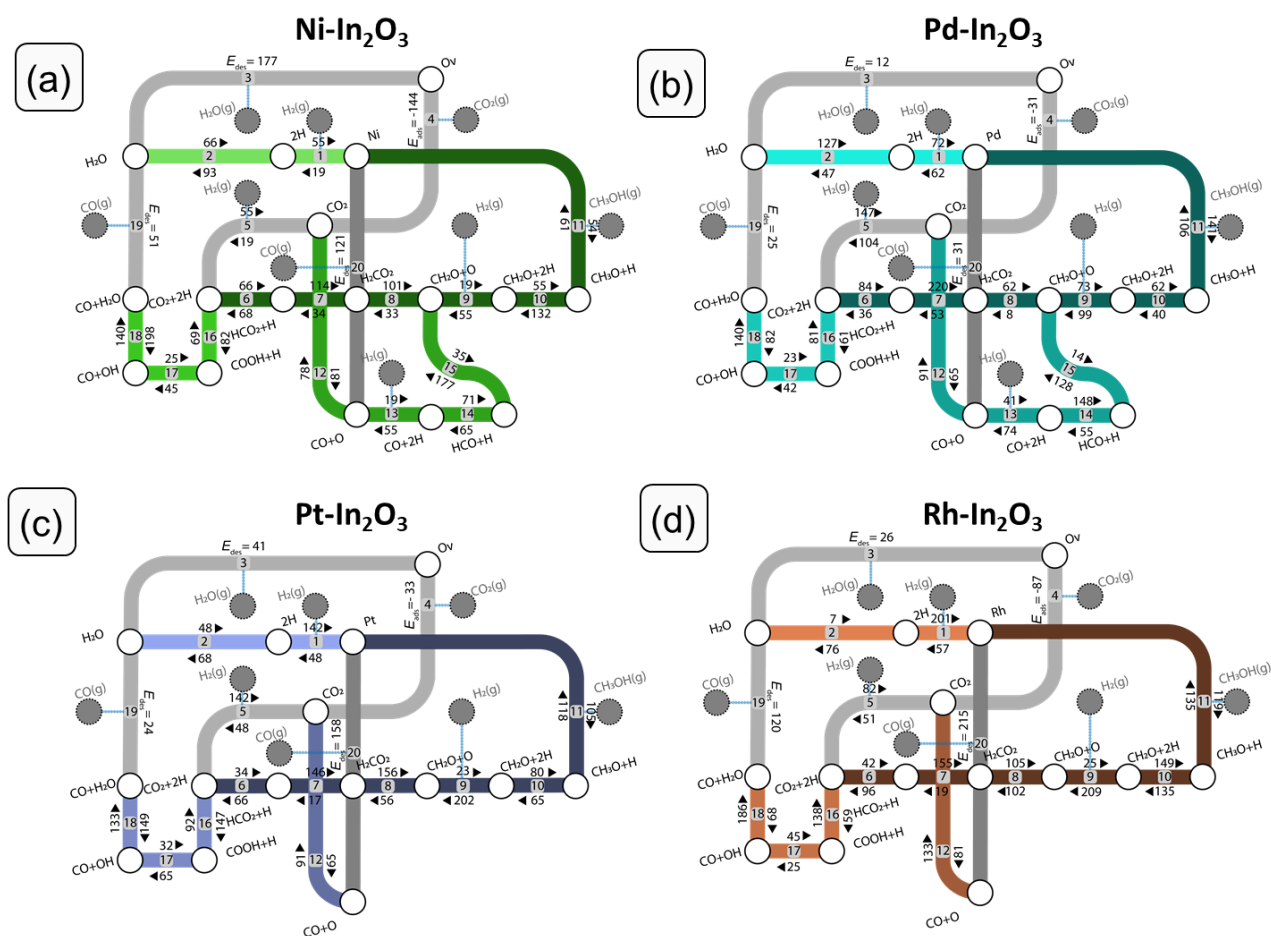


Figure 3.4. Complete reaction networks of CO₂ hydrogenation to CO and CH₃OH for (a) Ni-, (b) Pd-, (c) Pt- and (d) Rh-In₂O₃.

3.3.4.1 Oxygen vacancy formation

We first discuss the formation of oxygen vacancies (steps 1-3). On all SA-In₂O₃ surfaces, the oxygen corresponding to the lowest E_{O_v} value is removed. For Ni-, Pd and Pt-In₂O₃, this corresponds to forming an oxygen vacancy in position Ov₃ (Table A2 and Figure A3). For Rh-In₂O₃ formation of an oxygen vacancy in position Ov₂ is preferred. On all SA-In₂O₃ models, H₂ is heterolytically dissociated into SA-H and O-H moieties (step 1). Hydrogen activation is facile on Ni-In₂O₃ ($\Delta E_{a,Ni} = 19$ kJ/mol) and more difficult on Pd-, Pt- and Rh-In₂O₃ ($\Delta E_{a,Pd} = 62$ kJ/mol, $\Delta E_{a,Pt} = 48$ kJ/mol and $\Delta E_{a,Rh} = 57$ kJ/mol). Dissociative adsorption of H₂ is more exothermic on Pt- and Rh-In₂O₃ ($\Delta E_{R,Pt} = -94$ kJ/mol, $\Delta E_{R,Rh} = -144$ kJ/mol) than on Ni- and Pd-In₂O₃ ($\Delta E_{R,Ni} = -36$ kJ/mol, $\Delta E_{R,Pd} = -10$ kJ/mol). Oxygen vacancy formation proceeds via proton migration from a SA-H to an O-H moiety, resulting in adsorbed H₂O (step 2). This step has similar barriers for Ni-In₂O₃, Pt-In₂O₃ and Rh-In₂O₃ ($\Delta E_{a,Ni} = 93$ kJ/mol, $\Delta E_{a,Pt} = 68$ kJ/mol and $\Delta E_{a,Rh} = 76$ kJ/mol). Since the migration from OH to NiH might result in a change in oxidation state of the SA, we verified whether the Hubbard $+U$ correction was required for this model. The results of these calculations are reported in Figure A4 and Table A4, respectively. Using a $U = 6.3$ eV based on an earlier theoretical work on NiO,⁷¹ resulted in no significant change in the structure of the TS nor in the activation energies. On these models, this step is endothermic by 27, 69, and 27 kJ/mol, respectively. The lowest barrier is obtained for Pd-In₂O₃ ($\Delta E_a = 47$ kJ/mol; $\Delta E_R = 80$ kJ/mol). H₂O desorption completes the oxygen vacancy formation pathway (step 3). The highest desorption energy is computed on Ni-In₂O₃ ($\Delta E_{des,Ni} = 177$ kJ/mol), while this step is considerably easier on the other SA models ($\Delta E_{des,Pd} = 12$ kJ/mol, $\Delta E_{des,Pt} = 41$ kJ/mol and $\Delta E_{des,Rh} = 26$ kJ/mol). The overall reaction energy for oxygen vacancy formation with respect to gas-phase H₂ amounts to +150 kJ/mol (Ni), -72 kJ/mol (Pd), -41 kJ/mol (Pt) and +16 kJ/mol (Rh). The overall barriers with respect to gas-phase H₂ are 150, 72, 48 and 57 kJ/mol for Ni-, Pd-, Pt-, and Rh-In₂O₃, respectively.

3.3.4.2 Methanol synthesis via formate

For CO₂ hydrogenation, we first discuss the most stable adsorption configuration for CO₂ on the SA-In₂O₃ models. On Ni-, Pd- and Pt-In₂O₃ CO₂ adsorbs near the SA with one of its O atoms occupying the oxygen vacancy and the C atom bonding to the SA. On Rh-In₂O₃, the C atom coordinates directly to a lattice O instead of the SA. The adsorption energies of CO₂ are -144, -31, -33 and -87 kJ/mol for Ni-, Pd-, Pt- and Rh-In₂O₃, respectively. Thus, the interaction of CO₂ with Ni and Rh is relatively strong compared to Pd and Pt. This is in line with trends found in a previous computational study for CO₂ adsorption on low-index surfaces of transition metals.⁷²

Dissociative adsorption of H₂ (step 5) is heterolytic on all SA-In₂O₃ models and leads to O-H and SA-H moieties adjacent to adsorbed CO₂. This state constitutes the initial configuration for CO₂ hydrogenation.

Dissociative adsorption is facile on Ni-In₂O₃ ($\Delta E_{a,\text{Ni}} = 19$ kJ/mol), whereas higher barriers were computed for Pd-, Pt- and Rh-In₂O₃ ($\Delta E_{a,\text{Pd}} = 104$ kJ/mol, $\Delta E_{a,\text{Pt}} = 48$ kJ/mol, $\Delta E_{a,\text{Rh}} = 51$ kJ/mol). Next, methanol can be obtained via a mechanism involving a formate intermediate (steps 6-11). The PEDs of the formate pathway for the SA-In₂O₃ models are reported in Figure 3.5a. The C atom in CO₂ is hydrogenated by a SA-H to HCO₂ (step 6). The forward activation energies for Ni-, Pd- Pt, and Rh-In₂O₃ are respectively 66, 84, 34 and 42 kJ/mol. This reaction is endothermic for Pd-, Pt- and Rh-In₂O₃ with reaction energies of 48, 32 and 54 kJ/mol and slightly exothermic for Ni-In₂O₃ ($\Delta E_{\text{R}} = -2$ kJ/mol). The C atom in HCO₂ is protonated again via migration of a O-H to a SA-H moiety, resulting in H₂CO₂ (step 7). This endothermic step involves relatively high activation energies of 114, 220, 146, and 155 kJ/mol for Ni-, Pd- Pt- and Rh-In₂O₃, respectively. Notably, higher barriers are associated with migration from O-H to SA-H compared to direct hydrogenation of the C atom by a SA-A moiety. Furthermore, step 7 is the most difficult one in the formate pathway for all SAs. Direct migration of a O-H to hydrogenate the C atom in HCO₂ was not considered, as it will lead to even higher barriers. Next, scission of one of the C-O bonds in the H₂CO₂ intermediate results in CH₂O and O (step 8). This step leads to healing of the oxygen vacancy. This step is endothermic for Ni-, and Pd- and Pt-In₂O₃ surfaces with reaction energies of 68, 54 and 100 kJ/mol, respectively, whereas it is slightly exothermic for Rh-In₂O₃ ($\Delta E_{\text{R}} = -3$ kJ/mol). Furthermore, lower barriers are found for Pd- ($\Delta E_{\text{a}} = 62$ kJ/mol) than for Ni- ($\Delta E_{\text{a}} = 101$ kJ/mol), Pt- ($\Delta E_{\text{a}} = 156$ kJ/mol) and Rh-In₂O₃ ($\Delta E_{\text{a}} = 105$ kJ/mol). Another pathway preceding C-O bond scission involves hydrogenation of HCO₂ to HCO₂H. We could not find a TS for this reaction because of the very weak adsorption of HCO₂H. A similar issue was encountered in investigating the hydrogenation of H₂CO₂ to H₂CO₂H. On all SA-In₂O₃ models, dissociative adsorption of another H₂ leads to a SA-H and O-H moieties adsorbed next to CH₂O (step 9). The CH₂O moiety resulting from H₂CO₂ dissociation is then hydrogenated to CH₃O by proton migration from a SA-H moiety (step 10). This step has an activation energy of 55, 62, 80 and 149 kJ/mol for Ni-, Pd- Pt, and Rh-In₂O₃, respectively. Furthermore, it is endothermic for Pd-, Pt and Rh-In₂O₃ ($\Delta E_{a,\text{Pd}} = 18$ kJ/mol, $\Delta E_{a,\text{Pt}} = 15$ kJ/mol, $\Delta E_{a,\text{Rh}} = 14$ kJ/mol), exothermic for Ni-In₂O₃ ($\Delta E_{a,\text{Ni}} = -77$ kJ/mol). Finally, CH₃OH is obtained in a single concerted step from CH₃O via proton migration from the OH (step 11). This elementary reaction step has activation energies of 61, 106, 118 and 135 kJ/mol for Ni-, Pd- Pt, and Rh-In₂O₃, respectively. Furthermore, it is moderately exothermic for Ni-, Pd- and Pt-In₂O₃ ($\Delta E_{\text{R},\text{Ni}} = -7$ kJ/mol, $\Delta E_{\text{R},\text{Pd}} = -35$ kJ/mol, $\Delta E_{\text{R},\text{Pt}} = -13$ kJ/mol), slightly endothermic for Rh-In₂O₃ ($\Delta E_{\text{R},\text{Rh}} = 16$ kJ/mol).

3.3.4.3 Methanol formation via CO

We also considered methanol formation via CO hydrogenation. The PEDs pertaining to this pathway are reported in Figure 3.5b. After formation of an oxygen vacancy (steps 1-3) and CO₂ adsorption (step 4), direct C-O bond scission can take place (step 12). This step leads to healing of the oxygen vacancy and adsorbed CO and has activation energies of 91, 65, 65 and 81 kJ/mol for Ni-, Pd-, Pt-, and Rh-In₂O₃, respectively. Furthermore, it is exothermic for Pd-, Pt- and Rh-In₂O₃ with reaction energy of -26, -26 and -52, respectively, while it is slightly endothermic for Ni-In₂O₃ ($\Delta E_{R, Ni} = 9$ kJ/mol). In the final state, the resulting CO moiety is linearly adsorbed on the SA (SA-C distances: 1.73 Å (Ni), 1.85 Å (Pd), 1.82 Å (Pt) and 1.82 Å (Rh), while the O atom from CO₂ is used to heal the oxygen vacancy in the In₂O₃ surface. We did not find a TS for the two subsequent hydrogenation steps from CO to HCO and H₂CO for Pt- and Rh-In₂O₃. Accordingly, we only report methanol formation via CO for Ni- and Pd-In₂O₃.

For Ni- and Pd-In₂O₃, H₂ is heterolytically dissociated into a SA-H and an O-H moiety (step 13). Such mode of dissociative adsorption of H₂ is more facile on Ni-In₂O₃ ($\Delta E_{a, Ni} = 19$ kJ/mol) than on Pd-In₂O₃ ($\Delta E_{a, Pd} = 41$ kJ/mol). Such state where CO is adsorbed next to a SA-H and a O-H moiety constitutes the initial state of the CO hydrogenation pathway. CO hydrogenation to HCO proceeds using the H adsorbed on the SA (step 14) with activation energies of 71 kJ/mol (Ni-In₂O₃) and 148 kJ/mol (Pd-In₂O₃). In line with this difference, the reaction is much more endothermic for Pd ($\Delta E_{R, Pd} = 93$ kJ/mol) than for Ni ($\Delta E_{R, Ni} = 6$ kJ/mol). Subsequently, HCO is hydrogenated to CH₂O (step 15) with barriers of 177 kJ/mol (Ni-In₂O₃) and 128 kJ/mol (Pd-In₂O₃). We found that the preferential pathway involves migration of H from the OH moiety to the SA, followed by hydrogenation of HCO to CH₂O. Direct migration of a OH to hydrogenate the C atom in HCO would face a higher barrier and was therefore not studied. This elementary step is endothermic for both SA-In₂O₃ models ($\Delta E_{R, Ni} = 142$, $\Delta E_{R, Pd} = 114$ kJ/mol, respectively). The resulting CH₂O intermediate also occurs in the formate pathway to methanol discussed above. Thus, further hydrogenation of CH₂O to methanol will occur via steps 9 and 10.

3.3.4.4 CO formation via rWGS

The formation of CO can occur either via direct C-O bond cleavage of CO₂ (redox pathway, steps 4 and 20) or via a H-assisted pathway involving a COOH intermediate (carboxyl pathway, steps 16-19). In the redox pathway, after formation of H₂O (steps 1-3) and CO₂ adsorption (step 4) one of the C-O bonds in CO₂ is cleaved (step 12). These steps have been previously discussed. The desorption of CO (step 20) closes the rWGS catalytic cycle. The highest barriers for CO desorption are found on Pt- ($\Delta E_{des, Pt} = 158$ kJ/mol) and Rh-In₂O₃ ($\Delta E_{des, Rh} = 215$ kJ/mol) whereas lower values are found on Ni- ($\Delta E_{des, Ni} = 121$ kJ/mol) and Pd-In₂O₃ ($\Delta E_{des, Pd} = 31$ kJ/mol).

The carboxyl pathway proceeds by protonation of adsorbed CO₂ to form COOH by a SA-H moiety (step 16). The highest activation energies are computed for Ni-In₂O₃ ($\Delta E_a = 82$ kJ/mol) and Pt-In₂O₃ ($\Delta E_a = 147$ kJ/mol) followed by Pd-In₂O₃ ($\Delta E_a = 61$ kJ/mol) and Rh-In₂O₃ ($\Delta E_a = 59$ kJ/mol). Furthermore, this elementary step is endothermic for Ni- and Pt-In₂O₃ ($\Delta E_{R,Ni} = 74$ kJ/mol, $\Delta E_{R,Pt} = 55$ kJ/mol), whereas it is exothermic for Pd- and Rh-In₂O₃ ($\Delta E_{R,Pd} = -20$ kJ/mol, $\Delta E_{R,Rh} = -78$ kJ/mol). Formation a COOH intermediate is associated with higher barriers compared to formation of HCOO, in line with an earlier study on In₂O₃.⁷³ Next, COOH dissociates into CO and OH (step 17). This step features activation energies of 45, 42, 65, and 25 kJ/mol for Ni-, Pd-, Pt- and Rh-In₂O₃, respectively. Furthermore, it is endothermic for all SA-In₂O₃ surfaces ($\Delta E_{R,Ni} = 17$ kJ/mol, $\Delta E_{R,Pd} = 19$ kJ/mol, $\Delta E_{R,Pt} = 33$ kJ/mol, and $\Delta E_{R,Rh} = 20$ kJ/mol). Water is formed via proton transfer to the OH moiety obtained from COOH dissociation (step 18). This step features activation energies of 140, 140, 133 and 186 kJ/mol for Ni-, Pd-, Pt- and Rh-In₂O₃, respectively. Moreover, it is endothermic for Rh-, and Pd-In₂O₃ ($\Delta E_{R,Rh} = 107$ kJ/mol, and $\Delta E_{R,Pd} = 58$ kJ/mol), and exothermic for Ni- and Pt-In₂O₃ ($\Delta E_{R,Ni} = -58$ kJ/mol, and $\Delta E_{R,Pt} = -16$ kJ/mol). Notably, this step features the highest activation energy of the carboxyl pathway for all SA-In₂O₃. Desorption of CO (step 19) features a barrier of 51, 25, 24 and 120 kJ/mol for Ni-, Pd-, Pt- and Rh-In₂O₃, respectively, closing the carboxyl cycle.

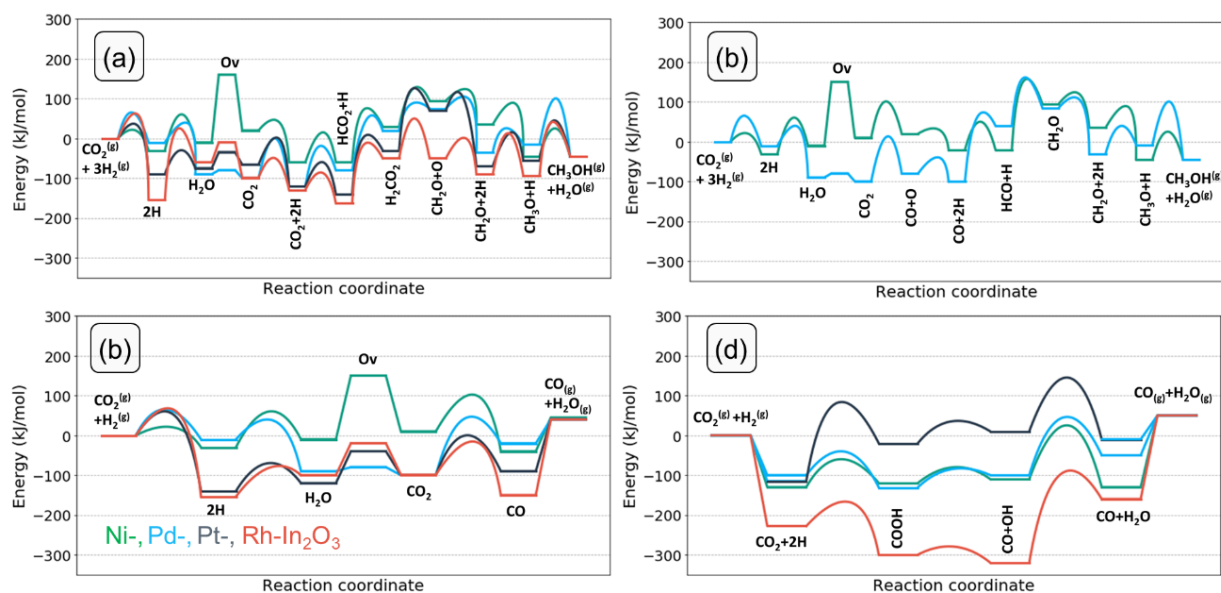


Figure 3.5. Potential energy diagrams of (a) formate pathway to CH₃OH, (b) CO hydrogenation pathway to CH₃OH and (c) redox pathway to CO and (d) carboxyl pathway to CO on different models.

3.3.5. Microkinetic simulations

3.3.5.1. Overall kinetics

To compare the catalytic activities of the various SA-In₂O₃ model surfaces, we calculate the CO₂ hydrogenation reaction rate using a microkinetic model based on DFT-computed reaction energetics. The active sites in our model consist of isolated single atoms, stabilized on the In₂O₃ support. We do not take migration of intermediates between different active sites into account. In other words, co-adsorbed species are modelled as distinct variations of a single active site. In this approximation, all elementary reaction steps are unimolecular, with exception of the adsorption and desorption steps. A detailed list of the elementary reaction steps is provided in Appendix A.

The CO₂ consumption rate and CH₃OH selectivity as a function of temperature for each SA-In₂O₃ model are displayed in Figure 3.6. The turnover frequencies (TOF) towards CH₃OH and CO (TOF_{CH₃OH} and TOF_{CO}, respectively) are reported in Figure A5. We also constructed a microkinetic model for unpromoted In₂O₃ based on the published DFT data of Frei et al.⁶³ Figure 3.6a shows that the CO₂ conversion rate decreases in the order Pd > Ni > Pt > Rh. Furthermore, none of the SA-In₂O₃ models show any appreciable methanol selectivity (Figure 3.6b), which is due to the much lower TOF_{CH₃OH} in comparison to TOF_{CO} (Figure A5c-d). Compared to bare In₂O₃, the adsorption of a SA on the In₂O₃(111) surface results in lower CO₂ consumption rates (Figure A5a) and TOF_{CH₃OH} for $T < 300$ °C (Figure A5c). In the same range, the TOF_{CO} decreases in the order Pd > Ni > bare In₂O₃ > Pt > Rh (Figure A5d).

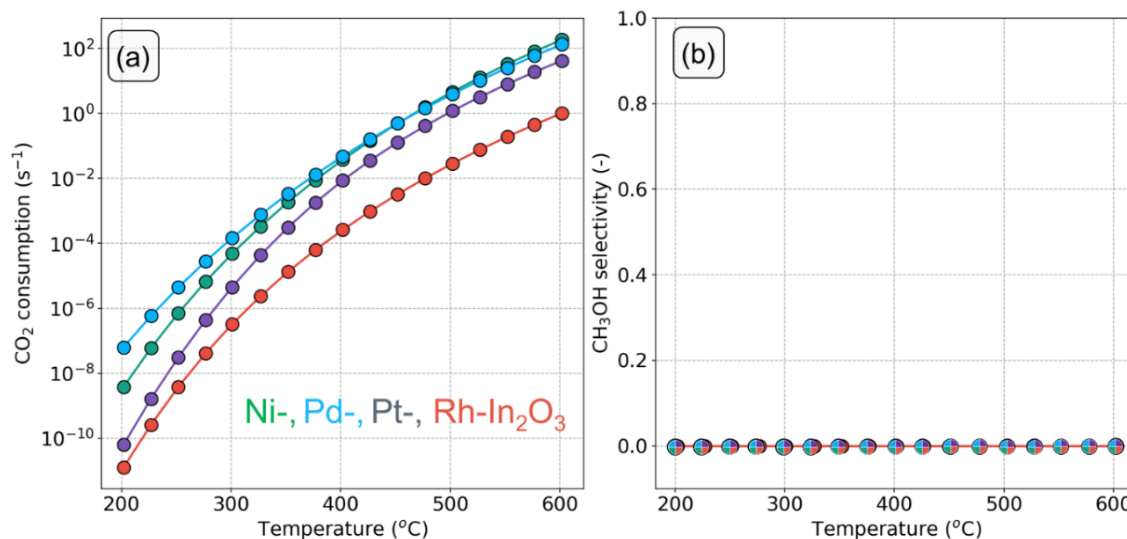


Figure 3.6. (a) CO₂ consumption rate (s⁻¹) and (b) CH₃OH selectivity as a function of temperature on SA-In₂O₃ models (p = 50 bar, H₂/CO₂ ratio =5).

The analysis of the surface state, apparent activation energy and reaction orders as function of temperature is given in Figure 3.7. The coverages in Figure 3.7 should be interpreted as the fraction of time the system spends in a particular state (i.e., the time average). According to the ergodicity principle in statistical thermodynamics, this equals the fraction of active sites that is in a particular state (i.e., the ensemble average).

On the Ni-In₂O₃ surface (Figure 3.7a), the dominant surface state at lower temperatures features two adsorbed H species (2H). The reason behind this can be understood from Figure 3.4a. Activation of H₂ and subsequent H₂O formation (steps 1-2) are facile ($\Delta E_a = 19$ kJ/mol and $\Delta E_a = 74$ kJ/mol, respectively), whereas water desorption (step 3) features a high barrier ($\Delta E_{des} = 177$ kJ/mol). The latter step is the most difficult one in the Ov formation pathway and limits the progress of the reaction. As water desorption is facilitated by a higher temperature, it leads to an increase in the number of oxygen vacancies and CO₂ adsorption. Consequently, the coverage of the 2H state decreases and the coverage of intermediate states in the formate pathway to methanol (CO₂+2H and HCO₂+H) increases. At $T > 400$ °C, the latter states become dominant. On the Ni-In₂O₃ model, hydrogenation of CO₂ to HCO₂ (step 6) has an activation energy of 66 kJ/mol and a reaction energy of -2 kJ/mol. In contrast, subsequent hydrogenation to H₂CO₂ (step 7) has a considerably higher activation energy of 114 kJ/mol and is endothermic. As formation of H₂CO₂ is difficult and the previous two states are comparable in terms of energy, CO₂+2H and HCO₂+H are the dominant states. At low temperature, the model predicts a reaction order of nearly zero in CO₂ and H₂ (Figure 3.7c). Under these conditions, the reaction is limited by the rate of H₂O removal, and an increase of the partial pressure of CO₂ or H₂ does not affect this process. Thus, the corresponding reaction orders in CO₂ and H₂ must be zero. At higher temperature, however, a negative reaction order in H₂ is found. A higher partial pressure of H₂ would lead to higher rates of H adsorption facilitating hydrogenation reactions. In turn, this pushes the reaction away from the CO product leading to a decrease in the overall rate. On the Ni-In₂O₃ model, the apparent activation energy (E_{app} , Figure 3.7c) has a constant value of at 175 kJ/mol between 200 °C and 400°C. This value corresponds to the desorption energy of H₂O. At higher temperature, a slight decrease in the E_{app} is observed, indicating a change in the rate-limiting step. This aspect will be clarified with a DRC analysis (*vide infra*).

On the Pd-In₂O₃ model, the COOH+H is the dominant state at $T < 450$ °C (Figure 3.7b). Figure 3.4b shows that hydrogenation of CO₂ to COOH (step 16) and its subsequent dissociation into CO and OH are facile ($\Delta E_a = 61$ kJ/mol and $\Delta E_a = 42$ kJ/mol, respectively). However, the subsequent step of OH hydrogenation has a higher activation energy and is endothermic ($\Delta E_a = 140$ kJ/mol and $\Delta E_R = 58$ kJ/mol, respectively). This makes the conversion of the COOH+H state difficult. At high temperature ($T > 450$ °C), the barrier for OH hydrogenation (step 17) can be more easily overcome, resulting in formation of oxygen vacancies.

As a result, the dominant state becomes the Pd-In₂O₃ surface with an oxygen vacancy (Ov). The model predicts a reaction order of zero in CO₂ and H₂ for $T < 450$ °C (Figure 3.7d). As the dominant working state already corresponds to intermediates derived from H₂ and CO₂, a change in the partial pressure of these reactants does not impact the activity. For $T > 450$ °C, the reaction orders in CO₂ and H₂ are positive, indicating that hydrogenation reactions are controlling the reaction rate. The E_{app} is approximately 150 kJ/mol at 200 °C and decreases with increasing temperature (Figure 3.7d).

On the Pt-In₂O₃ model, the HCO₂+H state is the dominant state for below 525 °C (Figure 3.7e). Hydrogenation of CO₂ to HCO₂ (step 6) is facile ($\Delta E_a = 34$ kJ/mol), while the subsequent step of HCO₂ hydrogenation to H₂CO₂ (step 7) is more difficult ($\Delta E_a = 146$ kJ/mol, $\Delta E_R = +129$ kJ/mol). This hampers the conversion of the HCO₂+H state. At higher temperature, the surface coverage of the HCO₂+H state decreases in favor of oxygen vacancies (Ov). The Ov state becomes dominant for $T > 525$ °C. The reaction order in CO₂ is zero at low temperature, because the surface is already covered with HCO₂+H resulting from CO₂ hydrogenation (Figure 3.7g). At higher temperature ($T > 475$ °C), the reaction order in CO₂ becomes positive indicating that CO₂ activation reactions are controlling the rate. The reaction order in H₂ is negative, as also found for Ni- and Pd-In₂O₃. The E_{app} stays almost constant for temperature below 300 °C at 200 kJ/mol and decreases with increasing temperature (Figure 3.7g).

Within the temperature range of 200 °C and 600 °C, the dominant state of Rh-In₂O₃ is the COOH+H state (Figure 3.7f). The reason becomes apparent from inspection of Figure 3.4d. Hydrogenation of CO₂ to COOH and its further dissociation (step 16-17) are facile ($\Delta E_a = 59$ and $\Delta E_a = 25$ kJ/mol, respectively). However, the subsequent step of OH hydrogenation is more difficult ($\Delta E_a = 186$ kJ/mol) and hampers the conversion of the CO+OH state. With respect to the dominant COOH+H state, an overall barrier of 341 kJ/mol must be overcome to complete the H-assisted rWGS cycle (Figure 3.5d). As a result, only for temperatures far above 600 °C, states other than COOH+H observed. The reaction order in CO₂ is zero at low temperature, because the surface is already covered with COOH+H resulting from CO₂ hydrogenation (Δh). The reaction order in H₂ is negative, indicating that a higher partial pressure of H₂ would push the reaction away from the dominant CO formation pathway. The apparent activation energy decreases from 260 kJ/mol to 220 kJ/mol between 200 and 400 °C (Figure 3.7h).

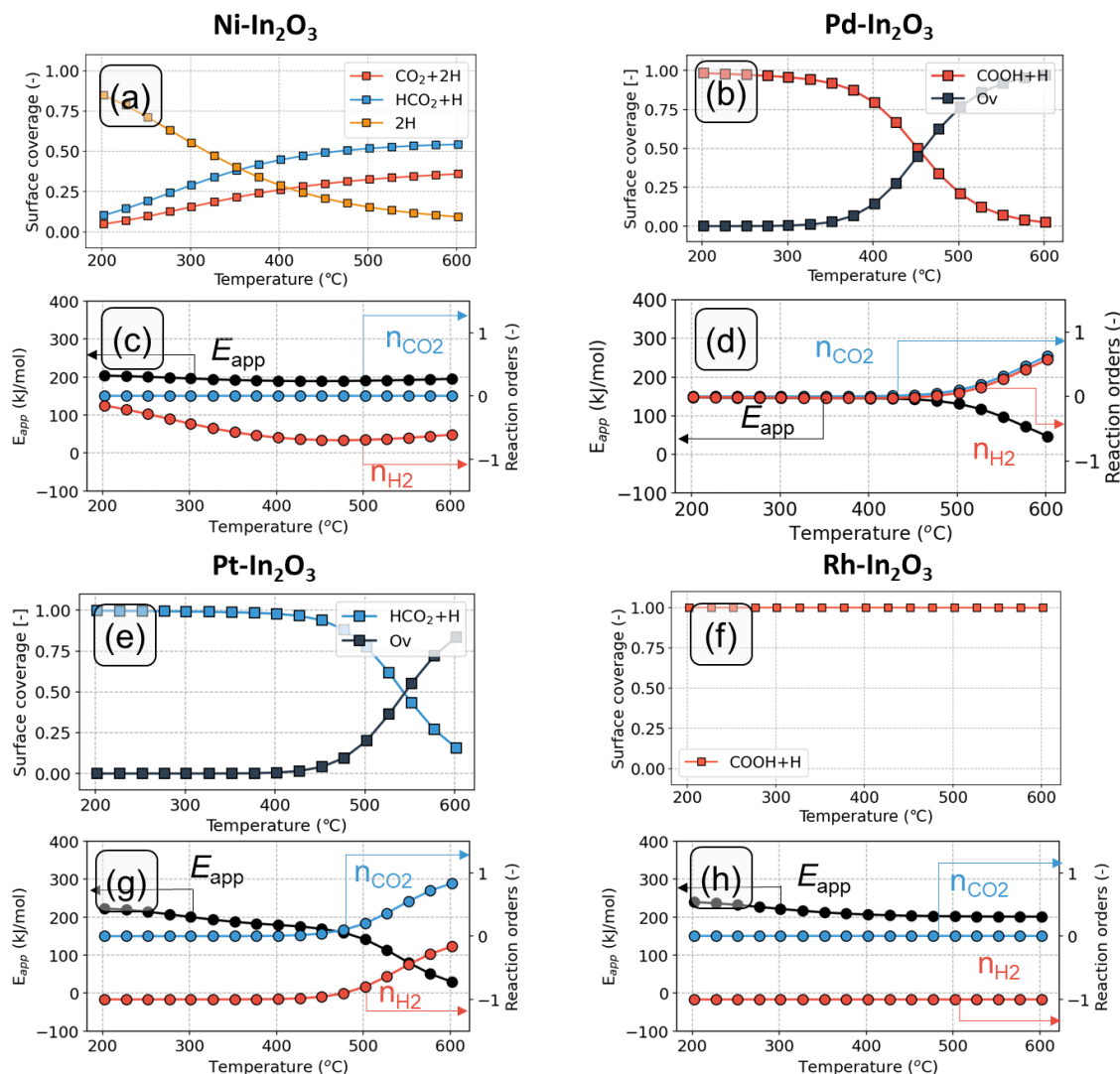


Figure 3.7. Surface state of the catalyst as a function of temperature for (a) Ni-, (b) Pd- (e) Pt- and (f) Rh-In₂O₃, respectively. Apparent activation energy (in kJ/mol) and reaction orders in CO₂ and H₂ as a function of temperature on (c) Ni-, (d) Pd- (g) Pt- and (h) Rh-In₂O₃, respectively.

3.3.5.2 Sensitivity analysis

In this section, we analyze in more depth the steps that lead to CH₃OH and CO during CO₂ hydrogenation on the SA-promoted In₂O₃ models. We identify the elementary steps that control the overall CO₂ consumption rate and the CH₃OH selectivity and investigate how these steps change with reaction temperature. For this purpose, we conduct a sensitivity analysis based on the degree of rate control (DRC) analysis.⁵³ At zero CO₂ conversion, the sum of the DRC coefficients is conserved at unity.⁵⁴

The DRC analysis and reaction flux analysis for the Ni-In₂O₃ model are shown in Figure 3.8a-b. At low temperature, the CO₂ consumption rate is mostly controlled by water desorption (step 3) preceding oxygen vacancy formation (Figure 3.8a). This result is in line with the dominant surface state being the 2H state, which precedes H₂O formation (Figure 3.7a). Furthermore, H₂O desorption has the highest barrier in the oxygen vacancy formation pathway ($\Delta E_{\text{des}} = 177$ kJ/mol), making formation of an oxygen vacancy difficult. At higher temperature ($T > 275$ °C), water desorption results in oxygen vacancies and CO₂ adsorption. As a result, the DRC coefficient of the H₂O desorption step decreases, in favor of the CO₂ dissociation step (step 12). At higher temperature, the latter becomes the main rate-limiting step. An increased rate of CO₂ dissociation would result in a higher flux towards CO, benefiting the formation of this product. The dominant pathway (Figure 3.8b) on the Ni-In₂O₃ model proceeds via formation of an oxygen vacancy followed by CO₂ adsorption and direct dissociation. The carboxyl pathway to CO is not taken because OH removal (step 18) is associated with a higher barrier than direct CO₂ dissociation ($\Delta E_{\text{a}} = 140$ kJ/mol and $\Delta E_{\text{a}} = 81$ kJ/mol, respectively). Compared to the dominant pathway to CO, methanol formation pathways feature considerably lower molar fluxes. This is in keeping with our finding that Ni-In₂O₃ mainly produces CO. The formate pathway is not taken because the steps of H₂CO hydrogenation to H₂CO₂ and its further dissociation into CH₂O and O (steps 7-8) result in a combined reaction energy of +180 kJ/mol. Hydrogenation of CO to methanol does not proceed because CH₂O formation from HCO has a high activation energy and is endothermic ($\Delta E_{\text{a}} = 177$ kJ/mol and $\Delta E_{\text{R}} = 142$ kJ/mol, respectively).

For Pd-In₂O₃ (Figure 3.8c), for $T < 425$ °C, the overall rate is mostly controlled by CO₂ dissociation (step 12, $E_{\text{act}} = 65$ kJ/mol). The dominant pathway on the Pd-In₂O₃ surface proceeds via formation of an oxygen vacancy and direct dissociation of CO₂ (Figure 3.8d). At higher temperature ($T > 400$ °C), a decrease in the DRC coefficient of step 12 is observed in favor of the step of OH removal in the carboxyl pathway (step 18, $\Delta E_{\text{a}} = 140$ kJ/mol) which becomes the main rate limiting step. The change in rate limiting steps indicates a change in the dominant pathway. Indeed, for $T > 425$ C, the carboxyl pathway is the dominant pathway of CO formation (Figure A5). Furthermore, this is in line with the increasing reaction order in H₂ with increasing temperature (Figure 3.7d). Compared to the dominant pathway to CO, methanol formation pathways have considerably lower molar fluxes. The formate pathway is not taken because the step of HCO₂ hydrogenation to H₂CO₂ has a high activation energy ($\Delta E_{\text{a}} = 220$ kJ/mol) and is endothermic ($\Delta E_{\text{R}} = 167$ kJ/mol). Furthermore, hydrogenation of CO to CH₃OH does not take place because the hydrogenation of CO to HCO has an activation energy of 148 kJ/mol, significantly higher than the CO desorption energy (31 kJ/mol). This makes further CO hydrogenation less favorable than its desorption.

The DRC analysis and reaction flux analysis for the Pt-In₂O₃ model are shown in Figure 3.8e and Figure 3.8f, respectively. At low temperature, the overall rate of is mainly controlled by CO desorption (step 20,

$\Delta E_{\text{des}} = 158$ kJ/mol). OH hydrogenation (step 18, $\Delta E_{\text{a}} = 133$ kJ/mol) controls the rate to a smaller extent as can be seen by its lower DRC coefficient. In line with Ni-In₂O₃, the dominant pathway proceeds via formation of an oxygen vacancy and direct dissociation of CO₂ (Figure 3.8f). The carboxyl pathway is not taken because the steps of COOH formation and OH removal are associated with high barriers ($\Delta E_{\text{a}} = 147$ kJ/mol and $\Delta E_{\text{a}} = 133$ kJ/mol, respectively). With increasing temperature, the DRC coefficient of CO desorption decreases in favor of CO₂ dissociation (step 12). This is in line with the positive reaction order in CO₂ calculated at higher temperature (Figure 3.7e). Compared to the dominant pathway to CO, hydrogenation of CO₂ to methanol is associated with significantly lower molar fluxes. The formate pathway is not taken because the hydrogenation of HCO₂ to H₂CO₂ has a high activation energy and is endothermic ($\Delta E_{\text{a}} = 146$ kJ/mol, $\Delta E_{\text{R}} = 129$ kJ/mol).

On Rh-In₂O₃, for $T < 300$ °C, the rate of CO₂ consumption is mainly controlled by CO desorption (step 20, $\Delta E_{\text{des}} = 215$ kJ/mol). At higher temperature, the DRC coefficient of this elementary step decreases in favor of CO₂ dissociation (step 12, $\Delta E_{\text{a}} = 81$ kJ/mol) that becomes the rate determining step (RDS) at $T > 450$ °C. In line with the other SA-In₂O₃ models, the dominant pathway proceeds via formation of an oxygen vacancy and direct dissociation of CO₂ (Figure 3.8h). The high barrier associated with OH hydrogenation (step 18, $\Delta E_{\text{a}} = 186$ kJ/mol) hampers the carboxyl pathway. Compared to the dominant pathway to CO, methanol synthesis from CO₂ is associated with significantly lower molar fluxes. The formate pathway is not taken because the hydrogenation of HCO₂ to H₂CO₂ has a high activation energy and is endothermic ($\Delta E_{\text{a}} = 155$ kJ/mol, $\Delta E_{\text{R}} = 136$ kJ/mol).

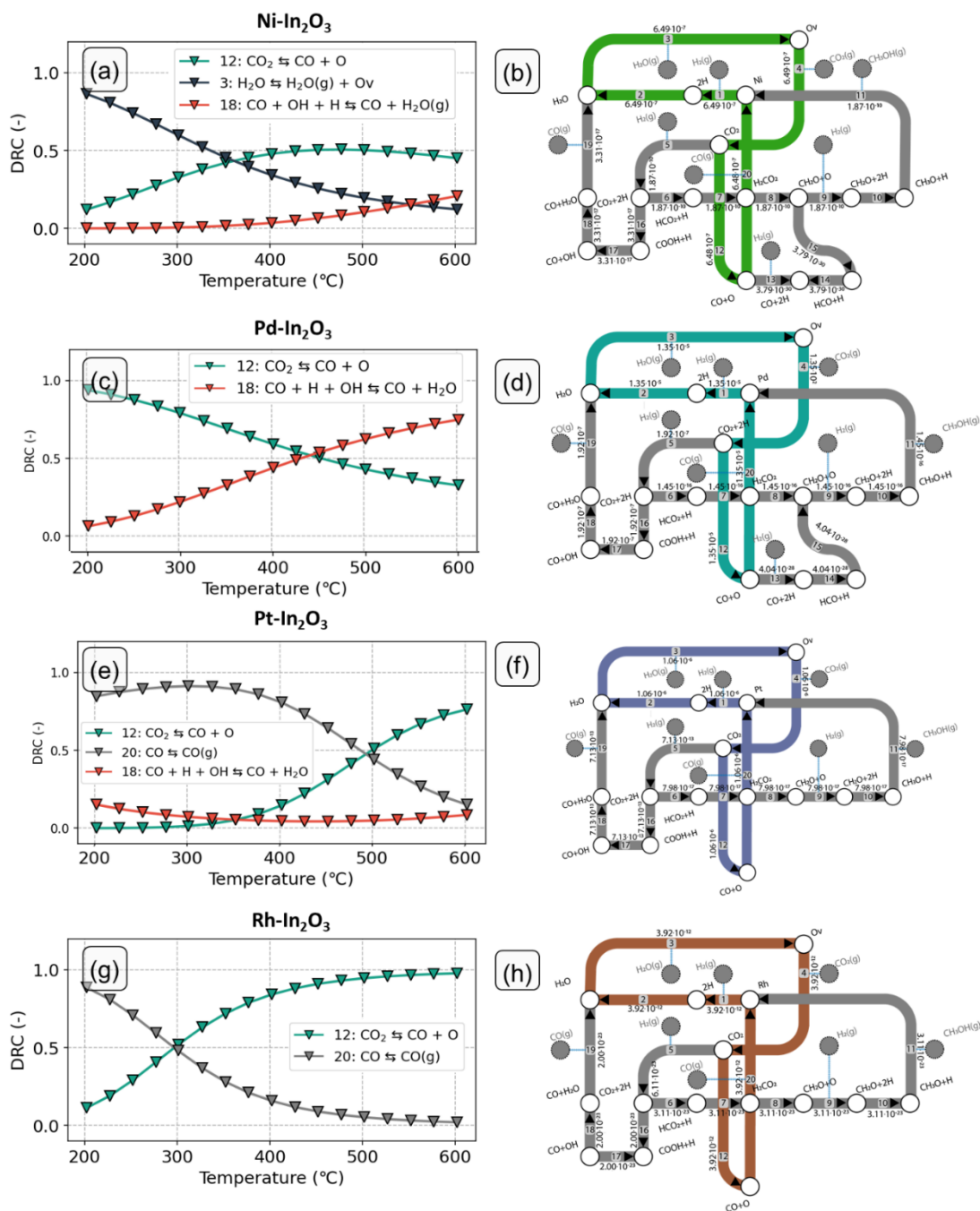


Figure 3.8. Degree of Rate Control and molar fluxes analysis for (a-b) Ni-, (c-d) Pd-, (e-f) Pt and (g-h) Rh-In₂O₃ models. The numbers in the arrows are molar reaction rates (s⁻¹) and are normalized with respect to the amount of adsorbed CO₂. The dominant pathway for each model is indicated by the colored pathways. The molar fluxes are reported at $T = 200$ °C.

3.3.6. General Discussion

The present study clarifies the role of single atoms of Pt, Pd, Ni and Rh adsorbed on the In₂O₃(111) surface in CO₂ hydrogenation. The explored reaction mechanism includes a direct route for CO₂ hydrogenation to methanol (formate pathway), a pathway to methanol via CO hydrogenation and the competing reverse water-gas shift (rWGS) reaction. Earlier studies pointed out that SAs on the In₂O₃ surface do not catalyze CH₄ formation.^{29,30,35} A key result of this study is that CO is the dominant reaction product for all SA-In₂O₃ models. CO is obtained via a redox mechanism involving oxygen vacancy formation followed by CO₂ adsorption and direct C-O bond cleavage. On all models, the CH₃OH selectivity was found to be negligibly small, because barriers associated with the hydrogenation of formate intermediates to methanol are significantly higher than those for the dominant redox pathway to CO.

Methanol formation on In₂O₃ involves the formation of oxygen vacancies and hydrogenation of formate intermediates.⁶¹ On the unpromoted In₂O₃(111) surface, oxygen vacancy formation has an overall barrier of 67 kJ/mol with respect to gas-phase H₂.^{65,61} When a single Pd, Pt or Rh atom is adsorbed on In₂O₃, oxygen vacancy formation exhibits comparable overall barriers of respectively 62, 48 and 57 kJ/mol. In contrast, a much higher overall barrier of 150 kJ/mol is computed for the single Ni atom on In₂O₃(111). Concerning the conversion of formate, HCO₂ hydrogenation to H₂CO₂ on an In₂O₃(110) surface was earlier found to exhibit an activation energy of 55 kJ/mol and a reaction energy of +5 kJ/mol.⁶⁸ On In₂O₃(111), similar activation and reaction energies are found (98 and 15 kJ/mol, respectively).⁶³ All SA-In₂O₃ models show higher activation energies for this step (step 7), which is the main cause of the very low methanol formation rate. We performed a sensitivity analysis of the microkinetic simulations involving decreasing the activation energies of steps 7 by 10, 20, 30 and 40 kJ/mol. The results given in Figure A6 show that decreasing barriers result in a higher methanol selectivity for Ni-, Pt- and Rh-In₂O₃. Herein, we consider methanol selectivity of at least 1% as significant. Methanol formation is least improved for Pd-In₂O₃, because the activation energy associated with HCO₂ hydrogenation (step 7) is very high (220 kJ/mol). In this case, a decrease of at least 80 kJ/mol is required to obtain significant CH₃OH selectivity. We extended the sensitivity analysis to include H₂CO₂ dissociation (step 8) and reported the results in Figure A7. Also in this case, decreasing barriers results in a higher methanol selectivity for Ni-, Pt- and Rh-In₂O₃, whereas methanol formation is less improved for Pd-In₂O₃ because the previous step has a higher barrier (220 kJ/mol and 62 kJ/mol for steps 7-8, respectively).

Our microkinetic simulations show that all SA-In₂O₃ have CO as the main product obtained via a redox mechanism. The activity for the rWGS reaction decreases in the order Pd > Ni > bare In₂O₃ > Pt > Rh (Figure A5d). We now explain this finding based on the DFT-computed activation energies and the analysis of the rate limiting steps. On all SA-In₂O₃ models, direct CO₂ dissociation (step 12) and subsequent CO

desorption (step 20) are the main rate-limiting steps towards CO formation. On Pd-In₂O₃, these steps have barriers of 65 and 31 kJ/mol, respectively. On Ni-In₂O₃, direct CO₂ dissociation and CO desorption are associated with barriers of 91 and 80 kJ/mol, respectively. On bare-In₂O₃, CO is obtained via carboxyl pathway involving a COOH intermediate. This pathway is mainly limited by the rate of COOH dissociation which is associated with a high barrier ($\Delta E_a = 150$ kJ/mol). Compared to Ni and Pd-In₂O₃, the barrier for CO₂ dissociation on Pt-In₂O₃ is similar ($\Delta E_a = 65$ kJ/mol), but CO desorption is associated with a higher barrier ($\Delta E_{des} = 158$ kJ/mol). On Rh-In₂O₃, desorption of CO is associated with a high desorption energy ($\Delta E_{des} = 215$ kJ/mol) hampering its formation. For this reason, this model shows the lowest activity to CO.

We now explain why the redox pathway is preferred over the carboxyl pathway for the formation of CO on our SA-In₂O₃ models. In the redox pathway, the C-O bond in CO₂ is broken directly resulting in CO binding to the SA and the O healing the vacancy. This process is associated with relatively low barriers on all models, in line with the strong SA-O bond (Table A9). Notably, on a bare In₂O₃(110) surface, where CH₃OH is the main product, replenishing the oxygen vacancy by CO₂ dissociation is associated with a reaction energy of 1.4 eV.⁶⁸ This indicates that direct CO₂ dissociation would have a barrier of at least 1.4 eV, making this elementary reaction step unlikely. In contrast with SA-promoted In₂O₃, on bare-In₂O₃, there is no active site available for accepting the CO molecule resulting from CO₂ dissociation. On the SA-In₂O₃ models, breaking the C-O bond on a COOH intermediate is also possible, however the subsequent step of OH removal via H₂O formation is associated with high barriers because it requires the migration of a OH moiety to the SA.

We also compare our results to those recently reported in the literature. In line with the present work, Frei et al. concluded from DFT calculations that a Ni SA on In₂O₃ would be active for the rWGS, because it features lower barriers compared to CO₂ hydrogenation to methanol.²⁹ Shen et al. deployed DFT to compare various pathways of CO₂ hydrogenation to methanol on a Ni₄/In₂O₃(111) model and found that methanol can be obtained via CO intermediate obtained by rWGS.⁷⁵ In an earlier computational work, we reported that single atoms of Ni either doped in or adsorbed on In₂O₃(111) surface would mainly catalyze CO formation, whereas small Ni clusters would mainly lead to methanol.²⁷ In line with this earlier work, we indicate here that the Ni-In₂O₃ model features low-barrier CO₂ dissociation resulting in a preference for CO formation over hydrogenation to methanol. Ye et al. reported that methanol is the main product of CO₂ hydrogenation via formate on a Pd₄/In₂O₃(111) model.⁷⁰ Our Pd-In₂O₃ model features higher barriers for the formate pathway compared to direct CO₂ dissociation precluding methanol formation in favor of CO. Liu et al. reported that methanol formation on a Pt₄/In₂O₃(111) model takes place via hydrogenation of CO resulting from CO₂ dissociation.³² Our Pt-In₂O₃ model does not allow a TS for the subsequent hydrogenation steps of CO to HCO and H₂CO precluding methanol formation from CO hydrogenation.

Clusters of Pd, Pt or Ni on the In₂O₃(111) surface catalyze the formation of methanol because hydrogenation of either formate or CO is favored over the rWGS reaction to CO. However, in the limit of a single atom of Pd, Pt or Ni on the In₂O₃(111) surface, pathways leading to methanol have higher barriers than the redox pathway to CO resulting in low methanol selectivity. In a recent theoretical study, Pinheiro Araújo et al. studied atomically dispersed metal atoms (Pd, Pt, Rh, Ni, Co, Au, Ir) on the In₂O₃ surface.²⁸ They speculated on the basis of energy diagrams that CO₂ hydrogenation to methanol via formate is favored over CO formation. Although this conclusion is at odds with our finding from microkinetic simulations that CO₂ hydrogenation on SA-promoted In₂O₃ would mainly lead to CO, it can be understood from the fact that the study of Pinheiro Araújo et al. only considered the COOH pathway to CO, i.e., they omitted the redox pathway.

3.4. Conclusions

Using microkinetic models and DFT calculations, we clarified the role of single atoms (SA) on In₂O₃ in CO₂ hydrogenation to CH₃OH and CO. We investigated the role of single atoms of Pt, Pd, Ni and Rh on the (111) surface of In₂O₃ for the formation of methanol via formate and CO as well as the competing rWGS reaction via redox and carboxyl pathways. Compared to the pristine In₂O₃(111) surface, adsorbing a single Pd, Pt or Rh atom results in comparable overall barriers for oxygen vacancy formation. In contrast, the presence of a single Ni atom on the In₂O₃ surface increases the overall barrier for oxygen vacancy formation significantly. Microkinetic simulations reveal that all SA-In₂O₃ models mainly catalyze CO via formation of an oxygen vacancy followed by CO₂ adsorption and direct C-O bond cleavage (redox pathway). The carboxyl pathway to CO is not taken, because OH removal resulting from COOH dissociation is associated with higher barriers compared to the dominant redox pathway. The model predicts that Pd is the preferred promoter for In₂O₃ model, achieving the highest activity among the transition metals considered due to a low barrier for CO₂ dissociation and a relatively weak adsorption strength of the CO product. For all models, the CH₃OH selectivity is negligibly low because high barriers are associated with the hydrogenation of HCO₂ to H₂CO₂ and its subsequent dissociation into CH₂O (formate pathway) compared to the dominant rWGS pathway.

3.5 References

- (1) González-Garay, A.; Frei, M. S.; Al-Qahtani, A.; Mondelli, C.; Guillén-Gosálbez, G.; Pérez-Ramírez, J. Plant-to-Planet Analysis of CO₂-Based Methanol Processes. *Energy Environ. Sci.* **2019**, *12*, 3425–3436.
- (2) Kondratenko, E. V.; Mul, G.; Baltrusaitis, J.; Larrazábal, G. O.; Pérez-Ramírez, J. Status and Perspectives of CO₂ Conversion into Fuels and Chemicals by Catalytic, Photocatalytic and Electrocatalytic Processes. *Energy Environ. Sci.* **2013**, *6*, 3112.
- (3) Dias, V.; Pochet, M.; Contino, F.; Jeanmart, H. Energy and Economic Costs of Chemical Storage. *Front. Mech. Eng.* **2020**, *6*, 21.
- (4) Álvarez, A.; Bansode, A.; Urakawa, A.; Bavykina, A. V.; Wezendonk, T. A.; Makkee, M.; Gascon, J.; Kapteijn, F. Challenges in the Greener Production of Formates/Formic Acid, Methanol, and DME by Heterogeneously Catalyzed CO₂ Hydrogenation Processes. *Chem. Rev.* **2017**, *117*, 9804–9838.
- (5) Zhong, J.; Yang, X.; Wu, Z.; Liang, B.; Huang, Y.; Zhang, T. State of the Art and Perspectives in Heterogeneous Catalysis of CO₂ Hydrogenation to Methanol. *Chem. Soc. Rev.* **2020**, *49*, 1385–1413.
- (6) Jiang, X.; Nie, X.; Guo, X.; Song, C.; Chen, J. G. Recent Advances in Carbon Dioxide Hydrogenation to Methanol via Heterogeneous Catalysis. *Chem. Rev.* **2020**, *120*, 7984–8034.
- (7) Wang, J.; Zhang, G.; Zhu, J.; Zhang, X.; Ding, F.; Zhang, A.; Guo, X.; Song, C. CO₂ Hydrogenation to Methanol over In₂O₃-Based Catalysts: From Mechanism to Catalyst Development. *ACS Catal.* **2021**, *2020*, 1406–1423.
- (8) Daza, Y. A.; Kuhn, J. N. CO₂ Conversion by Reverse Water Gas Shift Catalysis: Comparison of Catalysts, Mechanisms and Their Consequences for CO₂ Conversion to Liquid Fuels. *RSC Adv.* **2016**, *6*, 49675–49691.
- (9) Saeidi, S.; Amin, N. A. S.; Rahimpour, M. R. Hydrogenation of CO₂ to Value-Added Products - A Review and Potential Future Developments. *J. CO₂ Util.* **2014**, *5*, 66–81.
- (10) Li, W.; Wang, H.; Jiang, X.; Zhu, J.; Liu, Z.; Guo, X.; Song, C. A Short Review of Recent Advances in CO₂ Hydrogenation to Hydrocarbons over Heterogeneous Catalysts. *RSC Advances*. Royal Society of Chemistry February 16, **2018**, pp 7651–7669.
- (11) Gumber, S.; Gurumoorthy, A. V. P. Methanol Economy Versus Hydrogen Economy. *Methanol Sci. Eng.* **2018**, 661–674.
- (12) Olah, G. A. Beyond Oil and Gas: The Methanol Economy. *Angew. Chemie - Int. Ed.* **2005**, *44*, 2636–2639.
- (13) Goepfert, A.; Czaun, M.; Jones, J. P.; Surya Prakash, G. K.; Olah, G. A. Recycling of Carbon Dioxide to Methanol and Derived Products – Closing the Loop. *Chem. Soc. Rev.* **2014**, *43*, 7995–8048.
- (14) Baltes, C.; Vukojević, S.; Schüth, F. Correlations between Synthesis, Precursor, and Catalyst Structure and Activity of a Large Set of CuO/ZnO/Al₂O₃ Catalysts for Methanol Synthesis. *J. Catal.* **2008**, *258*, 334–344.
- (15) Behrens, M. Promoting the Synthesis of Methanol: Understanding the Requirements for an Industrial Catalyst for the Conversion of CO₂. *Angew. Chemie Int. Ed.* **2016**, *55*, 14906–14908.
- (16) Nakamura, J.; Choi, Y.; Fujitani, T. On the Issue of the Active Site and the Role of ZnO in Cu/ZnO Methanol Synthesis Catalysts. *Top. Catal.* **2003**, *22*, 277–285.
- (17) Fichtl, M. B.; Schlereth, D.; Jacobsen, N.; Kasatkin, I.; Schumann, J.; Behrens, M.; Schlögl, R.; Hinrichsen,

- O. Kinetics of Deactivation on Cu/ZnO/Al₂O₃ Methanol Synthesis Catalysts. *Appl. Catal. A Gen.* **2015**, *502*, 262–270.
- (18) Jiang, X.; Nie, X.; Guo, X.; Song, C.; Chen, J. G. Recent Advances in Carbon Dioxide Hydrogenation to Methanol via Heterogeneous Catalysis. *Chem. Rev.* **2020**, *120*, 7984–8034.
- (19) Ye, J.; Liu, C.; Ge, Q. DFT Study of Adsorption and Hydrogenation on the In₂O₃ Surface. *J. Phys. Chem. C* **2012**, *116*, 7817–7825.
- (20) Frei, M. S.; Mondelli, C.; Cesarini, A.; Krumeich, F.; Hauert, R.; Stewart, J. A.; Curulla Ferré, D.; Pérez-Ramírez, J. Role of Zirconia in Indium Oxide-Catalyzed CO₂ Hydrogenation to Methanol. *ACS Catal.* **2020**, *10*, 1133–1145.
- (21) Sun, Q.; Ye, J.; Liu, C.; Ge, Q. In₂O₃ as a Promising Catalyst for CO₂ Utilization: A Case Study with Reverse Water Gas Shift over In₂O₃. *Greenh. Gases Sci. Technol.* **2014**, *4*, 140–144.
- (22) Ye, J.; Liu, C.; Mei, D.; Ge, Q. Active Oxygen Vacancy Site for Methanol Synthesis from Hydrogenation on (110): A DFT Study. *ACS Catal.* **2013**, *3*, 1296–1306.
- (23) Cao, A.; Wang, Z.; Li, H.; Nørskov, J. K. Relations between Surface Oxygen Vacancies and Activity of Methanol Formation. *ACS Catal.* **2021**, *11*, 1780–1786.
- (24) Wang, J.; Zhang, G.; Zhu, J.; Zhang, X.; Ding, F.; Zhang, A.; Guo, X.; Song, C. CO₂ Hydrogenation to Methanol over In₂O₃-Based Catalysts: From Mechanism to Catalyst Development. *ACS Catal.* **2021**, *11*, 1406–1423.
- (25) Posada-Borbón, A.; Grönbeck, H. A First-Principles-Based Microkinetic Study of to CH₃OH over In₂O₃(110). *ACS Catal.* **2021**, *11*, 9996–10006.
- (26) Zhu, J.; Cannizzaro, F.; Liu, L.; Zhang, H.; Kosinov, N.; Filot, I. A. W.; Rabeah, J.; Brückner, A.; Hensen, E. J. M. Ni-In Synergy in CO₂ hydrogenation to Methanol. *ACS Catal.* **2021**, *11*, 11371–11384.
- (27) Cannizzaro, F.; Hensen, E. J. M.; Filot, I. A. W. The Promoting Role of Ni on In₂O₃ for CO₂ Hydrogenation to Methanol. *ACS Catal.* **2023**, *13*, 1875–1892.
- (28) Pinheiro Araújo, T.; Morales-Vidal, J.; Zou, T.; García-Muelas, R.; Willi, P. O.; Engel, K. M.; Safonova, O. V.; Faust Akl, D.; Krumeich, F.; Grass, R. N.; Mondelli, C.; López, N.; Pérez-Ramírez, J. Flame Spray Pyrolysis as a Synthesis Platform to Assess Metal Promotion in In₂O₃-Catalyzed CO₂ Hydrogenation. *Adv. Energy Mater.* **2022**, *12*.
- (29) Frei, M. S.; Mondelli, C.; García-Muelas, R.; Morales-Vidal, J.; Philipp, M.; Safonova, O. V.; López, N.; Stewart, J. A.; Ferré, D. C.; Pérez-Ramírez, J. Nanostructure of Nickel-Promoted Indium Oxide Catalysts Drives Selectivity in CO₂ Hydrogenation. *Nat. Commun.* **2021**, *12*, 1–9.
- (30) Frei, M. S.; Mondelli, C.; García-Muelas, R.; Kley, K. S.; Puértolas, B.; López, N.; Safonova, O. V.; Stewart, J. A.; Curulla Ferré, D.; Pérez-Ramírez, J. Atomic-Scale Engineering of Indium Oxide Promotion by Palladium for Methanol Production via CO₂ Hydrogenation. *Nat. Commun.* **2019**, *10*, 1–11.
- (31) Han, Z.; Tang, C.; Wang, J.; Li, L.; Li, C. Atomically Dispersed Ptn+ Species as Highly Active Sites in Pt/In₂O₃ Catalysts for Methanol Synthesis from CO₂ Hydrogenation. *J. Catal.* **2020**.
- (32) Sun, K.; Rui, N.; Shen, C.; Liu, C. J. Theoretical Study of Selective Hydrogenation of CO₂ to Methanol over

- Pt4/ Catalyst. *J. Phys. Chem. C* **2021**, *125*, 10926–10936.
- (33) Wang, J.; Sun, K.; Jia, X.; Liu, C. Jun. CO₂ Hydrogenation to Methanol over Rh/In₂O₃ Catalyst. *Catal. Today* **2021**, *365*, 341–347.
- (34) Dostagir, N. H. M.; Thompson, C.; Kobayashi, H.; Karim, A. M.; Fukuoka, A.; Shrotri, A. Rh Promoted In₂O₃ as a Highly Active Catalyst for to Methanol. *Catal. Sci. Technol.* **2020**, *10*, 8196–8202.
- (35) Dostagir, N. H. M.; Thompson, C.; Kobayashi, H.; Karim, A. M.; Fukuoka, A.; Shrotri, A. Rh Promoted In₂O₃ as a Highly Active Catalyst for CO₂ Hydrogenation to Methanol. *Catal. Sci. Technol.* **2020**, *10*, 8196–8202.
- (36) Ye, J.; Liu, C. J.; Mei, D.; Ge, Q. Methanol Synthesis from CO₂ Hydrogenation over a Pd4/In₂O₃ Model Catalyst: A Combined DFT and Kinetic Study. *J. Catal.* **2014**, *317*, 44–53.
- (37) Kresse, G.; Joubert, D. From Ultrasoft Pseudopotentials to the Projector Augmented-Wave Method. *Phys. Rev. B* **1999**, *59*, 1758.
- (38) Perdew, J. P.; Burke, K.; Ernzerhof, M. Generalized Gradient Approximation Made Simple. *Phys. Rev. Lett.* **1996**, *77*, 3865.
- (39) Kresse, G.; Hafner, J. Ab Initio Molecular-Dynamics Simulation of the Liquid-Metallamorphous-Semiconductor Transition in Germanium. *Phys. Rev. B* **1994**, *49*, 14251–14269.
- (40) Kresse, G.; Furthmüller, J. Efficiency of Ab-Initio Total Energy Calculations for Metals and Semiconductors Using a Plane-Wave Basis Set. *Comput. Mater. Sci.* **1996**, *6*, 15–50.
- (41) Henkelman, G.; Jónsson, H. Improved Tangent Estimate in the Nudged Elastic Band Method for Finding Minimum Energy Paths and Saddle Points. *J. Chem. Phys.* **2000**, *113*, 9978–9985.
- (42) Heidrich, D.; Quapp, W. Saddle Points of Index 2 on Potential Energy Surfaces and Their Role in Theoretical Reactivity Investigations. *Theor. Chim. Acta* **1986**, *70*, 89–98.
- (43) Nelson, R.; Ertural, C.; George, J.; Deringer, V. L.; Hautier, G.; Dronskowski, R. LOBSTER: Local Orbital Projections, Atomic Charges, and Chemical-Bonding Analysis from Projector-Augmented-Wave-Based Density-Functional Theory. *J. Comput. Chem.* **2020**, *41*, 1931–1940.
- (44) Maintz, S.; Volker, L.; Deringer, L.; Tchougr, A. L.; Dronskowski, R. ; LOBSTER: A Tool to Extract Chemical Bonding from Plane-Wave Based DFT. *J. Comput. Chem.*; **2016**, *37*, 11–12.
- (45) Yu, M.; Trinkle, D. R. Accurate and Efficient Algorithm for Bader Charge Integration. *J. Chem. Phys.* **2011**, *134*, 064111.
- (46) Brown, P. N.; Byrne, G. D.; Hindmarsh, A. C. VODE: A Variable-Coefficient ODE Solver. *SIAM J. on Scientific and Statistical Computing.* **2006**, *10*, 1038–1051.
- (47) Byrne, G. D.; Hindmarsh, A. C. Stiff ODE Solvers: A Review of Current and Coming Attractions. *J. Comput. Phys.* **1987**, *70*, 1–62.
- (48) Byrne, G. D.; Hindmarsh, A. C. A Polyalgorithm for the Numerical Solution of Ordinary Differential Equations. *ACM Trans. Math. Softw.* **1975**, *1*, 71–96.
- (49) Shomate, C. H. A Method for Evaluating and Correlating Thermodynamic Data. *J. Phys. Chem.* **2002**, *58*, 368–372.
- (50) NIST Chemistry WebBook <https://webbook.nist.gov/chemistry/> (accessed Feb 1, 2022).

- (51) Kozuch, S.; Shaik, S. A Combined Kinetic-Quantum Mechanical Model for Assessment of Catalytic Cycles: Application to Cross-Coupling and Heck Reactions. *J. Am. Chem. Soc.* **2006**, *128*, 3355–3365.
- (52) Kozuch, S.; Shaik, S. Kinetic-Quantum Chemical Model for Catalytic Cycles: The Haber-Bosch Process and the Effect of Reagent Concentration. *J. Phys. Chem. A* **2008**, *112*, 6032–6041.
- (53) Campbell, C. T. The Degree of Rate Control: A Powerful Tool for Catalysis Research. *ACS Catalysis*. American Chemical Society April 7, 2017, pp 2770–2779.
- (54) Filot, A. W. *Intoduction to microkinetic modeling*. Technische Universiteit Eindhoven, **2022**, ISBN: 978-90-386-4520-9.
- (55) Stegelmann, C.; Schiødt, N. C.; Campbell, C. T.; Stoltze, P. Microkinetic Modeling of Ethylene Oxidation over Silver. *J. Catal.* **2004**, *221*, 630–649.
- (56) Minibaev, R. F.; Bagatur'yants, A. A.; Bazhanov, D. I.; Knizhnik, A. A.; Alfimov, M. V. First-Principles Investigation of the Electron Work Function for the (001) Surface of Indium Oxide In₂O₃ and Indium Tin Oxide (ITO) as a Function of the Surface Oxidation Level. *Nanotechnologies Russ.* **2010**, *5*, 185–190.
- (57) Walsh, A.; Catlow, C. R. A.; Sokol, A. A.; Woodley, S. M. Physical Properties, Intrinsic Defects, and Phase Stability of Indium Sesquioxide. *Chem. Mater.* **2009**, *21*, 4962–4969.
- (58) Karazhanov, S. Z.; Ravindran, P.; Vajeeston, P.; Ulyashin, A.; Finstad, T. G.; Fjellvåg, H. Phase Stability, Electronic Structure, and Optical Properties of Indium Oxide Polytypes. *Phys. Rev. B - Condens. Matter Mater. Phys.* **2007**, *76*.
- (59) Gurlo, A.; Kroll, P.; Riedel, R. Metastability of Corundum-Type In₂O₃. *Chem. - A Eur. J.* **2008**, *14*, 3306–3310.
- (60) Liu, D.; Lei, W. W.; Zou, B.; Yu, S. D.; Hao, J.; Wang, K.; Liu, B. B.; Cui, Q. L.; Zou, G. T. High-Pressure x-Ray Diffraction and Raman Spectra Study of Indium Oxide. *J. Appl. Phys.* **2008**, *104*.
- (61) Frei, M. S.; Capdevila-Cortada, M.; García-Muelas, R.; Mondelli, C.; López, N.; Stewart, J. A.; Curulla Ferré, D.; Pérez-Ramírez, J. Mechanism and Microkinetics of Methanol Synthesis via CO₂ Hydrogenation on Indium Oxide. *J. Catal.* **2018**, *361*, 313–321.
- (62) Walsh, A.; Catlow, C. R. A. Structure, Stability and Work Functions of the Low Index Surfaces of Pure Indium Oxide and Sn-Doped Indium Oxide (ITO) from Density Functional Theory. *J. Mater. Chem.* **2010**, *20*, 10438–10444.
- (63) Frei, M. S.; Capdevila-Cortada, M.; García-Muelas, R.; Mondelli, C.; López, N.; Stewart, J. A.; Curulla Ferré, D.; Pérez-Ramírez, J. Mechanism and Microkinetics of Methanol Synthesis via CO₂ Hydrogenation on Indium Oxide. *J. Catal.* **2018**, *361*, 313–321.
- (64) Frei, M. S.; Mondelli, C.; García-Muelas, R.; Morales-Vidal, J.; Philipp, M.; Safonova, O. V.; López, N.; Stewart, J. A.; Ferré, D. C.; Pérez-Ramírez, J. Nanostructure of Nickel-Promoted Indium Oxide Catalysts Drives Selectivity in CO₂ Hydrogenation. *Nat. Commun.* **2021**, *12*, 1–9.
- (65) Albani, D.; Capdevila-Cortada, M.; Vilé, G.; Mitchell, S.; Martin, O.; López, N.; Pérez-Ramírez, J. Semihydrogenation of Acetylene on Indium Oxide: Proposed Single-Ensemble Catalysis. *Angew. Chemie Int. Ed.* **2017**, *56*, 10755–10760.

- (66) Jia, X.; Sun, K.; Wang, J.; Shen, C.; Liu, C. jun. Selective Hydrogenation of CO₂ to Methanol over Ni/In₂O₃ Catalyst. *J. Energy Chem.* **2020**, *50*, 409–415.
- (67) Zhu, J.; Cannizzaro, F.; Liu, L.; Zhang, H.; Kosinov, N.; Filot, I. A. W.; Rabeah, J.; Brückner, A.; Hensen, E. J. M. Ni-In Synergy in CO₂ Hydrogenation to Methanol. *ACS Catal.* **2021**, *11*, 11371–11384.
- (68) Ye, J.; Liu, C.; Mei, D.; Ge, Q. Active Oxygen Vacancy Site for Methanol Synthesis from CO₂ Hydrogenation on In₂O₃(110): A DFT Study. *ACS Catal.* **2013**, *3*, 1296–1306.
- (69) Ye, J.; Liu, C.; Ge, Q. DFT Study of CO₂ Adsorption and Hydrogenation on the In₂O₃ Surface. *J. Phys. Chem. C* **2012**, *116*, 7817–7825.
- (70) Ye, J.; Liu, C. J.; Mei, D.; Ge, Q. Methanol Synthesis from CO₂ Hydrogenation over a Pd₄/In₂O₃ Model Catalyst: A Combined DFT and Kinetic Study. *J. Catal.* **2014**, *317*, 44–53.
- (71) Rohrbach, A.; Hafner, J. Molecular Adsorption of NO on NiO(100): DFT and DFT+U Calculations. *Phys. Rev. B - Condens. Matter Mater. Phys.* **2005**, *71*, 1–7.
- (72) Liu, X.; Sun, L.; Deng, W. Q. Theoretical Investigation of CO₂ Adsorption and Dissociation on Low Index Surfaces of Transition Metals. *J. Phys. Chem. C* **2018**, *122*, 8306–8314.
- (73) Ye, J.; Liu, C.; Mei, D.; Ge, Q. Active Oxygen Vacancy Site for Methanol Synthesis from CO₂ Hydrogenation on In₂O₃(110): A DFT Study. *ACS Catal.* **2013**, *3*, 1296–1306.
- (74) Shen, C.; Bao, Q.; Xue, W.; Sun, K.; Zhang, Z.; Jia, X.; Mei, D.; Liu, C. jun. Synergistic Effect of the Metal-Support Interaction and Interfacial Oxygen Vacancy for CO₂ Hydrogenation to Methanol over Ni/In₂O₃ Catalyst: A Theoretical Study. *J. Energy Chem.* **2022**, *65*, 623–629.

Appendix A

A1. Binding energies of single atoms on In₂O₃(111)

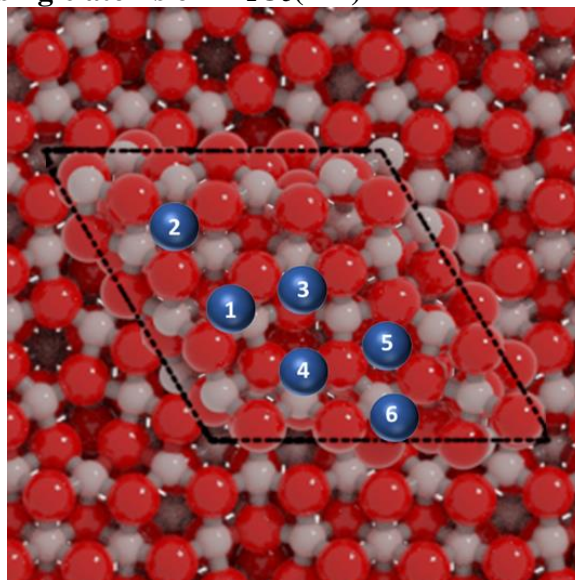


Figure A1. Adsorption sites for single atoms on In₂O₃(111). Blue: SA. Grey: In. Red: O.

Table A1. Adsorption energies (eV) of single atoms on the indicated by Figure S1. The reference for the metal (Ni, Pd, Pt and Rh) is a single atom in the gas phase.

ΔE_{ads} [eV]				
ID	Ni	Pd	Pt	Rh
1	-5.17	-3.44	-4.86	-3.63
2	-4.99	-3.32	-4.68	-4.31
3	-4.96	-3.22	-4.54	-4.08
4	-4.85	-3.19	-4.63	-3.89
5	-4.17	-3.15	-4.17	-3.54
6	-4.20	-3.19	-4.31	-3.33

A2. Electronic structure analysis

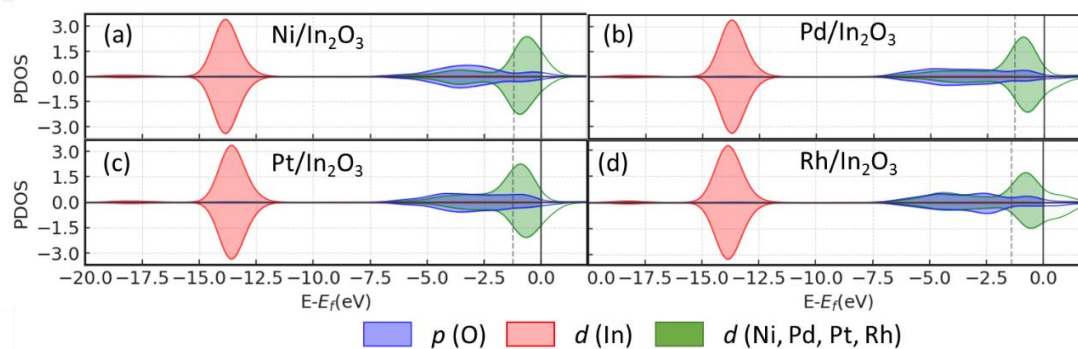


Figure A2. Partial density of state (PDOS) of Ni 3d, Pd 4d, Pt 5d and Rh 4d, O 2p (the O atom adjacent to the metal SA) and In d orbitals. (a) Ni-In₂O₃, (b) Pd-In₂O₃, (c) Pt-In₂O₃ and (d) Rh-In₂O₃.

A3. Oxygen vacancies

Table A2. Oxygen vacancy formation energies with respect to gas-phase O₂ (E_{Ov}/O_2) and H₂O (E_{Ov}/H_2O) in eV for bare In₂O₃ and SA-promoted In₂O₃ surfaces.

ID	In ₂ O ₃		Ni-In ₂ O ₃		Pd-In ₂ O ₃		Pt-In ₂ O ₃		Rh-In ₂ O ₃	
	E_{Ov}/O_2	E_{Ov}/H_2O	E_{Ov}/O_2	E_{Ov}/H_2O	E_{Ov}/O_2	E_{Ov}/H_2O	E_{Ov}/O_2	E_{Ov}/H_2O	E_{Ov}/O_2	E_{Ov}/H_2O
1	1.94	-0.68	3.98	1.46	1.75	-0.77	3.13	0.61	3.00	0.47
2	1.94	-0.68	3.99	1.47	2.23	-0.29	4.87	2.35	2.95	0.43
3	1.95	-0.67	3.98	1.46	1.75	-0.77	2.10	-0.41	3.64	1.12
4	2.04	-0.58	3.97	1.45	2.88	0.36	4.37	1.85	3.21	0.69
5	2.04	-0.58	4.09	1.56	2.84	0.32	4.31	1.79	2.96	0.44
6	2.76	-0.57	4.13	1.61	2.83	0.31	4.07	1.55	3.85	1.33
7	2.77	0.15	4.20	1.68	3.36	0.84	4.70	2.18	4.29	1.77
8	2.74	0.12	4.49	1.97	3.35	0.83	4.70	2.18	3.53	1.01
9	2.76	0.14	4.20	1.68	3.36	0.87	4.74	2.22	4.00	1.48
10	2.67	0.05	4.20	1.68	3.12	0.60	4.74	2.22	3.84	1.32
11	2.50	-0.12	4.26	1.74	3.11	0.59	4.47	1.95	3.85	1.33
12	2.50	-0.12	4.23	1.74	3.11	0.59	4.44	1.92	3.82	1.30

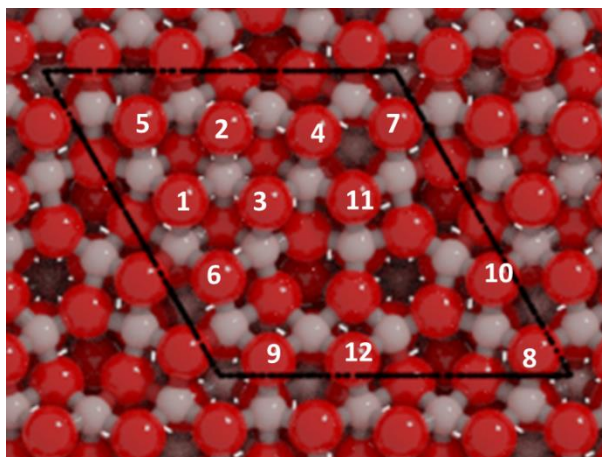
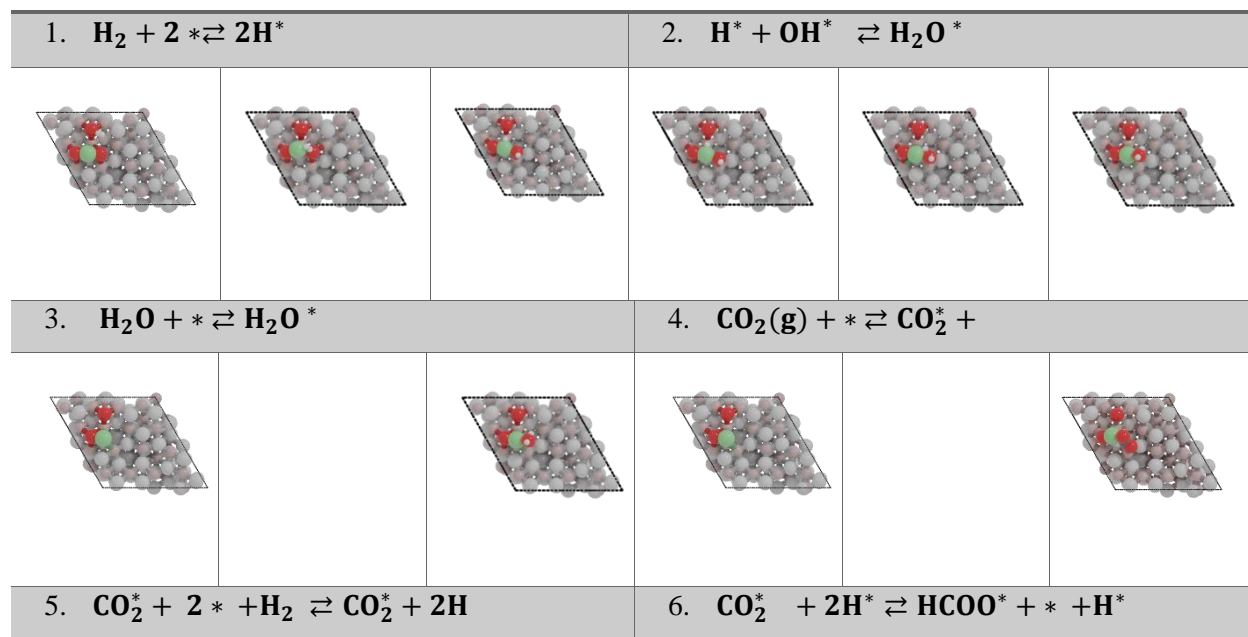


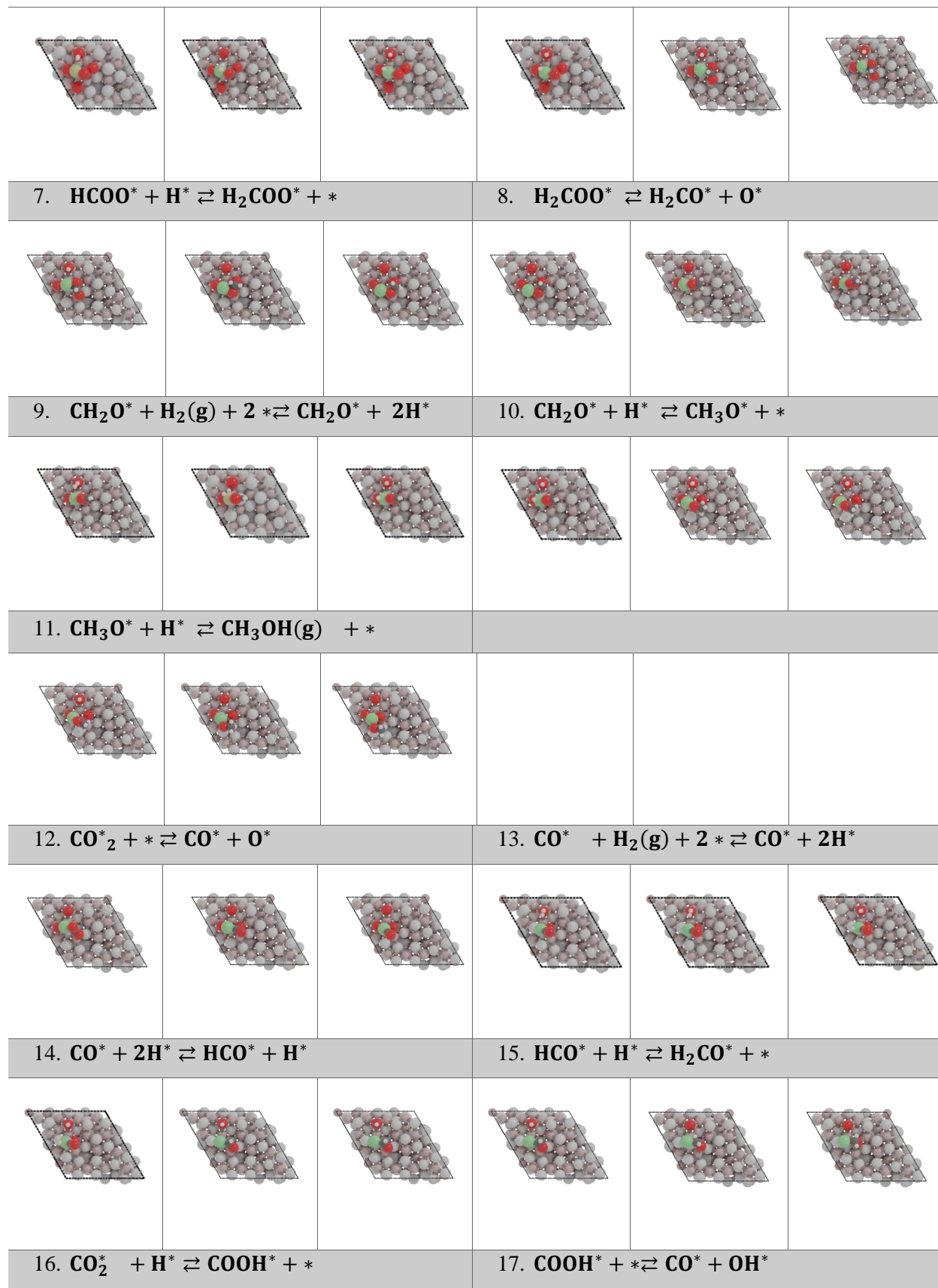
Figure A3. Positions of the 12 surface oxygens for the calculations reported in Table S2 (red: O; grey: In).

Table A3. Geometrical parameters (Å) and oxygen vacancy formation energy (E_{Ov} , in eV) for the O atom directly connected to the SA with the lowest E_{Ov} .

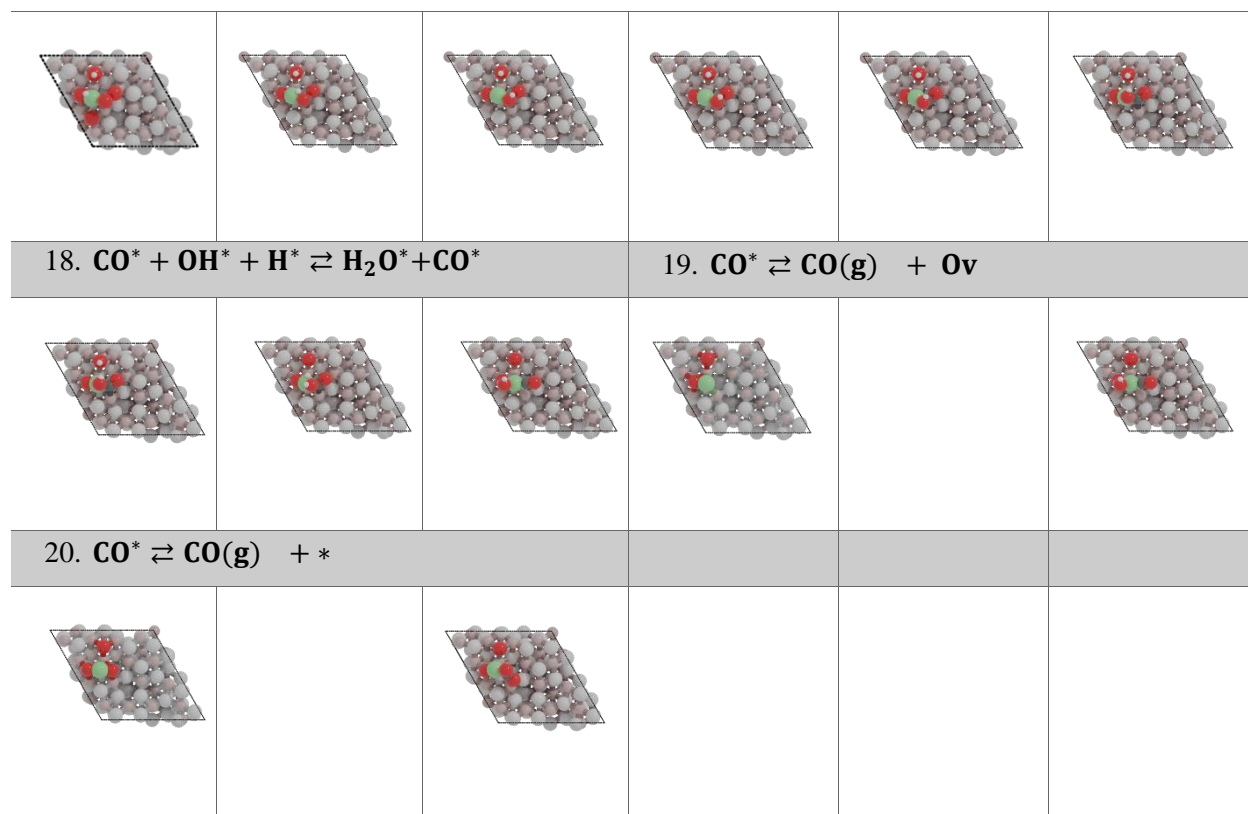
	Ni-In ₂ O ₃ (111)	Pd-In ₂ O ₃ (111)	Pt-In ₂ O ₃ (111)	Rh-In ₂ O ₃ (111)
d_{M-O} / Å	1.82	2.13	2.10	1.98
E_{Ov} / eV	1.46	-0.76	-0.43	0.17

A4. Geometries of elementary reaction steps on Ni-In₂O₃(111)

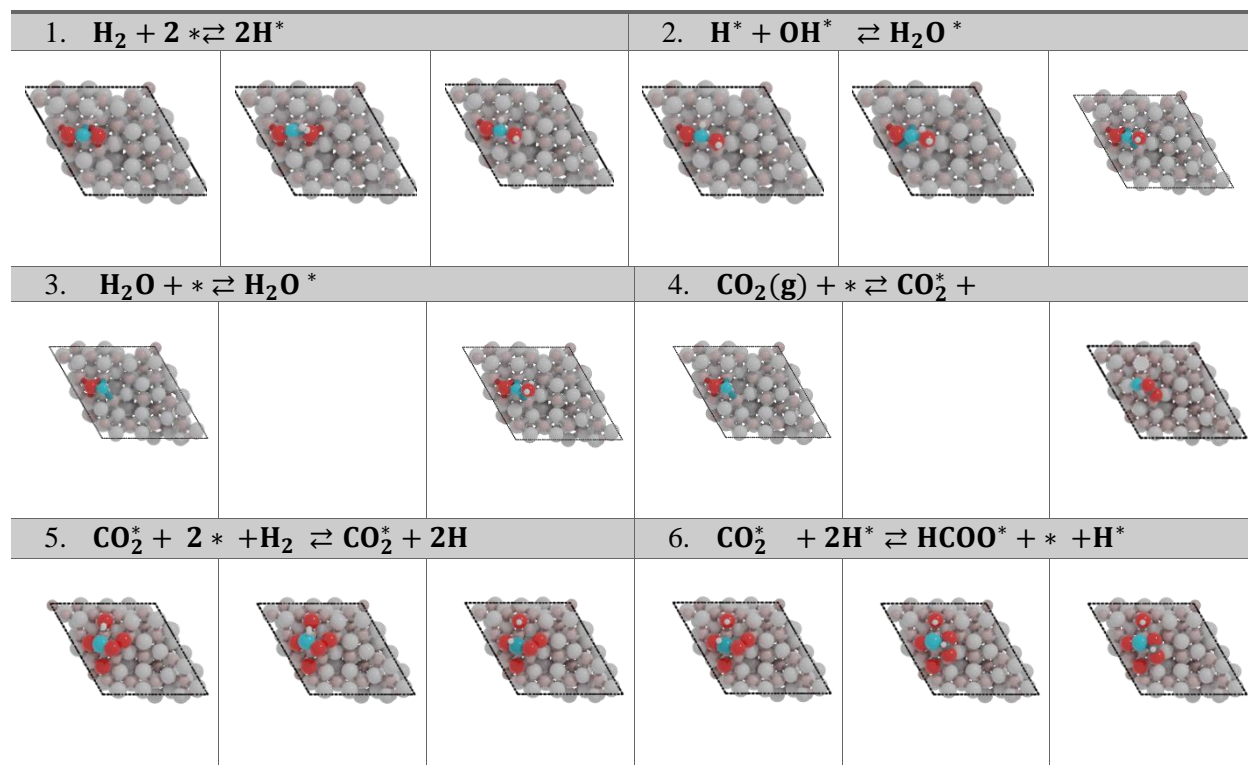


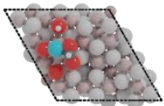
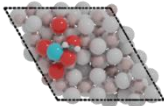
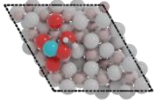
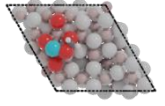
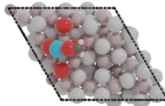
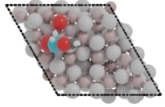
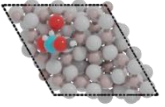
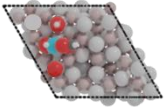
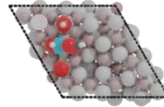
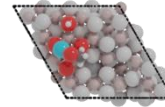
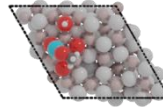
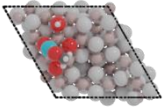
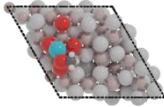
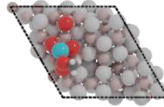
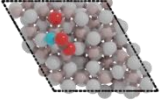
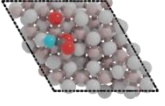
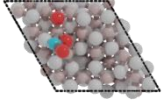
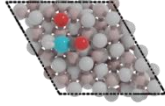
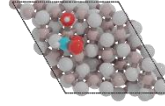
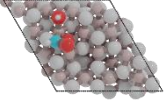
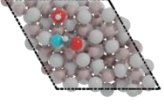
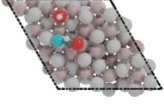
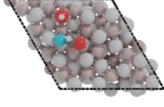
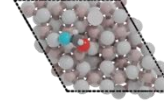
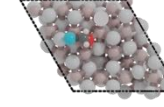
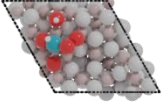
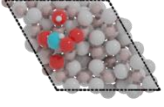
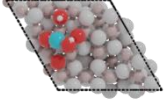
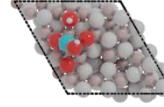
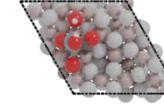


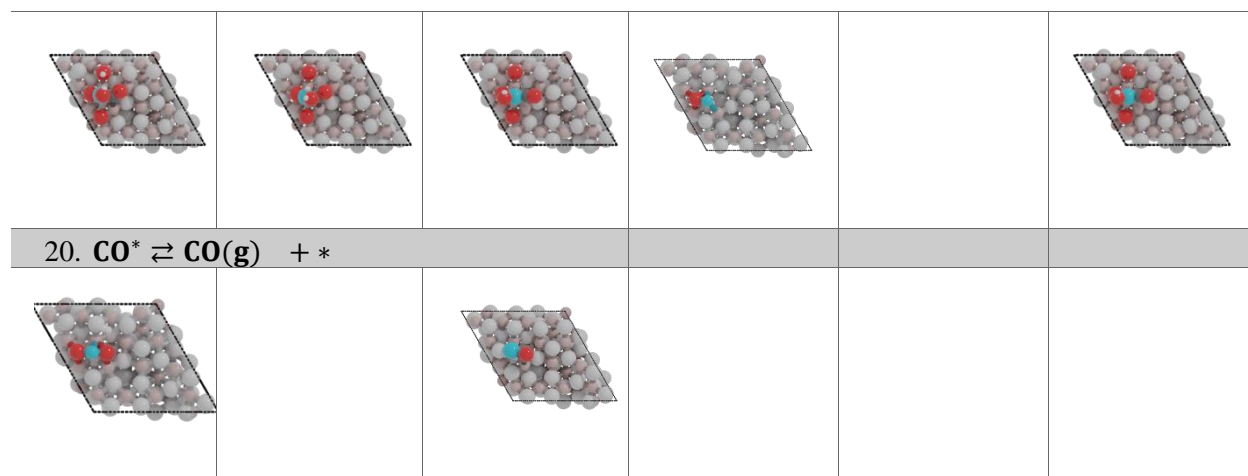
A computational study of CO₂ hydrogenation on single atoms of Pt, Pd, Ni and Rh on In₂O₃(111)



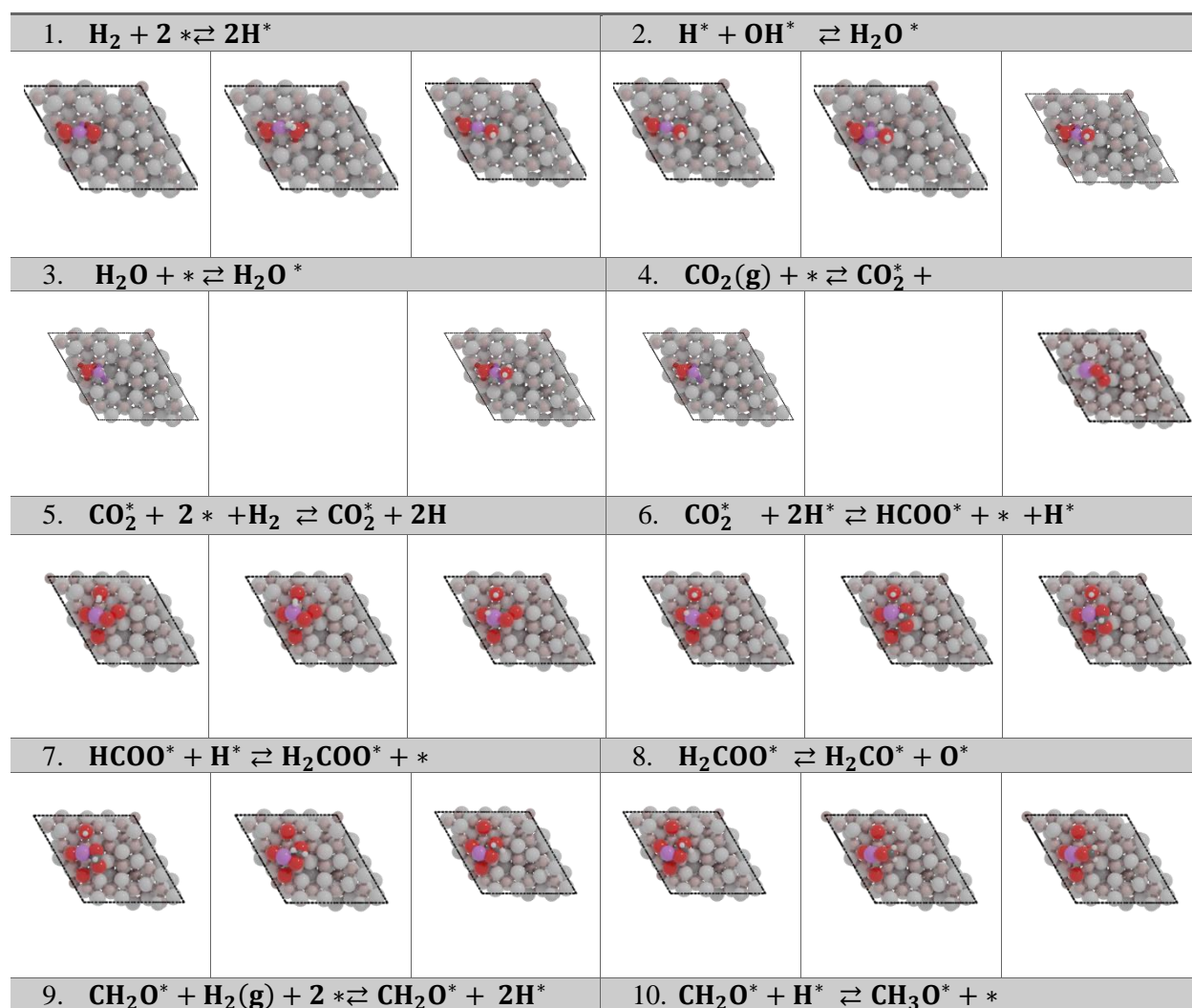
A5. Geometries of elementary reaction steps on Pd-In₂O₃(111)



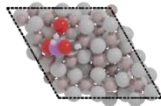
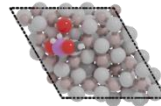
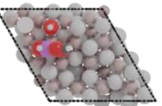
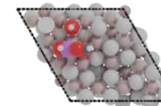
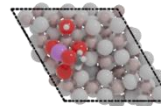
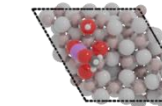
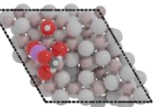
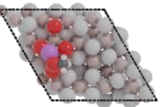
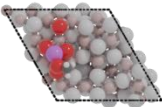
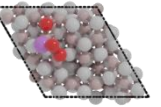
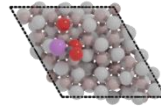
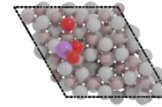
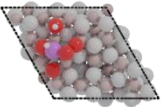
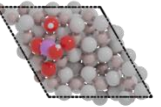
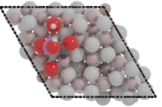
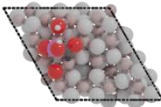
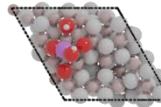
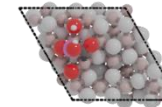
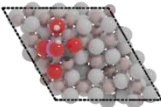
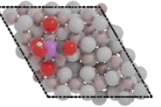
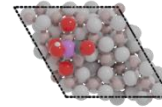
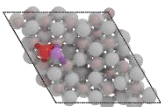
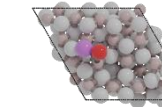
7. $\text{HCOO}^* + \text{H}^* \rightleftharpoons \text{H}_2\text{COO}^* + *$			8. $\text{H}_2\text{COO}^* \rightleftharpoons \text{H}_2\text{CO}^* + \text{O}^*$		
					
9. $\text{CH}_2\text{O}^* + \text{H}_2(\text{g}) + 2 * \rightleftharpoons \text{CH}_2\text{O}^* + 2\text{H}^*$			10. $\text{CH}_2\text{O}^* + \text{H}^* \rightleftharpoons \text{CH}_3\text{O}^* + *$		
					
11. $\text{CH}_3\text{O}^* + \text{H}^* \rightleftharpoons \text{CH}_3\text{OH}(\text{g}) + *$					
					
12. $\text{CO}_2^* + * \rightleftharpoons \text{CO}^* + \text{O}^*$			13. $\text{CO}^* + \text{H}_2(\text{g}) + 2 * \rightleftharpoons \text{CO}^* + 2\text{H}^*$		
					
14. $\text{CO}^* + 2\text{H}^* \rightleftharpoons \text{HCO}^* + \text{H}^*$			15. $\text{HCO}^* + \text{H}^* \rightleftharpoons \text{H}_2\text{CO}^* + *$		
					
16. $\text{CO}_2^* + \text{H}^* \rightleftharpoons \text{COOH}^* + *$			17. $\text{COOH}^* + * \rightleftharpoons \text{CO}^* + \text{OH}^*$		
					
18. $\text{CO}^* + \text{OH}^* + \text{H}^* \rightleftharpoons \text{H}_2\text{O}^* + \text{CO}^*$			19. $\text{CO}^* \rightleftharpoons \text{CO}(\text{g}) + \text{Ov}$		

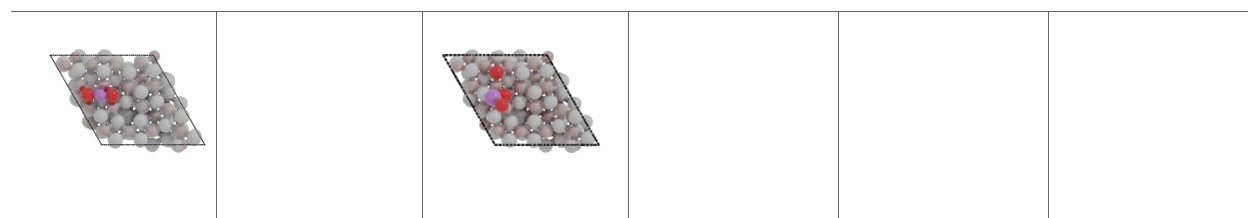


A6. Geometries of elementary reaction steps on Pt-In₂O₃(111)

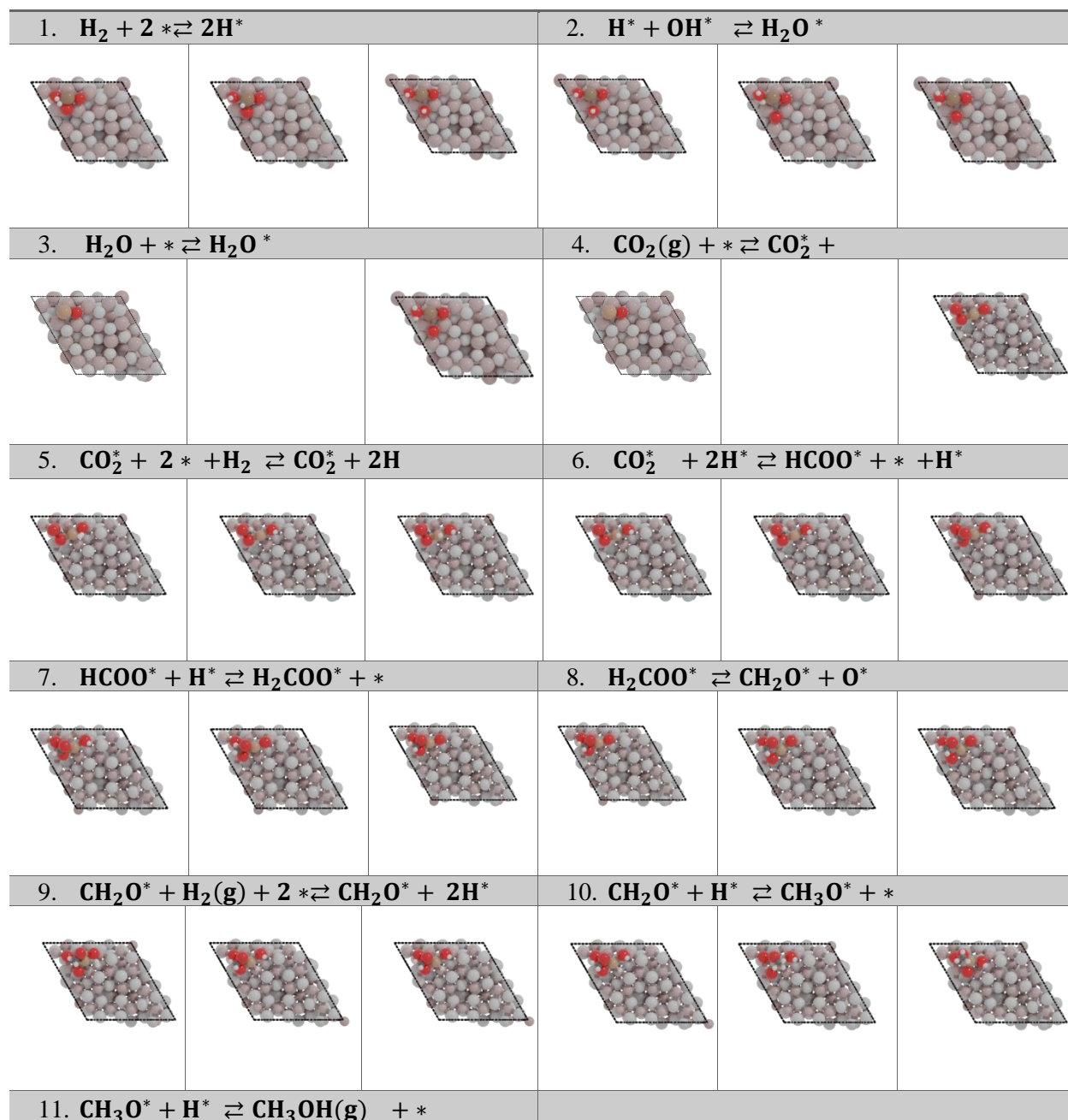


Chapter 3

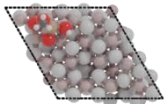
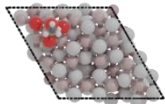
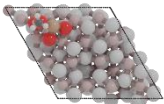
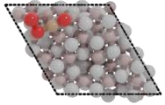
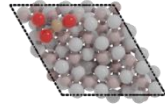
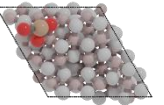
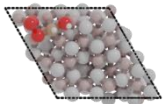
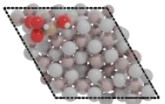
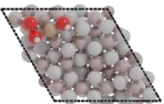
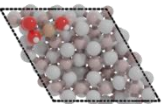
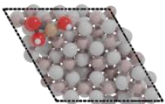
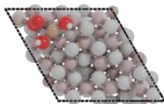
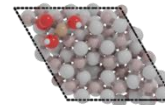
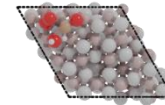
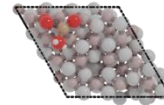
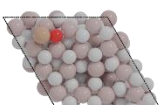
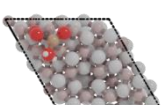
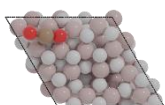
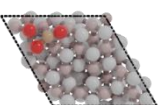
					
11. $\text{CH}_3\text{O}^* + \text{H}^* \rightleftharpoons \text{CH}_3\text{OH}(\text{g}) + *$					
					
12. $\text{CO}_2^* + * \rightleftharpoons \text{CO}^* + \text{O}^*$			13.		
			N.A.	N.A.	N.A.
14.			15.		
N.A.	N.A.	N.A.	N.A.	N.A.	N.A.
16. $\text{CO}_2^* + \text{H}^* \rightleftharpoons \text{COOH}^* + *$			17. $\text{COOH}^* + * \rightleftharpoons \text{CO}^* + \text{OH}^*$		
					
18. $\text{CO}^* + \text{OH}^* + \text{H}^* \rightleftharpoons \text{H}_2\text{O}^* + \text{CO}^*$			19. $\text{CO}^* \rightleftharpoons \text{CO}(\text{g}) + \text{Ov}$		
					
20. $\text{CO}^* \rightleftharpoons \text{CO}(\text{g}) + *$					



A7. Geometries of elementary reaction steps on Rh-In₂O₃(111)



Chapter 3

					
12. $\text{CO}_2^* + * \rightleftharpoons \text{CO}^* + \text{O}^*$			13. $\text{CO}^* + \text{H}_2(\text{g}) + 2 * \rightleftharpoons \text{CO}^* + 2\text{H}^*$		
			N.A.	N.A.	N.A.
14. $\text{CO}^* + 2\text{H}^* \rightleftharpoons \text{HCO}^* + \text{H}^*$			15. $\text{HCO}^* + \text{H}^* \rightleftharpoons \text{H}_2\text{CO}^* + *$		
N.A.	N.A.	N.A.	N.A.	N.A.	N.A.
16. $\text{CO}_2^* + \text{H}^* \rightleftharpoons \text{COOH}^* + *$			17. $\text{COOH}^* + * \rightleftharpoons \text{CO}^* + \text{OH}^*$		
					
18. $\text{CO}^* + \text{OH}^* + \text{H}^* \rightleftharpoons \text{H}_2\text{O}^* + \text{CO}^*$			19. $\text{CO}^* \rightleftharpoons \text{CO}(\text{g}) + \text{Ov}$		
					
20. $\text{CO}^* \rightleftharpoons \text{CO}(\text{g}) + *$					
					

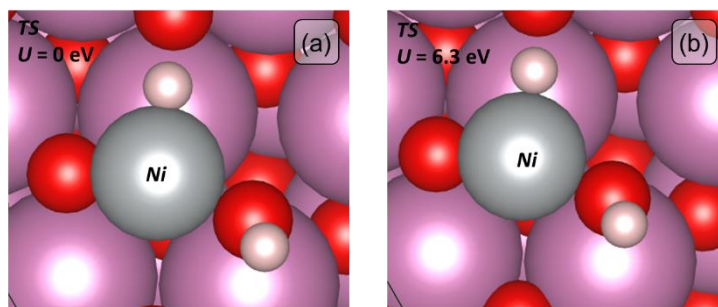


Figure A4. Transition state structures of the migration of OH to NiH with (a) $U = 0$ eV and (b) $U = 6.3$ eV.

Table A4. Activation energies, Ni-H and O-H distances with and without U correction.

	E_a [kJ/mol]	Ni-H [Å]	O-H [Å]
$U = 0$ eV	115	1.61	1.65
$U = 6.3$ eV*	121	1.67	1.60

A8. Parameters for microkinetic simulations

Table A5. Kinetic parameters for CO₂ hydrogenation to CH₃OH, CO and H₂O over Ni-In₂O₃ model.

	Elementary steps	Q _{TS} /Q _{IS}	Q _{TS} /Q _F	E _f (kJ/mol)	E _b
	Oxygen vacancy formation pathway				
1	H ₂ (g) + 2 * ⇌ 2H*	0.20	0.57	19	55
2	H* + OH* ⇌ H ₂ O* + O*	1.70	0.39	93	66
3	H ₂ O* ⇌ H ₂ O(g) + *	1.0	1.0	177	-
	Formate pathway to CH ₃ OH				
4	CO ₂ (g) + * ⇌ CO ₂ *	1.0	1.0	-	144
5	CO ₂ * + H ₂ (g) + 2 * ⇌ CO ₂ * + 2H*	0.20	0.57	19	55
6	CO ₂ * + 2H* ⇌ HCO ₂ * + H* + *	5.55	0.59	66	68
7	HCO ₂ * + H* ⇌ H ₂ CO ₂ * + *	0.17	1.44	114	34
8	H ₂ CO ₂ * + * ⇌ CH ₂ O* + O*	1.05	0.28	101	33
9	CH ₂ O* + H ₂ (g) + 2 * ⇌ CH ₂ O* + 2H*	0.20	0.57	19	55
10	CH ₂ O* + 2H* ⇌ CH ₃ O* + H*	0.47	0.54	55	132
11	CH ₃ O* + H* ⇌ CH ₃ OH(g)	0.06	0.61	61	54
	CO hydrogenation pathway to CH ₃ OH				
12	CO* ₂ + * ⇌ CO* + O*	0.52	0.17	81	78
13	CO* + H ₂ (g) + 2 * ⇌ CO* + 2H*	0.20	0.57	19	55
14	CO* + 2H* ⇌ HCO* + H*	0.52	0.17	71	65
15	HCO* + H* ⇌ CH ₂ O* + *	0.20	0.57	177	35
	rWGS pathway to CO				
16	CO* ₂ + 2H* ⇌ COOH* + H* + *	0.31	0.02	82	69
17	COOH* + * ⇌ CO* + OH*	1.13	0.33	45	25
18	CO* + OH* + H* ⇌ CO* + H ₂ O*	1.51	0.96	140	198
19	CO* ⇌ CO(g) + O _v	1.0	1.0	51	-
20	CO* ⇌ CO(g) + *	1.0	1.0	121	-
Activation energies (E _{act}) were obtained from DFT calculations. Numbers are the same as in Figure 3.3a. Pre-exponential factors were estimated by transition state theory at T = 550 K					

A computational study of CO₂ hydrogenation on single atoms of Pt, Pd, Ni and Rh on In₂O₃(111)

Table A6. Kinetic parameters for CO₂ hydrogenation to CH₃OH, CO and H₂O over Pd-In₂O₃ model.

	Elementary steps	Q _{TS} /Q _{IS}	Q _{TS} /Q _{FS}	E _f (kJ/mol)	E _b (kJ/mol)
	Oxygen vacancy formation pathway				
1	H ₂ (g) + 2 * ⇌ 2H*	0.20	0.57	62	72
2	H* + OH* ⇌ H ₂ O* + O*	1.70	0.39	47	127
3	H ₂ O* ⇌ H ₂ O(g) + *	1.0	1.0	12	-
	Formate pathway to CH ₃ OH				
4	CO ₂ (g) + * ⇌ CO ₂ *	1.0	1.0	-	31
5	CO ₂ * + H ₂ (g) + 2 * ⇌ CO ₂ * + 2H*	0.20	0.57	104	247
6	CO ₂ * + 2H* ⇌ HCO ₂ * + H* + *	5.55	0.59	40	12
7	HCO ₂ * + H* ⇌ H ₂ CO ₂ * + *	0.17	1.44	220	53
8	H ₂ CO ₂ * + * ⇌ CH ₂ O* + O*	1.05	0.28	62	8
9	CH ₂ O* + H ₂ (g) + 2 * ⇌ CH ₂ O* + 2H*	0.20	0.57	73	94
10	CH ₂ O* + 2H* ⇌ CH ₃ O* + H*	0.47	0.54	62	40
11	CH ₃ O* + H* ⇌ CH ₃ OH _(g)	0.06	0.61	106	141
	CO hydrogenation pathway to CH ₃ OH				
12	CO* ₂ + * ⇌ CO* + O*	0.52	0.17	65	91
13	CO* + H ₂ (g) + 2 * ⇌ CO* + 2H*	0.20	0.57	41	74
14	CO* + 2H* ⇌ HCO* + H*	1.0	1.0	55	148
15	HCO* + H* ⇌ CH ₂ O* + *	1.0	1.0	128	14
	rWGS pathway to CO				
16	CO* ₂ + 2H* ⇌ COOH* + H* + *	0.31	0.02	61	81
17	COOH* + * ⇌ CO* + OH*	1.13	0.33	42	23
18	CO* + OH* + H* ⇌ CO* + H ₂ O*	1.51	0.96	140	82
19	CO* ⇌ CO(g) + O _v	1.0	1.0	25	-
20	CO* ⇌ CO(g) + *	1.0	1.0	31	-
Activation energies (<i>E_{act}</i>) were obtained from DFT calculations. Numbers are the same as in Figure 3.3b. Pre-exponential factors were estimated by transition state theory at <i>T</i> = 550 K.					

Table A7. Kinetic parameters for CO₂ hydrogenation to CH₃OH, CO and H₂O over Pt-In₂O₃ model.

	Elementary steps	Q _{TS} /Q _{IS}	Q _{TS} /Q _{FS}	E _f (kJ/mol)	E _b (kJ/mol)
	Oxygen vacancy formation pathway				
1	H ₂ (g) + 2 * ⇌ 2H*	0.20	0.57	48	144
2	H* + OH* ⇌ H ₂ O* + O*	1.70	0.39	48	68
3	H ₂ O* ⇌ H ₂ O(g) + *	1.0	1.0	41	-
	Formate pathway to CH ₃ OH				
4	CO ₂ (g) + * ⇌ CO ₂ *	1.0	1.0	-	31
5	CO ₂ * + H ₂ (g) + 2 * ⇌ CO ₂ * + 2H*	0.20	0.57	48	142
6	CO ₂ * + 2H* ⇌ HCO ₂ * + H* + *	5.55	0.59	34	66
7	HCO ₂ * + H* ⇌ H ₂ CO ₂ * + *	0.17	1.44	146	17
8	H ₂ CO ₂ * + * ⇌ CH ₂ O* + O*	1.05	0.28	156	56
9	CH ₂ O* + H ₂ (g) + 2 * ⇌ CH ₂ O* + 2H*	0.20	0.57	23	203
10	CH ₂ O* + 2H* ⇌ CH ₃ O* + H*	0.47	0.54	80	65
11	CH ₃ O* + H* ⇌ CH ₃ OH _(g)	0.06	0.61	118	105
	rWGS pathway to CO				
12	CO* ₂ + * ⇌ CO* + O*	0.52	0.17	65	91
16	CO* ₂ + 2H* ⇌ COOH* + H* + *	0.31	0.02	140	147
17	COOH* + * ⇌ CO* + OH*	1.13	0.33	65	32
18	CO* + OH* + H* ⇌ CO* + H ₂ O*	1.51	0.96	133	149
19	CO* ⇌ CO(g) + Ov	1.0	1.0	24	-
20	CO* ⇌ CO(g) + *	1.0	1.0	158	-
	Activation energies (E _{act}) were obtained from DFT calculations. Numbers are the same as in Figure 3.3c. Pre-exponential factors were estimated by transition state theory at T = 550 K.				

A computational study of CO₂ hydrogenation on single atoms of Pt, Pd, Ni and Rh on In₂O₃(111)

Table A8. Kinetic parameters for CO₂ hydrogenation to CH₃OH, CO and H₂O over Rh-In₂O₃ model.

	Elementary steps	Q _{TS} /Q _{IS}	Q _{TS} /Q _{FS}	E _f (kJ/mol)	E _b (kJ/mol)
	Oxygen vacancy formation pathway				
1	H ₂ (g) + 2 * ⇌ 2H*	0.20	0.57	149	203
2	H* + OH* ⇌ H ₂ O* + O*	1.70	0.39	76	7
3	H ₂ O* ⇌ H ₂ O(g) + *	1.0	1.0	26	-
	Formate pathway to CH ₃ OH				
4	CO ₂ (g) + * ⇌ CO ₂ *	1.0	1.0	-	87
5	CO ₂ * + H ₂ (g) + 2 * ⇌ CO ₂ * + 2H*	0.20	0.57	51	85
6	CO ₂ * + 2H* ⇌ HCO ₂ * + H* + *	5.55	0.59	42	95
7	HCO ₂ * + H* ⇌ H ₂ CO ₂ * + *	0.17	1.44	155	19
8	H ₂ CO ₂ * + * ⇌ CH ₂ O* + O*	1.05	0.28	101	34
9	CH ₂ O* + H ₂ (g) + 2 * ⇌ CH ₂ O* + 2H*	0.20	0.57	25	209
10	CH ₂ O* + 2H* ⇌ CH ₃ O* + H*	0.47	0.54	149	133
11	CH ₃ O* + H* ⇌ CH ₃ OH(g)	0.06	0.61	135	119
	rWGS pathway to CO				
12	CO ₂ * + * ⇌ CO* + O*	0.52	0.17	80	78
16	CO ₂ * + 2H* ⇌ COOH* + H* + *	0.31	0.02	59	138
17	COOH* + * ⇌ CO* + OH*	1.13	0.33	42	23
18	CO* + OH* + H* ⇌ CO* + H ₂ O*	1.51	0.96	186	68
19	CO* ⇌ CO(g) + Ov	1.0	1.0	130	-
20	CO* ⇌ CO(g) + *	1.0	1.0	215	-
Activation energies (E _{act}) were directly obtained from DFT calculations. Numbers are the same as in Figure 3.3d. Pre-exponential factors were estimated by transition state theory at T = 550 K.					

A9. Microkinetic simulations

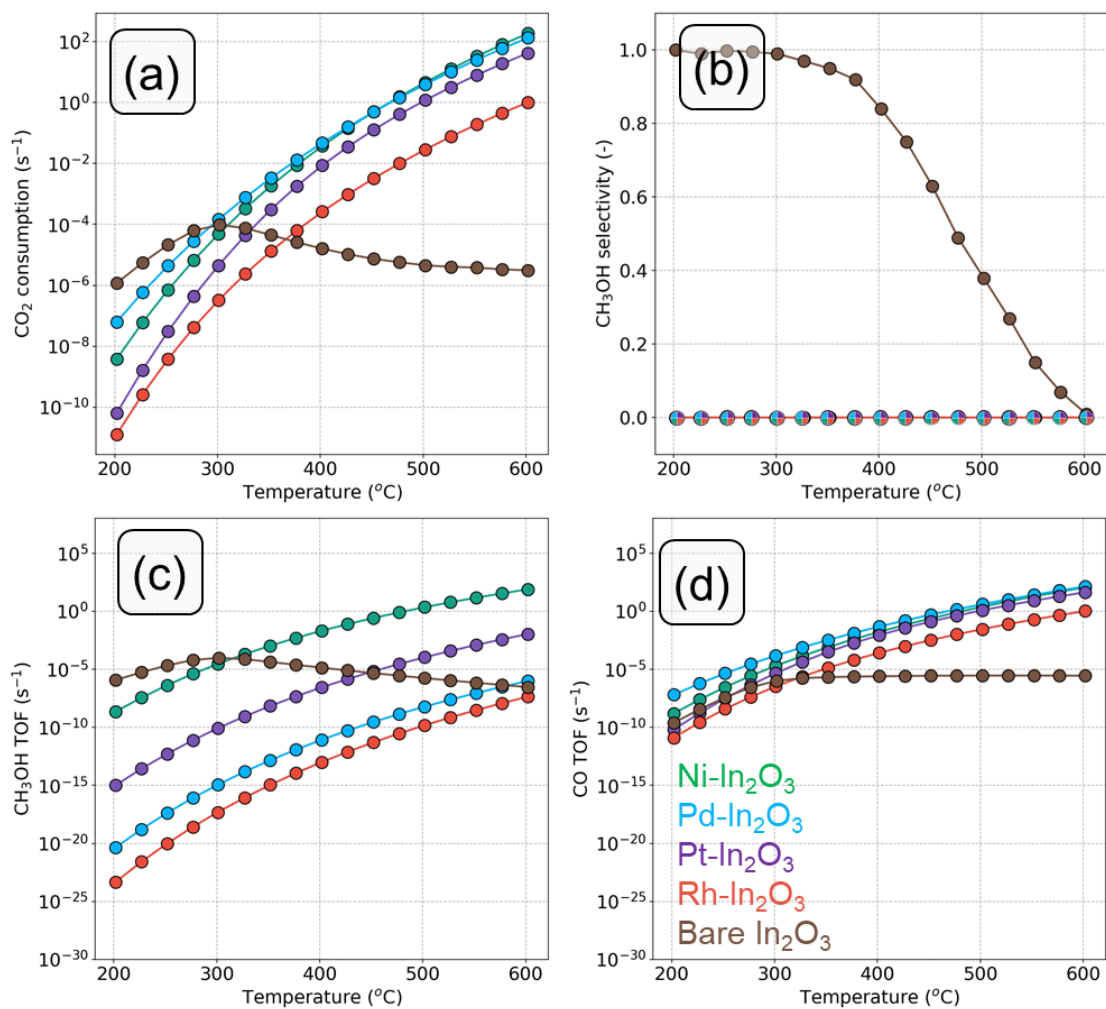


Figure. A5: (a) CO_2 consumption rate (s^{-1}), (b) CH_3OH selectivity, (c) CH_3OH TOF (s^{-1}) and (d) CO TOF in s^{-1} as a function of temperature on SA- In_2O_3 models ($p = 50$ bar, H_2/CO_2 ratio = 5). The data for In_2O_3 -bare are taken from reference [1]

Table A9. Binding energies of SA-O (SA = Ni, Pd, Pt and Rh) and In-O in kJ/mol taken from ref[2].

	E_b [kJ/mol]
Ni-O	391
Rh-O	377
In-O	360
Pt-O	347
Pd-O	234

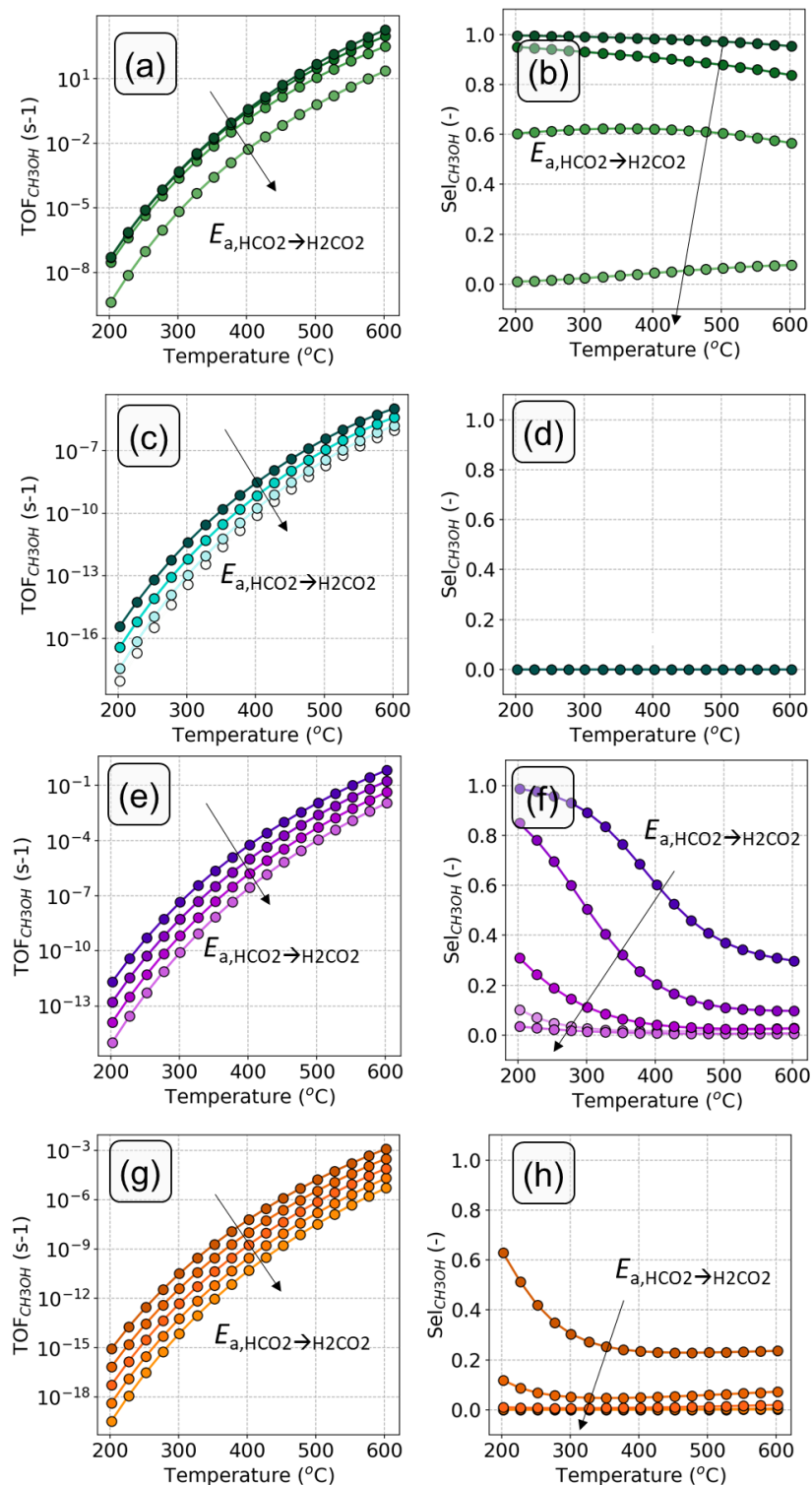


Figure A6. Sensitivity of the microkinetic simulations at different values of the barrier of the step of HCO₂ hydrogenation to H₂CO₂ (step 7). From light to dark the activation energy energy decreases by steps of 10 kJ/mol. (a-b) Ni-In₂O₃, (c-d) Pd-In₂O₃, (e-f) Pt-In₂O₃ and (g-h) Rh-In₂O₃.

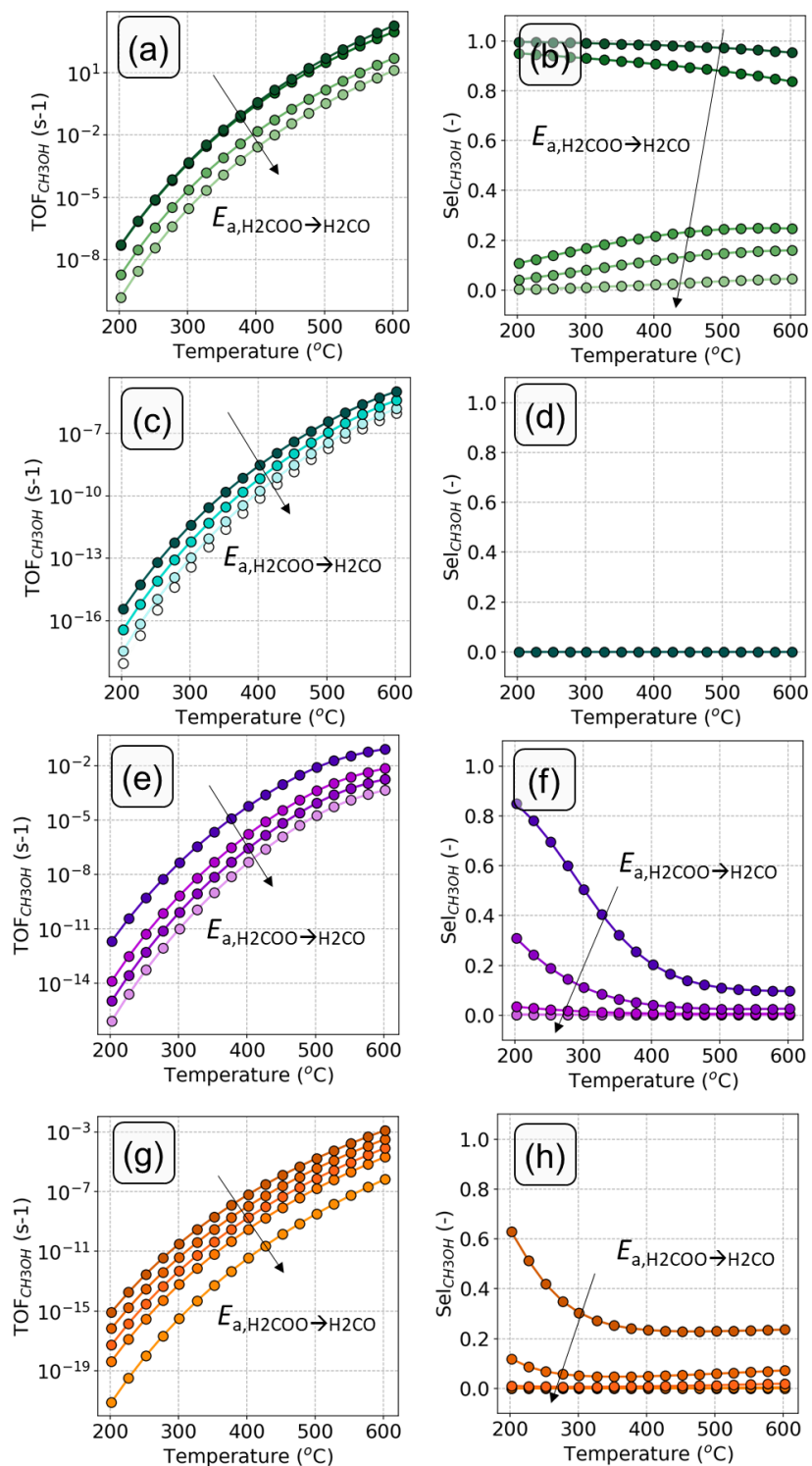


Figure A7. Sensitivity of the microkinetic simulations at different values of the barrier of the step of H_2CO_2 hydrogenation to CH_2O+O (step 8). From light to dark the activation energy energy decreases by steps of 10 kJ/mol. (a-b) Ni-In₂O₃, (c-d) Pd-In₂O₃, (e-f) Pt-In₂O₃ and (g-h) Rh-In₂O₃.

Appendix A References

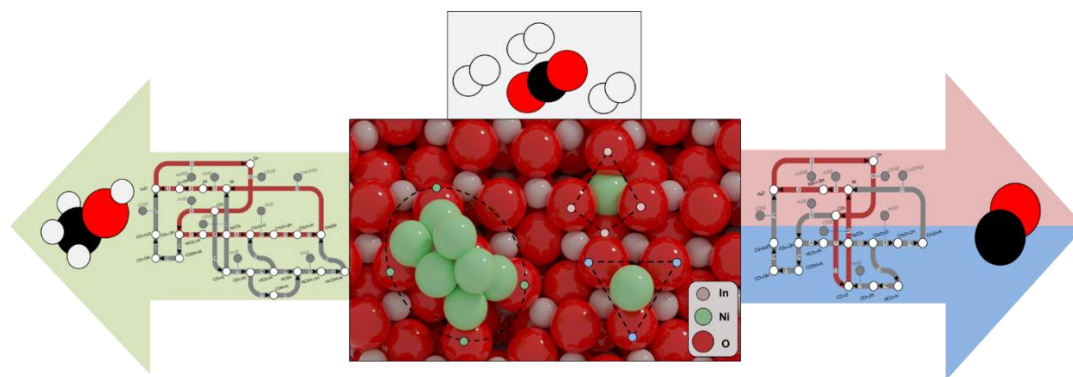
- 1 M. S. Frei, M. Capdevila-Cortada, R. García-Muelas, C. Mondelli, N. López, J. A. Stewart, D. Curulla Ferré and J. Pérez-Ramírez, *J. Catal.*, 2018, **361**, 313–321.
- 2 S. W. Benson, *J. Chem. Educ.*, 1965, **42**, 502–515.

CHAPTER 4

The promoting role of Ni on In₂O₃ for CO₂ hydrogenation to methanol

Abstract

Ni-promoted indium oxide (In₂O₃) is a promising catalyst for selective hydrogenation of CO₂ to CH₃OH, but the nature of the active Ni sites remains unknown. By employing density functional theory (DFT) and microkinetic modeling, we elucidate the promoting role of Ni in In₂O₃-catalyzed CO₂ hydrogenation. Three representative models have been investigated: (i) a single Ni atom doped in the In₂O₃(111) surface, (ii) a Ni atom adsorbed on In₂O₃(111) and (iii) a small cluster of 8 Ni atoms adsorbed on In₂O₃(111). Genetic algorithms are used to identify optimum structure of the Ni₈ clusters on the In₂O₃ surface. Compared to the pristine In₂O₃(111) surface, the Ni₈-cluster model offers a lower overall barrier to oxygen vacancy formation, whereas on both single atom models higher overall barriers are found. Microkinetic simulations reveal that only the supported Ni₈-cluster can lead to high methanol selectivity, whereas single Ni atoms either doped in or adsorbed on the In₂O₃ surface mainly catalyze CO formation. Hydride species obtained by facile H₂ dissociation on the Ni₈-cluster are involved in the hydrogenation of adsorbed CO₂ to formate intermediates and methanol. At higher temperatures, the decreasing hydride coverage shifts the selectivity to CO. On the Ni₈-cluster model, formation of methane is inhibited by high barriers associated with either direct or H-assisted CO activation. Comparison with a smaller Ni₆-cluster also obtained with genetic algorithms shows similar barriers for key rate limiting steps for the formation of CO, CH₄ and CH₃OH. Further microkinetic simulations show that also this model has appreciable selectivity to methanol at low temperature. Formation of CO over single Ni atoms either doped in or adsorbed on the In₂O₃ surface takes place via a redox pathway involving formation of oxygen vacancies and direct CO₂ dissociation.



This chapter has been published in *ACS Catal* **2023**, 13, 3, 1875–1892

4.1 Introduction

Anthropogenic CO₂ emissions due to combustion of fossil fuels constitute a serious environmental threat because of the negative impact on the climate such as global warming, sea-level rise, and ocean acidification.¹⁻³ One of the most attractive strategies to reduce these emissions is to close the carbon cycle by recycling CO₂ captured from combustion processes or directly from air followed by its conversion into chemical feedstocks and fuels. This can be achieved by converting CO₂ with hydrogen obtained from renewable resources.⁴⁻⁶ The use of carbon in a circular manner can eventually lead to the replacement of fossil fuels by renewable resources for covering the energy demand. Besides effectively mitigating emissions, CO₂ hydrogenation products can be used to synthesize important chemical feedstocks. In the overall context of sustainability, methanol is particularly attractive because it can be directly used as a fuel and a building block to produce a wide range of chemicals such as formaldehyde, dimethyl ether, olefins and hydrocarbon fuels.⁷⁻⁹

Currently, large-scale methanol production is based on the conversion of synthesis gas (CO/CO₂/H₂) over Cu/ZnO/Al₂O₃ catalysts at typical temperatures and pressures of respectively 473–573 K and 50–100 bar.^{10,11} Challenges arise however in the hydrogenation of CO₂ to CH₃OH. The commercial Cu-based catalyst shows significant activity for the reverse water-gas-shift reaction (rWGS), leading to the formation of unwanted CO.¹² Moreover, the catalyst is prone to sintering, decreasing the activity.^{13,14} Many efforts have been made to identify other catalyst formulations more suitable for the hydrogenation of CO₂ to CH₃OH.¹⁵⁻²¹ Among these, indium oxide (In₂O₃) was recently introduced as a promising catalyst for CO₂ hydrogenation to methanol, especially when supported on ZrO₂.²²⁻²⁵ Several density functional theory (DFT) studies emphasize the role of oxygen vacancies in the mechanism of CO₂ hydrogenation to methanol on In₂O₃.^{26-28,29-31} Although In₂O₃ enables high selectivity towards methanol by suppressing the competitive rWGS reaction, CO₂ conversion is limited by the low activity of indium oxide in dissociating molecular H₂. To enhance the rate of hydrogen activation, several metal promoters have been investigated. Rui et al. showed that addition of small Pd nanoparticles can enhance methanol synthesis.³² Supporting DFT calculations indicated that small Pd clusters increase the rate of H₂ activation, resulting in a larger amount of H atoms at the metal-oxide interface.³³ Frei et al. proposed that single atom (SA) Pd doped inside the In₂O₃ lattice can stabilize clusters of a few Pd atoms on the In₂O₃ surface, enhancing H₂ activation and, therefore, CH₃OH productivity.²⁵ Similar results have been reported for Pt-promoted In₂O₃.³⁴⁻³⁶ Given their price, it would be advantageous to replace Pd and Pt by Earth-abundant metals like first-row transition metals. Earlier investigations have shown that adding Co³⁷ and Cu³⁸ to In₂O₃ can enhance the activity of In₂O₃ for methanol synthesis. More recently, Jia et al. prepared a highly dispersed Ni-In₂O₃ catalyst with significantly enhanced CO₂ conversion compared to the unpromoted oxide while preserving high methanol selectivity.³⁹ Notably, no methane was found in the product stream. In another study, Snider et al. suggested

that the higher activity of bimetallic Ni–In catalysts for CO₂ hydrogenation to CH₃OH compared to In₂O₃ is due to the synergistic interactions between a Ni–In alloy and In₂O₃.⁴⁰ Furthermore, Frei et al. reported that highly dispersed InNi₃ patches formed on the In₂O₃ surface increase methanol production by supplying neutral H species, whereas Ni SAs were active for the rWGS.⁴¹ Shen et al. investigated the DFT pathways of CO₂ hydrogenation to methanol on a Ni₄-In₂O₃ model catalyst, demonstrating that oxygen vacancies are involved in CO₂ hydrogenation followed by hydrogenation of adsorbed CO₂ to methanol.⁴² In a recent experimental study, we showed that Ni-In₂O₃ catalysts prepared using flame spray pyrolysis synthesis have enhanced CH₃OH synthesis activity compared to bare In₂O₃.⁴³ X-ray photoelectron spectroscopy, X-ray absorption spectroscopy, and electron paramagnetic resonance analysis of the used catalysts suggest that the working state of the catalyst corresponds to single atoms or clusters of a few atoms of Ni dispersed on the In₂O₃ surface. However, differentiating the catalytic role of single Ni atoms and small clusters was challenging, meaning that the exact nature of Ni species in the active sites of Ni-In₂O₃ catalysts remains unclear. Supporting DFT calculations indicate that Ni promotion of methanol synthesis from CO₂ on In₂O₃ is mainly due to low-barrier H₂ dissociation, yet the mechanism of CO₂ conversion to methanol was not explored yet.

In the present study, we employ DFT in combination with genetic algorithms (GA) and microkinetic modeling to systematically investigate the nature of the active sites and the mechanism of CO₂ hydrogenation to methanol on Ni-In₂O₃. To understand the nature of the active site, we consider the following three model systems: (i) SA doped in and (ii) SA adsorbed on In₂O₃(111) and (iii) a Ni₈ cluster placed on a In₂O₃(111) surface. Genetic algorithms are used to identify optimum structural models for supported clusters, while DFT calculations are used to determine the elementary reaction steps for CO₂ conversion to CH₃OH, CO and H₂O. On the basis of these first-principles data, we construct microkinetic models to predict the CO₂ consumption rate and the product distribution as a function of temperature as well as surface coverages, reaction orders and apparent activation energies. We perform a sensitivity analysis of the kinetic network to identify the elementary steps that control the rate of CO₂ consumption and CH₃OH selectivity. We herein show the factors underlying different activity and selectivity patterns on Ni-In₂O₃ model catalysts during CH₃OH synthesis from CO₂ hydrogenation, highlighting that small clusters are the most active and selective form of Ni for obtaining the desired methanol product whereas, on Ni SA models, the competing rWGS is preferred wherein CO₂ is hydrogenated to CO and H₂O.

4.2. Computational Methods

4.2.1 Density Functional Theory Calculations

All DFT calculations were conducted using the projector augmented wave (PAW) method⁴⁴ and the Perdew–Burke–Ernzerhof (PBE)⁴⁵ exchange–correlation functional as implemented in the Vienna Ab Initio

Simulation Package (VASP) code.^{46,47} Solutions to the Kohn-Sham equations were calculated using a plane-wave basis set with a cut-off energy of 400 eV. The valence 5s and 5p states of In were treated explicitly as valence states within the scalar-relativistic PAW approach. All calculations were spin-polarized. The Brillouin zone was sampled using a 3x3x1 Monkhorst-Pack grid. Electron smearing was employed using Gaussian smearing with a smearing width (σ) of 0.1 eV. We chose the $\text{In}_2\text{O}_3(111)$ surface termination, because it is more stable than the (110) and (100) surfaces, as shown in a previous computational study.⁴⁸ The stoichiometric $\text{In}_2\text{O}_3(111)$ surface was modelled as a 2D slab with periodic boundary conditions. A 15.0 Å vacuum region was introduced in the c -direction to avoid the spurious interaction with neighbouring super cells. It was verified that the electron density approached zero at the edges of the periodic super cell in the c -direction. In all calculations, the bottom two layers were frozen, while the top two layers were allowed to perturb. The supercell has dimensions of 14.57 Å \times 14.57 Å \times 26.01 Å. The $\text{In}_2\text{O}_3(111)$ slab consisted of 96 O atoms and 64 In atoms, distributed in four atomic layers on top of which the Ni species were placed. The electronic energies of gas-phase H_2 , H_2O , CO, CO_2 and CH_3OH were calculated using a cubic unit cell with lattice vector of 8 Å. The Brillouin zone was sampled using a 1x1x1 Monkhorst-Pack grid (G-point only). Gaussian smearing was employed. Electronic energies were corrected for zero-point energies of adsorbates and gas-phase molecules and finite-temperature contributions of the translational and rotational energies of gas-phase molecules.

The global minimum structure of In_2O_3 -supported Ni clusters of either 6 or 8 atoms (Ni_6 and Ni_8) was determined by an in-house written genetic algorithm procedure based on the earlier approach of Hammer et al.^{49,50} In this procedure, evolutionary processes including crossover and mutation were employed to generate new candidate structures whose geometry was optimized using the conventional conjugate gradient method. This resulted in increasingly more stable clusters whilst maintaining a statistically diverse population to ensure that sufficiently distinct new candidates could be generated. The algorithm was seeded using 12 randomly generated clusters. Each iteration of the algorithm produced a new generation of clusters until population stagnation was observed, i.e. until no new clusters stabler than the existing clusters in the population pool were found. For the Ni_8 -cluster, a total of 513 structures were generated of which the 201 most stable clusters were selected for further analysis. For the Ni_6 -cluster, 136 stable candidates were identified out of 346 structures obtained in total. The structure with the lowest energy in the pool of candidates was designated as the global minimum (GM) structure. To better understand the structures obtained with the GA, a statistical analysis based on Boltzmann statistics and a similarity analysis based on the minimum Hilbert-Schmidt (HS) norm was employed. In the latter, a distance matrix for each cluster was produced wherein each matrix element represents the distance between any two atoms in a single cluster. The similarity between any two clusters in the set can then be expressed as the minimum HS norm

of the difference of their distance matrices, wherein the minimum is established by evaluating all possible permutations over the indices for one of the distance matrices.

The influence of oxygen vacancies on the reaction energetics was investigated by removing oxygen atoms from the In₂O₃(111) lattice. The energy required to remove a surface oxygen to form a vacancy (ΔE_{Ov}) was calculated using either O₂ or H₂O as reference, according to the following two equations for the oxygen vacancy formation energy

$$\Delta E_{\text{Ov}} = E_{\text{defective slab}} - E_{\text{stoichiometric slab}} + E_{1/2\text{O}_2}, \quad (4.1)$$

$$\Delta E_{\text{Ov}} = E_{\text{defective slab}} - E_{\text{stoichiometric slab}} + E_{\text{H}_2\text{O}} - E_{\text{H}_2}, \quad (4.2)$$

where $E_{\text{defective slab}}$ is the electronic energy of the catalyst containing one oxygen vacancy, $E_{\text{stoichiometric slab}}$ is the reference energy of the stoichiometric slab. $E_{1/2\text{O}_2}$, $E_{\text{H}_2\text{O}}$ and E_{H_2} are the DFT-calculated energies of gas-phase O₂, H₂O and H₂, respectively.

The stable states in the chemo-kinetic network were calculated using the conjugate-gradient algorithm. Transition states were determined using the climbing-image nudged elastic band (CI-NEB) method.⁵¹ A frequency analysis was performed to all states. Specifically, it was verified that stable states have no imaginary frequencies and transition states have a single imaginary frequency in the direction of the reaction coordinate.⁵² The Hessian matrix in this frequency analysis was constructed using a finite difference approach with a step size of 0.015 Å for displacement of individual atoms along each Cartesian coordinate. The corresponding normal mode vibrations were also used to calculate the zero-point energy (ZPE) correction and the vibrational partition functions.

Partial Density of State (pDOS) and projected Crystal Orbital Hamiltonian Population (pCOHP) analysis are conducted to analyze the electronic structure of each Ni-In₂O₃ model catalyst using the Lobster package.^{53,54} The atomic charges of Ni atoms were calculated using the Bader charge method.⁵⁵

4.2.2 Microkinetic simulations

Microkinetic simulations were conducted based on the DFT-calculated activation barriers and reaction energies to investigate the kinetics of CO₂ hydrogenation to methanol. The chemo-kinetic network was modelled using a set of ordinary differential equations involving rate constants, surface coverages and partial pressures of gas-phase species. Time-integration of the differential equations was conducted using the linear multistep backwards differential formula method with a relative and absolute tolerance of 10⁻⁸.⁵⁶⁻

For the adsorption processes, the net rate of a gas-phase species i was calculated as:

$$r_i = k_{i,\text{ads}}\theta^*p_i - k_{i,\text{des}}\theta_i \quad (4.3)$$

where θ^* and θ_i are the fraction of free sites and the fraction of coverage species i , respectively. $k_{i,\text{ads}/\text{des}}$ is the rate constant for the adsorption/desorption process and p_i is the partial pressure of species i .

To derive a rate for the adsorption processes, we assumed that the adsorbate loses one translational degree of freedom in the transition state with respect to the initial state. From this assumption, the rate of adsorption derived from transition state theory can be expressed as follows:

$$k_{i,\text{ads}} = \frac{p A_{st}}{\sqrt{2\pi m_i k_B T}}, \quad (4.4)$$

where A_{st} and m_i are the effective area of an adsorption site and the molar mass of the gas species, respectively. p and T are the total pressure and temperature, respectively, and k_B is the Boltzmann constant. The gas-phase entropy of the adsorbates was calculated using the thermochemical Shomate equation as given by

$$S^0 = A \cdot \ln(T) + B \cdot T + \frac{C \cdot T^2}{2} + \frac{D \cdot T^3}{3} - \frac{E}{2 \cdot T^2} + G, \quad (4.5)$$

where S^0 is the standard molar entropy.⁵⁹ The parameters A-G from equation (4.5) were obtained from the NIST Chemistry Webbook.⁶⁰ For the corresponding desorption processes, we assumed that the species gains two translational degrees of freedom and three rotational degrees of freedom in the transition state with respect to the initial state. From this assumption, the rate of desorption derived from transition state theory can be expressed as follows:

$$k_{\text{des}} = \frac{k_B \cdot T^3}{h^3} \cdot \frac{A_{st}(2\pi m k_B)}{\sigma \theta_{\text{rot}}} \cdot e^{\frac{\Delta E_{\text{des}}}{k_B T}} \quad (4.6)$$

Herein, k_{des} is the rate constant for the desorption of the adsorbate, h is the Planck constant, σ is the symmetry number and corresponds to the number of rotational operations in the point group of each molecule. θ_{rot} the rotational temperature, and ΔE_{ads} the desorption energy. The value of A_{st} is equal to $9 \cdot 10^{-19} \text{ m}^2$.

Finally, the rate constant (k) of an elementary reaction step is given by

$$k = \frac{k_B T}{h} \frac{Q^\ddagger}{Q} e^{\left(\frac{-\Delta E_{\text{act}}}{k_B T}\right)}, \quad (4.7)$$

where Q^\ddagger and Q are the partition functions of the activated complex and its corresponding initial state, respectively, and ΔE_{act} is the ZPE-corrected activation energy.

To identify the steps that control the CO₂ consumption rate and the product distribution, we employed the concepts of the degree of rate control (DRC) developed by Kozuch and Shaik⁶¹⁻⁶² and popularized by Campbell⁶³ as well as the degree of selectivity control (DSC).⁶³⁻⁶⁵

Herein, the degree of rate control coefficient is defined as

$$X_{RC,i} = \left(\frac{\partial \ln r_i}{\partial \ln k_i} \right)_{k_{j \neq i}, K_i} \quad (4.8)$$

A positive DRC coefficient indicates that the elementary reaction step is rate-controlling, whereas a negative coefficient suggests that the step is rate-inhibiting. When a single elementary reaction step has a DRC coefficient of 1, this step is identified as the rate-determining step.

The DSC quantifies the extent to which a particular elementary reaction step influences the selectivity for certain products. The DSC of a particular key component is expressed as

$$X_{SC,i,c} = \left(\frac{\partial \eta_c}{\partial \ln k_i} \right)_{k_{j \neq i}, K_i}, \quad (4.9)$$

where $X_{SC,i,c}$ is the DSC of product C due to a change in the kinetics of elementary reaction step i , and η_c is the selectivity towards a key product (methanol in this work). Note that the relationship between DRC and DSC coefficient is given by

$$X_{SC,i,c} = \eta_c (X_{c,i} - X_{\text{reactant},i}). \quad (4.10)$$

4.3 Results and discussion

4.3.1 Structure of Ni-In₂O₃ models

To understand the nature of the active sites for Ni-In₂O₃ in CO₂ hydrogenation to methanol, three model systems were considered, namely single atoms (SA) of Ni either (i) doped in the In₂O₃(111) surface (denoted as Ni₁-doped) or (ii) adsorbed on the In₂O₃(111) surface (Ni₁-adsorbed), a cluster of (iii) 8 Ni atoms adsorbed on top of the In₂O₃(111) surface (Ni₈-cluster). The models are shown in Figure 4.1. We also compare our Ni₈-cluster with a smaller Ni₆-cluster obtained at the same level of theory. To determine the most stable location of Ni for the Ni₁-doped In₂O₃(111) model system, the energy of substituting an In atom for a Ni atom was calculated. The reported substitution energies (E_{sub}) are given with respect to bulk Ni and In by

$$E_{\text{sub}} = E_{\text{Ni}/\text{In}_2\text{O}_3(111)} + E_{\text{In,bulk}} - E_{\text{Ni,bulk}} - E_{\text{In}_2\text{O}_3(111)}, \quad (4.11)$$

where $E_{\text{Ni}/\text{In}_2\text{O}_3(111)}$ is the energy of each Ni₁-doped In₂O₃(111) surface, $E_{\text{In,bulk}}$, $E_{\text{Ni,bulk}}$ and $E_{\text{In}_2\text{O}_3(111)}$ are the energies of In bulk, Ni bulk and In₂O₃(111) surface models, respectively. The resulting substitution

energies for all the doping positions are collected in Table B1. DFT calculations indicate that Ni substitution is favored in position 1 as shown in Figure 4.1a ($E_{\text{sub}} = -0.35$ eV). Ni prefers nearly perfect octahedral coordination by oxygen in the first metal layer of the structure (position 1). The 6 sites nearest to position 1 are slightly less stable (i.e., with substitution energies $\sim +0.15$ eV compared to position 1) due to a slight distortion of the octahedral environment around the Ni substituent. Compared to these sites, substitution at other positions in the first metal layer is unfavorable with substantially larger exchange energies. We also studied the possibility of substituting an In atom in the bulk of In_2O_3 by a Ni atom (Figure B2a). Our calculations indicate substitution of a Ni SA in subsurface layers is unfavorable ($E_{\text{sub}} = +0.51$ eV). Next, we evaluated the possibility of replacing a second In atom in the surface (Figure B2b). Such replacement in the surface layer is also disfavored ($E_{\text{sub}} = +0.59$ eV). Our findings are in line with a previous study on Pd-doped In_2O_3 .²⁵

The preferred location of a Ni SA on the $\text{In}_2\text{O}_3(111)$ surface is bridging between two lattice oxygens (Figure 4.1b). The adsorption energies for all investigated sites are reported in Table B2. In its most stable configuration, the Ni-O distances are $r(\text{Ni-O}_\alpha) = 1.79$ Å and $r(\text{Ni-O}_\beta) = 1.81$ Å (Figure 4.1b and Figure B3b). In its least stable adsorption configuration (position 6), Ni coordinates to a single oxygen atom and an In atom. The Ni-O and Ni-In distances are 2.14 and 2.54 Å, respectively. The Ni-O distance increases from 1.79 to 2.14 Å from the most stable to the least stable adsorption configuration, in line with a weaker binding of the Ni SA with the surface. In general, more stable configurations feature multiple Ni-O bonds. Furthermore, we determined barriers for the diffusion of a single Ni atom between stable adsorption sites (Table B3). Migration from position 1 to position 3 (Figure 4.1b) is associated with a barrier of 95 kJ/mol and is endothermic by 21 kJ/mol. Migration from position 3 to position 4 has a higher barrier (165 kJ/mol) and is endothermic by 11 kJ/mol. Lastly, migration from position 4 to position 5 is associated with a barrier of 142 kJ/mol and is endothermic by 65 kJ/mol.

In a recent experimental study on Ni- In_2O_3 , it was found that Ni is present in clustered form under reducing reaction conditions.⁴³ These clusters were relatively small in optimized catalysts as no methane was observed during CO_2 hydrogenation. Methane was only formed at much higher Ni loading, where Ni nanoparticles were present on In_2O_3 . To model small Ni clusters, we used clusters containing either 8 or 6 Ni atoms (Ni_8 and Ni_6 , respectively) on the $\text{In}_2\text{O}_3(111)$ surface as a compromise between computational tractability and a reasonable description of supported metal clusters that often adopt a bilayer structure.⁴⁹ For comparison, we also determined the most stable structure of clusters in the gas phase of the Ni_8 and Ni_6 clusters (Figure 4.1c and Figure 4.1e, respectively). The DFT-based GA identified 201 and 136 stable candidate structures for the Ni_8 and Ni_6 -cluster models, respectively. The algorithm did not find new configurations that were significantly different from the energy minimum within an energy threshold of 0.1 eV after 57 and 36 genetic iterations for the Ni_8 and Ni_6 -cluster models, respectively. The minimum-energy

structures for gas-phase and supported Ni₈ and Ni₆ clusters are shown in Figure 4.1c-e and Figure 4.1d-f, respectively. In the gas phase, the most stable free clusters adopt a square bipyramidal shape, in line with an earlier computational study.⁶⁶ The most stable supported Ni₈-cluster obtained by our DFT-GA (Figure 4.1d) consists of a bilayer structure where 6 Ni atoms form the bottom layer with the other two Ni atoms placed on three-fold sites of the first Ni layer. For the supported Ni₆-cluster (Figure 4.1f), 5 Ni atoms form the bottom layer and the sixth Ni atom is placed on a three-fold site. The different shapes of the Ni-clusters in the gas phase and on the In₂O₃(111) support are caused by strong metal-support interactions (MSI) between Ni and In₂O₃. Such MSI were quantified by computing the cohesive energy per Ni atom of the GA-optimized Ni₈ clusters in the gas phase and supported on In₂O₃ (Table B4). Placing the Ni₈-cluster on the (111) surface of In₂O₃ increases the cohesive energy from 268 kJ/mol/atom for the gas-phase cluster to 358 kJ/mol/atom for the cluster on the In₂O₃ support. For a Ni₆-cluster, the stabilization effect is slightly higher (111 kJ/mol/atom).

The stability of the supported Ni clusters can be further evaluated by determining the barrier needed to remove a single Ni atom from the cluster via migration on the In₂O₃ surface. We performed such DFT calculations and reported the results in Table B5-6. Removing a Ni atom from a Ni₆-cluster has a barrier of 201 kJ/mol and is endothermic by 179 kJ/mol. For the Ni₈-cluster, the corresponding values are 232 and 192 kJ/mol. Thus, it is clear that the redispersion of Ni clusters into single atoms is prohibitive from the kinetic and thermodynamic point of view.

To determine whether other configurations of the Ni-clusters will also contribute to the catalytic performance, we analyzed the Boltzmann probability distribution for the structures (section B3.2 of the SI). This analysis demonstrated that, for both clusters, one other structure occurs with a sufficiently large contribution at a reaction temperature at 400 K. Based on a structural similarity analysis (Table B7), it was found that this structure is nearly the same as the minimum energy structure for both the Ni₆ and Ni₈-cluster models. Accordingly, we focused only on the minimum energy structure of the Ni₈-cluster in the following.

The electronic structure of the Ni-In₂O₃ models can be compared on the basis of the partial density of states (pDOS, Figure B6). In all cases, overlap between Ni 3*d* and O 2*p* orbitals is observed. The In 4*d* orbitals are core orbitals and, therefore, do not show appreciable overlap with O 2*p* or Ni 3*d* orbitals. For optimized doped and adsorbed SA models, the calculated Bader charges of the Ni atoms are +1.26 |e| and +0.66 |e|, respectively. The Bader charge analysis further shows that Ni₈-clusters on In₂O₃(111) carry a cumulative charge of +1.07|e| (Table B8 and Figure B7a). The 6 Ni atoms located at the bottom layer of the cluster carry a positive charge, while the two Ni atoms adsorbed on top carry a slightly negative charge. Thus, for all models there is a net flow of electrons from Ni to the O atoms of the In₂O₃ surface.

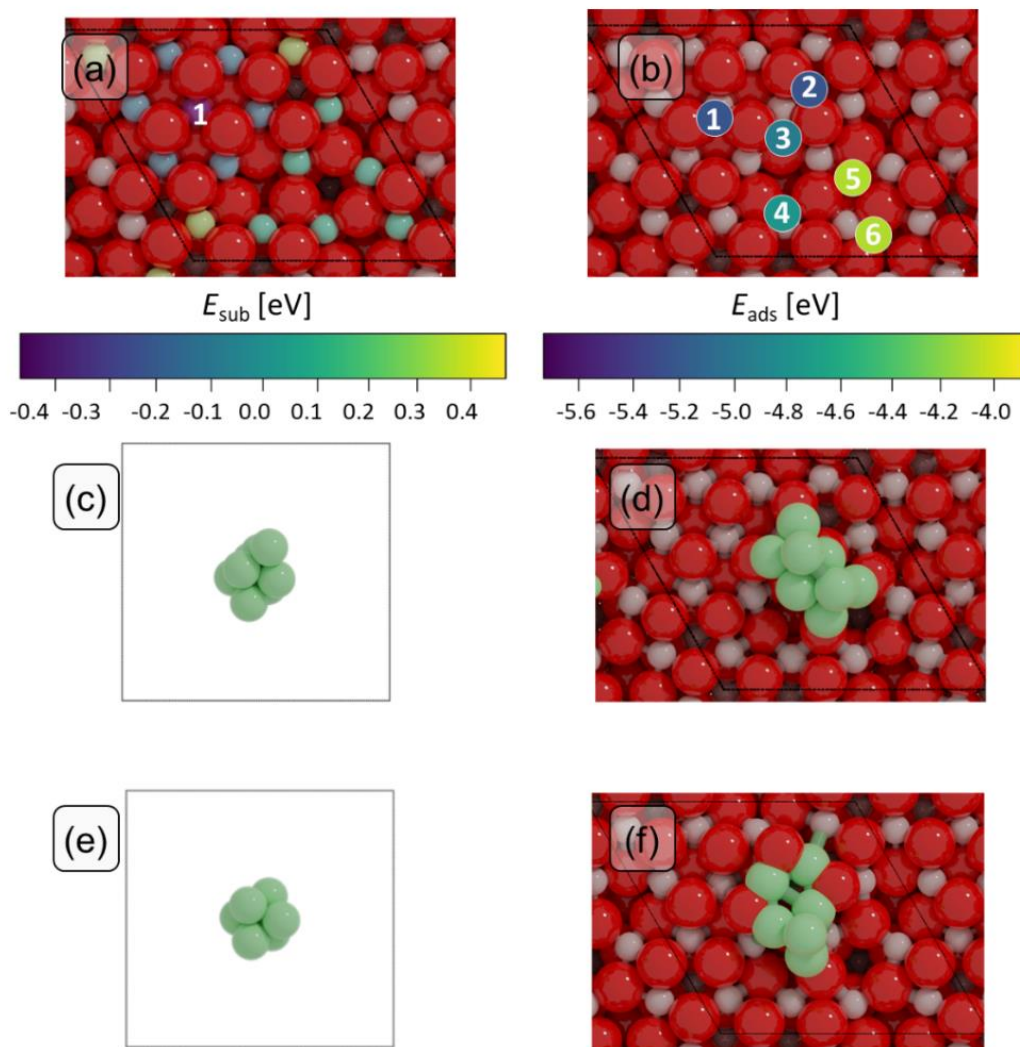


Figure 4.1. (a) Substitution energy of In/Ni substitution in In_2O_3 . The coloring of In atoms at the surface represents the energy associated with their replacement by Ni (E_{sub}). Position 1 marks the most stable substitution site. (b) Adsorption energy of Ni SAs on $\text{In}_2\text{O}_3(111)$. The coloring of the atom at the surface represents their adsorption energy (E_{ads}). Position 1 marks the most stable adsorption site. Energy minima structures obtained by the GA for gas-phase (c, e) and supported (d, f) Ni_8 and Ni_6 clusters, respectively. Red: O; grey: In; green: Ni.

4.3.2 Oxygen vacancy formation

The role of oxygen vacancies (Ov) on the In_2O_3 surface has been emphasized for the adsorption and activation of CO_2 .^{26–28} To assess how the addition of Ni affects the formation of such vacancies, we compared the energy required to form such Ov (E_{Ov} , in eV) for the Ni- In_2O_3 surfaces with unpromoted In_2O_3 (Figure 4.2). The computed energies are referenced to gaseous O_2 . On the bare $\text{In}_2\text{O}_3(111)$ surface (Figure

4.2a), the energy needed to remove an oxygen atom ranges from 1.8 to 3.0 eV, in line with previous calculations.^{48,67} We also calculated the Ov formation energies with respect to H₂O, because oxygen vacancies are usually formed in the presence of H₂. In this case, the E_{Ov} lies between -0.65 and 0.99 eV.

Doping In₂O₃ with a Ni SA (Figure 4.2b) lowers the energy for Ov formation significantly. Values for E_{Ov} referenced to O₂ lie between 0.94 and 1.86 eV. Considering H₂O formation, oxygen vacancy formation is exothermic for all surface oxygens considered (E_{Ov} between -1.58 eV and -0.66 eV). As can be seen from Figure 4.2b, the O atoms bonded to Ni are more easily removed than O atoms bonded to In. In its most/stable doping position, the Ni-O bond distance is 1.94 Å, which is 0.25 Å shorter than the In-O distance measured for an In atom occupying the same lattice position on the bare oxide. This suggests that doping a smaller Ni atom in In₂O₃ leads to lattice contraction bringing the O atoms closer to each other. This enhances electron-electron repulsion between the relatively large electron clouds around the negatively charged O atoms, weakening the Ni-O bonds and thereby explaining the lower E_{Ov} . Adsorbing a Ni atom on top of the In₂O₃ (Figure 4.2c) significantly increases the oxygen vacancy formation energy, resulting in E_{Ov} values between 3.42 and 4.41 eV referenced to O₂ and between 0.89 and 1.87 eV referenced to H₂O. For a supported Ni₆-cluster (Figure 4.2d), oxygen vacancy formation via direct thermal desorption of O₂ lies between 2.65 eV to 3.52 eV. Considering alternatively H₂O formation, values of E_{Ov} values lie between 0.12 and 1.16 eV. For a supported Ni₈-cluster (Figure 4.2e), similar values are found with for oxygen vacancy formation energies via direct thermal desorption (2.48 eV to 3.51 eV). Thus, adsorbed Ni phases increase the oxygen vacancy formation energy compared to the reference pristine In₂O₃ case. This is in line with our knowledge that the Ni-O bond (396 kJ/mol) is stronger than the In-O bond (346 kJ/mol).⁶⁸

More careful inspection of Figure 4.2b-d shows that, for each of the Ni-promoted surfaces, formation of vacancies is easier for oxygens directly bonding to Ni species compared to O atoms bonding only to In atoms. To understand this point, we performed a projected Crystal Orbital Hamiltonian Population (pCOHP) analysis of the Ni-O and In-O bonds (Figure B8), where we compare the stoichiometric In₂O₃ surface with Ni-promoted ones. On In₂O₃ (Figure B8a), the character of In-O interactions is bonding. For all other Ni-promoted surface models (Figure B8b-i), the pCOHP exhibits antibonding Ni-O and In-O interactions close to the Fermi level for oxygen atoms adjacent to Ni. This explains why less energy is needed to remove these oxygens compared to oxygens at larger distances from Ni. We infer that the addition of Ni to In₂O₃ causes electron transfer from Ni to O, which results in the formation of antibonding N-O and In-O interactions. Furthermore, Bader charge analysis shows that, upon formation of an oxygen vacancy, the excess charge is redistributed mainly to the nearest Ni atom from the cluster (Figure B7b). In this way, Ni atoms can contribute to stabilize the oxygen-defective Ni-In₂O₃ surface, resulting in easier formation of vacancies at the Ni-In₂O₃ interface. In summary, with respect to the stoichiometric In₂O₃ surface, only the

Ni₁-doped model feature more exothermic oxygen vacancy formation energies, whereas the other Ni-In₂O₃ models feature more endothermic oxygen vacancy formation energies. To understand whether oxygen vacancies will be formed on these models we investigate the DFT pathways of oxygen vacancy formation via surface reduction by H₂ and perform microkinetic simulations (*vide infra*).

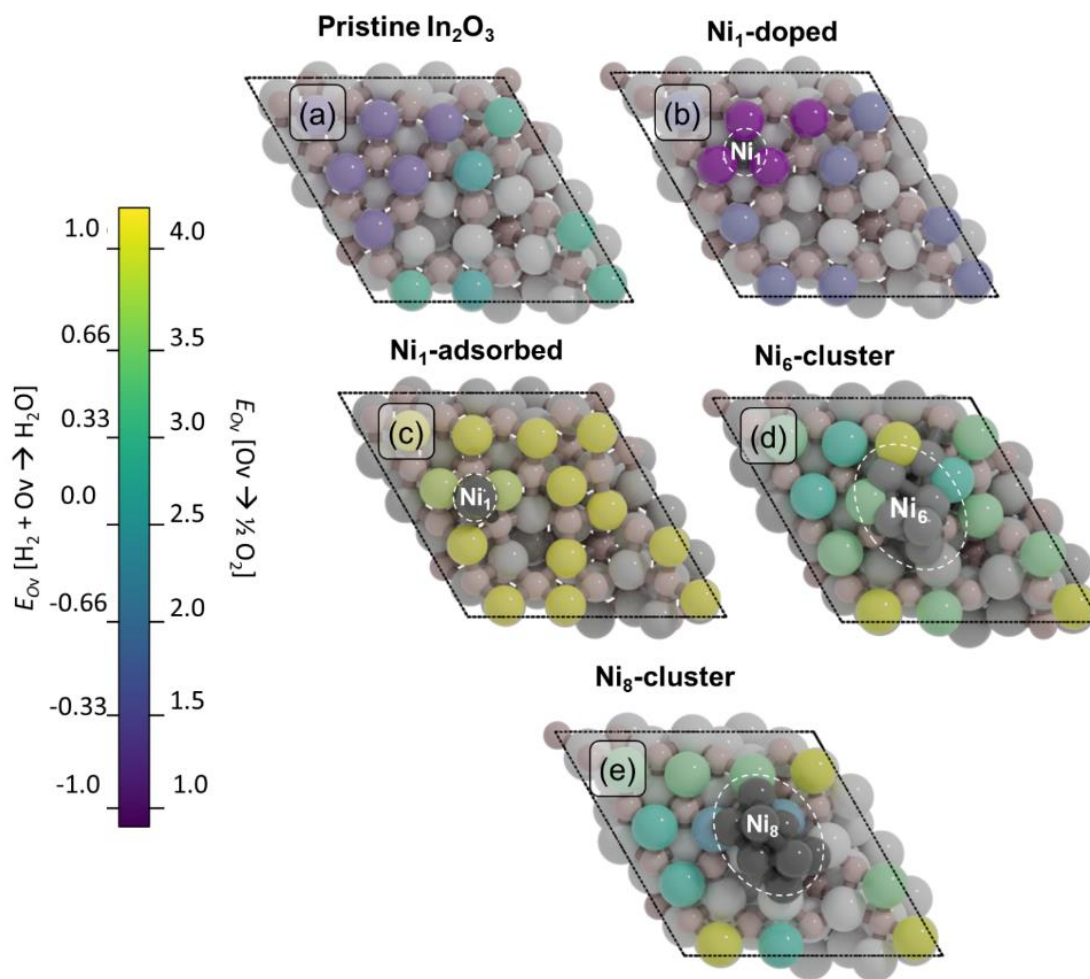


Figure 4.2: Oxygen vacancy formation energies (E_{Ov}) for the 12 surface oxygens on (a) bare In₂O₃, (b) Ni₁-doped in and (c) Ni₁-adsorbed on In₂O₃, (d) Ni₆-cluster and (e) Ni₈-cluster. The coloring of the 12 surface oxygen atoms represents their E_{Ov} . Ni atoms are colored in dark grey, while all other atoms are colored in light grey. The Ni species are highlighted inside dashed circles.

4.3.3 Elementary reaction steps

We performed DFT calculations to elucidate the reaction mechanism of CO₂ hydrogenation to methanol (CH₃OH), carbon monoxide (CO) and water (H₂O). No methane was observed during CO₂ hydrogenation experiments for a Ni-In₂O₃ catalyst with a low Ni loading.^{32,34} To verify that CO₂ methanation on small

In₂O₃-supported Ni clusters is difficult, we studied direct and H-assisted CO dissociation as the most likely rate-limiting steps in CO₂ methanation. The reaction network explored in this study is depicted in Figure 4.3. Based on previous computational studies, we investigate specific pathways for the formation of oxygen vacancies via H₂O, for the formation of CH₃OH via formate, and for the reverse water-gas shift (rWGS) pathway leading to CO.^{24,70,71} The latter can take place either via direct cleavage of one C-O bond in CO₂ or via an H-assisted pathway involving the COOH intermediate. In addition, a pathway via the CO intermediate towards CH₃OH has been included for the Ni₁-adsorbed and Ni₈-cluster model surfaces.

We will discuss the elementary reaction steps in this network for the Ni₁-doped, Ni₁-adsorbed and Ni₈-cluster model surfaces and highlight the main trends in activation energies and transition-state structures. We also compare key elementary reaction steps for the formation of CO, CH₄ and CH₃OH between Ni₆ and Ni₈-clusters. The activation barriers are given with respect to the most stable adsorbed state for each intermediate. All the elementary reaction steps along with the corresponding forward and backward activation energies are tabulated in the Appendix B in section B7 (Tables B9a-c). The geometries corresponding to initial, transition and final states are reported in sections B8-B10 of Appendix B.

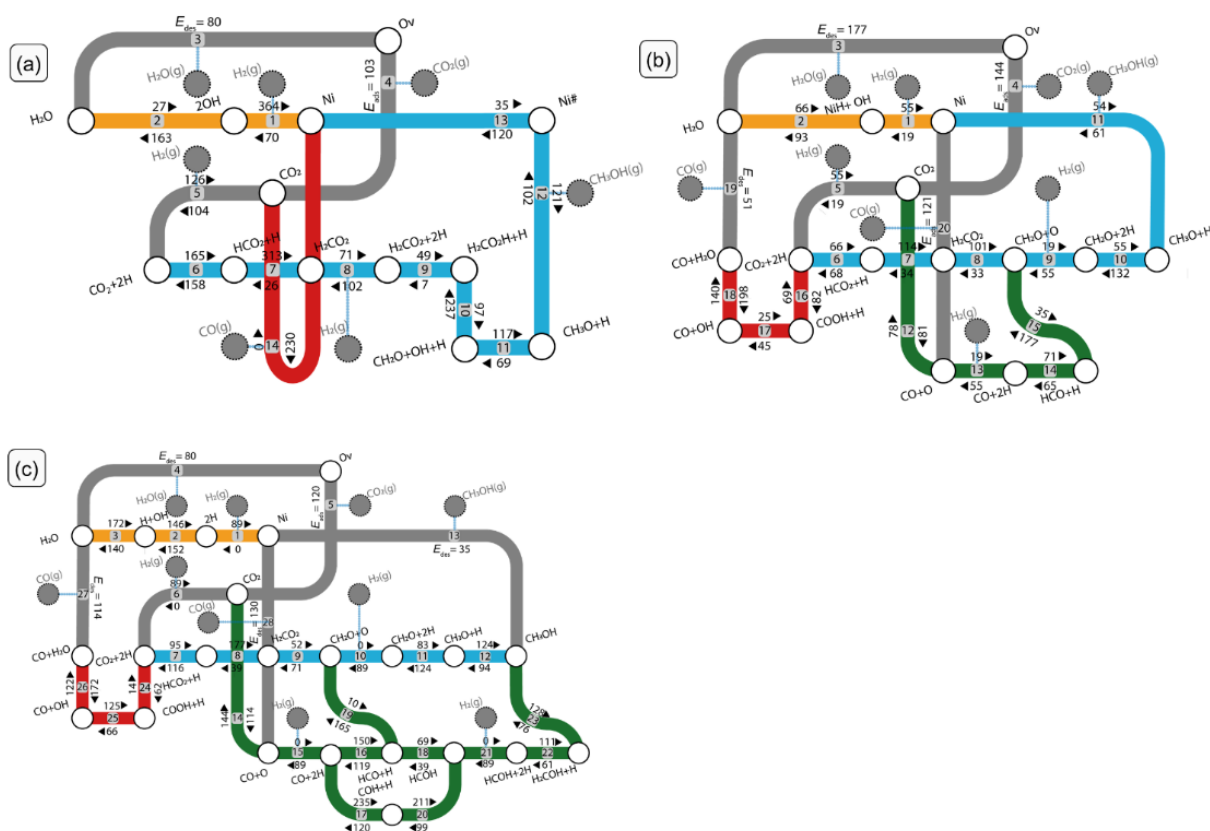


Figure 4.3. Full kinetic networks for CO₂ hydrogenation to CO and CH₃OH for (a) Ni₁-doped (b) Ni₁-adsorbed and (c) Ni₈-cluster models. Orange: oxygen vacancy formation pathway; blue: formate pathway to CH₃OH; green: CO hydrogenation pathway to CH₃OH; red: rWGS to CO; grey: adsorption/desorption elementary steps. The numbers correspond to the elementary reaction steps as listed in Tables B9a-c.

4.3.3.1 Methanol synthesis on Ni₁-doped In₂O₃

We first discuss the reaction energetics of CO₂ hydrogenation to methanol over the Ni₁-doped system. The reaction network is shown in Figure 4.3a and the corresponding potential energy diagram (PED) in Figure 4a. The geometries of initial, transition and final states can be found in Appendix B (Section B8). H₂ dissociation on the Ni₁-doped In₂O₃(111) surface (step 1) is homolytic, similar to the In₂O₃ surface and leads to the formation of two OH^{δ+} groups.⁷² This step has an activation energy of 70 kJ/mol and is exothermic by $\Delta E_R = -294$ kJ/mol, indicative of the high stability of the surface hydroxyl groups. The relatively high barrier for H₂ activation can be understood by considering that the surface O anions cannot stabilize the negatively charged H atoms during dissociation.⁴³ Subsequent water formation has a barrier of 163 kJ/mol and is endothermic by 137 kJ/mol. H₂O desorption ($\Delta E_{des} = 80$ kJ/mol; step 3) completes oxygen vacancy formation. Overall, the process of oxygen vacancy formation is associated with a reaction energy of -80 kJ/mol and an activation barrier of 70 kJ/mol with respect to gas-phase H₂.

Next, CO₂ adsorbs at the oxygen vacancy (step 4). The carbon atom coordinates to a lattice oxygen instead of the Ni SA, which is due to the steric hindrance around Ni due to its location in the surface. The adsorption energy of CO₂ is exothermic by $\Delta E_{ads} = -103$ kJ/mol. Dissociative adsorption of another H₂ molecule (step 5) leads to two hydroxyl groups adjacent to CO₂. This step has an activation energy of 104 kJ/mol and is exothermic by $\Delta E_R = -22$ kJ/mol. CO₂ hydrogenation to HCO₂+H (step 6) proceeds by proton migration from an adjacent hydroxyl species with a forward activation energy of 165 kJ/mol ($\Delta E_R = 8$ kJ/mol). Another proton migration step leads to H₂CO₂ (step 7) with a forward barrier of 313 kJ/mol ($\Delta E_R = 287$ kJ/mol). Notably, high activation energies are associated with the formation of a bond between a slightly positively charged C atom and the H atom of the OH group, which is also positively charged, in line with a previous work on In₂O₃.²⁴ The possibility of hydrogenating one of the O atom in HCO₂ giving HCOOH was also investigated. However, no TS could be found for this elementary step because the HCOOH moiety does not adsorb stably on the surface. No TS has been found also for the direct dissociation of H₂CO₂ into CH₂O+O. However, the CH₂O intermediate can be obtained from H₂CO₂H dissociation. After dissociative adsorption of another H₂ molecule (step 8; $\Delta E_a = 71$ kJ/mol, $\Delta E_R = -32$ kJ/mol), one of the two oxygens of H₂CO₂ is protonated (step 9) to form H₂CO₂H+H ($\Delta E_a = 49$ kJ/mol, $\Delta E_R = 42$ kJ/mol). The subsequent cleavage of a C-O bond of H₂CO₂H yields CH₂O and a OH moiety, which occupies the oxygen vacancy (step 10). This step has an activation energy of 97 kJ/mol and is exothermic by 140 kJ/mol. Next, the CH₂O

moiety is hydrogenated to CH₃O via proton migration from a neighboring OH group (step 11). This step is endothermic by 49 kJ/mol and has a forward activation energy of 117 kJ/mol. Finally, CH₃O is hydrogenated by the hydroxyl species obtained from H₂CO₂H dissociation forming methanol, which immediately desorbs (step 12). This concerted elementary step has an activation energy of 102 kJ/mol and is exothermic by $\Delta E_R = -19$ kJ/mol. Finally, oxygen migration (step 13) restores the initial stoichiometric surface. This step has an activation energy of 120 kJ/mol and is endothermic by $\Delta E_R = 85$ kJ/mol.

CO is observed during experiments on Ni-In₂O₃ as a by-product of the reverse water-gas shift (rWGS) reaction (Figure 4a, red). On the Ni₁-doped model, CO can be formed via a redox mechanism involving the formation of H₂O (steps 1-3), adsorption of CO₂ on an oxygen vacancy (step 4) and subsequent dissociation and desorption of CO (step 14). The energy penalty associated with replenishing one oxygen vacancy by CO₂, thus restoring the stoichiometric surface, is 234 kJ/mol. Ye et al. observed that the same process on an In₂O₃(110) model surface has a barrier of 1.4 eV.^{27,28} The higher barrier for our model is in keeping with the result that doping In₂O₃ with Ni results in a more exothermic oxygen vacancy formation energy. A hydrogen-assisted rWGS pathway to CO via COOH intermediate is generally also followed. We explored this pathway for the Ni₁-doped model, however, no TS could be found for the dissociation of COOH into CO and OH as there is no active site to accept the OH.

4.3.3.2 Methanol synthesis on Ni₁-adsorbed In₂O₃

Next, we discuss the mechanism of CO₂ hydrogenation over the Ni₁-adsorbed system. The reaction network is shown in Figure 4.3b and the PED in Figure 4b. The geometries of initial, transition and final states can be found in Section B9. On this surface, H₂ is heterolytically dissociated to form a NiH^{δ-} and a OH^{δ+} species (step 1), as we reported in another study.⁴³ This step is mildly activated ($\Delta E_a = 19$ kJ/mol) and exothermic by -36 kJ/mol. Notably, H₂ dissociation has a lower activation energy compared to the formation of two OH group as found for the Ni₁-doped system ($\Delta E^{\text{doped}}_a = 70$ kJ/mol). Next, formation of an oxygen vacancy proceeds by H migration from the Ni-H moiety to form H₂O (step 2). This step has an activation energy of 93 kJ/mol and a reaction energy of +27 kJ/mol. Water desorption from the surface (step 3) is associated with a desorption energy of 177 kJ/mol. The overall barrier and reaction energy of oxygen vacancy formation with respect to gas-phase H₂ on this surface amount to 150 kJ/mol, which is considerably higher than the corresponding values for the Ni₁-doped surface (70 kJ/mol and -80 kJ/mol, respectively).

CO₂ adsorbs in the oxygen vacancy coordinating to the Ni SA (step 4). In its most stable adsorption configuration, the carbon atom of CO₂ binds to the Ni atom ($\Delta E_{\text{ads}} = -144$ kJ/mol). A second H₂ molecule can dissociate, forming two OH species (step 5). Homolytic dissociative adsorption of H₂ is preferred because of steric hinderance of the Ni atom which is also involved in Ni-C bond with adsorbed CO₂. This step has an activation energy of 19 kJ/mol and is exothermic by $\Delta E_R = -36$ kJ/mol. Along the formate

pathway to methanol (steps 6-11), first a H species migrates from the lattice oxygen to the Ni SA and hydrogenates CO_2 to form HCO_2 (step 6). This step has a forward activation energy of 66 kJ/mol and is slightly exothermic ($\Delta E_R = -2$ kJ/mol). The subsequent hydrogenation to H_2CO_2 (step 7) has a forward activation energy of 114 kJ/mol ($\Delta E_R = 80$ kJ/mol). Notably, the formation a C-H bond on the Ni_1 -adsorbed model is easier than on the Ni_1 -doped model. This can be ascribed to the hydride character of the H atom adsorbed to Ni. Next, cleavage of a C-O bond in the H_2CO_2 intermediate takes place (step 8, $\Delta E_a = 101$ kJ/mol, $\Delta E_R = 33$ kJ/mol), leading to CH_2O and an O atom, the latter healing the oxygen vacancy. After adsorption of another H_2 molecule (step 9; $\Delta E_a = 19$ kJ/mol; $\Delta E_R = -36$ kJ/mol), the CH_2O moiety is hydrogenated to CH_3O (step 10; $\Delta E_a = 55$ kJ/mol $\Delta E_R = -79$ kJ/mol). Finally, CH_3O hydrogenation to methanol and its subsequent desorption (step 11) take place in a single elementary reaction step with an activation energy of 61 kJ/mol.

On the Ni_1 -adsorbed model surface, methanol can also be obtained via CO hydrogenation as seen in Figure 4.3b. This involves steps 12-15 in the CO hydrogenation pathway followed by steps 9-11 in the formate pathway. Upon adsorption on an oxygen vacancy, CO_2 can directly dissociate (step 12) into CO and O ($\Delta E_a = 81$ kJ/mol, $\Delta E_R = 3$ kJ/mol), where the O replenishes the oxygen vacancy restoring the stoichiometric surface. From this state, CO is further hydrogenated to HCO (step 14) after adsorption of another H_2 molecule (step 13; $\Delta E_a = 19$ kJ/mol; $\Delta E_R = -36$ kJ/mol). Herein, CO hydrogenation to HCO has an activation energy of 71 kJ/mol ($\Delta E_R = 6$ kJ/mol). Subsequently, HCO is hydrogenated to CH_2O (step 15), which has a barrier of 177 kJ/mol and is endothermic by 142 kJ/mol. The resulting CH_2O fragment is part of the formate pathway and, thus, its subsequent hydrogenation of methanol can proceed via this pathway.

The CO by-product can be obtained via formation of H_2O (steps 1-3), followed by direct cleavage of the C-O bond in CO_2 and subsequent desorption of CO from a stoichiometric surface (steps 12 and 20). The desorption of CO from a stoichiometric surface is associated with a barrier of 121 kJ/mol. In addition, a H-assisted rWGS pathway was investigated. After adsorption of CO_2 on an oxygen vacancy (step 5) and dissociative adsorption of H_2 (step 6), protonation of CO_2 takes place (step 16), yielding COOH ($\Delta E_a = 82$ kJ/mol; $\Delta E_R = 13$ kJ/mol). Next, COOH dissociates (step 17) into CO and OH ($\Delta E_a = 45$ kJ/mol, $\Delta E_R = 20$ kJ/mol). OH hydrogenation to form water (step 18) is associated with an activation energy of 140 kJ/mol and is endothermic by -58 kJ/mol. Finally, desorption of CO and H_2O (steps 19 and 3) proceed with desorption energies of 51 kJ/mol and 177 kJ/mol, respectively, closing the catalytic cycle.

4.3.3.3 Methanol synthesis on Ni_8 -cluster In_2O_3

The network diagram and PEDs of CO_2 conversion to CH_3OH and CO on the Ni_8 -cluster model are depicted in Figure 4.3c and 4.4c, respectively. The geometries of initial, transition and final states can be found in Section B10. H_2 adsorbs molecularly on the nanocluster ($\Delta E_R = -49$ kJ/mol) and then homolytically

dissociates into H atoms ($\Delta E_a = 22$ kJ/mol, $\Delta E_R = -40$ kJ/mol). Overall, the process of H₂ activation (step 1) is exothermic by -89 kJ/mol. Notably, H₂ activation on the Ni₈-cluster model is more facile than on the SA models, which is expected for a Ni cluster with a metallic character. Next, one interfacial O atom can be hydrogenated to form H₂O. The barriers for the two consecutive hydrogenation steps are 152 kJ/mol (step 2) and 140 kJ/mol (step 3). Water desorption from the surface (step 4) costs 80 kJ/mol. The oxygen vacancy formation involves overall reaction and activation energies of -22 and 57 kJ/mol, respectively, with respect to gas-phase H₂. On the oxygen-defective surface, CO₂ adsorbs ($\Delta E_{\text{ads}} = -120$ kJ/mol; step 5) at the metal-oxide interface with the carbon coordinating to a lattice oxygen next to two Ni-H fragments. From this state, CO₂ can be hydrogenated to methanol via a formate intermediate (steps 7-12). First, CO₂ is hydrogenated to HCO₂ by a Ni-H species (step 7), which is exothermic by -25 kJ/mol and has an activation energy of 95 kJ/mol. Next, HCO₂ is hydrogenated to H₂CO₂ (step 8) by another Ni-H species. This step features the highest forward barrier of the formate pathway ($\Delta E_a = 177$ kJ/mol) and is endothermic by $\Delta E_R = 138$ kJ/mol. Next, cleavage of a C-O bond in the H₂CO₂ intermediate yields CH₂O and O (step 9), the latter replenishing the oxygen vacancy. This elementary reaction step has a barrier of 52 kJ/mol and is exothermic by $\Delta E_R = -30$ kJ/mol. After adsorption of another H₂ on the Ni₈-cluster (step 10; $\Delta E_R = -89$ kJ/mol), two further hydrogenation steps towards CH₃O and CH₃OH with activation energies of 83 kJ/mol (step 11; $\Delta E_r = 41$ kJ/mol) and 124 kJ/mol (step 12; $\Delta E_r = -39$ kJ/mol), respectively, lead to methanol. Desorption of methanol costs 35 kJ/mol (step 13).

Besides H-assisted CO₂ dissociation via formate intermediate, C-O bond scission can also proceed in a direct fashion following oxygen vacancy formation. Herein, the vacancy is healed upon C-O bond scission in adsorbed CO₂. CO₂ can adsorb on the Ni₈-cluster with a slightly lower adsorption energy of $\Delta E_{\text{ads}} = -88$ kJ/mol than on the vacancy (-120 kJ/mol). Subsequent dissociation of CO₂ adsorbed on the cluster results in an O atom that heals the oxygen vacancy and adsorbed CO. This reaction has a barrier of 114 kJ/mol and is exothermic by 30 kJ/mol (step 14). This barrier is higher than the corresponding barrier over the Ni₁-adsorbed system ($\Delta E_{\text{a,adsorbed}} = 81$ kJ/mol). CO is a precursor for methanol synthesis along the CO-hydrogenation pathway (Figure 4.3c and 4.4c, green). After CO₂ dissociation, CO can either desorb ($\Delta E_{\text{ads}} = -130$ kJ/mol; step 28), which would be representative of an alternative rWGS pathway to the one discussed below or be hydrogenated to either HCO ($\Delta E_a = 150$ kJ/mol; step 16) or COH ($\Delta E_a = 235$ kJ/mol; step 17). HCO can be hydrogenated towards HCOH (step 18). This step is endothermic by 30 kJ/mol and features a barrier of 69 kJ/mol. Alternatively, HCOH can also be formed from COH by hydrogenation involving a barrier of 211 kJ/mol (step 20; $\Delta E_r = 50$ kJ/mol). HCOH can subsequently be hydrogenated to H₂COH (step

22; $\Delta E_R = -52$ kJ/mol) and then to CH₃OH (step 23). These two hydrogenation steps have activation energies of $\Delta E_a = 111$ kJ/mol and $\Delta E_a = 76$ kJ/mol, respectively.

To verify our hypothesis that CO₂ methanation on small In₂O₃-supported Ni clusters does not occur, we computed the barriers for direct and H-assisted CO dissociation. These steps are the most likely rate-limiting steps in CO₂ methanation.⁷³ We included direct and H-assisted CO dissociation pathways and the results are reported in Table B10. The structures of the TS can be found in Table B11. We can compare these results to data for CO dissociation pathways on extended surfaces of Ni by Sterk et al.⁷³ Compared to Ni(110), direct cleavage of the C-O bond on a Ni₈-cluster model is associated with a very high barrier ($\Delta E_a = 312$ kJ/mol for the cluster vs. $\Delta E_a = 150$ kJ/mol for Ni(110)). On the Ni₈-cluster, the barrier of H-assisted CO dissociation via an HCO intermediate of 174 kJ/mol is more facile than the barrier for direct CO dissociation. However, this barrier is still significantly higher than the one computed for Ni(110) ($\Delta E_a = 117$ kJ/mol). Furthermore, we argue that the structure of the Ni₈-cluster model would also lead to high barriers for alternative CO dissociation reactions involving COH, H₂CO and H₃CO intermediates. Indeed, the absence of step-edge sites on the Ni₈-In₂O₃ model results in high barriers for CO activation, in line with the expectations based on experimental evidence.⁴³

In line with the Ni₁-adsorbed model, on the Ni₈-cluster model CO can be obtained via formation of H₂O (steps 1-4), followed by direct cleavage of the C-O bond in CO₂ and subsequent desorption of CO from a stoichiometric surface (steps 14 and 28, respectively). The desorption of CO from a stoichiometric surface has a barrier of 130 kJ/mol. Finally, we discuss the formation of CO from CO₂ via the H-assisted rWGS pathway. Herein, one of the oxygen atoms of the CO₂ molecule is protonated to form COOH (step 24) with an activation energy of 62 kJ/mol. This step is endothermic by 48 kJ/mol. In turn, COOH can dissociate on the Ni₈-cluster into CO and OH (step 25; $\Delta E_a = 66$ kJ/mol). This step is exothermic by 59 kJ/mol. The resulting hydroxyl fragment is hydrogenated to H₂O (step 26; $\Delta E_a = 122$ kJ/mol). Finally, H₂O and CO desorb leaving a vacancy on the surface with ΔE_{des} of 80 and 114 kJ/mol, respectively.

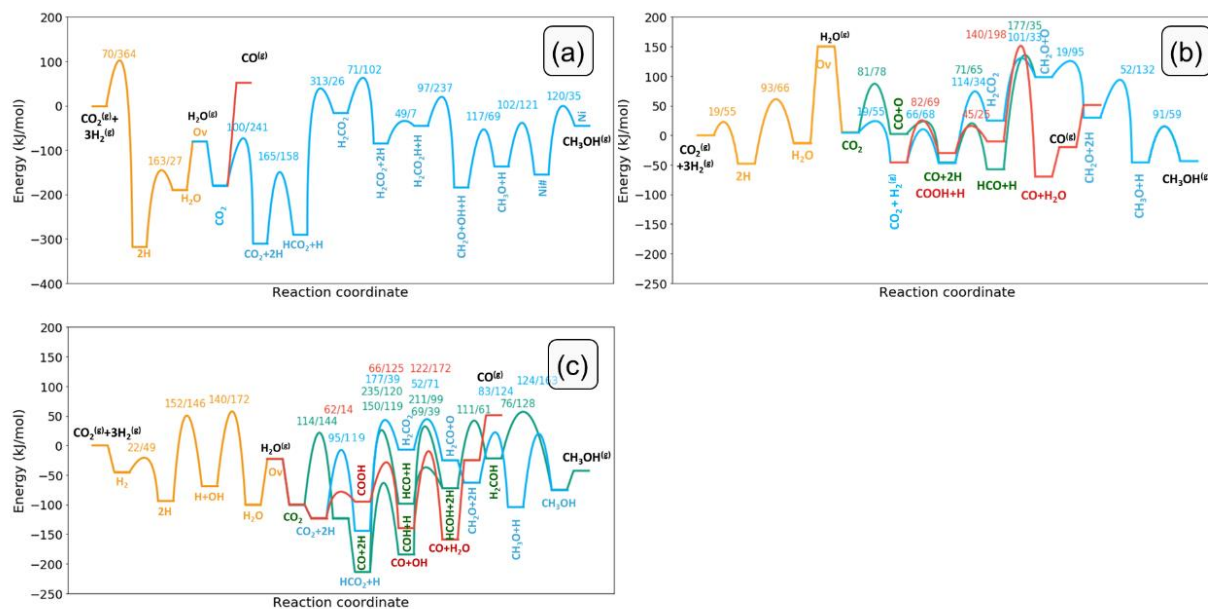


Figure 4.4. Potential energy diagrams of the conversion of CO₂ and H₂ to CO, CH₃OH, and H₂O on (a) Ni₁-doped, (b) Ni₁-adsorbed and (c) Ni₈-cluster model. Reaction barriers are reported in X/Y format wherein X corresponds to the forward barrier and Y to the backward barrier. All energies are given in kJ/mol. Orange: oxygen vacancy formation pathway; blue: formate pathway to CH₃OH; green: CO hydrogenation pathway to CH₃OH; red: rWGS (direct or H-assisted) to CO.

4.3.4 Microkinetic simulations

4.3.4.1 Overall kinetics

To compare the catalytic performance of the different Ni-In₂O₃ models, we compute the CO₂ hydrogenation reaction rate employing microkinetic simulations and the DFT reaction energetics. The active sites in our model consist of either isolated single Ni atoms, i.e. either the Ni₁-adsorbed or the Ni₁-doped model, or clusters (Ni₈- and Ni₆-cluster models) stabilized on the In₂O₃ support. We do not take migration of intermediates between the active sites into account. Co-adsorbed species are modelled as distinct varieties of a single active site. In this approximation, all elementary reaction steps are unimolecular, with exception of the adsorption and desorption steps. A detailed list of the elementary reaction steps is provided in Appendix B.

The CO₂ consumption rate and the CH₃OH selectivity as a function of temperature are plotted in Figure 4.5 for the three systems considered. The turnover frequencies (TOF) towards CH₃OH and CO are given in Figure B9. As can be seen from Figure 4.5a, the Ni₁-doped and Ni₈-cluster models exhibit the highest CO₂ consumption rate below 275 °C. Above 300 °C, the Ni₁-adsorbed and Ni₁-doped systems are more active

than the Ni₈-cluster model. From Figure 4.5b, it can be seen that the CH₃OH selectivity for the Ni₈-cluster is 95% at 200 °C. With increasing temperature, the rate of CO formation increases faster than the rate of methanol formation (Figure B9a-b), resulting in a decrease of the methanol selectivity. Above 350 °C, CO becomes the main reaction product, in line with experimental results. Both the Ni₁-adsorbed and Ni₁-doped models show a negligible CH₃OH selectivity (Figure 4.5b), indicating that these two models are mainly active for the rWGS reaction.

To highlight the promoting effect of Ni on In₂O₃, we constructed a microkinetic model for unpromoted In₂O₃ based on the published DFT data of Frei et al.²⁴ The resulting predictions in terms of activity and selectivity are provided in Figure B10. These data clearly show the promoting effect of Ni clusters on In₂O₃ for CO₂ hydrogenation at relevant temperatures. Notably, these results are qualitatively in line with the experimental results published by Jia et al.³⁹ Overall, this implies that the Ni₈-In₂O₃ model presents the highest methanol reaction rate in line with our earlier experimental work.⁶⁹

We also verify that methane formation on the Ni₈-cluster model is unlikely by performing microkinetic simulations using the barrier for direct CO dissociation calculated on the Ni₈-cluster (312 kJ/mol) and the data by Sterk et al.⁷³ for the C-H coupling steps. Sensitivity analysis shows that appreciable methane selectivity takes place only if the activation energy of the CO dissociation step is below 60 kJ/mol (Figure B11).

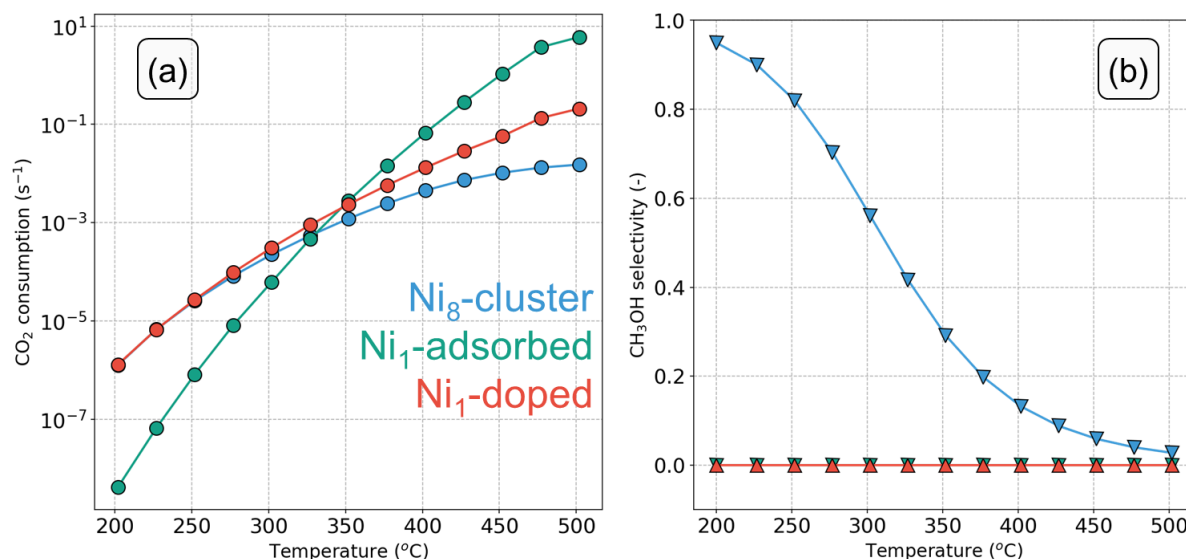


Figure 4.5. (a) CO₂ consumption rate (s⁻¹) and (b) CH₃OH selectivity as a function of temperature on different models ($p = 50$ bar, H₂/CO₂ ratio =5).

The results in terms of coverage, apparent activation energy (E_{app}) and reaction orders as a function of temperature are given in Figure 4.6. The coverages in Figures 4.6a-c should be interpreted as the fraction

of time the system spends in a particular state (i.e., the time average). According to the ergodicity principle in statistical thermodynamics, this equals the fraction of active sites that is in a particular state (i.e., the ensemble average). The Ni₈-cluster (Figure 4.6a) predominantly resides in the HCO₂+H state at lower temperatures (200 °C < T < 300 °C). The reaction order in H₂ (Figure 4.6d) is positive, while the reaction order in CO₂ is close to zero. A higher H₂ partial pressure is beneficial, because it increases the rate of hydrogenation of HCO₂ to methanol. As the surface is dominated by a CO₂-derived intermediate, further increasing the CO₂ partial pressure will not increase its coverage and the reaction rate, explaining the close to zero reaction order in this reactant. The kinetic parameters for the Ni₈-cluster model lie within the range of values reported in the experimental literature for In₂O₃. For instance, Frei et al. reported a positive reaction order in H₂ (0.33) and a close-to-zero order for CO₂ at 250 °C.⁷² We find that, with increasing temperature, the reaction order in H₂ decreases and the one in CO₂ increases. This is because the oxygen vacancy state becomes the dominant state at high temperature (Figure 4.6a, in grey). In the limit of the empty surface, a higher partial pressure of CO₂ results in a higher coverage with reaction intermediates, increasing the CO₂ turnover rate. This behavior is also reflected in the E_{app} trend (Figure 4.6d). The E_{app} is approximately constant below 400 °C and decreases at higher temperature. This reflects a change in the changing coverages. By comparing Figure 4.6a and 4.6d, it can be seen that the decrease in the apparent activation energy goes together with an increase of the oxygen vacancies, resulting in a higher coverage of CO₂. The exothermic energy of CO₂ adsorption ($\Delta E_{ads} = -120$ kJ/mol) lowers the apparent activation energy of the overall reaction. The computed E_{app} for the Ni₈-cluster model is in line with the experimental values reported on Ni-In₂O₃ (80 kJ/mol between 200 and 300 °C).³⁹ We also performed simulations with either CO or CH₃OH as key component to better understand the decrease of the E_{app} with decreasing temperature (Figure B12). On the Ni₈-cluster, the E_{app} for CH₃OH synthesis is lower than the one for CO production (Figure B12a), in line with the selectivity trend depicted in Figure 4.5b. The trends in kinetic parameters as shown in Figure 4.6a and 4.6d for the Ni₈ cluster are also in keeping with the changing selectivity from CH₃OH to CO. To further understand these aspects, we investigate these trends in more detail with a degree of rate control (DRC) and a flux analysis (*vide infra*).

For the Ni₁-adsorbed model (Figure 4.6b), at lower temperature, the dominant surface state features two adsorbed H species (NiH+H) on a stoichiometric Ni₁-In₂O₃(111) surface. Subsequent water desorption along the oxygen vacancy formation pathway is associated with a relatively high barrier ($\Delta E_{des, H_2O} = 177$ kJ/mol). This step is the most difficult one along the most favorable pathway as can be seen in Figure 4.3b and 4b. As a result, the NiH+H state is dominant. With increasing temperatures, H₂O desorption will be easier, resulting in more vacancies where CO₂ can adsorb. This results in a decreasing contribution of the NiH+H state in favor of intermediates in the CO₂ hydrogenation pathway, such as CO₂+2H and HCO₂+H. The reasons behind the latter two states being dominant can be understood from Figure 4.3b. CO₂ binds

strongly to the surface ($\Delta E_{\text{ads}} = -144$ kJ/mol) and subsequent hydrogenation of CO_2 to HCO_2 has a low activation energy of only 66 kJ/mol (step 6 in Figure 4.3b), whereas the subsequent hydrogenation step to H_2CO_2 has a considerably higher activation energy of 114 kJ/mol (step 7 in Figure 4.3b). Consequently, the HCO_2+H state together with the CO_2+2H state, which only differ by 2 kJ/mol, are found to be the dominant states.

At low temperature, the reaction orders in both CO_2 and H_2 (Figure 4.6e) are close to zero. Under these conditions, the reaction is limited by the rate of H_2O removal, the last step towards oxygen vacancy formation (step 3 in Figure 4.3b). The rate of H_2O desorption is not affected by the partial pressure of H_2 and CO_2 . A temperature increase thus results in formation of oxygen vacancy and CO_2 adsorption (Figure 4.6b). Under these conditions, an increased partial pressure of H_2 leads to a higher rate of H adsorption which, together with the presence of adsorbed CO_2 , results in CO_2+2H and HCO_2+H states becoming dominant. However, these elementary reaction steps proceed towards a branch in the kinetic network away from the dominant product (CO). Thus, under these conditions the reaction order in H_2 is negative.

For the Ni_1 -adsorbed model, E_{app} (Figure 4.6e) is constant at 175 kJ/mol for temperatures below 300 °C. This value corresponds to the desorption energy of H_2O . As the temperature increases, the E_{app} decreases. On this model, the E_{app} for the CH_3OH product is higher than the E_{app} for the CO by-product (Figure B12b), in line with the selectivity trend depicted in Figure 4.5b. Together these findings suggest that oxygen vacancy formation controls the overall reaction rate at low temperature while, at high temperature, either CO_2 activation or hydrogenation are limiting the overall rate. These aspects can be better appreciated by means of a DRC analysis (*vide infra*).

When Ni is doped inside In_2O_3 (Figure 4.6c), the surface is predominantly in the CO_2+2H and HCO_2+H working states. Although CO_2 hydrogenation to HCO_2 is possible on the catalyst's surface, further hydrogenation towards methanol is limited by the high barrier for HCO_2 hydrogenation to H_2CO_2 ($E_{\text{act}} = 313$ kJ/mol, $\Delta E_r = 287$ kJ/mol). The reaction order in CO_2 is zero because the dominant working state (either CO_2+2H or HCO_2+H) already corresponds to intermediates derived from CO_2 . The reaction order in H_2 is negative at low temperature, indicating that a higher partial pressure of H_2 would push the network away from the dominant pathway. On the Ni_1 -doped model, the E_{app} (Figure 4.6f) is constant to a value of 130 kJ/mol in the explored temperature range. In line with the Ni_1 -adsorbed model, on the Ni_1 -doped system the E_{app} for the CH_3OH product is higher than the E_{app} for the CO by-product (Figure B12c).

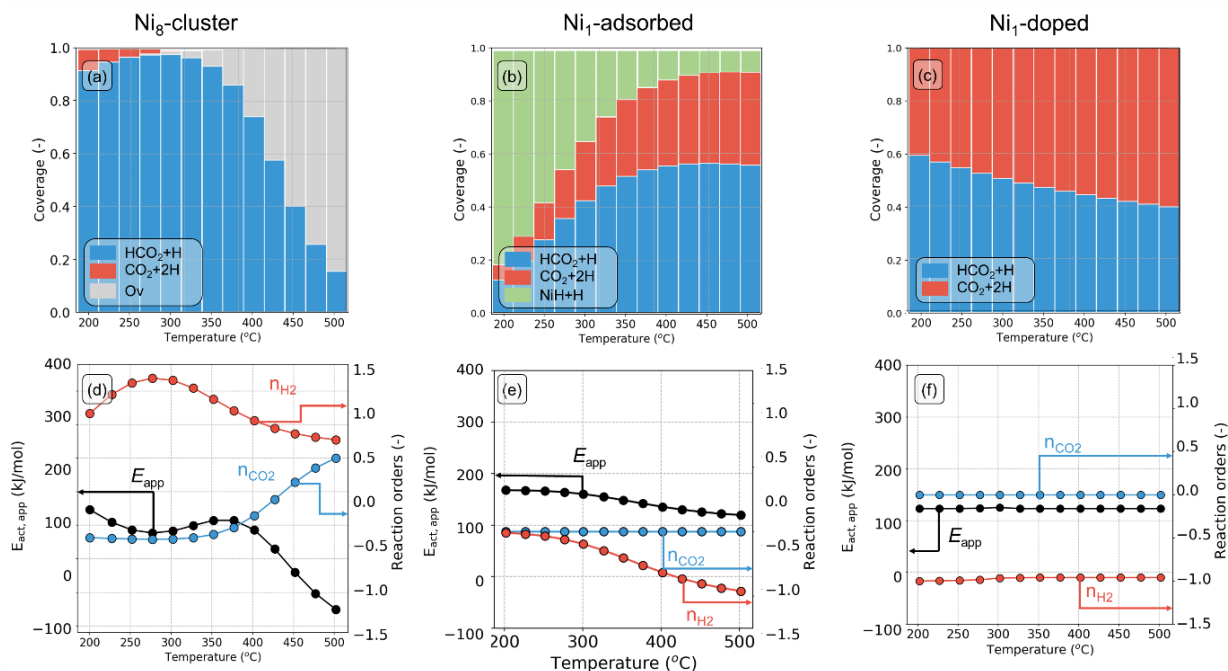


Figure 4.6. Surface state of the model catalysts (a-c), reaction orders and apparent activation energies (d-f) with CO₂ as key component as a function of temperature.

4.3.4.2 Rate and selectivity control of the reaction network

In this section, we discuss in detail the reaction network that leads to CH₃OH and CO formation from CO₂ hydrogenation on the three Ni-In₂O₃ models. We identify the elementary steps that control the overall CO₂ consumption rate and the CH₃OH selectivity and investigate how these steps change with reaction temperature. For this purpose, we conduct a sensitivity analysis based on Campbell's degree of rate control (DRC)⁶³ and selectivity control (DSC).^{65,74} Under zero extent of reaction, the sum of the DRC coefficients is conserved at one.⁷⁵ The DSC quantifies the extent to which a particular elementary reaction step influences the selectivity to certain products for which methanol is of our primary interest. Note that the sum of the DSC values of all elementary reaction steps for a single product equals zero.⁶⁴

4.3.4.2.1 Ni₈-cluster

The DRC and DSC analyses for the Ni₈-cluster model are reported in Figures 7a and 7b, respectively. From these figures, it can be seen that at low temperature (200 °C < T < 300 °C), the rate of CO₂ consumption is almost exclusively controlled by the rate of HCO₂ hydrogenation to H₂CO₂ (step 8 in Figure 4.7c), which has the highest activation energy in the dominant pathway as seen from Figure 4.7c (pathway highlighted in red). Other elementary steps, such as CH₂O and CH₃O hydrogenation (steps 11 and 12 in Figure 4.7c) control the kinetics to a smaller extent. These results are consistent with the positive reaction order in H₂

and a reaction order in CO_2 of zero (Figure 4.6d). A higher partial pressure of H_2 would increase the concentration of Ni-H states necessary for the hydrogenation reactions thus enhancing the overall rate, whereas a change in the partial pressure of CO_2 would not affect these reactions. The DSC analysis (Figure 4.7b) shows that the same elementary steps that are controlling the rate are also controlling methanol selectivity. An increased rate of HCO_2 hydrogenation (step 8) would result in a higher flux in the route towards methanol, benefiting its formation at the expense of CO formation. With increasing temperature, a change in the selectivity from methanol to CO is observed (Figure 4.5b), which is reflected by the DRC analysis. Herein, the DRC coefficient of HCO_2 hydrogenation to H_2CO_2 decreases as function of temperature, whereas the DRC coefficient of OH hydrogenation to H_2O (step 26 in Figure 4.7c) increases. This last step pertains to the rWGS branch in the kinetic network. Thus, this step is observed to inhibit the selectivity towards methanol. Figure 4.7b shows that, at higher temperature, the steps of CH_2O hydrogenation to CH_3O and its further hydrogenation to CH_3OH (steps 11 and 12, respectively) control the selectivity to the desired methanol product. These two steps require more Ni-H species to occur than HCO_2 hydrogenation (step 8). However, Ni-H species are less abundant at high temperature, as we previously observed (Figure 4.6a), suggesting that steps requiring less surface hydrogen, like the ones pertaining the rWGS pathway, are facilitated at high temperature. This can explain the observed shift in selectivity towards CO and is also consistent with the decrease in the computed reaction orders in H_2 (Figure 4.6d). To confirm the effect of H_2 partial pressure on CH_3OH selectivity, we performed a simulation with a $\text{H}_2:\text{CO}_2$ ratio of 1:5 (instead of 5:1) and observed that the selectivity to CH_3OH decreases to 20% at 250 °C (Figure B13). Thus, the selectivity shift to CO observed at high temperature can be explained by the lower availability of Ni-H species at such temperatures.

Figure 4.7c and 4.7d show the flux analysis at low and high temperature, respectively. Following the pathways with the largest molar fluxes readily reveals the dominant kinetic pathway at those conditions (highlighted in red). At low temperature (Figure 4.7c), the dominant pathway corresponds to methanol formation via formate, whereas at high temperature (Figure 4.7d) the dominant pathway shifts to the H-assisted rWGS route. This is consistent with the activity and selectivity trends predicted by the microkinetic model. The reaction flux diagram also shows that the pathway of CO hydrogenation to methanol features significantly lower rates ($2.20 \cdot 10^{-14} \text{ mol} \cdot \text{s}^{-1}$; steps 14-23) than the formate pathway ($2.65 \cdot 10^{-5} \text{ mol} \cdot \text{s}^{-1}$; steps 7-12), indicating that it is not taken. Indeed, hydrogenation of CO to HCO and CO to COH is associated with activation energies of 150 kJ/mol and 235 kJ/mol, respectively, while CO desorption is associated with a lower barrier of $\Delta E_{\text{des}} = 130 \text{ kJ/mol}$. Therefore, desorption of CO is more favorable than its further hydrogenation to methanol. Concerning the formation of CO, Figure 4.7c-d shows that direct CO_2 dissociation has lower rates ($2.61 \cdot 10^{-8} \text{ mol} \cdot \text{s}^{-1}$; step 14) as compared to the H-assisted rWGS pathway ($4.79 \cdot 10^{-6} \text{ mol} \cdot \text{s}^{-1}$; step 24). This difference can be ascribed to the higher activation energy for direct CO_2

dissociation as compared to its hydrogenation to COOH (114 kJ/mol and 62 kJ/mol, respectively) which makes the H-assisted rWGS more facile.

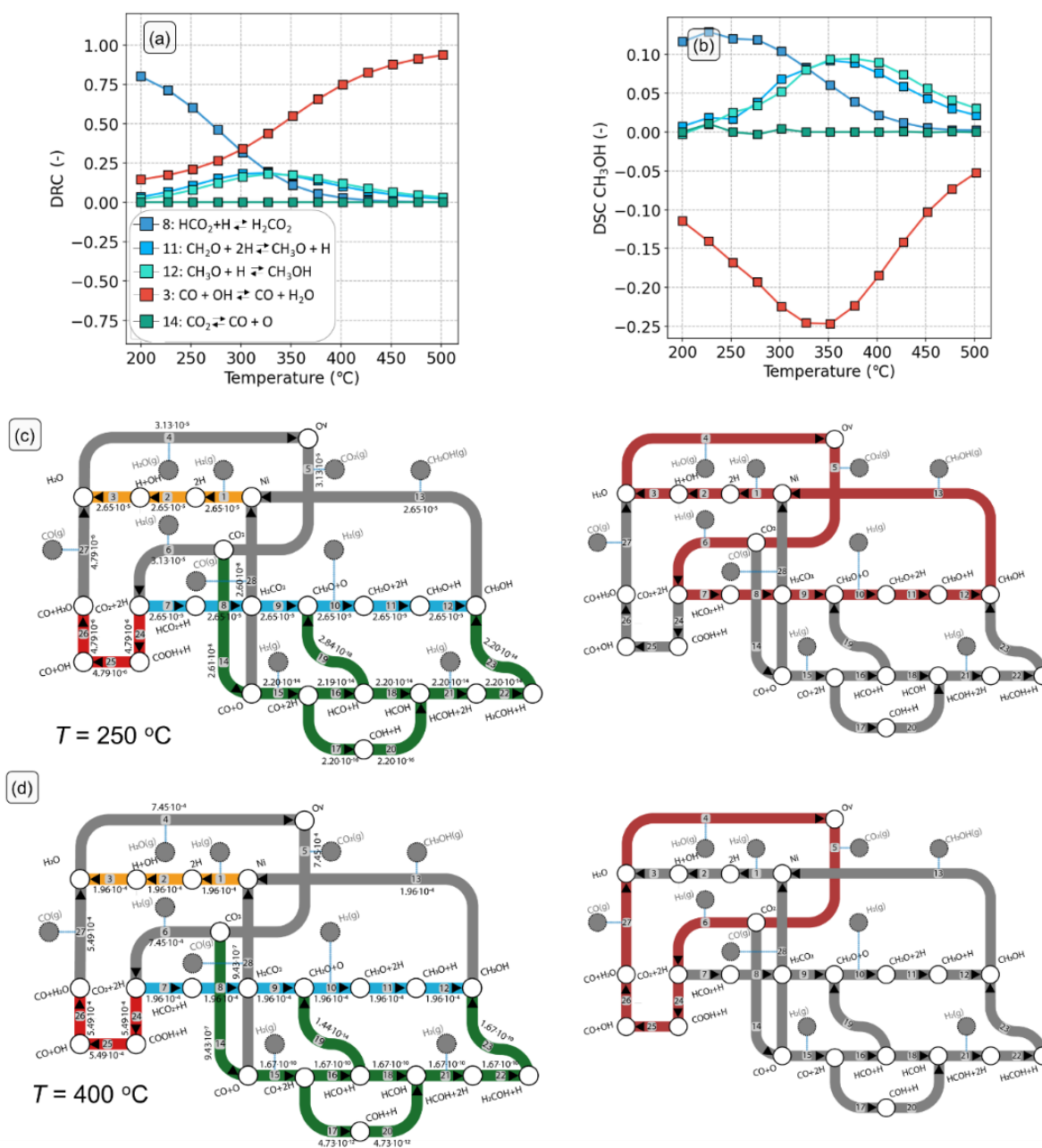


Figure 4.7. Degree of rate control (a) and degree of selectivity control (b) with CO₂ as key component as a function of temperature for the Ni₈-cluster model. (c-d) Reaction network analysis (left) and dominant pathways (right, highlighted in red) for CO₂ hydrogenation to CH₃OH, CO and H₂O. (c) $T = 250\text{ }^{\circ}\text{C}$, (d) $T = 400\text{ }^{\circ}\text{C}$ ($p_{\text{tot}} = 50\text{ bar}$, $\text{H}_2/\text{CO}_2 = 5$). The numbers in the arrows are molar reaction rates (s^{-1}) and are normalized with respect to the amount of adsorbed CO₂.

4.3.4.2.1 Ni₁-doped and Ni₁-adsorbed

From Figure 4.5b, it was established that neither the Ni₁-doped nor the Ni₁-adsorbed models produce methanol. As such, we only consider the DRC and flux analyses as the DSC analysis will evidently only show coefficients close to zero for all elementary reaction steps.

The DRC analysis and reaction flux analysis for the Ni₁-adsorbed model are shown in Figure 4.8a and Figure 4.8b, respectively. At low temperature, the CO₂ consumption rate is mostly controlled by the rate of H₂O desorption (step 3), because this elementary step has the highest barrier among the steps pertaining to the oxygen vacancy formation pathway ($\Delta E_{\text{des}} = 177$ kJ/mol). This result is consistent with the surface state of the catalyst featuring mostly adsorbed hydrogen species (NiH+H, in Figure 4.6b), which is a state that precedes H₂O formation. At higher temperature ($T > 275$ °C), formation of oxygen vacancies and subsequent adsorption of CO₂ result in a decrease in the DRC coefficient of the H₂O desorption in favor of CO₂ dissociation (step 12) which becomes the dominant rate controlling step. An increased rate of CO₂ dissociation (step 12) would result in a higher rate towards the main product CO. As can be seen in Figure 4.8b, the branch of the mechanism going towards CO₂ hydrogenation via the formate pathway features considerably lower rates than the one proceeding towards CO₂ dissociation ($2.10 \cdot 10^{-6}$ s⁻¹ and $6.68 \cdot 10^{-2}$ s⁻¹, respectively). The formate pathway is not taken because the steps of H₂CO hydrogenation to H₂CO₂ (step 7) and its further dissociation into CH₂O and O (step 9) are highly activated and endothermic, resulting in an overall reaction energy and barrier of 150 and 172 kJ/mol, respectively. The dominant pathway (highlighted in red in Figure 4.8b, right) on the Ni₁-adsorbed model proceeds thus via direct dissociation of CO₂ yielding CO which desorbs from the surface, closing the rWGS catalytic cycle. In line with the Ni₈-cluster model, the pathway of CO hydrogenation to methanol is not taken (steps 13-15 in Figure 4.8b). This is due to the step of HCO hydrogenation to CH₂O being associated with high a activation energy ($\Delta E_{\text{a}} = 177$ kJ/mol) and endothermic ($\Delta E_{\text{R}} = 142$ kJ/mol). Concerning the formation of CO, the direct dissociation of CO₂ is preferred over the H-assisted rWGS ($6.54 \cdot 10^{-2}$ s⁻¹ and $1.05 \cdot 10^{-4}$ s⁻¹, respectively). This is because the H-assisted rWGS pathway is limited by the activation energy of OH hydrogenation ($\Delta E_{\text{a}} = 140$ kJ/mol) which is significantly higher than the one of the CO₂ dissociation and subsequent CO desorption elementary steps (81 and 121 kJ/mol, respectively).

The DRC analysis and reaction flux analysis for the Ni₁-doped model are shown in Figure 4.8c and Figure 4.8d, respectively. The elementary reaction step of CO₂ dissociation and CO desorption (step 14) has a DRC coefficient of 1, thus it is the rate determining step (RDS) in the mechanism under the explored temperature range (Figure 4.8c). This step is rate determining because it has the highest activation energy in the rWGS pathway (Figure 4.3a and 4.4a). The dominant pathway for the Ni₁-doped model at $T = 250$ °C (Figure 4.8d right highlighted in red) involves the hydrogenation of CO₂ to CO via a mechanism

involving the formation of an oxygen vacancy (steps 1-3), adsorption of CO₂ on an oxygen vacancy (step 4), subsequent formation of CO and healing of the vacancy (step 14). Concerning the formation of CH₃OH, negligible reaction fluxes for the formate pathway are found ($3.43 \cdot 10^{-26} \text{ s}^{-1}$), in line with the $\text{TOF}_{\text{CH}_3\text{OH}}$ computed by the microkinetic model (Figure B7a). This is due high activation energy associated with the hydrogenation of HCO₂ to H₂CO₂ ($\Delta E_a = 313 \text{ kJ/mol}$, $\Delta E_R = 287 \text{ kJ/mol}$), which makes methanol formation unfavorable.

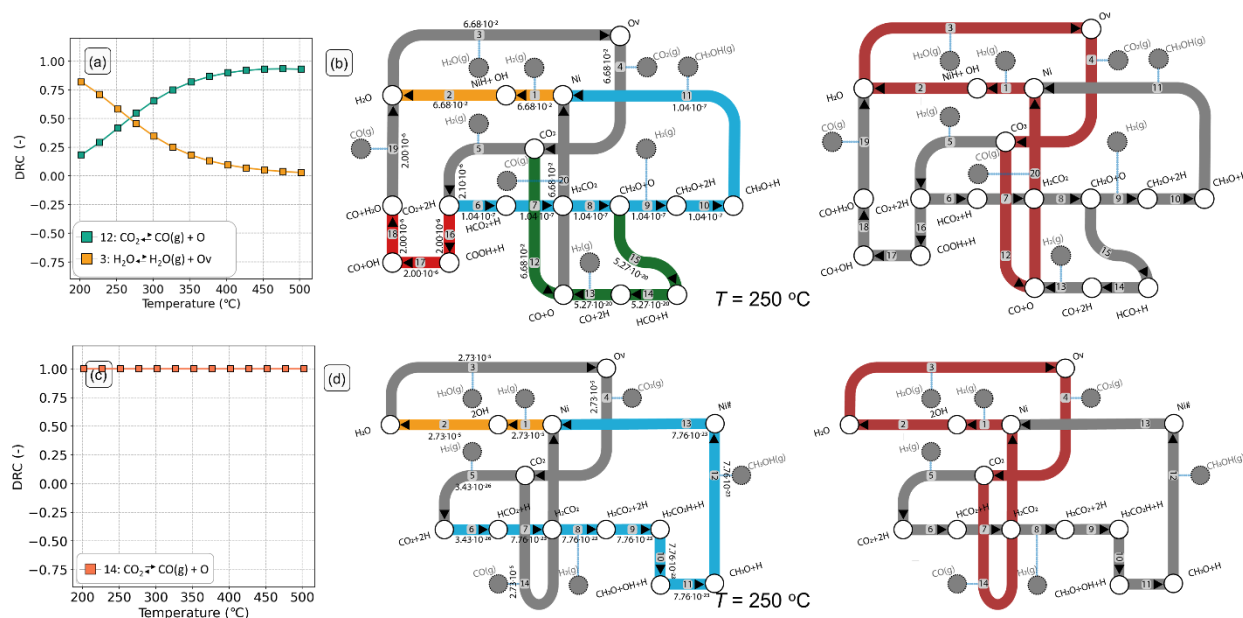


Figure 4.8. Degree of rate control analysis with CO₂ as key component as a function of temperature for (a) Ni₁-adsorbed and (c) Ni₁-doped model surfaces. Reaction network analysis (left) and dominant pathways (right, highlighted in red) for CO₂ hydrogenation to CH₃OH, CO and H₂O for (b) Ni₁-adsorbed and (d) Ni₁-doped model surfaces. ($T = 250 \text{ }^\circ\text{C}$, $p_{\text{tot}} = 50 \text{ bar}$, $\text{H}_2/\text{CO}_2 = 5$). The numbers in the arrows are molar reaction rates (s^{-1}) and are normalized with respect to the amount of adsorbed CO₂. The pathways with the highest molar fluxes are highlighted in red.

4.3.5 General Discussion

The present study provides new insights into the role of promoting Ni species in the In₂O₃-catalyzed hydrogenation of CO₂ to methanol. Methanol formation involves oxygen vacancies in the In₂O₃ support. Frei et al. reported oxygen vacancy formation on a In₂O₃(111) surface via homolytic dissociation of molecular hydrogen forming two surface OH groups, followed by water formation and desorption.⁷² Oxygen vacancy formation has an overall barrier of 67 kJ/mol with respect to gas-phase H₂.⁴⁸ Heterolytic H₂ dissociation on this surface was found to have a similar overall barrier.⁷⁶ The presence of a Ni₈-cluster on the In₂O₃ surface results in a lower overall barrier (57 kJ/mol) whereas when a single Ni atom is either

doped in or adsorbed onto the $\text{In}_2\text{O}_3(111)$ surface higher overall barriers are found (70 and 150 kJ/mol, respectively). Since the Ni_6 -cluster has the same metallic character and interface with the In_2O_3 as the Ni_8 -cluster, we infer that the overall barriers to oxygen vacancy formation on the two clusters should be similar. Thus, oxygen vacancies are likely to be present under reaction conditions of methanol synthesis. Their formation and role in the reaction mechanism were explicitly taken into account in the microkinetic models for methanol synthesis based on DFT calculations covering reaction mechanisms involving methanol formation via formates and CO.

On the Ni_8 -cluster model, at relatively low temperature, the rate of CO_2 consumption is mainly limited by the elementary step of HCO_2 hydrogenation to H_2CO_2 . The main reaction pathway to methanol on Ni_8 -cluster is via low-barrier C-O bond dissociation in a H_2CO_2 intermediate. This results in a high methanol selectivity at low temperature. With increasing temperature, the selectivity shifts to CO in line with experimental observations.^{39,43} The dependence of the selectivity on the temperature is associated with the availability of NiH^δ species. Analysis of the surface coverages shows that, at relatively low temperature, hydrides mainly occupy the surface, favoring hydrogenation reactions. With increasing temperature, the coverage of surface hydrogen rapidly decreases, as it is used to reduce the surface by creating oxygen vacancies. Since the rWGS reaction requires only two hydrogenation steps, whereas methanol formation requires four, the former reaction becomes dominant under surface-hydrogen-lean conditions.

The outcomes of the simulations might be affected by the size and shape of the cluster. For this reason, we compare our Ni_8 -cluster with a smaller Ni_6 -cluster, which was also obtained with our DFT-based genetic algorithm. We looked into key elementary reaction steps that are limiting the rate for the formation of CH_4 , CO and CH_3OH based on the microkinetic analysis for CO_2 hydrogenation on the supported Ni_8 -cluster. The forward and backward activation energies for these steps are reported in Table B12 and the structures of IS, TS and FS are depicted in Table B13. As can be seen from Table B12, the forward and backward activation energies for the Ni_6 -cluster are comparable to those obtained for the Ni_8 -cluster. Based on these results, we constructed a microkinetic model for the Ni_6 -cluster, assuming that all the other elementary reaction steps are the same as for the Ni_8 -cluster. The results highlighted in Figure B14 show that also the Ni_6 -cluster exhibits significant selectivity to CH_3OH at low temperature (50% at 200 °C). This indicates that the choice of an 8-atom cluster is representative of a small In_2O_3 -supported Ni cluster.

We also briefly discuss here our results in comparison to the findings recently reported by Shen et al., who investigated by DFT possible pathways of CO_2 hydrogenation to methanol on a $\text{Ni}_4/\text{In}_2\text{O}_3$ model catalysts.⁴² In line with our work, interfacial oxygen vacancies not only contribute to the adsorption of CO_2 but also facilitate the hydrogenation of intermediate species to methanol. Shen et al. speculated on the basis of energy diagrams that formation of CO from CO_2 followed by its hydrogenation to methanol is favored over

the formate pathway. This is at odds with our finding from microkinetic simulations that CO₂ hydrogenation to methanol involves formates.

For the Ni₁-adsorbed system, H₂ dissociation is heterolytic, resulting in NiH^{δ-} and OH^{δ+} species. On this model, oxygen vacancy formation is endothermic and is furthermore kinetically limited by H₂O desorption. As oxygen vacancy formation is endothermic, healing the oxygen vacancy is favorable resulting in a relatively low barrier for direct CO₂ dissociation into CO and O, the latter healing the vacancy. This, together with the lower availability of NiH^{δ-} species, results in a preference for CO formation over hydrogenation to methanol, explaining the predicted high CO selectivity. In line with our work, Frei et al. suggested that Ni SA on In₂O₃ would be active for the rWGS reaction.⁴¹

The Ni₁-doped system also does not lead to methanol. For this model, the abundance of OH^{δ+} species causes high activation energies for formation of C-H bonds.²⁴ For instance, a barrier of 313 kJ/mol is associated with HCO₂ hydrogenation to H₂CO₂ making methanol formation unfavorable. Furthermore, because of the doped configuration of Ni, there is steric hindrance preventing the carbon atom to effectively bond to Ni. This prevents the direct involvement of Ni in catalytic reaction. The dominant pathway on the Ni₁-doped model features the formation of CO via a redox pathway involving the formation of oxygen vacancy, adsorption of CO₂ on such vacancy and subsequent dissociation yielding CO. On this model, the elementary step of CO₂ dissociation is the rate determining step in the temperature range investigated.

4.4. Conclusions

Using DFT to compute the electronic structure and reaction energy diagrams and construct the input for microkinetic simulations, we investigated the promoting role of Ni on In₂O₃ for CO₂ hydrogenation to methanol. As the exact location and nuclearity of the Ni promoter in Ni-In₂O₃ catalysts is unknown, we considered three representative model systems: (i) a single Ni atom doped in the In₂O₃(111) surface, (ii) a Ni atom adsorbed on In₂O₃(111), and (iii) a small cluster of 8 Ni atoms adsorbed on In₂O₃(111). With respect to the pristine In₂O₃(111) surface the Ni₈-cluster model offers a lower overall barrier to oxygen vacancy formation whereas the Ni₁-doped and Ni₁-adsorbed model feature higher overall barriers. Microkinetic simulations reveal that significant methanol formation occurs only for the Ni₈-cluster model. The metallic cluster allows for facile H₂ activation, providing hydride (Ni-H) species needed for the formation of oxygen vacancies in In₂O₃ and hydrogenation reactions of adsorbed surface intermediates. Methanol synthesis at intermediate temperatures involves the hydrogenation of CO₂ adsorbed on an oxygen vacancy to a H₂CO₂ intermediate (formate pathway). At higher temperatures, the lack of Ni-H species at the surface results in a shift of the selectivity to CO via a mechanism involving a COOH intermediate. On the Ni₈-cluster model, high barriers associated with either direct or H-assisted CO activation inhibit methane formation. We compared our Ni₈-cluster with a smaller Ni₆-cluster also obtained with our DFT-based genetic algorithm.

Our DFT calculations show similar barriers for key rate limiting steps for the formation of CO, CH₄ and CH₃OH for the two clusters. Based on this, we investigated the kinetics of the Ni₆-cluster with microkinetic modeling and found appreciable selectivity to methanol at low temperature. Therefore, we conclude that our choice of an 8-atom cluster is representative of a small In₂O₃-supported Ni cluster. When a single Ni atom is adsorbed on the In₂O₃ surface, CO is the main product because a relatively low barrier for direct CO₂ dissociation is available. When a single Ni atom is doped in the In₂O₃ surface, the acidic nature of the H atoms adsorbed on the oxygen anions of In₂O₃ results in high activation barriers for CO₂ hydrogenation reactions, precluding methanol formation.

4.5 References

- (1) González-Garay, A.; Frei, M. S.; Al-Qahtani, A.; Mondelli, C.; Guillén-Gosálbez, G.; Pérez-Ramírez, J. Plant-to-Planet Analysis of CO₂-Based Methanol Processes. *Energy Environ. Sci.* **2019**, *12*, 3425–3436.
- (2) Kondratenko, E. V.; Mul, G.; Baltrusaitis, J.; Larrazábal, G. O.; Pérez-Ramírez, J. Status and Perspectives of CO₂ Conversion into Fuels and Chemicals by Catalytic, Photocatalytic and Electrocatalytic Processes. *Energy Environ. Sci.* **2013**, *6*, 3112.
- (3) Dias, V.; Pochet, M.; Contino, F.; Jeanmart, H. Energy and Economic Costs of Chemical Storage. *Front. Mech. Eng.* **2020**, *6*, 21.
- (4) Álvarez, A.; Bansode, A.; Urakawa, A.; Bavykina, A. V.; Wezendonk, T. A.; Makkee, M.; Gascon, J.; Kapteijn, F. Challenges in the Greener Production of Formates/Formic Acid, Methanol, and DME by Heterogeneously Catalyzed CO₂ Hydrogenation Processes. *Chem. Rev.* **2017**, *117*, 9804–9838.
- (5) Zhong, J.; Yang, X.; Wu, Z.; Liang, B.; Huang, Y.; Zhang, T. State of the Art and Perspectives in Heterogeneous Catalysis of CO₂ Hydrogenation to Methanol. *Chem. Soc. Rev.* **2020**, *49*, 1385–1413.
- (6) Jiang, X.; Nie, X.; Guo, X.; Song, C.; Chen, J. G. Recent Advances in Carbon Dioxide Hydrogenation to Methanol via Heterogeneous Catalysis. *Chem. Rev.* **2020**, *120*, 7984–8034.
- (7) Gumber, S.; Gurumoorthy, A. V. P. Methanol Economy Versus Hydrogen Economy. *Methanol Sci. Eng.* **2018**, 661–674.
- (8) Olah, G. A. Beyond Oil and Gas: The Methanol Economy. *Angew. Chemie - Int. Ed.* **2005**, *44*, 2636–2639.
- (9) Goepfert, A.; Czaun, M.; Jones, J. P.; Surya Prakash, G. K.; Olah, G. A. Recycling of Carbon Dioxide to Methanol and Derived Products – Closing the Loop. *Chem. Soc. Rev.* **2014**, *43*, 7995–8048.
- (10) Baltes, C.; Vukojević, S.; Schüth, F. Correlations between Synthesis, Precursor, and Catalyst Structure and Activity of a Large Set of CuO/ZnO/Al₂O₃ Catalysts for Methanol Synthesis. *J. Catal.* **2008**, *258*, 334–344.
- (11) Sehested, J. Industrial and Scientific Directions of Methanol Catalyst Development. *J. Catal.* **2019**, *371*, 368–375.
- (12) Behrens, M. Promoting the Synthesis of Methanol: Understanding the Requirements for an Industrial Catalyst for the Conversion of CO₂. *Angew. Chemie Int. Ed.* **2016**, *55*, 14906–14908.
- (13) Nakamura, J.; Choi, Y.; Fujitani, T. On the Issue of the Active Site and the Role of ZnO in Cu/ZnO Methanol Synthesis Catalysts. *Top. Catal.* **2003**, *22*, 277–285.

- (14) Fichtl, M. B.; Schlereth, D.; Jacobsen, N.; Kasatkin, I.; Schumann, J.; Behrens, M.; Schlögl, R.; Hinrichsen, O. Kinetics of Deactivation on Cu/ZnO/Al₂O₃ Methanol Synthesis Catalysts. *Appl. Catal. A Gen.* **2015**, *502*, 262–270.
- (15) Wang, J.; Li, G.; Li, Z.; Tang, C.; Feng, Z.; An, H.; Liu, H.; Liu, T.; Li, C. A Highly Selective and Stable ZnO-ZrO₂ Solid Solution Catalyst for CO₂ Hydrogenation to Methanol. *Sci. Adv.* **2017**, *3*.
- (16) Li, C. S.; Melaet, G.; Ralston, W. T.; An, K.; Brooks, C.; Ye, Y.; Liu, Y. S.; Zhu, J.; Guo, J.; Alayoglu, S.; Somorjai, G. A. High-Performance Hybrid Oxide Catalyst of Manganese and Cobalt for Low-Pressure Methanol Synthesis. *Nat. Commun.* **2015**, *6*.
- (17) Posada-Perez, S.; Vines, F.; Ramirez, P. J.; Vidal, A. B.; Rodriguez, J. A.; Illas, F. The Bending Machine: CO₂ Activation and Hydrogenation on Delta-MoC(001) and Beta-Mo₂C(001) Surfaces. *Phys Chem Chem Phys* **2014**, *16*, 14912–14921.
- (18) Christian Kunkel Vines, Francesc Illas, F. Transition Metal Carbides as Novel Materials for CO₂ Capture, Storage, and Activation. *Energy Environ. Sci* **2016**, *1*, 141–144.
- (19) Duyar, M. S.; Tsai, C.; Snider, J. L.; Singh, J. A.; Gallo, A.; Yoo, J. S.; Medford, A. J.; Abild-Pedersen, F.; Studt, F.; Kibsgaard, J.; Bent, S. F.; Nørskov, J. K.; Jaramillo, T. F. A Highly Active Molybdenum Phosphide Catalyst for Methanol Synthesis from CO and CO₂. *Angew. Chemie - Int. Ed.* **2018**, *57*, 15045–15050.
- (20) Fiordaliso, E. M.; Sharafutdinov, I.; Carvalho, H. W. P.; Grunwaldt, J. D.; Hansen, T. W.; Chorkendorff, I.; Wagner, J. B.; Damsgaard, C. D. Intermetallic GaPd₂ Nanoparticles on SiO₂ for Low-Pressure CO₂ Hydrogenation to Methanol: Catalytic Performance and in Situ Characterization. *ACS Catal.* **2015**, *5*, 5827–5836.
- (21) Studt, F.; Sharafutdinov, I.; Abild-Pedersen, F.; Elkjær, C. F.; Hummelshøj, J. S.; Dahl, S.; Chorkendorff, I.; Nørskov, J. K. Discovery of a Ni-Ga Catalyst for Carbon Dioxide Reduction to Methanol. *Nat. Chem.* **2014**, *6*, 320–324.
- (22) Frei, M. S.; Mondelli, C.; Cesarini, A.; Krumeich, F.; Hauert, R.; Stewart, J. A.; Curulla Ferré, D.; Pérez-Ramírez, J. Role of Zirconia in Indium Oxide-Catalyzed CO₂ Hydrogenation to Methanol. *ACS Catal.* **2020**, *10*, 1133–1145.
- (23) Frei, M. S.; Mondelli, C.; Pérez-Ramírez, J. Development of In₂O₃-Based Catalysts for CO₂-Based Methanol Production. *Chimia (Aarau).* **2020**, *74*, 257–262.
- (24) Frei, M. S.; Capdevila-Cortada, M.; García-Muelas, R.; Mondelli, C.; López, N.; Stewart, J. A.; Curulla Ferré, D.; Pérez-Ramírez, J. Mechanism and Microkinetics of Methanol Synthesis via CO₂ Hydrogenation on Indium Oxide. *J. Catal.* **2018**, *361*, 313–321.
- (25) Frei, M. S.; Mondelli, C.; García-Muelas, R.; Kley, K. S.; Puértolas, B.; López, N.; Safonova, O. V.; Stewart, J. A.; Curulla Ferré, D.; Pérez-Ramírez, J. Atomic-Scale Engineering of Indium Oxide Promotion by Palladium for Methanol Production via CO₂ Hydrogenation. *Nat. Commun.* **2019**, *10*, 1–11.
- (26) Sun, Q.; Ye, J.; Liu, C.; Ge, Q. In₂O₃ as a Promising Catalyst for CO₂ Utilization: A Case Study with Reverse Water Gas Shift over In₂O₃. *Greenh. Gases Sci. Technol.* **2014**, *4*, 140–144.
- (27) Ye, J.; Liu, C.; Ge, Q. DFT Study of CO₂ Adsorption and Hydrogenation on the In₂O₃ Surface. *J. Phys. Chem.*

- C* **2012**, *116*, 7817–7825.
- (28) Ye, J.; Liu, C.; Mei, D.; Ge, Q. Active Oxygen Vacancy Site for Methanol Synthesis from CO₂ Hydrogenation on In₂O₃ (110): A DFT Study. *ACS Catal.* **2013**, *3*, 1296–1306.
- (29) Cao, A.; Wang, Z.; Li, H.; Nørskov, J. K. Relations between Surface Oxygen Vacancies and Activity of Methanol Formation from CO₂ Hydrogenation over In₂O₃ Surfaces. *ACS Catal.* **2021**, *11*, 1780–1786.
- (30) Wang, J.; Zhang, G.; Zhu, J.; Zhang, X.; Ding, F.; Zhang, A.; Guo, X.; Song, C. CO₂ Hydrogenation to Methanol over In₂O₃-Based Catalysts: From Mechanism to Catalyst Development. *ACS Catal.* **2021**, *11*, 1406–1423.
- (31) Posada-Borbón, A.; Grönbeck, H. A First-Principles-Based Microkinetic Study of CO₂ Reduction to CH₃OH over In₂O₃(110). *ACS Catal.* **2021**, *11*, 9996–10006.
- (32) Ye, J.; Liu, C. J.; Mei, D.; Ge, Q. Methanol Synthesis from CO₂ Hydrogenation over a Pd₄/In₂O₃ Model Catalyst: A Combined DFT and Kinetic Study. *J. Catal.* **2014**, *317*, 44–53.
- (33) Ye, J.; Liu, C.; Mei, D.; Ge, Q. Methanol Synthesis from CO₂ Hydrogenation over a Pd₄/In₂O₃ Model Catalyst: A Combined DFT and Kinetic Study. *J. Catal.* **2014**, *317*, 44–53.
- (34) Sun, K.; Rui, N.; Zhang, Z.; Sun, Z.; Ge, Q.; Liu, C. J. A Highly Active Pt/In₂O₃ catalyst for CO₂ hydrogenation to Methanol with Enhanced Stability. *Green Chem.* **2020**, *22*, 5059–5066.
- (35) Sun, K.; Rui, N.; Shen, C.; Liu, C. J. Theoretical Study of Selective Hydrogenation of CO₂ to Methanol over Pt₄/In₂O₃ Model Catalyst. *J. Phys. Chem. C* **2021**, *125*, 10926–10936.
- (36) Han, Z.; Tang, C.; Wang, J.; Li, L.; Li, C. Atomically Dispersed Ptⁿ⁺ Species as Highly Active Sites in Pt/In₂O₃ Catalysts for Methanol Synthesis from CO₂ Hydrogenation. *J. Catal.* **2020**.
- (37) Bavykina, A.; Yarulina, I.; Al Abdulghani, A. J.; Gevers, L.; Hedhili, M. N.; Miao, X.; Galilea, A. R.; Pustovarenko, A.; Dikhtiarenko, A.; Cadiou, A.; Aguilar-Tapia, A.; Hazemann, J.-L.; Kozlov, S. M.; Oud-Chikh, S.; Cavallo, L.; Gascon, J. Turning a Methanation Co Catalyst into an In–Co Methanol Producer. *ACS Catal.* **2019**, *9*, 6910–6918.
- (38) Shi, Z.; Tan, Q.; Tian, C.; Pan, Y.; Sun, X.; Zhang, J.; Wu, D. CO₂ Hydrogenation to Methanol over Cu–In Intermetallic Catalysts: Effect of Reduction Temperature. *J. Catal.* **2019**, *379*, 78–89.
- (39) Jia, X.; Sun, K.; Wang, J.; Shen, C.; Liu, C. jun. Selective Hydrogenation of CO₂ to Methanol over Ni/In₂O₃ Catalyst. *J. Energy Chem.* **2020**, *50*, 409–415.
- (40) Snider, J. L.; Streibel, V.; Hubert, M. A.; Choksi, T. S.; Valle, E.; Upham, D. C.; Schumann, J.; Duyar, M. S.; Gallo, A.; Abild-Pedersen, F.; Jaramillo, T. F. Revealing the Synergy between Oxide and Alloy Phases on the Performance of Bimetallic In–Pd Catalysts for CO₂ Hydrogenation to Methanol. *ACS Catal.* **2019**, *9*, 3399–3412.
- (41) Frei, M. S.; Mondelli, C.; García-Muelas, R.; Morales-Vidal, J.; Philipp, M.; Safonova, O. V.; López, N.; Stewart, J. A.; Ferré, D. C.; Pérez-Ramírez, J. Nanostructure of Nickel-Promoted Indium Oxide Catalysts Drives Selectivity in CO₂ Hydrogenation. *Nat. Commun.* **2021**, *12*, 1–9.
- (42) Shen, C.; Bao, Q.; Xue, W.; Sun, K.; Zhang, Z.; Jia, X.; Mei, D.; Liu, C. jun. Synergistic Effect of the Metal-Support Interaction and Interfacial Oxygen Vacancy for CO₂ Hydrogenation to Methanol over Ni/In₂O₃

- Catalyst: A Theoretical Study. *J. Energy Chem.* **2022**, *65*, 623–629.
- (43) Zhu, J.; Cannizzaro, F.; Liu, L.; Zhang, H.; Kosinov, N.; Filot, I. A. W.; Rabeah, J.; Brückner, A.; Hensen, E. J. M. Ni-In Synergy in CO₂ Hydrogenation to Methanol. *ACS Catal.* **2021**, *11*, 11371–11384.
- (44) Kresse, G.; Joubert, D. From Ultrasoft Pseudopotentials to the Projector Augmented-Wave Method. *Phys. Rev. B* **1999**, *59*, 1758.
- (45) Perdew, J. P.; Burke, K.; Ernzerhof, M. Generalized Gradient Approximation Made Simple. *Phys. Rev. Lett.* **1996**, *77*, 3865.
- (46) Kresse, G.; Hafner, J. Ab Initio Molecular-Dynamics Simulation of the Liquid-Metallamorphous-Semiconductor Transition in Germanium. *Phys. Rev. B* **1994**, *49*, 14251–14269.
- (47) Kresse, G.; Furthmüller, J. Efficiency of Ab-Initio Total Energy Calculations for Metals and Semiconductors Using a Plane-Wave Basis Set. *Comput. Mater. Sci.* **1996**, *6*, 15–50.
- (48) Albani, D.; Capdevila-Cortada, M.; Vilé, G.; Mitchell, S.; Martin, O.; López, N.; Pérez-Ramírez, J. Semihydrogenation of Acetylene on Indium Oxide: Proposed Single-Ensemble Catalysis. *Angew. Chemie Int. Ed.* **2017**, *56*, 10755–10760.
- (49) Chang, M. W.; Zhang, L.; Davids, M.; Filot, I. A. W.; Hensen, E. J. M. Dynamics of Gold Clusters on Ceria during CO Oxidation. *J. Catal.* **2020**, *392*, 39–47.
- (50) Vilhelmsen, L. B.; Hammer, B. A Genetic Algorithm for First Principles Global Structure Optimization of Supported Nano Structures. *J. Chem. Phys.* **2014**, *141*, 044711.
- (51) Henkelman, G.; Jónsson, H. Improved Tangent Estimate in the Nudged Elastic Band Method for Finding Minimum Energy Paths and Saddle Points. *J. Chem. Phys.* **2000**, *113*, 9978–9985.
- (52) Heidrich, D.; Quapp, W. Saddle Points of Index 2 on Potential Energy Surfaces and Their Role in Theoretical Reactivity Investigations. *Theor. Chim. Acta* **1986**, *70*, 89–98.
- (53) Nelson, R.; Ertural, C.; George, J.; Deringer, V. L.; Hautier, G.; Dronskowski, R. LOBSTER: Local Orbital Projections, Atomic Charges, and Chemical-Bonding Analysis from Projector-Augmented-Wave-Based Density-Functional Theory. *J. Comput. Chem.* **2020**, *41*, 1931–1940.
- (54) Maintz, S.; Volker, L.; Deringer, L.; Tchougr, A. L.; Dronskowski, R. ; LOBSTER: A Tool to Extract Chemical Bonding from Plane-Wave Based DFT. *J. Comput. Chem.*; **2016**, *37*, 11–12.
- (55) Yu, M.; Trinkle, D. R. Accurate and Efficient Algorithm for Bader Charge Integration. *J. Chem. Phys.* **2011**, *134*, 064111.
- (56) Brown, P. N.; Byrne, G. D.; Hindmarsh, A. C. VODE: A Variable-Coefficient ODE Solver. *J. Sci. Stat. Comput.*, **1989**, *10*, 5, 1038-1051
- (57) Byrne, G. D.; Hindmarsh, A. C. Stiff ODE Solvers: A Review of Current and Coming Attractions. *J. Comput. Phys.* **1987**, *70*, 1–62.
- (58) Byrne, G. D.; Hindmarsh, A. C. A Polyalgorithm for the Numerical Solution of Ordinary Differential Equations. *ACM Trans. Math. Softw.* **1975**, *1*, 71–96.
- (59) Shomate, C. H. A Method for Evaluating and Correlating Thermodynamic Data. *J. Phys. Chem.* **2002**, *58*, 368–372.

- (60) NIST Chemistry WebBook <https://webbook.nist.gov/chemistry/> (accessed Feb 1, 2022).
- (61) Kozuch, S.; Shaik, S. A Combined Kinetic-Quantum Mechanical Model for Assessment of Catalytic Cycles: Application to Cross-Coupling and Heck Reactions. *J. Am. Chem. Soc.* **2006**, *128*, 3355–3365.
- (62) Kozuch, S.; Shaik, S. Kinetic-Quantum Chemical Model for Catalytic Cycles: The Haber-Bosch Process and the Effect of Reagent Concentration. *J. Phys. Chem. A* **2008**, *112*, 6032–6041.
- (63) Campbell, C. T. The Degree of Rate Control: A Powerful Tool for Catalysis Research. *ACS Catalysis*. American Chemical Society April 7, 2017, pp 2770–2779.
- (64) Filot, A. W. *Introduction to microkinetic modeling*; Technische Universiteit Eindhoven, **2022**. ISBN: 978-90-386-5573-4.
- (65) Stegelmann, C.; Schiødt, N. C.; Campbell, C. T.; Stoltze, P. Microkinetic Modeling of Ethylene Oxidation over Silver. *J. Catal.* **2004**, *221*, 630–649.
- (66) de Amorim, R. V.; Batista, K. E. A.; Nagurniak, G. R.; Orenha, R. P.; Parreira, R. L. T.; Piotrowski, M. J. CO, NO, and SO Adsorption on Ni Nanoclusters: A DFT Investigation. *Dalt. Trans.* **2020**, *49*, 6407–6417.
- (67) Qin, B.; Li, S. First Principles Investigation of Dissociative Adsorption of H₂ during CO₂ Hydrogenation over Cubic and Hexagonal In₂O₃ Catalysts. *Phys. Chem. Chem. Phys.* **2020**, *22*, 3390–3399.
- (68) Li, Y.; Xu, W.; Liu, W.; Han, S.; Cao, P.; Fang, M.; Zhu, D.; Lu, Y. High-Performance Thin-Film Transistors with Aqueous Solution-Processed NiInO Channel Layer. *ACS Appl. Electron. Mater.* **2019**, *1*, 1842–1851.
- (69) Zhu, J.; Cannizzaro, F.; Liu, L.; Zhang, H.; Kosinov, N.; Filot, I. A. W.; Rabeah, J.; Brückner, A.; Hensen, E. J. M. Ni-In Synergy in CO₂ Hydrogenation to Methanol. *ACS Catal.* **2021**, *11*, 11371–11384.
- (70) Ye, J.; Liu, C.; Mei, D.; Ge, Q. Active Oxygen Vacancy Site for Methanol Synthesis from CO₂ Hydrogenation on In₂O₃(110): A DFT Study. *ACS Catal.* **2013**, *3*, 1296–1306.
- (71) Ye, J.; Liu, C.; Ge, Q. DFT Study of CO₂ Adsorption and Hydrogenation on the In₂O₃ Surface. *J. Phys. Chem. C* **2012**, *116*, 7817–7825.
- (72) Frei, M. S.; Capdevila-Cortada, M.; García-Muelas, R.; Mondelli, C.; López, N.; Stewart, J. A.; Curulla Ferré, D.; Pérez-Ramírez, J. Mechanism and Microkinetics of Methanol Synthesis via CO₂ Hydrogenation on Indium Oxide. *J. Catal.* **2018**, *361*, 313–321.
- (73) Sterk, E. B.; Nieuwelink, A. E.; Monai, M.; Louwen, J. N.; Vogt, E. T. C.; Filot, I. A. W.; Weckhuysen, B. M. Structure Sensitivity of CO₂ Conversion over Nickel Metal Nanoparticles Explained by Micro-Kinetics Simulations. *J. Am. Chem. Soc.* **2022**.
- (74) Stegelmann, C.; Andreasen, A.; Campbell, C. T. Degree of Rate Control: How Much the Energies of Intermediates and Transition States Control Rates. *J. Am. Chem. Soc.* **2009**, *131*, 8077–8082.
- (75) Qin, B.; Li, S. First Principles Investigation of Dissociative Adsorption of H₂ during CO₂ Hydrogenation over Cubic and Hexagonal In₂O₃ Catalysts. *Phys. Chem. Chem. Phys.* **2020**, *22*, 3390–3399.

Appendix B

B1: Stability of Ni SA doped in In₂O₃

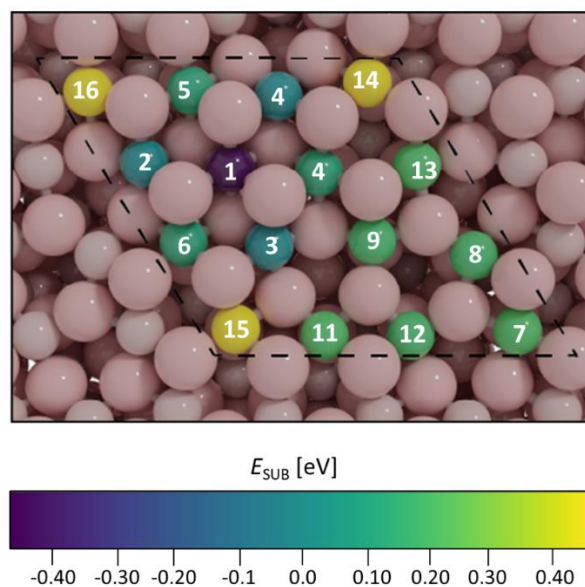


Figure B1. Substitution energy of replacing a surface In atom with a Ni atom. The coloring of atoms at the surface represents the energy associated with their replacement by Ni (E_{sub} , in eV) as can be read in the colorbar. The most stable substitution is indicated by position 1.

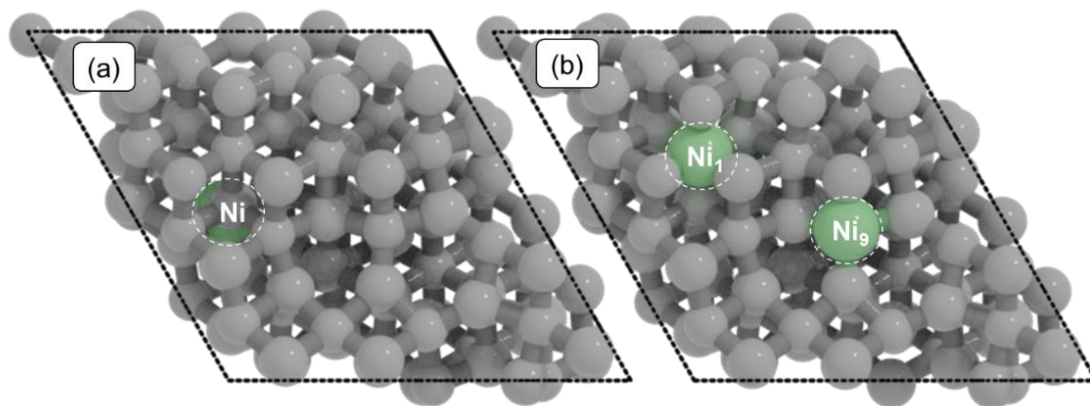
Here we have defined the substitution energy E_{SUB} , as:

$$E_{\text{SUB}} = E_{\text{Ni}/\text{In}_2\text{O}_3(111)} + E_{\text{In,bulk}} - E_{\text{Ni,bulk}} - E_{\text{In}_2\text{O}_3(111)} \quad (\text{B.1})$$

where $E_{\text{Ni}/\text{In}_2\text{O}_3(111)}$ is the energy of each Ni₁-doped In₂O₃(111) surface, $E_{\text{In,bulk}}$, $E_{\text{Ni,bulk}}$ and $E_{\text{In}_2\text{O}_3(111)}$ are the energies of In bulk, Ni bulk and In₂O₃(111) surface models, respectively. A more negative value indicates a stronger atomic binding.

Table B1. Substitution energy of Ni single atoms inside $\text{In}_2\text{O}_3(111)$ As shown in Figure B1.

Doping site	E_{sub} [eV]
Ni-1	-0.34573437
Ni-2	-0.19080619
Ni-3	-0.17845143
Ni-4	-0.15901192
Ni-5	-0.04374681
Ni-6	-0.03785749
Ni-7	0.03865669
Ni-8	0.04338165
Ni-9	0.06744435
Ni-10	0.17168803
Ni-11	0.35099871
Ni-12	0.43707849
Ni-13	0.59568647
Ni-14	0.60240986
Ni-15	0.60681143
Ni-16	0.61352356

**Figure B2.** (a) Ni atom doped in the In_2O_3 bulk, one layer underneath the surface. (b) two Ni atoms doped on different positions labeled as in Figure B1. Ni atoms are highlighted in green, all the other atoms are in grey.

B2: Stability of Ni single atom adsorbed on top of In₂O₃

Table B2. Adsorption energy of adsorbed single atoms on In₂O₃(111).

Adsorption site	E_{ads} [eV]
A1	-5.17
A2	-5.17
A3	-4.96
A4	-4.85
A5	-4.17
A6	-4.20

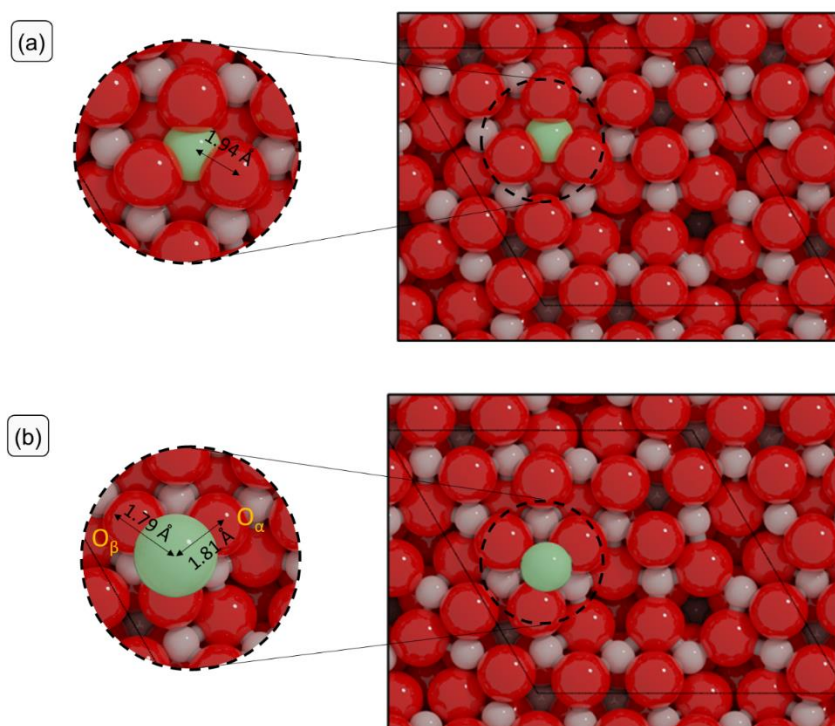


Figure B3. Most stable structures for (a) SA doped and (b) SA adsorbed. The Ni-O distances are depicted on the left.

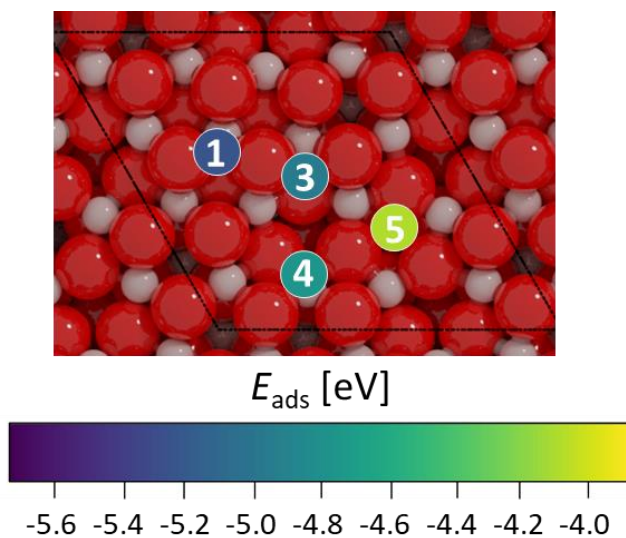


Figure B4. Adsorption sites used to study the migration of Ni single atoms on the $\text{In}_2\text{O}_3(111)$ surface.

Table B3. Migration barriers of adsorbed single atoms on $\text{In}_2\text{O}_3(111)$. The positions are shown in Figure B4.

	E_a [kJ/mol]	E_R [eV]
Pos1 \rightarrow Pos3	95	21
Pos3 \rightarrow Pos4	165	11
Pos4 \rightarrow Pos5	142	65

B3. Analysis of GA-obtained Ni- In_2O_3 clusters

B3.1 Metal support interactions of Ni- In_2O_3 clusters

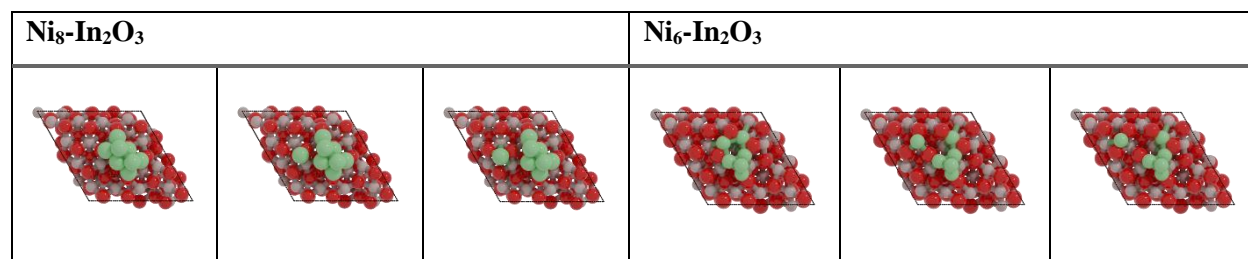
Table B4. Cohesive energies for gas-phase ($E_{\text{COH, free}}$) and supported ($E_{\text{COH, supp}}$) Ni_8 - and Ni_6 - In_2O_3 models.

Model	$E_{\text{COH, free}}$ [kJ/mol/atom]	$E_{\text{COH, supp}}$ [kJ/mol/atom]
Ni_6	249	360
Ni_8	268	358

Table B5. Activation and reaction energies (in kJ/mol) for the removal of a single Ni atom from supported Ni_8 - and Ni_6 - In_2O_3 models.

Model	E_a [kJ/mol]	E_R [kJ/mol]
Ni ₆ /In ₂ O ₃	201	179
Ni ₈ /In ₂ O ₃	232	192

Table B6. Initial, transition and final states the calculations as reported in Table B5.



B3.2 Structure analysis of GA-obtained Ni-In₂O₃ clusters

To assess the probability to find a structure different than the energy minimum one, we performed an analysis based on the Boltzmann probability distribution as given by:

$$\frac{p_i}{p_j} = e^{\frac{\epsilon_j - \epsilon_i}{kT}} \quad (\text{B.2})$$

where p_i is the probability of the system being in state i , ϵ_i is the energy of that state, ϵ_j the energy of the energy minimum structure, and kT is the product of Boltzmann's constant k and temperature T . This function gives the probability that the system will be in a certain state (e.g., a given cluster configuration) as a function of the energy of that state and the temperature. The result of this analysis for In₂O₃-supported Ni₈ and a Ni₆ clusters are given in Figure B5a and Figure B5c, respectively. Herein, we focus on candidate structures having a relative probability of at least 10% with respect to the most stable cluster in the population. As can be seen from Figure B5a, we identified only one Ni₈-cluster structure (cand_2 in Figure B5b) that has a sufficiently large relative probability at 400 K other than the energy minimum one. Similarly, for Ni₆-In₂O₃, only one structure other than the energy minimum one has a probability of at least 10% at 400 K (cand_2 in Figure B5d).

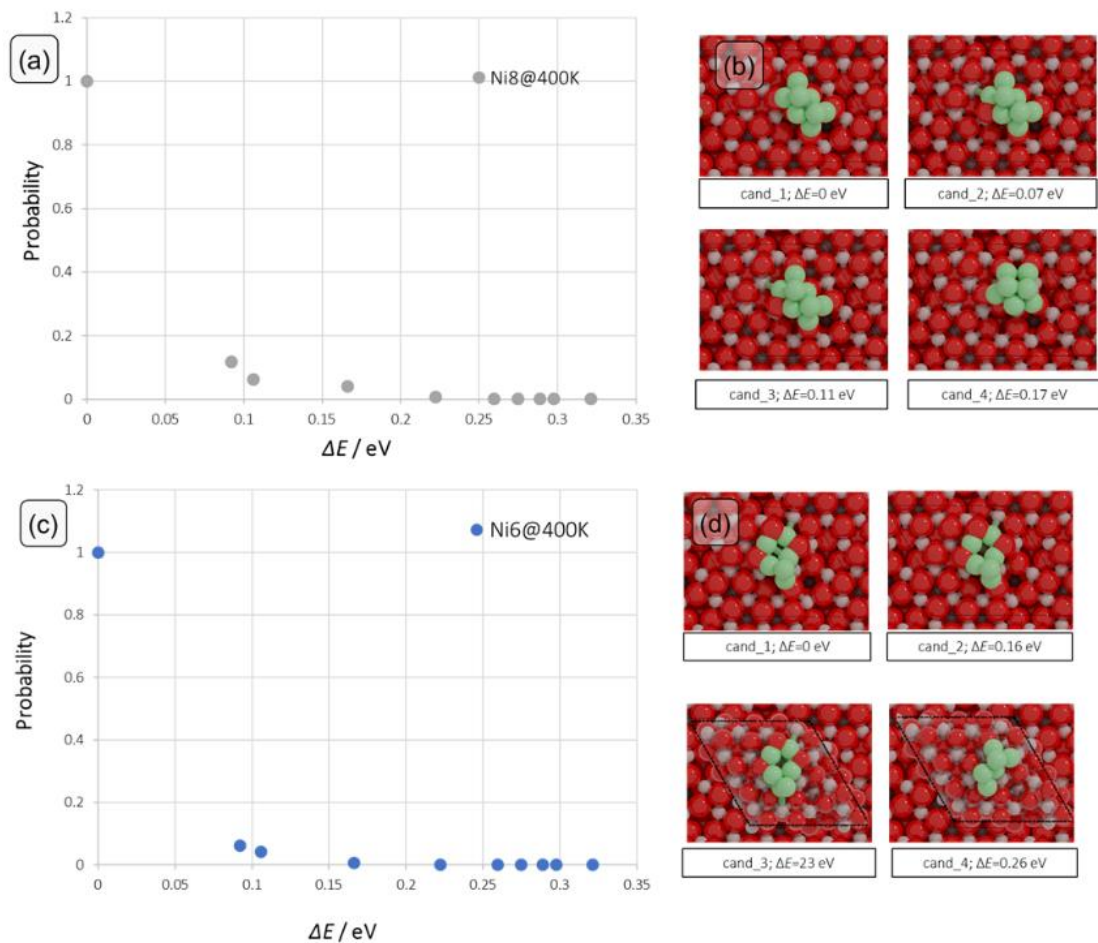


Figure B5. (a), (c) Boltzmann probability distribution of the candidate structures for In₂O₃-supported Ni₈ and Ni₆ clusters, respectively. (b), (d) top-view of the candidate structures with at least 10% probability and their energy relative to the energy minimum for In₂O₃-supported Ni₈ and Ni₆ clusters, respectively.

To perform a similarity analysis of the GA-obtained structures, a distance matrix $\mathbf{A}(i)$ for each cluster was produced wherein each matrix element represents the distance between any two atoms in a single cluster. The similarity between any two clusters in the set can then be expressed as the minimum Hilbert-Schmidt (HS) norm of the difference of their distance matrices, wherein the minimum is established by evaluating all possible permutations over the indices for one of the distance matrices. The minimized HS norm (mHS) for a pair of clusters ($\mathbf{A}(i)$, $\mathbf{A}(j)$) is given by

$$d_{ij} = \min \|\mathbf{H}\mathbf{A}(i)\mathbf{H}^T - \mathbf{A}(j)\|_F \quad (\text{B.3})$$

where $\|\cdot\|_F$ is the Frobenius norm and \mathbf{H} is a permutation over the indices for one of the distance matrices.

Table B7 collects the results of the minimum Hilbert-Schmidt norm of the distance matrix for the structures reported in Figure B5. As can be seen from Table B7, for the Ni₈-cluster, the mHS value between the minimum energy structure and cand_2 amounts to 0.64. Concerning a Ni₆-cluster, a value of 0.18 is found. We can better understand this value by calculating a hypothetical minimized HS norm of an 8-atom cluster with a perturbation of 0.1 Å per atom with respect to an arbitrary cluster configuration. The minimized HS norm (equation B.3) is then given by $\|A\|_{HS} = \sqrt{N^2} * 0.1 = 0.8$. Thus, a value of the HS norm of 0.64 indicates that the coordinates of the atoms in the two clusters differ, on average, less than 0.1 Å. From a careful visual inspection of the cand_1 and cand_2 structures for both Ni₆ and Ni₈ clusters, we infer that these clusters have identical structure, and that CO₂ hydrogenation would likely follow similar reaction pathways.

Table B7. Minimum Hilbert-Schmidt norm of the distance-matrix for the structures reported in Figure B5. Cand_1 corresponds to the energy minimum structure. The first two lines report the results for the Ni₈-In₂O₃ model, while the last two lines report the results for the Ni₆-In₂O₃ model.

Ni ₈	Cand_1	Cand_2	Cand_3	Cand_4
Cand_1	0	0.64	0.80	4.79
Ni₆				
Cand_1	0	0.18	0.91	3.83

B4: Electronic structure analysis of Ni-In₂O₃ model catalyst

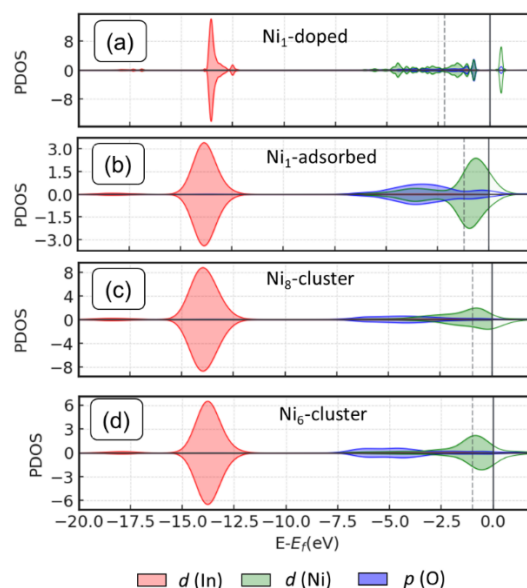


Figure B6. Partial density of states (PDOS) of Ni 3*d*, O 2*p* and In 4*d* orbitals (the O atom adjacent to Ni) in (a) Ni₁-doped, (b) Ni₁-adsorbed and (c) Ni₈- and (d) Ni₆-cluster. The *d*-band center is shown with a dashed grey line. The Fermi level is set at zero.

B5. Bader Charge analysis of the Ni₈/In₂O₃ model

Table B8. Bader charges of stoichiometric and oxygen-defective Ni₈/In₂O₃(111) surfaces.

Cluster	$q[\text{Nix}] / e $
Ni ₈ -cluster stoichiometric	1.07
Ni ₈ -cluster with one Ov	0.67

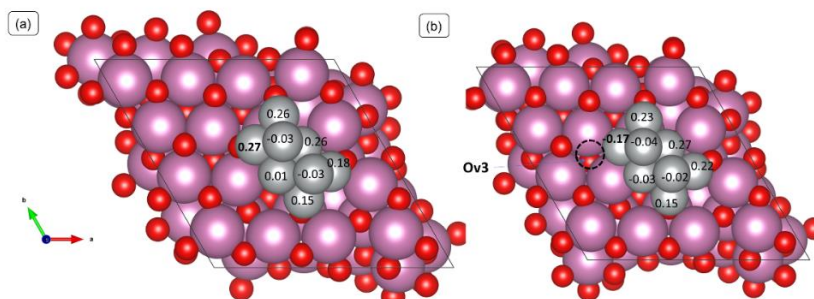


Figure B7. Bader charge analysis of (a) Ni₈-cluster stoichiometric and (b) Ni₈-cluster with one oxygen vacancy (Ov3) indicated by a dashed circle. Upon formation of an oxygen vacancy, the excess charge is redistributed towards the closest Ni atom from the cluster.

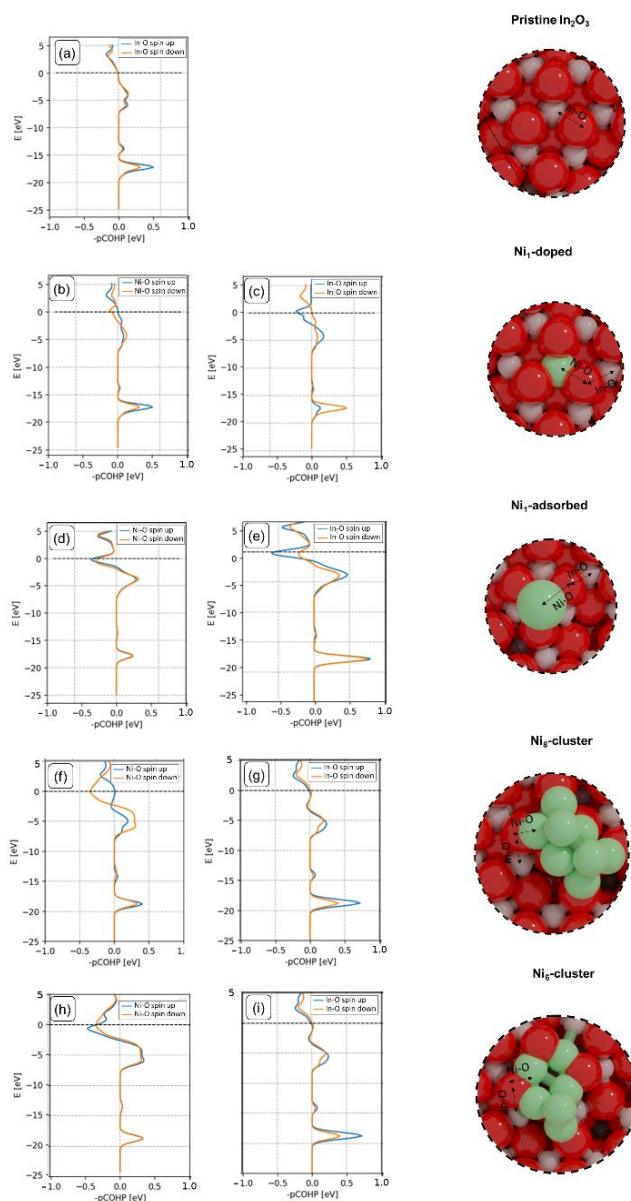
B6: pCOHP analysis of O bonding on Ni- In_2O_3


Figure B8. Projected crystal hamiltonian population (pCOHP) analysis of Ni-O and In-O bonds. (a) In-O interactions for a surface oxygen on bare In_2O_3 . (b-c) Ni-O and In-O interactions for a surface oxygen atom bonding the Ni_1 -doped (b-c) and Ni_1 -adsorbed (d-e), respectively. (f-g) Ni-O and In-O interactions for a surface oxygen atom at the Ni- In_2O_3 interface in the Ni_8 -cluster model. Positive (negative) pCOHP values indicate (anti)bonding interactions. The Fermi level is set at zero. The structures on the right show the interactions taken into account for each model surface.

B7. DFT Tables

Table B9a. Kinetic parameters for CO₂ hydrogenation to CH₃OH, CO and H₂O over Ni₁-doped In₂O₃ model catalyst

	Elementary steps	Q _{TS} /Q _{TS}	Q _{TS} /Q _{FS}	E _f (kJ/mol)	E _b (kJ/mol)
ID	Oxygen vacancy formation pathway				
1	H ₂ (g) + 2 * ⇌ 2H*	2.51	1.79	70	364
2	2OH* ⇌ H ₂ O* + O*	0.19	2.91	164	27
3	H ₂ O* ⇌ H ₂ O(g) + *	-	-	80	-
	Formate pathway				
4	CO ₂ (g) + * ⇌ CO ₂ *	1.0	1.0	103	-
5	CO ₂ * + H ₂ (g) + 2 * ⇌ CO ₂ * + 2H*	2.51	1.79	104	126
6	CO ₂ * + 2H* ⇌ HCO ₂ * + H* + *	0.086	0.47	165	158
7	HCO ₂ * + H* ⇌ H ₂ CO ₂ * + *	0.05	0.93	313	26
8	H ₂ CO ₂ * + H ₂ (g) + 2 * ⇌ H ₂ CO ₂ * + 2H*	2.51	1.79	71	102
9	H ₂ CO ₂ * + 2H* ⇌ H ₂ CO ₂ H* + H*	2.64	1.82	49	7
10	H ₂ CO ₂ H* + H* ⇌ CH ₂ O* + H* + OH*	1.00	1.00	97	237
11	CH ₂ O* + OH* + H* ⇌ CH ₃ O* + O* + H*	3.453	2.16	117	69
12	CH ₃ O* + H* ⇌ CH ₃ OH(g)	0.728	4.30	102	121
13	Ni# ⇌ Ni	1.0	1.0	120	35
	rWGS pathway				
14	CO ₂ * ⇌ CO(g) + O*	-	-	230	-
	Activation energies were directly obtained from DFT calculations.				
	Pre-exponential factors were estimated by transition state theory at T = 550 K.				
	Elementary steps ID correspond to Figure 4.3a				

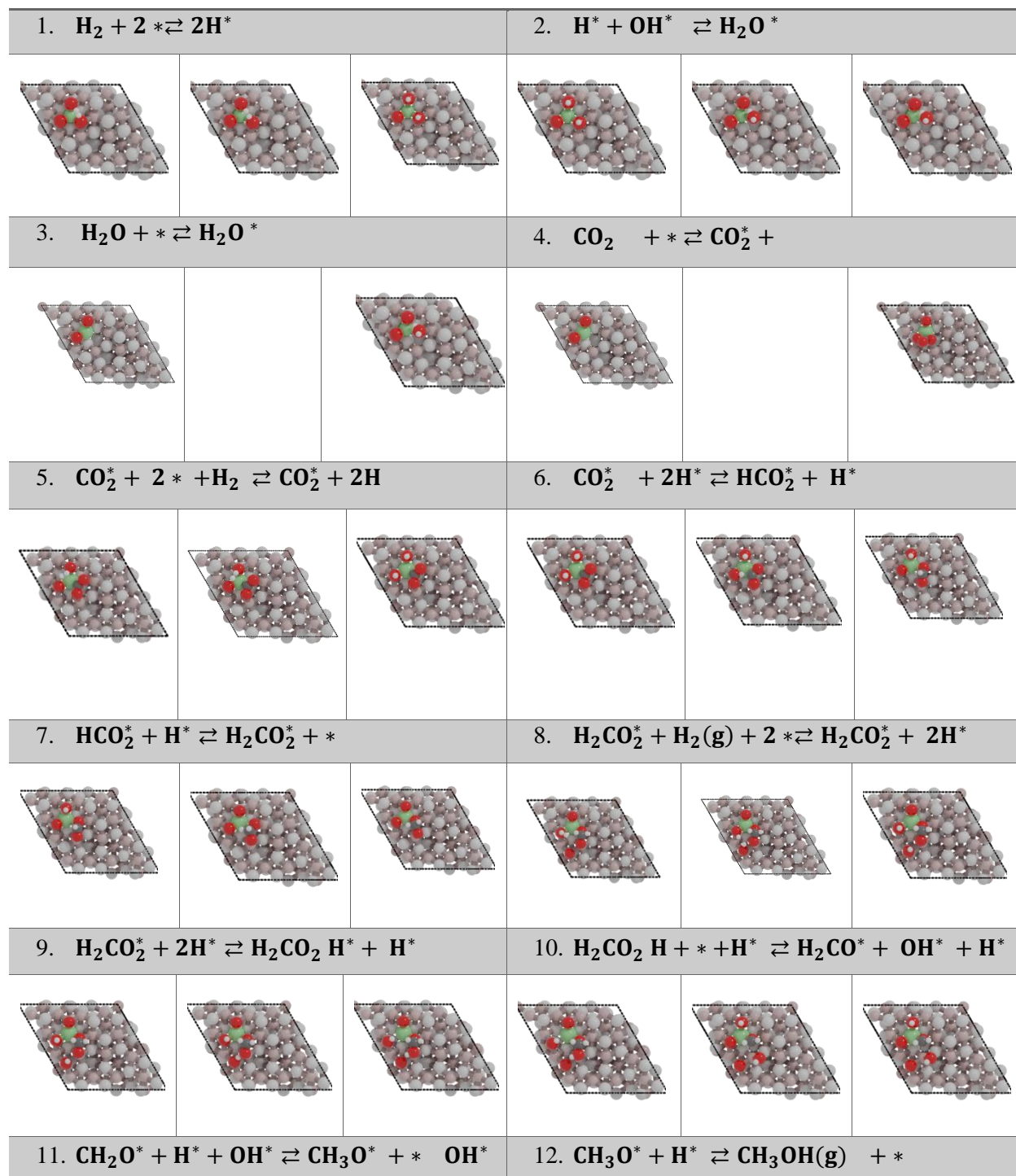
Table B9b. Kinetic parameters for CO₂ hydrogenation to CH₃OH, CO and H₂O over Ni₁-adsorbed In₂O₃ model catalyst.

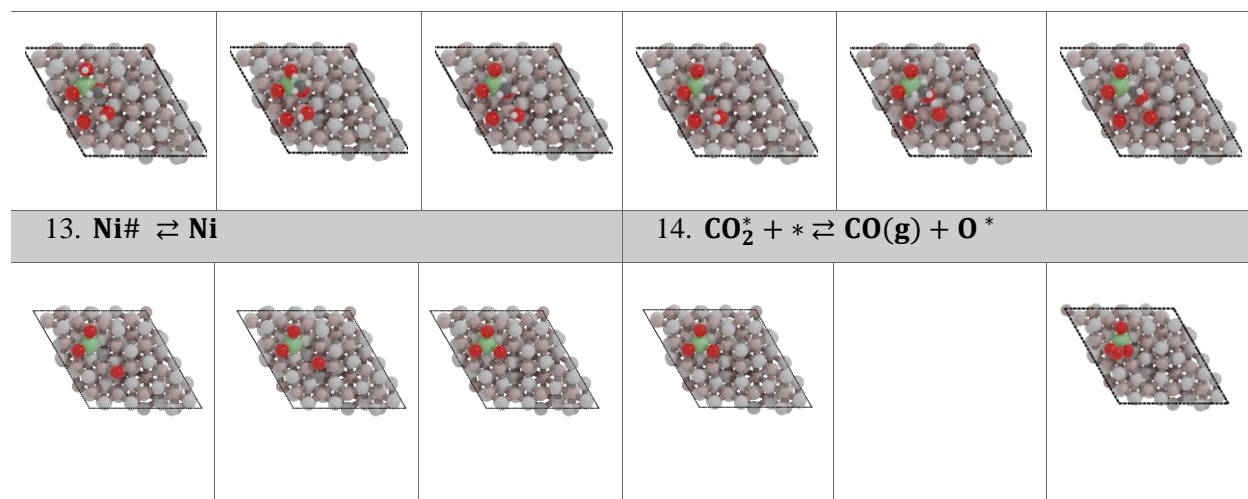
	Elementary steps	Q _{TS} /Q _{IS}	Q _{TS} /Q _{FS}	E _t (kJ/mol)	E _b (kJ/mol)
ID	Oxygen vacancy formation pathway				
1	H ₂ (g) + 2 * ⇌ 2H*	0.20	0.57	19	55
2	H* + OH* ⇌ H ₂ O* + O*	1.70	0.39	93	66
3	H ₂ O* ⇌ H ₂ O(g) + *	-	-	177	-
	Formate pathway				
4	CO ₂ (g) + * ⇌ CO ₂ *	1.0	1.0	144	-
5	CO ₂ * + H ₂ (g) + 2 * ⇌ CO ₂ * + 2H*	0.20	0.57	19	55
6	CO ₂ * + 2H* ⇌ HCO ₂ * + H* + *	5.55	0.59	66	68
7	HCO ₂ * + H* ⇌ H ₂ CO ₂ * + *	0.17	1.44	114	34
8	H ₂ CO ₂ * + * ⇌ CH ₂ O* + O*	1.05	0.28	101	33
9	CH ₂ O* + H ₂ (g) + 2 * ⇌ CH ₂ O* + 2H*	0.20	0.57	19	55
10	CH ₂ O* + 2H* ⇌ CH ₃ O* + H*	0.47	0.54	55	132
11	CH ₃ O* + H* ⇌ CH ₃ OH(g)	0.06	0.61	61	54
	CO hydrogenation pathway				
12	CO* ₂ + * ⇌ CO* + O*	0.52	0.17	81	78
13	CO* + H ₂ (g) + 2 * ⇌ CO* + 2H*	0.20	0.57	19	55
14	CO* + 2H* ⇌ HCO* + H*	0.52	0.17	71	65
15	HCO* + H* ⇌ CH ₂ O* + *	0.20	0.57	177	35
	rWGS pathway				
16	CO* ₂ + 2H* ⇌ COOH* + H* + *	0.31	0.02	82	69
17	COOH* + * ⇌ CO* + OH*	1.13	0.33	42	25
18	CO* + OH* + H* ⇌ CO* + H ₂ O*	1.51	0.96	140	198
19	CO* ⇌ CO(g) + Ov	-	-	51	-
20	CO* ⇌ CO(g) + *	-	-	121	-
	Activation energies were directly obtained from DFT calculations. Pre-exponential factors were estimated by transition state theory at T = 550 K. Elementary steps ID correspond to Figure 4.3b				

Table B9c. Kinetic parameters for CO₂ hydrogenation to CH₃OH, CO and H₂O over Ni₈/In₂O₃ model catalyst.

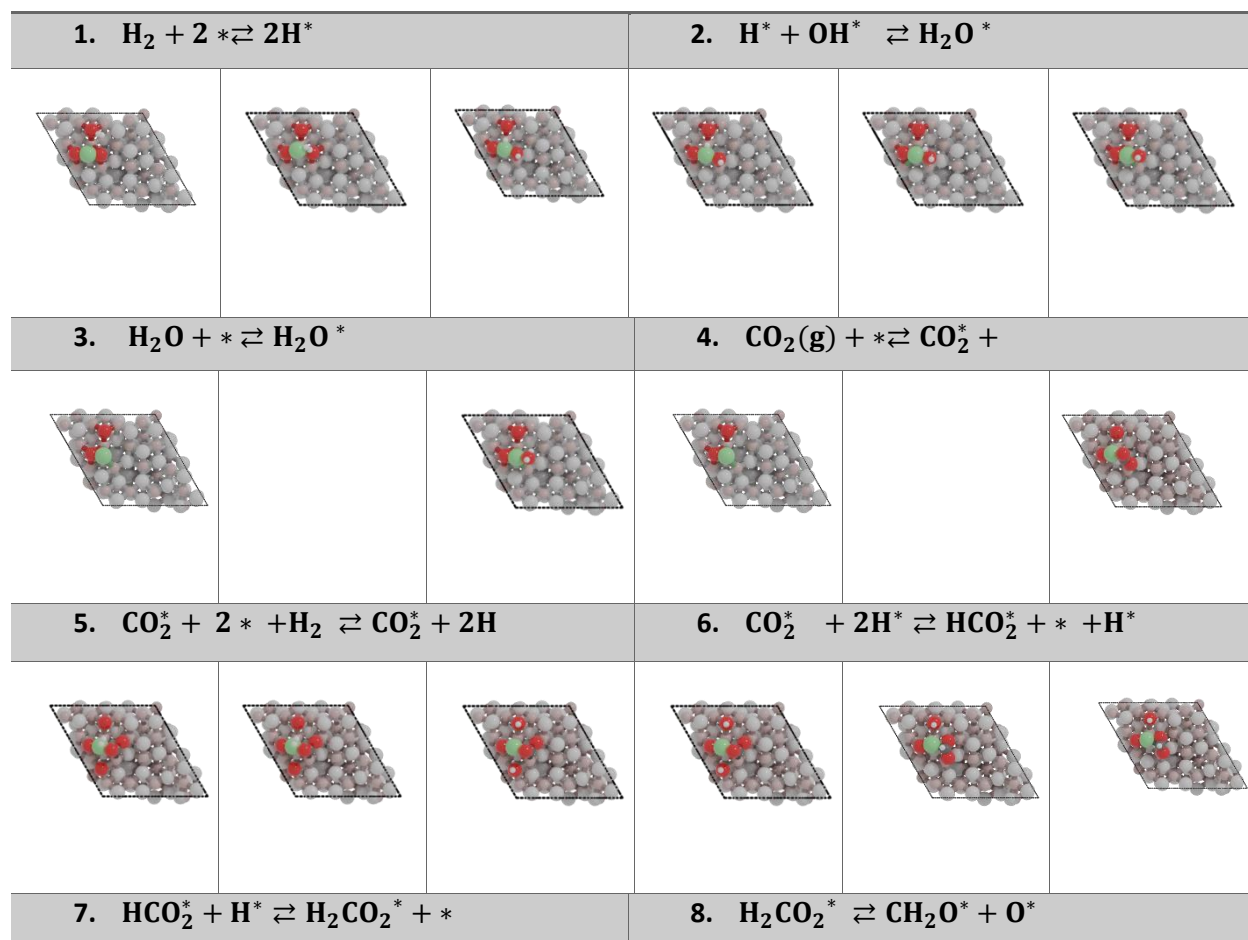
	Elementary steps	Q _{TS} /Q _{IS}	Q _{TS} /Q _{FS}	E _r (kJ/mol)	E _b (kJ/mol)
ID	Oxygen vacancy formation pathway				
1	H ₂ (g) + 2 * ⇌ 2H*	2.51	1.79	0	89
2	2H* + O ⇌ H* + OH*	2.93	0.51	152	146
3	H* + OH* ⇌ H ₂ O* + *	0.13	0.40	140	172
4	H ₂ O* ⇌ H ₂ O(g) + *	-	-	80	-
	Formate pathway				
5	CO _{2(g)} + * ⇌ CO ₂ *	1.0	1.0	144	-
6	CO ₂ * + H ₂ (g) + 2 * ⇌ CO ₂ * + 2H*	2.51	1.79	0	89
7	CO ₂ * + 2H* ⇌ HCO ₂ * + H* + *	1.01	0.9	95	116
8	HCO ₂ * + H* ⇌ H ₂ CO ₂ *	0.56	0.85	177	39
9	H ₂ CO ₂ * + * ⇌ CH ₂ O* + O*	2.64	1.82	52	71
10	CH ₂ O* + H ₂ (g) + 2 * ⇌ CH ₂ O* + 2H*	2.51	1.79	0	89
11	CH ₂ O* + 2H* ⇌ CH ₃ O* + H* + *	1.61	4.78	83	124
12	CH ₃ O* + H* ⇌ CH ₃ OH* + *	0.82	1.31	124	94
13	CH ₃ OH* ⇌ CH ₃ OH(g) + *	-	-	35	-
	CO hydrogenation pathway				
14	CO* ₂ + * ⇌ CO* + O*	1.72	0.75	114	144
15	CO* + H ₂ (g) + 2 * ⇌ CO* + 2H*	2.51	1.79	0	89
16	CO* + 2H* ⇌ HCO* + H**	1.3	1.1	150	119
17	CO* + 2H* ⇌ COH* + H* + *	1.2	0.54	235	120
18	HCO* + H* ⇌ HCOH* + *	0.48	0.90	69	39
19	HCO* + H* ⇌ CH ₂ O* + *	0.48	0.51	165	10
20	COH* + H* ⇌ HCOH* + *	0.48	0.90	211	99
21	HCOH* + H ₂ (g) + 2 * ⇌ HCOH* + 2H*	2.51	1.79	0	89
22	HCOH* + 2H* ⇌ CH ₂ OH* + H*	0.67	3.13	111	61
23	CH ₂ OH* + H* ⇌ CH ₃ OH* + *	1.0	1.0	76	128
	rWGS pathway				
24	CO* ₂ + 2H* ⇌ COOH* + H* + *	0.73	0.89	62	14
25	COOH* + * ⇌ CO* + OH*	7.32	3.55	66	125
26	CO* + OH* + H* ⇌ H ₂ O* + CO**	0.67	0.67	122	172
27	CO* ⇌ CO(g) + O _v	-	-	114	-
28	CO* ⇌ CO(g) + *	-	-	130	-
	Activation energies were directly obtained from DFT calculations. Pre-exponential factors were estimated by transition state theory at T = 550 K. Elementary steps ID correspond to Figure 4.3c				

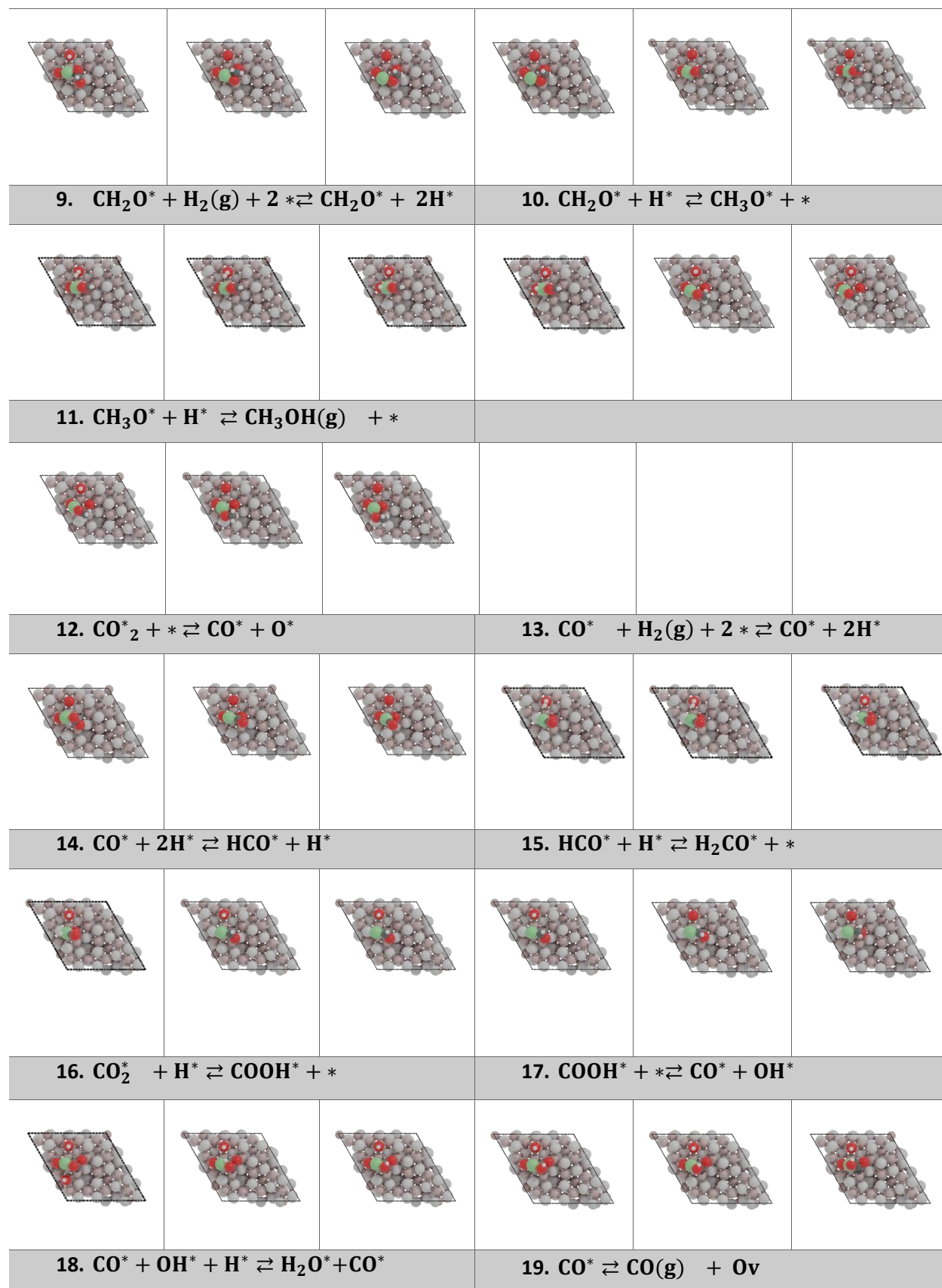
B8. Geometries of elementary reaction steps on Ni₁-doped model

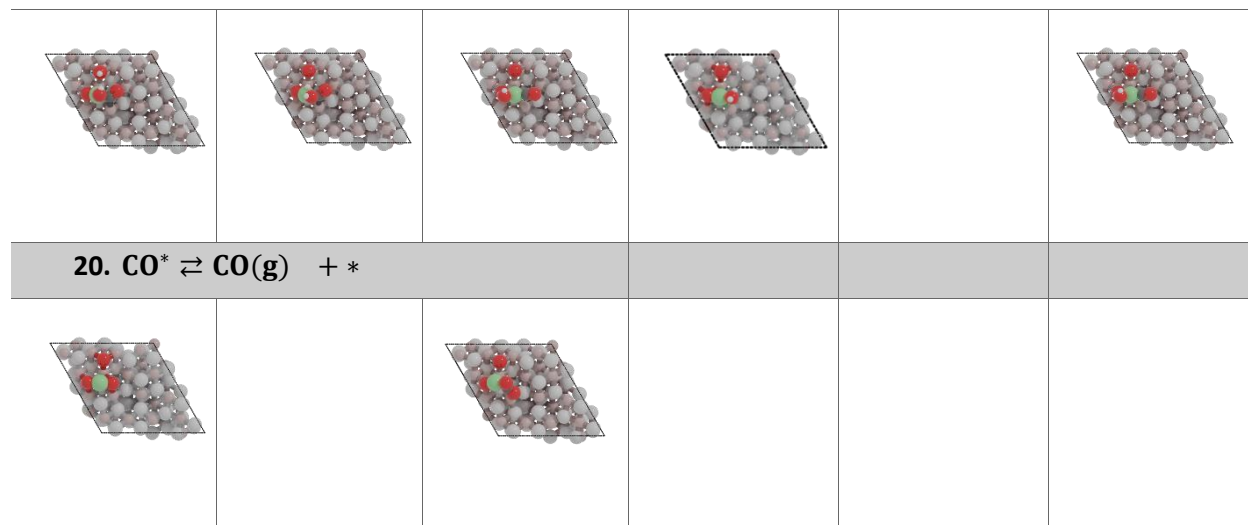




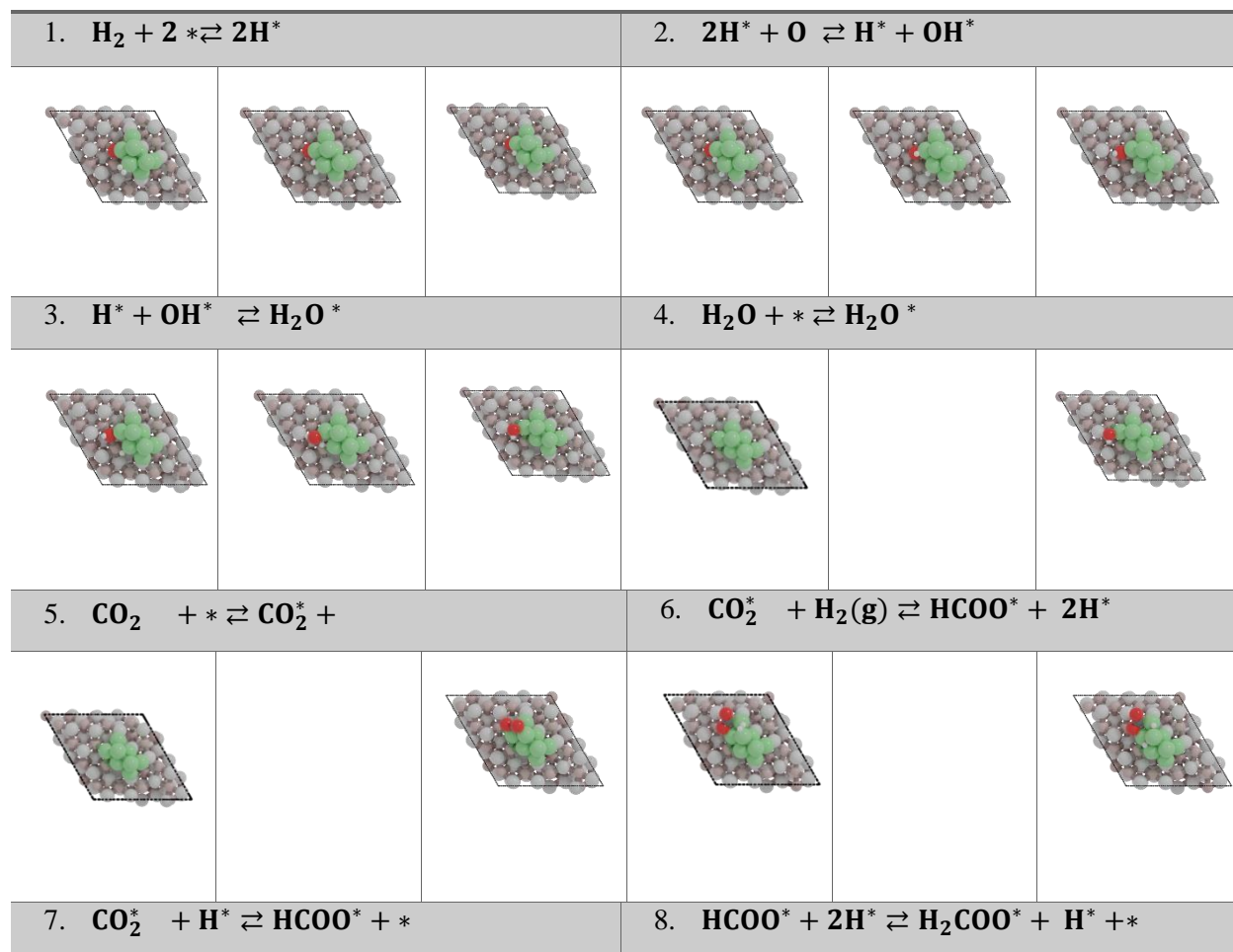
B9. Geometries of elementary reaction steps on Ni₁-adsorbed model

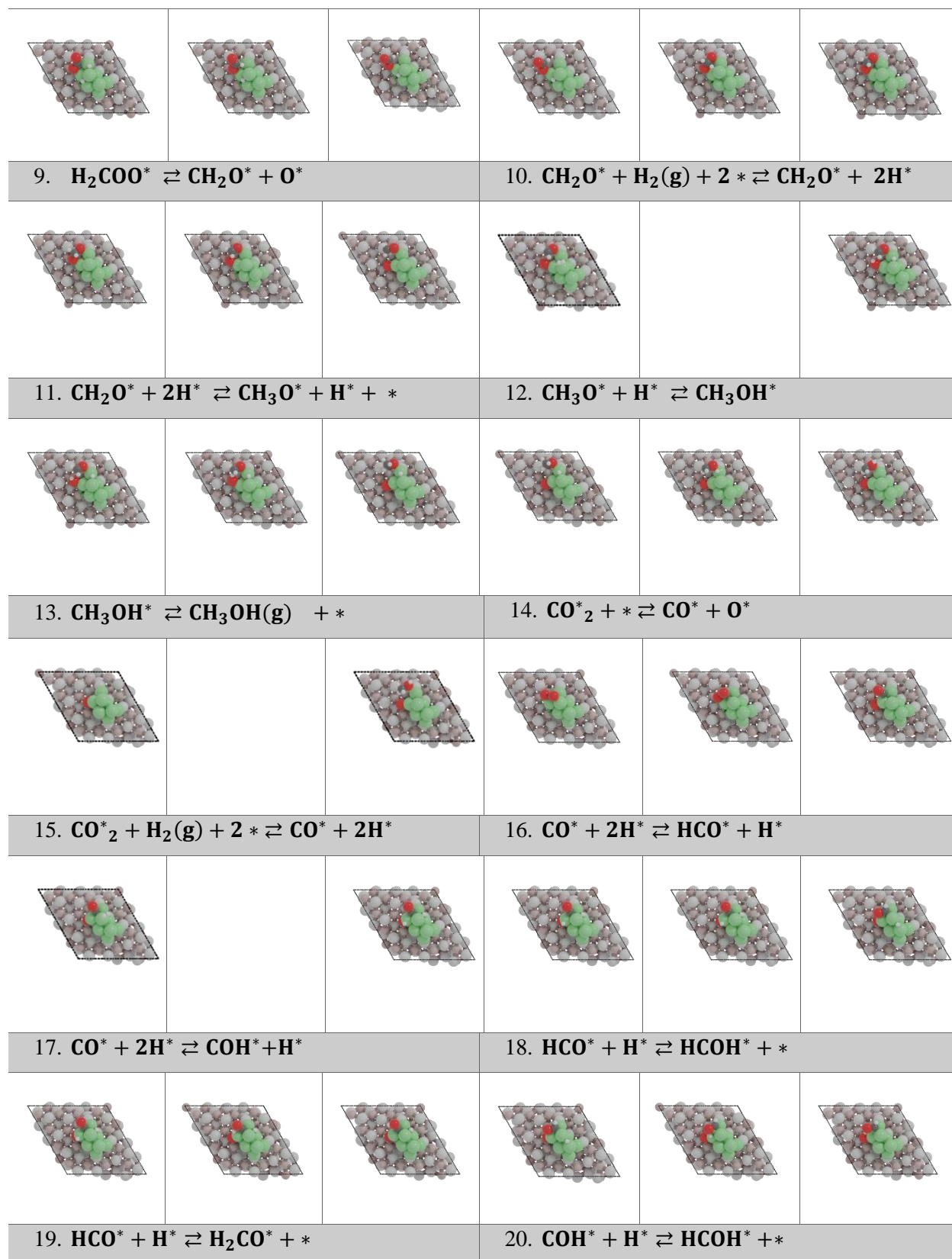






B10. Geometries of elementary reaction steps on Ni₈-cluster model





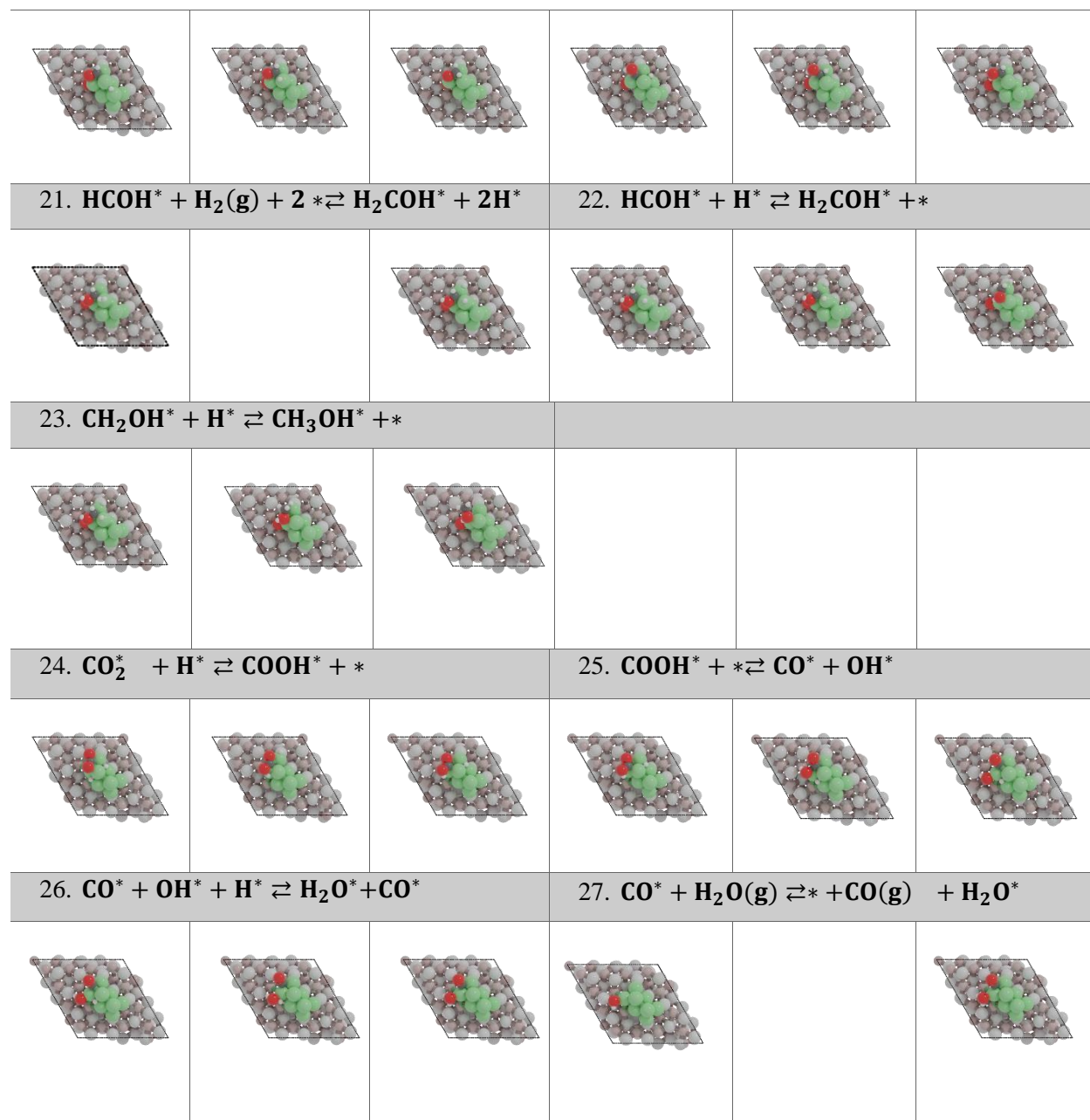
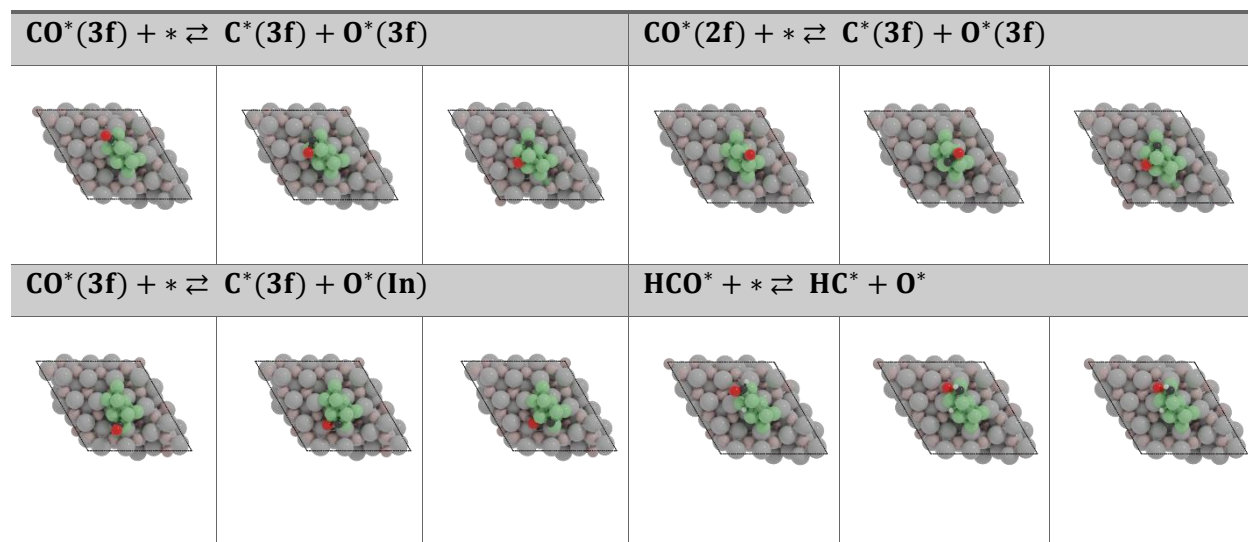


Table B10. Forward and backward activation energies (in kJ/mol) for CO activation elementary steps. A comparison with Sterk et al.¹ is included.

Elementary Reaction Step	E_a	E_b	Ref
$\text{CO}^*(3\text{f}) + * \rightleftharpoons \text{C}^*(3\text{f}) + \text{O}^*(3\text{f})$	312	265	This work
$\text{CO}^*(2\text{f}) + * \rightleftharpoons \text{C}^*(3\text{f}) + \text{O}^*(3\text{f})$	231	135	This work
$\text{CO}^*(3\text{f}) + * \rightleftharpoons \text{C}^*(3\text{f}) + \text{O}^*(\text{In})$	241	75	This work
$\text{COH}^* + * \rightleftharpoons \text{HC}^* + \text{O}^*$	N.A.	N.A.	This work
$\text{HCO}^* + * \rightleftharpoons \text{HC}^* + \text{O}^*$	174	34	This work
$\text{H}_2\text{CO}^* + * \rightleftharpoons \text{H}_2\text{C}^* + \text{O}^*$	N.A.	N.A.	This work
$\text{H}_3\text{CO}^* + * \rightleftharpoons \text{H}_3\text{C}^* + \text{O}^*$	N.A.	N.A.	This work
$\text{CO}^* + * \rightleftharpoons \text{C}^* + \text{O}^*$	150	99	Ni(110) ¹
$\text{COH}^* + * \rightleftharpoons \text{HC}^* + \text{O}^*$	154	32.	Ni(110) ¹
$\text{HCO}^* + * \rightleftharpoons \text{HC}^* + \text{O}^*$	117	31	Ni(110) ¹
$\text{H}_2\text{CO}^* + * \rightleftharpoons \text{H}_2\text{C}^* + \text{O}^*$	82	68	Ni(110) ¹
$\text{H}_3\text{CO}^* + * \rightleftharpoons \text{H}_3\text{C}^* + \text{O}^*$	182	198	Ni(110) ¹

Table B11. Structures of IS, TS and FS for the CO dissociation elementary reaction steps



B11. Further microkinetic simulations

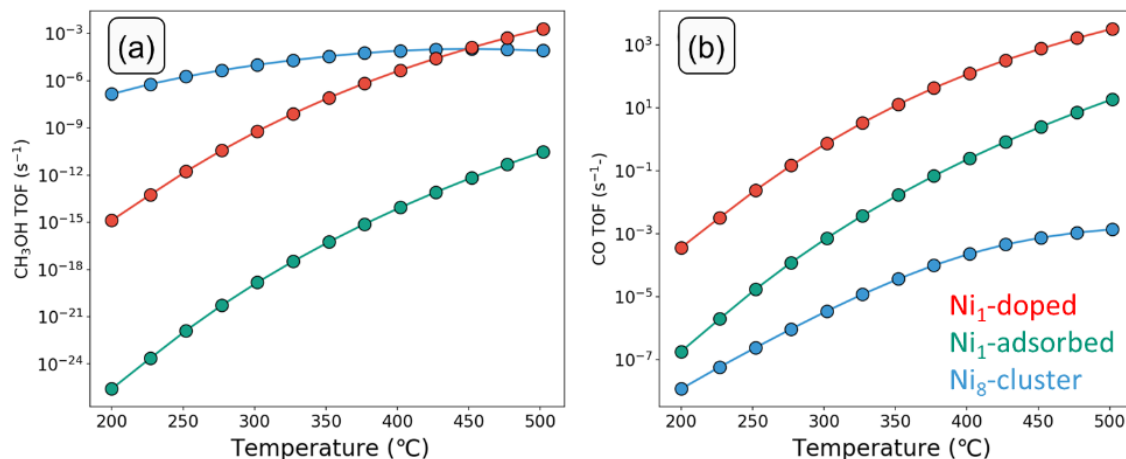


Figure B9. (a) TOF to CH₃OH (s⁻¹) and (b) TOF to CO (s⁻¹) as a function of temperature obtained by the microkinetic model for the three Ni-In₂O₃ model catalysts.

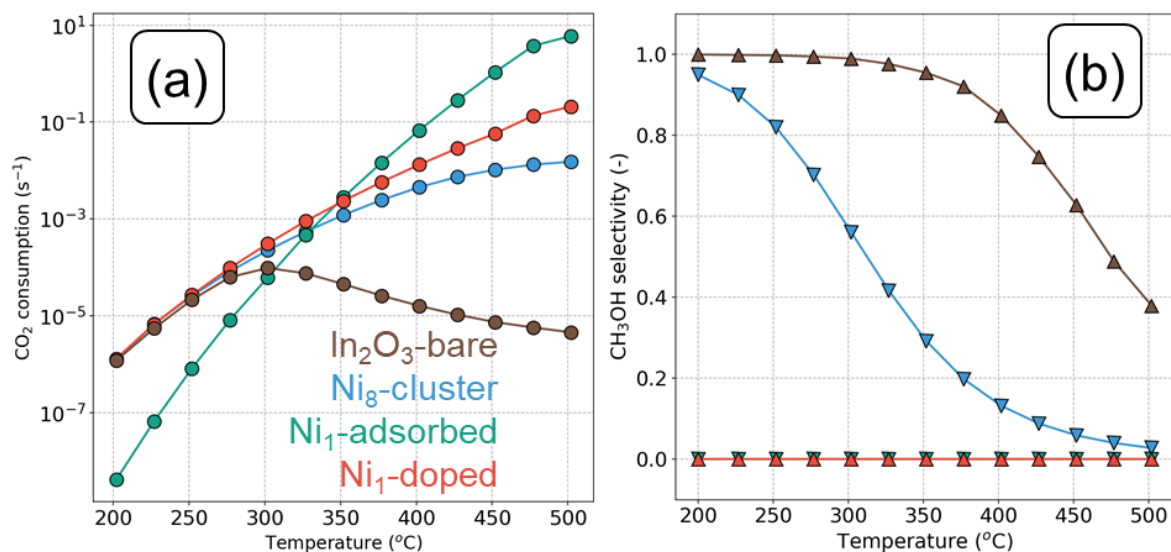


Figure B10. (a) CO₂ consumption rate (s⁻¹) and (b) CH₃OH selectivity as a function of temperature on different models ($p = 50$ bar, H₂/CO₂ ratio =5). The data for In₂O₃-bare are taken from reference [2]

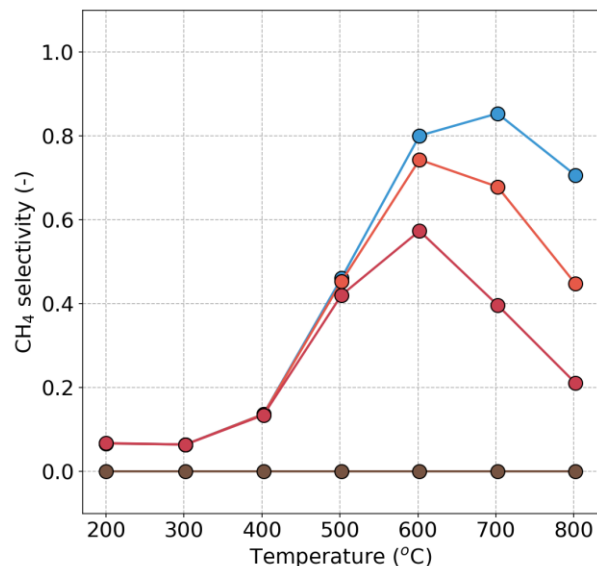


Figure B11. Methane selectivity as a function of the temperature. Blue: $E_{act}(\text{CO diss}) = 30$ kJ/mol; light red: $E_{act}(\text{CO diss}) = 40$ kJ/mol, dark red: $E_{act}(\text{CO diss}) = 50$ kJ/mol, brown: $E_{act}(\text{CO diss}) = 60$ kJ/mol.

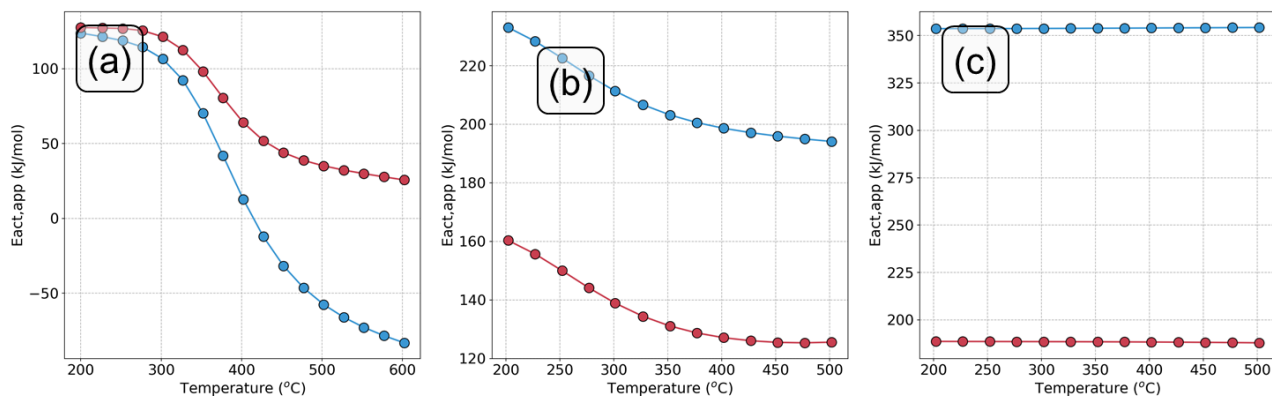


Figure B12. Apparent activation energy with CH₃OH (blue) or CO (red) as key component for (a) Ni₈-cluster, (b) Ni₁-adsorbed and (c) Ni₁-doped.

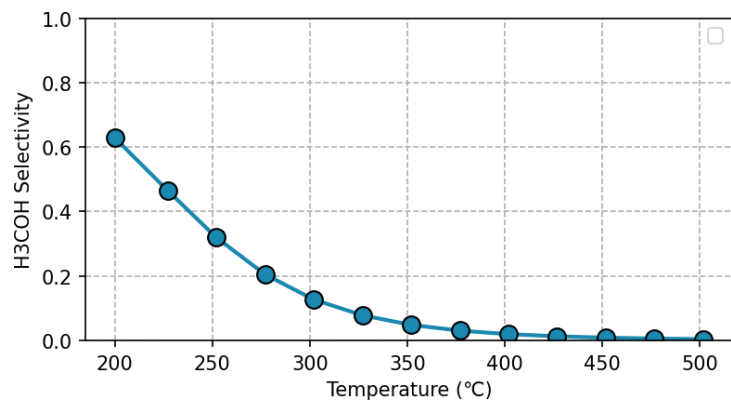
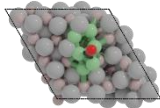
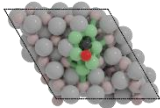
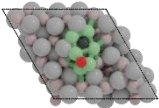
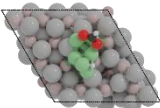
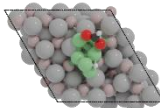
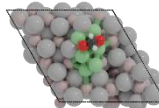
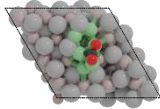
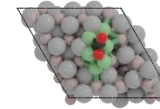
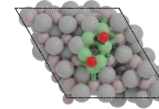


Figure B13. Methanol selectivity at lower H₂ partial pressure (H₂:CO₂ = 1:5).

B12. Comparison with Ni₆-cluster model**Table B12.** Forward and backwards activation energies (in kJ/mol) for key elementary reaction steps on Ni₈- and Ni₆-In₂O₃ models.

Elementary Reaction Step	Ni ₈		Ni ₆	
	E_a	E_b	E_a	E_b
$\text{CO}^* + * \rightleftharpoons \text{C}^* + \text{O}^*$	231	135	270	154
$\text{HCO}_2^* + \text{H}^* \rightleftharpoons \text{H}_2\text{CO}_2^* + *$	177	40	133	76
$\text{CO}_2^* + * \rightleftharpoons \text{CO}^* + \text{O}^*$	114	144	98	121

Table B13. Initial, transition and final states the calculations on Ni₆-In₂O₃ as reported in Table S8.

$\text{CO}^* + * \rightleftharpoons \text{C}^* + \text{O}^*$			$\text{HCO}_2^* + \text{H}^* \rightleftharpoons \text{H}_2\text{CO}_2^* + *$		
					
$\text{CO}_2^* + * \rightleftharpoons \text{CO}^* + \text{O}^*$					
					

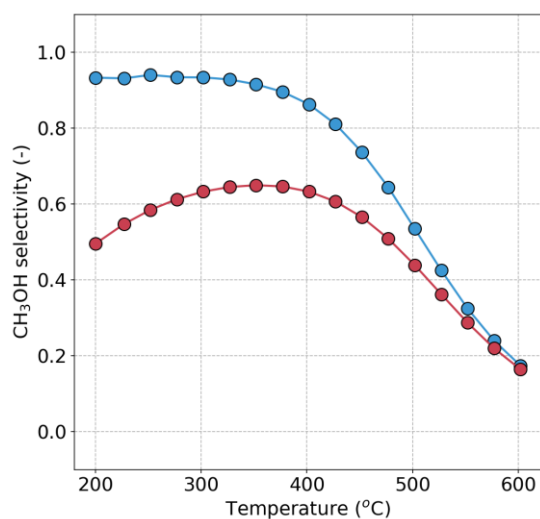


Figure B16. Methanol selectivity for different Ni clusters as a function of temperature. Red: Ni₆-In₂O₃; blue: Ni₈-In₂O₃.

Appendix B References

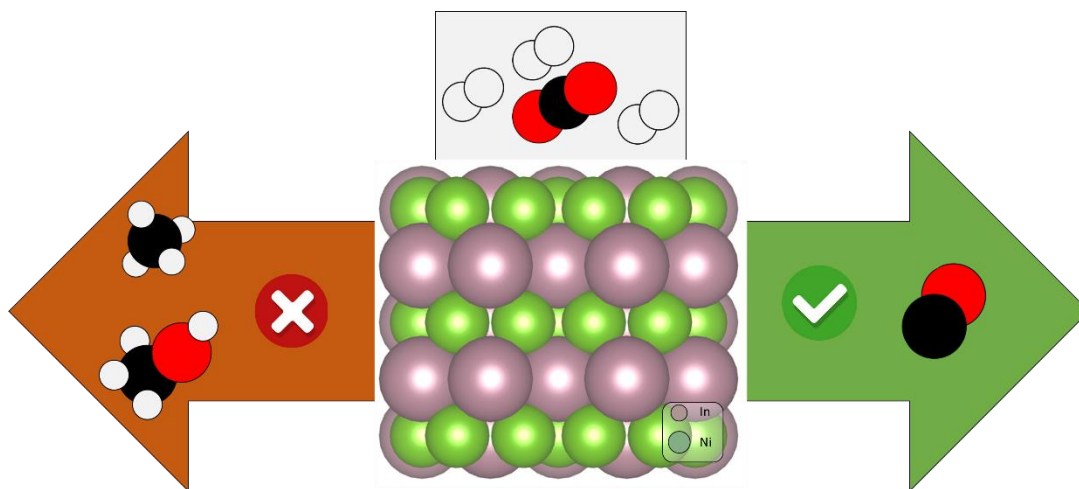
- (1) Sterk, E. B.; Nieuwelink, A. E.; Monai, M.; Louwen, J. N.; Vogt, E. T. C.; Filot, I. A. W.; Weckhuysen, B. M. Structure Sensitivity of CO₂ Conversion over Nickel Metal Nanoparticles Explained by Micro-Kinetics Simulations. *J. Am. Chem. Soc.* **2022**.
- (2) Frei, M. S.; Capdevila-Cortada, M.; García-Muelas, R.; Mondelli, C.; López, N.; Stewart, J. A.; Curulla Ferré, D.; Pérez-Ramírez, J. Mechanism and Microkinetics of Methanol Synthesis via CO₂ Hydrogenation on Indium Oxide. *J. Catal.* **2018**, *361*, 313–321.

CHAPTER 5

Microkinetic modeling of the reverse water-gas shift on Ni-In catalysts

Abstract

The reverse water-gas shift (rWGS) reaction can significantly contribute to renewable energy storage based on CO₂ hydrogenation, because synthesis gas is a platform to the production of a wide range of fuels and chemicals. Ni-In bimetallic catalysts are highly active and CO-selective catalysts. Herein, we investigated the hydrogenation of CO₂ to CO, CH₃OH and CH₄ on a NiIn(100) surface using density functional theory and microkinetic simulations. The NiIn alloy surface converts CO₂ to CO with a high CO selectivity, predominantly involving a redox mechanism where one of the C-O bonds of CO₂ is directly cleaved. The O atom is removed by O hydrogenation followed by OH disproportionation. Formation of methane is suppressed by the high activation energy for C-O bond cleavage. These barriers are high because of the dilution of the Ni surface with less reactive In atoms as verified by additional calculations that the barrier for CO dissociation on a step-edge NiIn(101) surface is also too high. CH₃OH formation is inhibited by the high barriers for the hydrogenation of CO₂ or CO.



5.1 Introduction

Controlling CO₂ emissions is key to fight global warming and its negative impact on the climate.¹⁻³ Capturing CO₂ from combustion processes or directly from air and transforming it into liquid fuels and chemicals allows reducing such emissions. The use of carbon in a circular manner can lead to the replacement of fossil fuels by renewable energy sources. CO₂ conversion to fuels and chemicals can be achieved by thermochemical reduction with hydrogen obtained from renewable resources.⁴⁻⁶ Catalytic hydrogenation of CO₂ can be used to obtain C₁ products via the reverse water-gas shift reaction (rWGS, CO₂+H₂⇌CO+H₂O), methanation (CO₂+4H₂⇌CH₄+2H₂O) and methanol synthesis (CO₂+3H₂⇌CH₃OH+H₂O).^{1,3,7-11} The topic of CO₂ hydrogenation to C₁ products has been reviewed recently.¹¹⁻¹⁵ An alternative approach is to convert CO₂ directly to longer hydrocarbons and aromatics.^{3,16} This can also be done in an indirect manner via synthesis gas (CO + H₂), which is a common feedstock for the already commercial methanol and Fischer-Tropsch processes. Given that several processes based on synthesis gas are practiced at a large scale, it is clear that rWGS to convert CO₂ to CO will grow in importance.

The rWGS reaction is an equilibrium-limited endothermic reaction ($\Delta H_R = +41.17$ kJ/mol). Therefore, high temperatures in the range of 400–800 °C are typically required to achieve a high CO₂ conversion and CO selectivity. Practical implementation of the rWGS reaction requires the development of active and selective catalysts. Precious metal-based catalysts such as Rh,⁹ Au,¹⁷ Pd,^{18,19} and Pt²⁰ are known to be active catalysts for the rWGS reaction. However, methane may be easily produced on some of these metals due to their ability to dissociate the C-O bond in the desired CO product as well.²¹⁻²³ Bimetallic alloys based on these metals have also been investigated.²⁴⁻²⁶ For instance, alloying Co with Pt increases the CO selectivity during CO₂ hydrogenation from 82% (Co-only) to 100% (PtCo) at the expenses of the methane selectivity.²⁴ Bimetallic PdIn on SiO₂ shows lower activity but higher selective to CO compared to a Pd/SiO₂ catalyst.²⁷ A density functional theory (DFT) study revealed that a PdIn alloy is less active for H₂ dissociation than Pd. This together with the weaker adsorption of CO on PdIn alloy compared to Pd resulted in a lower hydrogenation rate of CO to CH₄ on PdIn. Given the scarcity of precious group metals, it would be advantageous to replace them with more Earth-abundant transition metals.²⁸ As Cu is widely used in low-temperature WGS reactors, supported Cu catalysts have also been explored as rWGS catalysts. A major problem is the rapid sintering of the active Cu phase under the harsh conditions of the rWGS reaction (high temperature, high water partial pressure).²⁹ Alloying Cu with Fe can increase the CO selectivity and the CO₂ conversion.^{30,31} Bimetallic CuIn on ZrO₂ exhibited significantly higher CO₂ conversion than a Cu/ZrO₂ catalyst.³² DFT calculations suggested that oxygen removal is improved in Fe-Co mixed oxides compared to a Co(001) surface.³³ Another example is the alloying of Mo with Fe, resulting in a higher activity than the Fe-only catalyst.^{26,30} Although Ni is active in the rWGS reaction, its high activity in the hydrogenation

of CO₂ to methane makes pure Ni catalysts a less obvious choice.³⁵ As such, promoting Ni with other metals has been explored to decrease CH₄ formation. For instance, combining Ni with In can result in a higher selectivity to CO and CH₃OH.³⁶⁻³⁷ A InNi₃C_{0.5} catalyst was found to enhance CO₂ dissociation on Ni-C sites, leading to high CO selectivity by suppressing methanation pathways.³⁸ A computational study reported that bilayer structures with the InNi₃ composition placed on the In₂O₃(111) surface can increase methanol reaction rates by providing hydride species, whereas extended surfaces of InNi₃ and Ni favor CO and CH₄ formation, respectively.³⁹ In a recent experimental study of CO₂ hydrogenation on silica-supported Ni catalyst, we found that a 50:50 Ni-In alloy gave the best result in terms of high activity and negligible methane selectivity. However, understanding of the active phase and reaction mechanism of CO₂ hydrogenation on NiIn catalysts is still lacking.

In the present study, we employ DFT calculations in combination with microkinetic modeling to investigate the mechanism of CO₂ hydrogenation to CO, CH₃OH and CH₄ on a NiIn(100) surface model. We calculated the energetics of the elementary reaction steps for CO₂ conversion with H₂. Based on the reaction energetics, we construct microkinetic models to predict the CO₂ consumption rate and the product distribution as a function of temperature. We perform a sensitivity analysis of the kinetic network to identify the elementary steps that control the rate of CO₂ consumption and product selectivity. The key finding is that the reaction involves a direct redox mechanism where one of the C-O bonds in CO₂ is cleaved, followed by O hydrogenation to H₂O. The formation of CH₄ is suppressed by the high activation energy for CO dissociation on NiIn surfaces. CH₃OH is not formed on such surfaces due to the high barriers associated with hydrogenation of either CO₂ or CO.

5.2 Computational Methods

5.2.1 Density Functional Theory Calculations

All DFT calculations were conducted using the projector augmented wave (PAW) method⁴⁰ and the Perdew–Burke–Ernzerhof (PBE)⁴¹ exchange-correlation functional as implemented in the Vienna Ab Initio Simulation Package (VASP) code.^{42,43} Solutions to the Kohn-Sham equations were calculated using a plane-wave basis set with a cut-off energy of 450 and 400 eV for the NiIn bulk and NiIn surfaces, respectively. All calculations were spin-polarized. The Brillouin zone was sampled using a 9x9x9 and a 7x7x1 Monkhorst-Pack grid for the NiIn bulk and NiIn surfaces, respectively. An energy cut-off of 400 eV and convergence criteria of the force on each relaxed atom below 0.05 eV Å⁻¹ were found to give converged results in the current work. Van der Waals interactions were accounted for by the semiempirical DFT-D3 method.⁴⁴ The electronic energies of gas-phase H₂, H₂O, CO, CO₂ and CH₃OH were calculated using a cubic unit cell with lattice vector of 8 Å. The Brillouin zone was sampled using a 1x1x1 Monkhorst-Pack grid (G-point only). Gaussian smearing was employed. Electronic energies were corrected for zero-point

energies of adsorbates and gas-phase molecules and finite-temperature contributions of the translational and rotational energies of gas-phase molecules.

NiIn has a hexagonal P6/mmm crystal structure. The bulk lattice constant of NiIn was optimized, yielding a value of 5.72 Å.⁴⁵ The InNi(100) surface was modelled as a 4-layer and 2×2 slab with periodic boundary conditions. A 15 Å vacuum region was introduced in the *c*-direction to avoid the spurious interaction of neighbouring super cells. It was verified that the electron density approached zero at the edges of the periodic super cell in the *c*-direction.

The stable states of the elementary reaction steps pertaining to CO₂ hydrogenation were calculated using the conjugate-gradient algorithm. Adsorption energies of adsorbates (ΔE_X^{ads}) are defined as:

$$\Delta E_X^{\text{ads}} = E_{X+\text{slab}} - E_{\text{slab}} - E_X . \quad (5.1)$$

where $E_{X+\text{slab}}$ is the electronic energy of the catalyst plus adsorbate system, E_{slab} is the reference energy of the NiIn slab and E_X is the DFT-calculated energy of the adsorbate in the gas phase. Herein, we include the electronic energy and the zero-point energy correction.

The stable states in the chemo-kinetic network were calculated using the conjugate-gradient algorithm. Transition states were determined using the climbing-image nudged elastic band (CI-NEB) method.⁴⁶ A frequency analysis was performed to all states. Specifically, it was verified that stable states have no imaginary frequencies and transition states have a single imaginary frequency in the direction of the reaction coordinate.⁴⁷ The Hessian matrix in this frequency analysis was constructed using a finite difference approach with a step size of 0.015 Å for displacement of individual atoms along each Cartesian coordinate. The corresponding normal mode vibrations were also used to calculate the zero-point energy (ZPE) correction and the vibrational partition functions.

Partial Density of State (pDOS) and projected Crystal Orbital Hamiltonian Population (pCOHP) analysis are conducted to analyze the electronic structure of each Ni and NiIn surface using the Lobster package.^{48,49} The atomic charges of Ni atoms were calculated using the Bader charge method.⁵⁰

5.2.2 Microkinetic simulations

Microkinetic simulations were conducted based on the DFT-calculated activation energies and reaction energies to investigate the kinetics of CO₂ hydrogenation to methanol. The chemo-kinetic network was modelled using a set of ordinary differential equations involving rate constants, surface coverages and partial pressures of gas-phase species. Time-integration of the differential equations was conducted using the linear multistep backwards differential formula method with a relative and absolute tolerance of 10⁻⁸.⁵¹⁻
53

For the adsorption processes, the net rate of a gas-phase species i was calculated as:

$$r_i = k_{i,ads}\theta^*p_i - k_{i,des}\theta_i \quad (5.2)$$

where θ^* and θ_i are the fraction of free sites and the fraction of coverage species i , respectively. $k_{i,ads/des}$ is the rate constant for the adsorption/desorption process and p_i is the partial pressure of species i .

To derive a rate for the adsorption processes, we assumed that the adsorbate loses one translational degree of freedom in the transition state with respect to the initial state. From this assumption, the rate of adsorption derived from transition state theory can be expressed as follows:

$$k_{i,ads} = \frac{p A_{st}}{\sqrt{2\pi m_i k_B T}}, \quad (5.3)$$

where A_{st} and m_i are the effective area of an adsorption site and the molar mass of the gas species, respectively. p and T are the total pressure and temperature, respectively, and k_B is the Boltzmann constant. The gas-phase entropy of the adsorbates was calculated using the thermochemical Shomate equation as given by

$$S^0 = A \cdot \ln(T) + B \cdot T + \frac{C \cdot T^2}{2} + \frac{D \cdot T^3}{3} - \frac{E}{2 \cdot T^2} + G, \quad (5.4)$$

where S^0 is the standard molar entropy.⁵⁴ The parameters A-G from equation (5.4) were obtained from the NIST Chemistry Webbook.⁵⁵ ³² For the corresponding desorption processes, we assumed that the species gains two translational degrees of freedom and three rotational degrees of freedom in the transition state with respect to the initial state. From this assumption, the rate of desorption derived from transition state theory can be expressed as follows:

$$k_{des} = \frac{k_B \cdot T^3}{h^3} \cdot \frac{A_{st}(2\pi m k_B)}{\sigma \theta_{rot}} \cdot e^{-\frac{\Delta E_{des}}{k_B T}} \quad (5.5)$$

Herein, k_{des} is the rate constant for the desorption of the adsorbate, h is the Planck constant, σ is the symmetry number and corresponds to the number of rotational operations in the point group of each molecule. θ_{rot} the rotational temperature, and ΔE_{ads} the desorption energy. A_{st} is equal to $1 \cdot 10^{-19} \text{ m}^2$.

Finally, the rate constant (k) of an elementary reaction step is given by

$$k = \frac{k_{\text{B}}T}{h} \frac{Q^\ddagger}{Q} e^{\left(\frac{-\Delta E_{\text{act}}}{k_{\text{B}}T}\right)}, \quad (5.6)$$

where Q^\ddagger and Q are the partition functions of the activated complex and its corresponding initial state, respectively, and ΔE_{act} is the ZPE-corrected activation energy.

To identify the steps that control the CO_2 consumption rate and the product distribution, we employed the concepts of the degree of rate control (DRC) developed by Kozuch and Shaik^{56,57} and popularized by Campbell.^{58,59}

Herein, the degree of rate control coefficient is defined as

$$X_{\text{RC},i} = \left(\frac{\partial \ln r_i}{\partial \ln k_i} \right)_{k_{j \neq i}, K_i} \quad (5.7)$$

A positive DRC value for a particular elementary reaction step indicates that this step limits the reaction rate. A decrease in the activation energy for the transition state of this elementary reaction step would increase the overall rate. Negative DRC values point to rate-inhibiting elementary reaction steps. Lowering the barrier of such a reaction step decreases the overall reaction rate. Under zero extent of reaction, the sum of the DRC coefficients is conserved at one.⁴⁵ When a single elementary reaction step has a DRC coefficient of 1, this step is identified as the rate-determining step.

5.3 Results and discussion

5.3.1 Bulk and surface NiIn models

To select representative surface models of NiIn catalysts, we calculated the surface free energy of several surface terminations obtained from a NiIn bulk model. NiIn crystallizes in the bulk forming a hexagonal structure belonging to the P6/mmm space group (Figure C1). Ni is bonded to 10 other metal atoms, i.e., 4 equivalent Ni and 6 In atoms. All Ni–Ni bond lengths are 2.61 Å. There are two shorter (2.61 Å) and 4 longer (2.64 Å) Ni–In bond lengths. There are two different In sites in this structure. One type of In is 6-fold coordinated to exclusively Ni atoms, while the second type is bonded in a hexagonal planar geometry to 6 Ni atoms.

Based on an optimized bulk structure of NiIn, we computed the surface free energies for the low-index surface terminations, i.e. (101), (100), (110), (111), (211) and (321) of NiIn (Table C1). The resulting surface free energies of these NiIn surface terminations are listed in Table C1. Based on these results, we chose the NiIn(100) and as model for a flat surface (Figure 5.1). This surface exposes the same number of Ni and In atoms. As can be seen from Figure 1, the NiIn(100) facet contains a threefold fcc site composed of two Ni atoms and one In atom (fcc_Ni₂In) and three different bridge sites (b_Ni₂, b_In₂ and b_NiIn). For completeness, we mention that the step-edge NiIn(101) surface also exposes the same number of Ni and In atoms. In contrast, other surfaces such as (100), (111), (211) and (321) can expose Ni and In atoms in different ratios (Table C1).

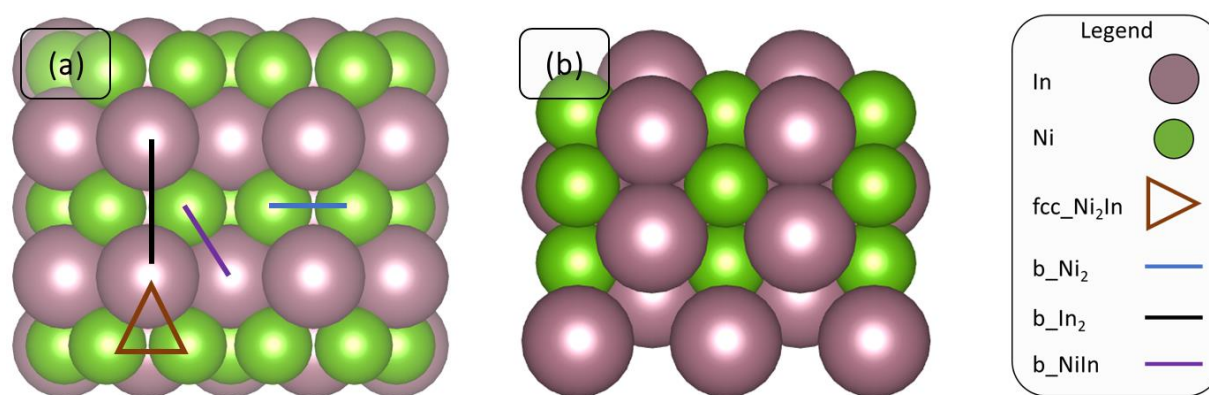


Figure 5.1. Schematic representation of the NiIn(100). (a) top view and (b) side view. Adsorption sites include threefold-fcc (fcc_Ni₂In) and bridge sites (b_Ni₂, b_In₂ and b_NiIn).

5.3.2 Reaction mechanism

We then used DFT to calculate the energetics of the elementary reaction steps in the hydrogenation of CO₂ hydrogenation to methanol, methane, carbon monoxide and water for the NiIn(100) surface. The reaction network explored in this study is depicted in Figure 5.2. Based on previous computational studies,^{38,60,61} we investigated two different pathways for the reverse water-gas shift (rWGS) reaction leading to CO. CO formation can take place either via direct cleavage of one of the C-O bonds in CO₂ (redox pathway) or via a H-assisted pathway involving the COOH intermediate (carboxyl pathway). The removal of oxygen as H₂O is also taken into account. Furthermore, several pathways for the hydrogenation of CO₂ to CH₃OH via H₂CO₂, H₂COH, COHOH or CO intermediates were considered. Finally, we investigated the formation of CH₄ via CO₂ hydrogenation via formates and CO hydrogenation.

We will discuss the elementary reaction steps of this network. The activation energies are given with respect to the most stable adsorbed state for each intermediate. A full list is provided in Table C2. The geometries corresponding to initial, transition and final states are reported in section C3 in Appendix C.

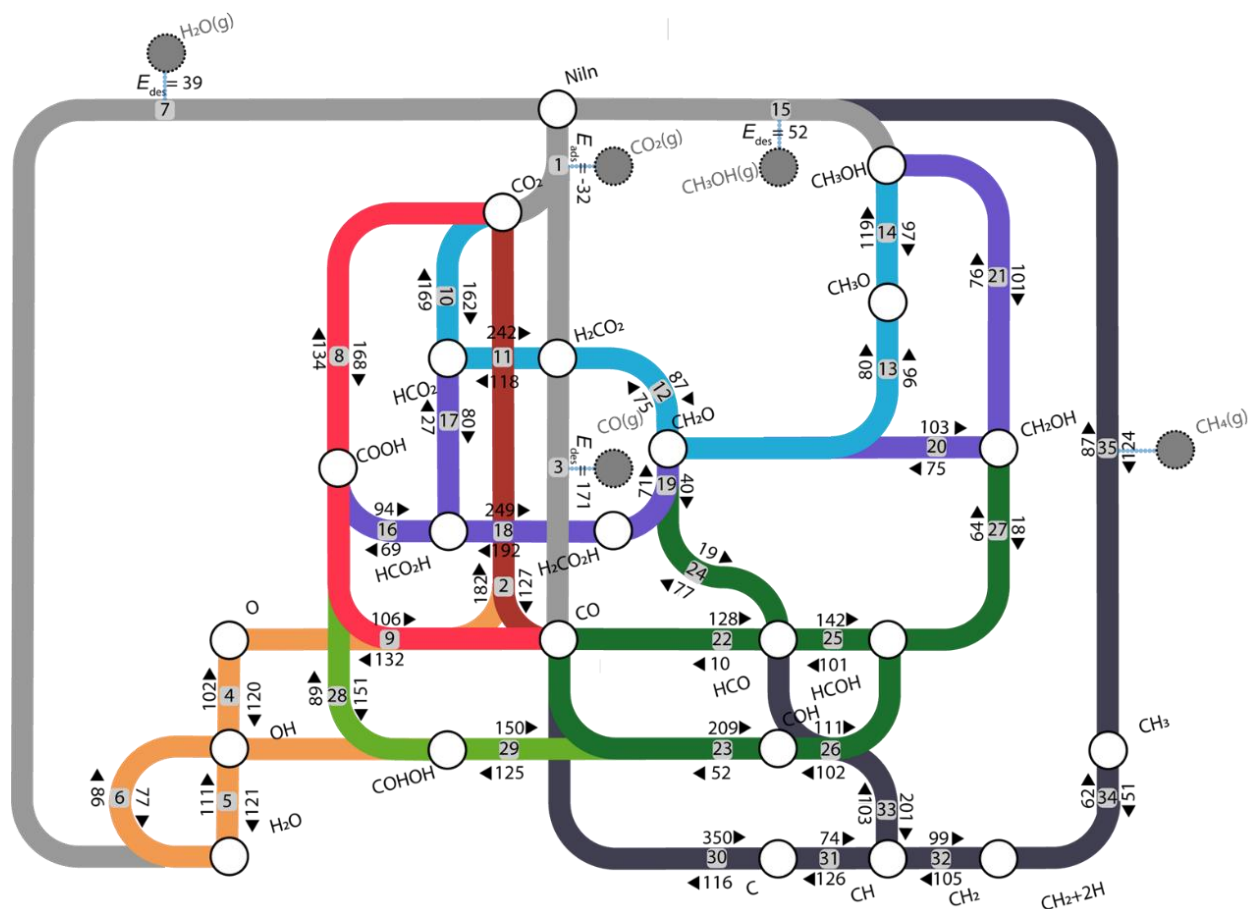


Figure 5.2. Complete reaction network for CO_2 hydrogenation to CO , CH_4 and CH_3OH . Dark red: redox pathway to CO ; light red: carboxyl pathway to CO ; orange: oxygen removal via H_2O formation; light blue: formate pathway to CH_3OH ; dark green: CO hydrogenation pathway to methanol; purple: HCO_2H pathway to CH_3OH ; light green: COHOH pathway to CH_3OH ; dark grey: CO_2 methanation pathway.

5.3.2.1 CO formation

The rWGS reaction was modeled based on the redox^{62–64} and carboxyl (COOH) mechanisms.^{65,66} Formate intermediates are usually considered to be spectators not actively participating in the formation of CO .^{67,68} The redox mechanism is represented by steps 1–3, while steps 8–9 constitute the carboxyl mechanism. Oxygen removal via H_2O formation is considered by steps 4–7. The potential energy diagrams for these reactions are given in Figure 5.3–5.

The adsorption energy of CO_2 of $\Delta E_{\text{ads}} -32$ kJ/mol is similar to the value obtained in a previous computational study on a bimetallic NiIn model surface.³⁸ Moreover, this value is comparable to the CO_2 adsorption energy on a Ni(110) surface.^{60,39} On the NiIn(100) model, the C atom and one of the O atoms bind to the Ni atom, while the other O atom binds to an adjacent In atom. In the redox mechanism, direct dissociation of CO_2 to CO and O (step 2) has an activation energy of 127 kJ/mol and is exothermic by ΔE_{R}

= -55 kJ/mol. This activation energy is considerably higher than values of 49 and 78 kJ/mol for respectively terrace Ni(111) and stepped Ni(311) surfaces.⁴⁰ In the transition state (TS), one of the O atoms resides in a quasi-bridge configuration between Ni and In. In the final state (FS), the CO product occupies a bridge site between two Ni atoms (b_{Ni_2}), whereas the O atom is located in a bridge site between two In atoms (b_{In_2}). O removal proceeds via H_2O formation. Dissociative adsorption of H_2 is barrierless and results in the formation of 2 Ni-H species ($\Delta E_R = -89$ kJ/mol). The O adsorbate is hydrogenated to OH (step 4, $\Delta E_a = 120$ kJ/mol), which occupies a fcc threefold site (fcc_{Ni_2In}). Next, OH can be hydrogenated to H_2O adsorbed on a b_{Ni_2} site (step 5, $\Delta E_a = 121$ kJ/mol). Alternatively, H transfer between two OH adsorbates can yield H_2O and again an O atom (step 6, $\Delta E_a = 77$ kJ/mol). Compared to direct OH hydrogenation, the latter proton migration has a lower barrier, as also found for extended metal surfaces of Rh and Ru.^{69,70} The desorption of CO and H_2O (steps 3 and 7, respectively) close the rWGS pathway. These elementary steps are associated with desorption energies of 171 and 39 kJ/mol, respectively. These adsorption energies are comparable with values reported for extended Ni surfaces.⁶⁰ In the carboxyl mechanism, cleavage of the C-O bond in CO_2 takes place via a H-assisted pathway involving a COOH intermediate. This pathway involves protonation of adsorbed CO_2 to form COOH (step 8). This elementary step features a forward barrier of 168 kJ/mol and is endothermic by $\Delta E_R = 34$ kJ/mol. Next, COOH dissociates into CO and OH (step 9) with an activation energy of 132 kJ/mol ($\Delta E_R = -26$ kJ/mol). A comparison of the two pathways shows that the direct redox pathway has a lower overall barrier than the carboxyl pathway.

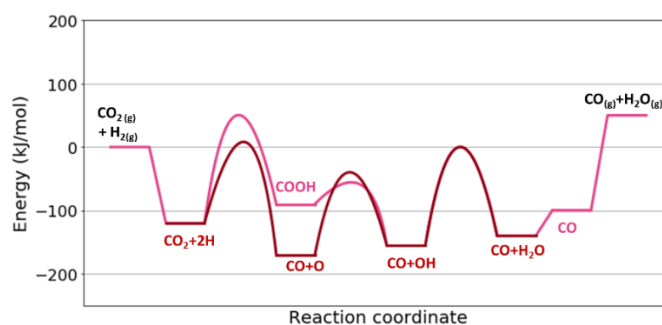


Figure 5.3. Potential energy diagrams of the conversion of CO_2 and H_2 to CO and H_2O via the rWGS pathway. Red: redox mechanism. Ped: carboxyl mechanism.

5.3.2.2 Methanol formation

As shown in Figure 5.2, CH_3OH can be obtained from CO_2 and H_2 following different pathways. The corresponding PEDs are depicted in Figure 5.4a-b. The geometries of IS, TS and FS are reported in Table S3 of the SI. On the NiIn(100) surface, methanol can be obtained from CO_2 and H_2 via formate (steps 10-15). The C atom in CO_2 is hydrogenated by a surface hydride to form HCO_2 , occupying a b_{Ni_2} site (step 10). This step has an activation energy of 162 kJ/mol and is slightly exothermic ($\Delta E_R = -7$ kJ/mol). Next, HCO_2 can be further hydrogenated by another hydride to form H_2CO_2 (step 11). This elementary reaction

step has a very high forward barrier of 242 kJ/mol and is endothermic by 124 kJ/mol. The resulting H_2CO_2 can dissociate into CH_2O and O (step 12) with an activation energy of 87 kJ/mol and a reaction energy of $\Delta E_{\text{R}} = 12$ kJ/mol. In the FS, the O occupies a $\text{fcc_Ni}_2\text{In}$ site and the CH_2O moiety a b_Ni_2 site. The CH_2O moiety can be hydrogenated to CH_3O and CH_3OH in two consecutive steps (steps 13-14) with respective activation energies of 80 and 119 kJ/mol. The CH_3O and CH_3OH adsorbates occupy b_Ni_2 sites. Methanol desorption (step 15) closes the catalytic cycle and is associated with a desorption energy of 52 kJ/mol.

Methanol can also be obtained via a pathway involving a HCO_2H intermediate (steps 16-21). One of the O atoms of the COOH intermediate can be protonated to form HCO_2H , which occupies a b_Ni_2 site (step 16). This elementary step has an activation energy of 94 kJ/mol and is endothermic by 25 kJ/mol. Protonation of one of the O atoms in HCO_2 (step 17) can occur with a lower barrier ($\Delta E_{\text{a}} = 80$ kJ/mol, $\Delta E_{\text{R}} = 53$ kJ/mol). The resulting HCO_2H moiety binds to the surface by forming an O-In bond. Further hydrogenation to $\text{H}_2\text{CO}_2\text{H}$ (step 18) is associated with a barrier of 249 kJ/mol and is endothermic by 57 kJ/mol. Notably, this step has the highest forward barrier for the HCO_2H pathway. The dissociation of $\text{H}_2\text{CO}_2\text{H}$ into CH_2O and OH has a barrier of 71 kJ/mol and is endothermic by 31 kJ/mol (step 19). In the FS, the CH_2O and OH intermediates occupy b_Ni_2 and $\text{fcc_Ni}_2\text{In}$ sites, respectively. The resulting CH_2O intermediate can be hydrogenated towards CH_2OH (step 20; $\Delta E_{\text{a}} = 103$ kJ/mol, $\Delta E_{\text{R}} = 29$ kJ/mol). The last hydrogenation step from CH_2OH to CH_3OH (step 21) has an activation energy of 76 kJ/mol and is exothermic by $\Delta E_{\text{R}} = -25$ kJ/mol. Alternatively, CH_2O can be hydrogenated to CH_3O and CH_3OH in two steps (steps 13-14) as discussed previously.

Methanol can also be obtained via a pathway involving adsorbed CO (steps 22-27) obtained via direct cleavage of the C-O bond in CO_2 (step 2), followed by oxygen removal via H_2O formation (steps 4-7). From this state, CO can be hydrogenated to either HCO (step 22, $\Delta E_{\text{a}} = 128$ kJ/mol, $\Delta E_{\text{R}} = 118$ kJ/mol) or COH (step 23, $\Delta E_{\text{a}} = 209$ kJ/mol, $\Delta E_{\text{R}} = 157$ kJ/mol). In the FS, both HCO and COH occupy a b_Ni_2 site. Notably, C-H bond formation is more facile than O-H bond formation, as also observed in a previous computational work.⁷⁰ The HCO intermediate can be hydrogenated to CH_2O (step 24, $E_{\text{act}} = 77$ kJ/mol, $\Delta E_{\text{R}} = 58$ kJ/mol), which is also an intermediate in the formate pathway for methanol formation. Alternatively, HCO can be hydrogenated to HCOH (step 25). This step is endothermic by 41 kJ/mol and features a barrier of 142 kJ/mol. The HCOH intermediate can also be obtained from COH hydrogenation (step 26) with a lower barrier ($\Delta E_{\text{a}} = 111$ kJ/mol, $\Delta E_{\text{R}} = 9$ kJ/mol). Two subsequent hydrogenation steps of the HCOH intermediate lead to methanol. The C atom in HCOH can be hydrogenated to CH_2OH (step 27, $\Delta E_{\text{a}} = 64$ kJ/mol, $\Delta E_{\text{R}} = 46$ kJ/mol), followed by further hydrogenation to CH_3OH (step 21, $\Delta E_{\text{a}} = 76$ kJ/mol, $\Delta E_{\text{R}} = -25$ kJ/mol).

CH_3OH can also be obtained from CO_2 via a COHOH intermediate according to steps 28-29. In this pathway, adsorbed CO_2 is protonated twice, resulting first in COOH (step 10, rWGS pathway) and then in COHOH (steps 33). The first protonation step yielding COOH was discussed earlier. The second protonation step to form COHOH is associated with an activation energy of 151 kJ/mol and is endothermic by 62 kJ/mol. In the FS, the COHOH moiety occupies a b_Ni_2 site. The subsequent dissociation of COHOH into COH (step 29) and OH has an activation energy of 150 kJ/mol and endothermic by 25 kJ/mol. In the FS, the COH and OH moieties occupy a b_Ni_2 and a $\text{fcc_Ni}_2\text{In}$ site, respectively. Next, COH can be hydrogenated to CH_3OH following the steps 30-32 as discussed earlier.

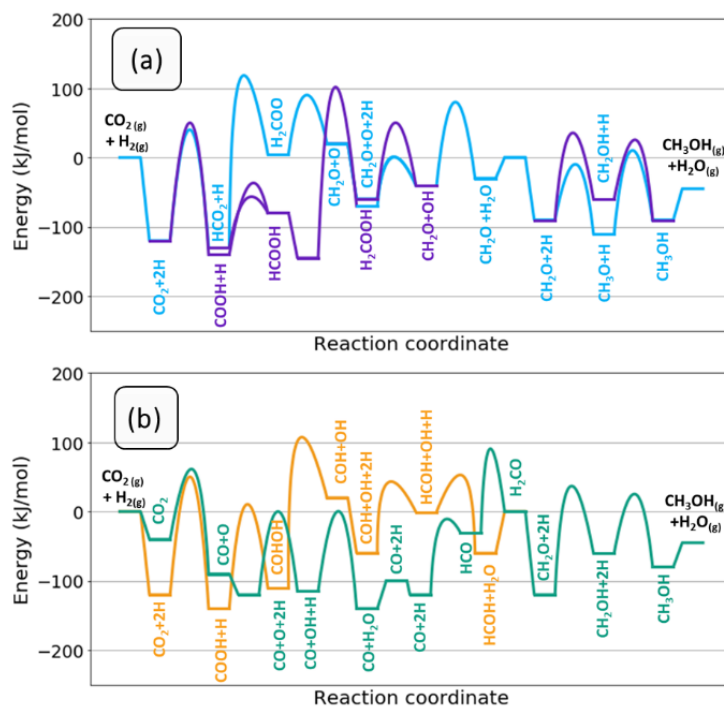


Figure 5.4. Potential energy diagrams of the conversion of CO_2 and H_2 to CH_3OH via (a) HCO_2 (light blue) and HCO_2H (purple), (b) CO (green) and COHOH (orange).

5.3.2.3 Methane formation

The hydrogenation steps of CO_2 to methane are given in Figure 5.2 (steps 30-35) in the form of a network diagram. Figure 5.5 shows the corresponding PEDs. The geometries of IS, TS and FS are reported in Table C3. Adsorption and dissociation of CO_2 result in adsorbed CO (steps 1-2). Upon removal of the O via H_2O formation (steps 4-9), adsorbed CO is obtained, which adsorbs linearly on a b_Ni_2 site. From this state, direct CO dissociation, leading to atomic carbon and O is associated with an activation energy of 350 kJ/mol and is endothermic by 234 kJ/mol (step 30). In the FS, the C and O atom occupy b_Ni_2 and $\text{fcc_Ni}_2\text{In}$ sites, respectively. Furthermore, compared to extended Ni surfaces, the barrier for CO activation on NiIn(100) is significantly higher irrespectively of the Ni surface termination considered

This CO dissociation barrier is prohibitively high and points to the inability of the alloyed surface to dissociate CO. Various CO dissociation pathways are possible on extended Ni surfaces.^{43,44} An alternative mode of CO dissociation involves hydrogenation of CO to HCO (step 22), followed by C-O bond dissociation to yield CH and O (step 33). This elementary reaction step has a forward barrier of 201 kJ/mol and is endothermic by 98 kJ/mol. Thus, a significantly lower barrier is obtained for the H-assisted pathway. The preference for the H-assisted pathway has also been reported for extended Ni surfaces.⁶⁰ After removal of adsorbed O via H₂O formation, atomic C can be hydrogenated to CH (step 31, $\Delta E_a = 74$ kJ/mol, $\Delta E_R = -52$ kJ/mol). Consecutive hydrogenation steps lead to CH₂ (step 32, $\Delta E_a = 99$ kJ/mol, $\Delta E_R = -6$ kJ/mol), CH₃ (step 34, $\Delta E_a = 62$ kJ/mol, $\Delta E_R = 11$ kJ/mol) and gas-phase CH₄ (step 35, $\Delta E_a = 87$ kJ/mol, $\Delta E_R = -37$ kJ/mol).

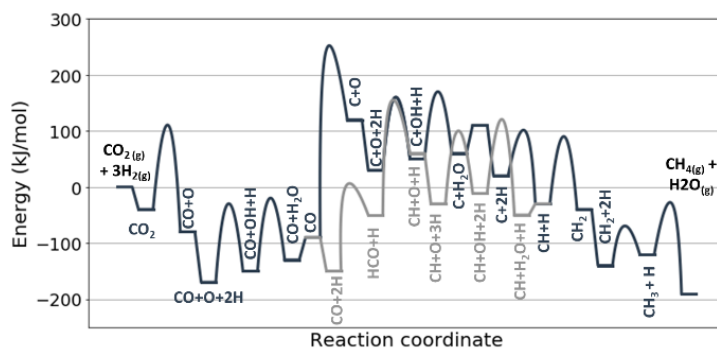


Figure 5.5. Potential energy diagrams of CO₂ methanation on NiIn(100). Dark grey: direct CO dissociation, light grey: H-assisted CO dissociation via HCO.

5.3.4 Microkinetic simulations

5.3.4.1 Overall kinetics

To systematically evaluate the catalytic activity of the NiIn(100) model surface, we compute the CO₂ hydrogenation reaction rate using microkinetic simulations with the DFT reaction energetics as input. In our simulations, a total pressure (p_{tot}) of 1 bar and a H₂/CO₂ ratio of 4 were chosen.³⁸ The calculated turnover frequencies (TOF) of CO, CH₃OH and CH₄ formation and the product distribution as a function of temperature are shown in Figure 5.6a. The microkinetic model predicts the highest TOF for CO, while formation of CH₃OH and especially CH₄ proceeds at very low rates. As a result, the model predicts a CO selectivity close to 100% (Figure 5.6b). The CO selectivity predicted by the microkinetic model is in good agreement with experimental observations. Cheng et al. reported a selectivity of 100% to CO on a InNi₃C_{0.5} catalyst.³⁸

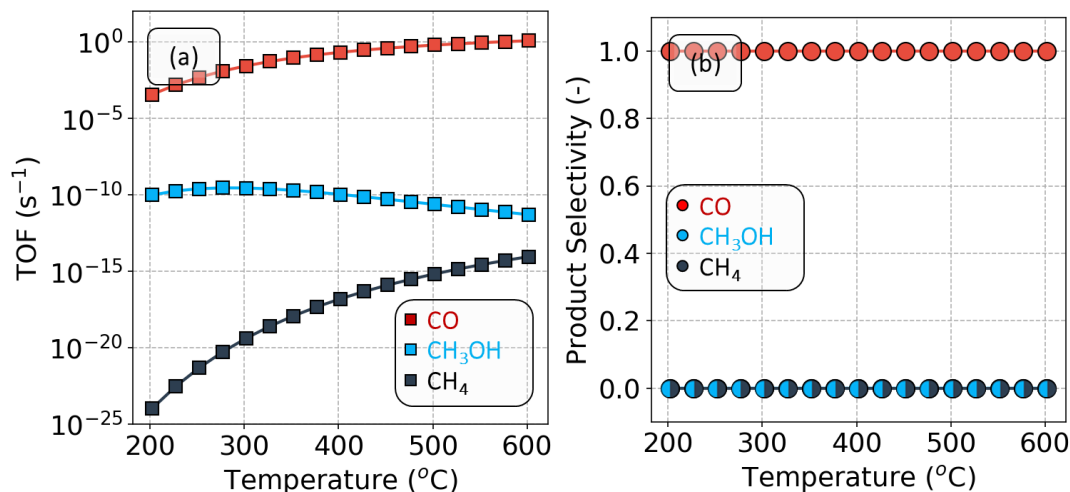


Figure 5.6. Results of the microkinetic model as a function of temperature on NiIn(100). (a) Turnover frequency (s^{-1}) and (b) selectivity calculated for CO (red), CH_3OH and CH_4 (grey) ($p_{\text{tot}} = 1$ bar, H_2/CO_2 ratio =4:1).

The analysis of the surface state, apparent activation energy and reaction orders as a function of temperature is given in Figure 5.7. At low temperature, the surface is mainly covered by H with a coverage of 0.60 at 250 °C (Figure 5.7a). The H adatoms occupy b_{Ni_2} sites on the NiIn(100) surface. Adsorbed O and CO occupy the surface to a smaller extent as can be seen by their lower coverages of 0.1 and 0.02, respectively, at 250 °C. At higher temperature, the coverage of H decreases in favour of the fraction of free sites, the latter becoming dominant for $T > 300$ °C.

Concerning the reaction orders, we observe that at low temperature ($T < 400$ °C) the reaction order H_2 is negative because the surface is mainly covered by adsorbed H species (Figure 5.7b). Increasing the temperature leads to a lower H coverage, explaining the higher reaction order with respect to H_2 that is nearly zero for $T > 400$ °C. The reaction order in CO_2 is positive and reaches one for $T > 250$ °C indicating that CO_2 dissociation might be rate-limiting (*vide infra*). The microkinetic model predicts an apparent activation energy ranging between 120 and 40 kJ/mol in the temperature range investigated.

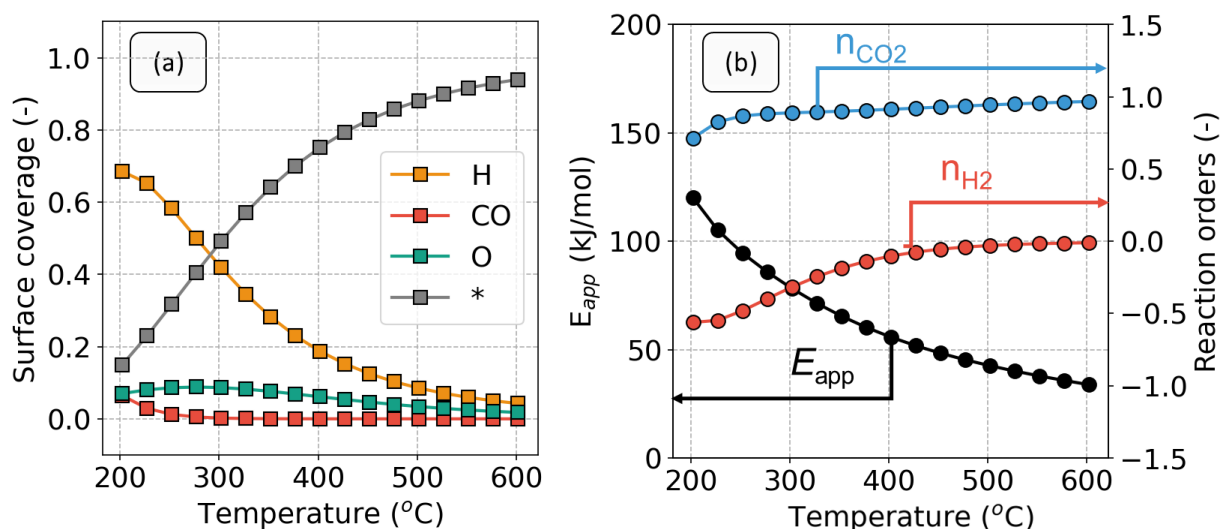


Figure 5.7. (a) Surface coverage and (b) reaction orders of CO_2 and H_2 and apparent activation energy with CO_2 as key component as a function of temperature. ($p_{tot} = 1$ bar, H_2/CO_2 ratio = 4).

5.3.4.2 Sensitivity analysis of the kinetic network

In this section, we discuss in detail the reaction network that leads to CO, CH_3OH and CH_4 from CO_2 hydrogenation on NiIn(100). We identify elementary steps that control the overall CO_2 consumption rate and investigate how these steps change with reaction temperature. To this aim, we conduct a detailed sensitivity analysis based on Campbell's degree of rate control (DRC).³⁵

The results of this analysis are shown in Figure 5.8. At low temperature ($200\text{ °C} < T < 250\text{ °C}$), the CO_2 consumption rate is mostly limited by CO_2 dissociation (step 2) with CO desorption (step 3) and OH disproportionation (step 6) also contributing slightly to the rate control. At $T > 250\text{ °C}$, the CO_2 dissociation step has a DRC coefficient of approximately 1, reflecting it has become the rate-determining step (RDS) of the reaction.

The dominant pathway for CO formation in CO_2 hydrogenation for the NiIn(100) surface is shown in Figure 5.8b. First CO_2 adsorbs on a b_NiIn site (step 1) where one of the two C-O bonds is broken (step 2) followed by desorption of CO (step 3). Oxygen is removed by formation of water proceeding via hydrogenation of O to OH (step 4) followed by a disproportionation of two OH moieties (step 6) and H_2O desorption (step 7). Direct OH hydrogenation is not taken because it has a significantly higher activation energy compared to the disproportionation step ($\Delta E_a = 121\text{ kJ/mol}$ and $\Delta E_a = 76\text{ kJ/mol}$, respectively). Hydrogenation of CO_2 to CO via the carboxyl pathway contributes only little to CO formation, because CO_2 hydrogenation to COOH is more difficult than direct CO_2 dissociation with respective barriers of 168 and 127 kJ/mol. Furthermore, our calculations also confirm that formate intermediates are not relevant for CO formation

The most favorable pathway for methanol formation involves the hydrogenation of CO obtained by direct CO₂ dissociation (Figure 5.8b) to HCO and CH₂O (steps 22 and 24), followed by further hydrogenation steps to CH₃O and CH₃OH (steps 153-15). The contribution of methanol formation is very low, because hydrogenation of CO to CH₂O via HCO has an overall barrier of 209 kJ/mol with respect to adsorbed CO and H. This overall barrier is significantly higher compared to CO₂ dissociation ($\Delta E_a = 127$ kJ/mol). Direct hydrogenation of CO₂ to methanol via formates does not occur because HCO₂ hydrogenation to H₂CO₂ and HCO₂H hydrogenation to H₂CO₂H are associated with very high barriers ($\Delta E_a = 242$ kJ/mol and $\Delta E_a = 249$ kJ/mol, respectively). The pathway to methanol via COHOH intermediate is not taken because high barriers are associated with protonation of CO₂ to COOH ($\Delta E_a = 168$ kJ/mol) and COOH to COHOH ($\Delta E_a = 151$ kJ/mol).

The rate of methane formation via CO hydrogenation (step 22), cleavage of C-O in HCO (step 33) followed by sequential hydrogenation to CH₄ (steps 32, 34-35) is very low. The overall barrier for CO₂ methanation with respect to adsorbed CO and H amounts to 311 kJ/mol resulting in low molar fluxes. Direct CO dissociation is also not feasible with a barrier of 350 kJ/mol.

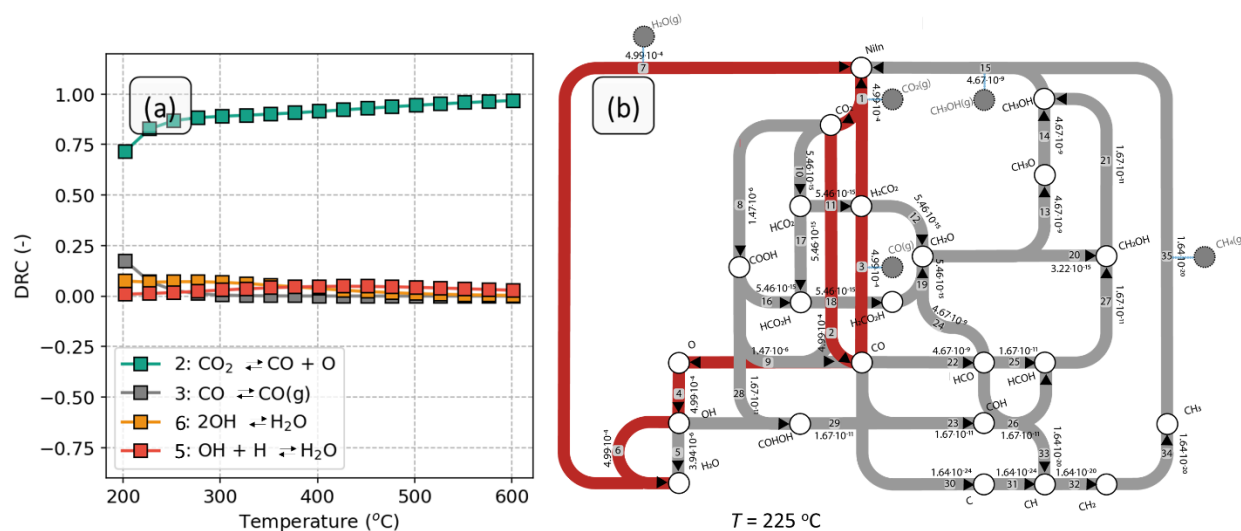


Figure 5.8. (a) Degree of rate control analysis of the mechanism of CO₂ hydrogenation to CO, CH₄, and CH₃OH on NiIn(100) with CO₂ as keycomponent as a function of temperature. (b) Reaction flux analysis at $T = 225$ °C. The dominant pathway is highlighted in red.

5.3.4.3 CO dissociation on Ni and NiIn surfaces

It is well established that stepped surfaces are key to C-O bond dissociation on metal nanoparticles.^{60,71,72,57} As such, such reactions are often controlling the reaction rate in CO₂ methanation. Our results so far for the close-packed NiIn(100) highlight the difficulty in cleaving the C-O bond in CO, although this can be due to the alloying of the less reactive In metal with Ni. To understand whether a different topology of the NiIn surface could lead to lower barriers for CO dissociation, we compare direct CO dissociation on flat and

stepped surface terminations for both NiIn and Ni. The NiIn(100) and NiIn(101) are the most stable low-index surfaces and represent respectively flat and step-edge surfaces (Table C1 and Figure C2). We compare the CO dissociation barriers of these two surface with those on Ni(111) and Ni(311) surface from an earlier study.⁶⁰ The results of this analysis are shown in Figure 5.8. Further details such as the CO adsorption energy, the forward activation energy and the reaction energy can be found in Table C3. Compared to a flat NiIn(100) surface, the activation energy on a step-edge NiIn(101) is lower by 35 kJ/mol (Figure 5.8a). In contrast, the difference in activation energy between Ni(311) and Ni(100) amounts to 115 kJ/mol (Figure 5.8b). We thus find that the presence of a step-edge NiIn surface does not lead to a substantial lowering of the activation energy of CO dissociation.

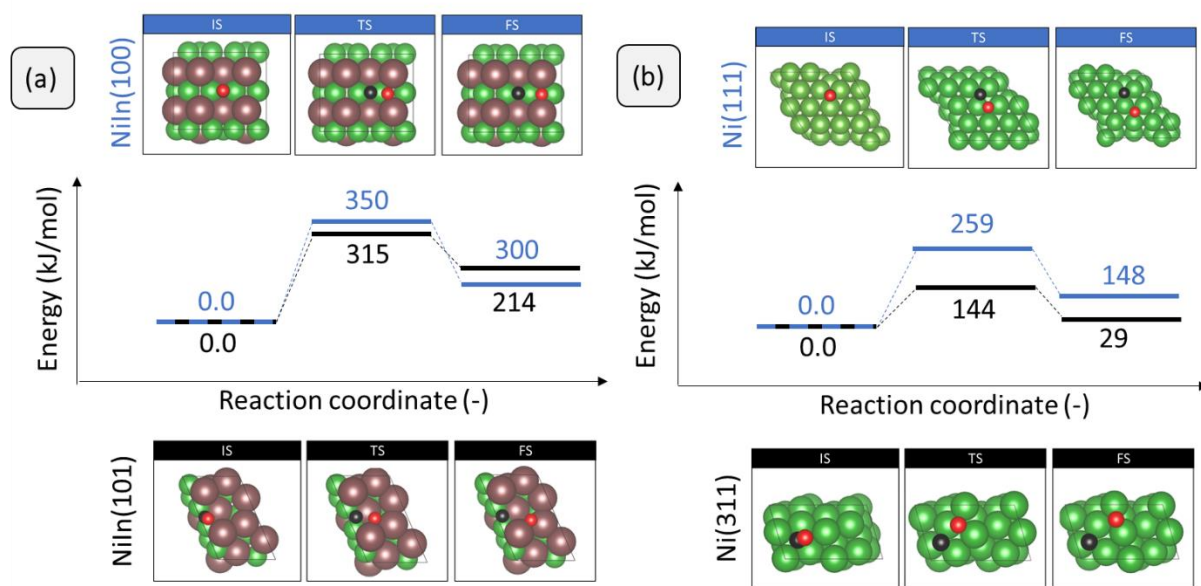


Figure 5.8. Potential energy diagram and structures for direct CO dissociation on (a) NiIn and (b) Ni surfaces. The reference state is adsorbed CO to the surface. Nickel: green, indium: brown, carbon: black, oxygen: red.

To rationalize the differences in CO activation energies, we studied the electronic structure of the initial state for each of these models. In Figure C3, the partial density of states (pDOS) for the Ni and/or In upon adsorption of CO is shown. Compared to Ni surfaces, the *d*-band of NiIn surfaces is narrower which is to be expected because less Ni atoms are available for the latter surfaces to supply *d*-electrons. Furthermore, we observe that the average *d*-band position of the stepped surfaces lies closer to the Fermi level in comparison to the flat surfaces. This is caused by the presence of low-coordinated surface metal atoms for the step-edge models. Thus, when CO binds to these low-coordinated active sites, it acquires more electron density compared to adsorption on a terrace site. This is reflected by the the calculated Bader charges of

CO on NiIn(100) and NiIn(101), that are $-0.18 |e|$ and $-0.22 |e|$, respectively. A similar difference is observed for the pure Ni surface, wherein we observe a charge on CO of $-0.40 |e|$ and $-0.44 |e|$ for Ni(111) and Ni(311), respectively. As expected, electron back-donation from Ni is larger than for NiIn, which can explain the trends in the CO dissociation energies, namely an increase of the electron density on the CO molecule in the initial state correlates with a decrease of the activation energy.

To understand the latter relation, we performed a pDOS analysis of the adsorbed CO molecule (Figures 5.9a-9e) and a Crystal Orbital Hamiltonian Population (COHP) analysis for the C-O bond (Figures 5.9f-9j). Comparing gas-phase CO (Figure 5.9a) and adsorbed CO (Figures 5.9b-9e) shows that the 3σ , 4σ and 1π molecular orbitals of CO do not change significantly upon adsorption to the metal surface. In contrast, the 5σ , 6σ and $2\pi^*$ molecular orbitals strongly mix with the metallic d -states leading to significant broadening of the DOS. The value of the integrated pDOS (ipDOS) reported in Figure 5.9a-e at the Fermi level is in very good agreement with the computed Bader charges. Differences between the two are caused by the different partitioning schemes used to divide the total electron density among the atoms. More electron density resides on the CO molecule for Ni, as also discussed above. From the COHP analysis (Figure 5.9f-j) we observe that, in all cases, the bonding 3σ , 4σ and 1π molecular orbitals become less bonding upon interaction with the surface. Moreover, the electron density originally corresponding to the anti-bonding 5σ , 6σ and $2\pi^*$ molecular orbitals for CO in the gas phase has become a broadened anti-bonding feature upon adsorption. The bonding character of the 3σ , 4σ and 1π molecular orbitals is less bonding for step-edge surfaces compared to flat surfaces. Furthermore, the anti-bonding character of the broadened band above 1π (6σ and $2\pi^*$) becomes more anti-bonding for step-edge surface compared to flat ones. Figures 5.9f-9j also show the integrated COHP for each of the peaks and shoulders. To analyze the total (anti-)bonding of the molecular orbitals of CO, we use the value for the integrated COHP (iCOHP) at Fermi level. We find that the weakening of the CO bond is more prominent on Ni surfaces ($i\text{COHP}_{\text{Ni}(111)} = -17.74$ and $i\text{COHP}_{\text{Ni}(311)} = -16.51$) compared to weakening on NiIn surfaces ($i\text{COHP}_{\text{NiIn}(100)} = -19.02$ and $i\text{COHP}_{\text{NiIn}(101)} = -18.52$). This is in line with the higher C-O bond scission activation energies for the alloys (Figure 5.8). Thus, adding In to Ni results in a narrower d -band (Figure C2), which implies that less electronic density can be donated to weaken the C-O bond (Figure 5.9). This increases the barrier of CO dissociation compared to Ni surfaces.

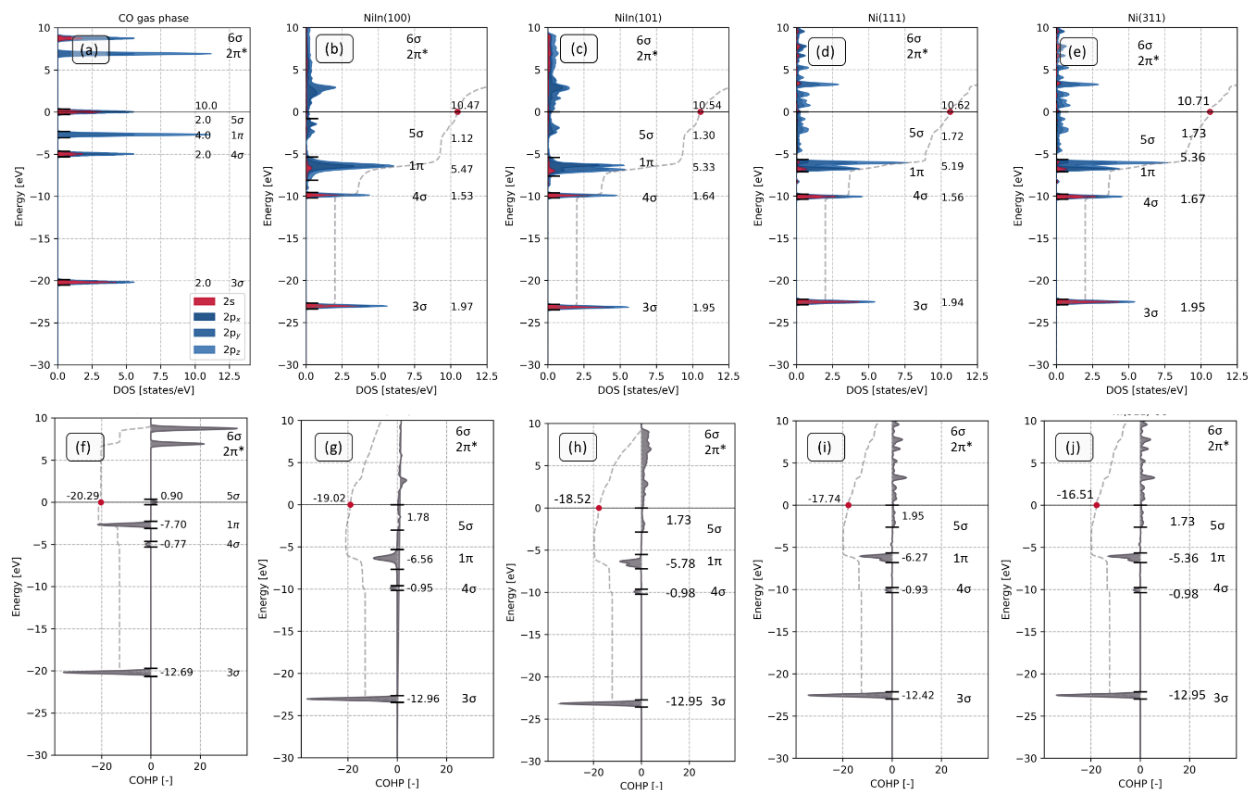


Figure 5.9. COHP and DOS spectra (a, e) gas-phase CO, (b, g) CO bond on NiIn(100), (c, h) CO on NiIn(101), (d, i) CO on Ni(111) and (e, j) CO on Ni(311). The Fermi level is set at zero. The gray dashed line is the IDOS (a-d) or the ICOHP (e-j). The ICOHP and IDOS at the Fermi level are shown by the value above the black line at zero energy at the red dot. The value right from each individual peak, defined by black markers, is the peak area obtained through integration. The labels of CO's molecular orbitals are indicate in the figures.

5.4 Conclusions

We explored the reaction mechanism of CO₂ hydrogenation to CO, CH₃OH and CH₄ on a NiIn(100) surface, representing a NiIn alloy, using DFT and microkinetic simulations. NiIn(100) catalyzes the formation of CO, which follows the redox mechanism involving adsorption of CO₂ on isolated Ni sites surrounded by In atoms. Subsequent CO₂ dissociation yields the CO product. The O atom is removed by forming H₂O via a disproportionation mechanism involving two OH moieties. At low temperature, the dominant rate-limiting step is CO₂ dissociation with a small contribution of OH disproportionation. Formation of methane is suppressed by high activation energies of the C-O bond dissociation step in CO-type intermediates. Comparison with a step-edge NiIn(101) surface revealed that a surface topology conducive to facile CO dissociation does not lead to strongly decreased barriers that would allow for CH₄ formation. Partial density of state, Bader charge and Crystal Orbital Hamiltonian Population analysis of adsorbed CO NiIn and Ni surfaces show that on NiIn surfaces less charge is transferred to CO than on Ni ones. This results in less

destabilization of the C-O bond on NiIn surfaces. The formation of CH₃OH is inhibited by the high barriers of subsequent elementary steps of hydrogenation of CO to HCO and H₂CO. As such, the present data explain the preference of CO formation during CO₂ hydrogenation on NiIn alloys.

5.5 References

- (1) Kondratenko, E. V.; Mul, G.; Baltrusaitis, J.; Larrazábal, G. O.; Pérez-Ramírez, J. Status and Perspectives of CO₂ Conversion into Fuels and Chemicals by Catalytic, Photocatalytic and Electrocatalytic Processes. *Energy Environ. Sci.* **2013**, *6* (11), 3112–3135.
- (2) Dias, V.; Pochet, M.; Contino, F.; Jeanmart, H. Energy and Economic Costs of Chemical Storage. *Front. Mech. Eng.* **2020**, *6*, 21.
- (3) Gao, P.; Li, S.; Bu, X.; Dang, S.; Liu, Z.; Wang, H.; Zhong, L.; Qiu, M.; Yang, C.; Cai, J.; Wei, W.; Sun, Y. Direct Conversion of CO₂ into Liquid Fuels with High Selectivity over a Bifunctional Catalyst. *Nat. Chem.* **2017**, *9* (10), 1019–1024.
- (4) Zhong, J.; Yang, X.; Wu, Z.; Liang, B.; Huang, Y.; Zhang, T. State of the Art and Perspectives in Heterogeneous Catalysis of CO₂ Hydrogenation to Methanol. *Chem. Soc. Rev.* **2020**, *49* (5), 1385–1413.
- (5) Jiang, X.; Nie, X.; Guo, X.; Song, C.; Chen, J. G. Recent Advances in Carbon Dioxide Hydrogenation to Methanol via Heterogeneous Catalysis. *Chem. Rev.* **2020**, *120* (15), 7984–8034.
- (6) Kaiser, P.; Unde, R. B.; Kern, C.; Jess, A. Production of Liquid Hydrocarbons with CO₂ as Carbon Source Based on Reverse Water-Gas Shift and Fischer-Tropsch Synthesis. *Chem. Ing. Tech.* **2013**, *85* (4), 489–499.
- (7) Porosoff, M. D.; Yan, B.; Chen, J. G. Catalytic Reduction of CO₂ by H₂ for Synthesis of CO, Methanol and Hydrocarbons: Challenges and Opportunities. *Energy Environ. Sci.* **2016**, *9* (1), 62–73.
- (8) Dang, S.; Yang, H.; Gao, P.; Wang, H.; Li, X.; Wei, W.; Sun, Y. A Review of Research Progress on Heterogeneous Catalysts for Methanol Synthesis from Carbon Dioxide Hydrogenation. *Catal. Today* **2018**, *330* (March 2018), 61–75.
- (9) Guan, H.; Chen, Y.; Ruan, C.; Lin, J.; Su, Y.; Wang, X.; Qu, L. Versatile Application of Wet-Oxidation for Ambient CO Abatement over Fe(OH)_x Supported Subnanometer Platinum Group Metal Catalysts. *Chin. J. Catal.* **2020**, *41* (4), 613–621.
- (10) Gong, J.; Chu, M.; Guan, W.; Liu, Y.; Zhong, Q.; Cao, M.; Xu, Y. Regulating the Interfacial Synergy of Ni/Ga₂O₃ for CO₂ Hydrogenation toward the Reverse Water–Gas Shift Reaction. *Ind. Eng. Chem. Res.* **2021**, *60*, 26, 9448–9455.
- (11) Alam, M. I.; Cheula, R.; Moroni, G.; Nardi, L.; Maestri, M. Mechanistic and Multiscale Aspects of Thermo-Catalytic CO₂ Conversion to C₁ Products. *Catal. Sci. Technol.* **2021**, *11* (20), 6601–6629.
- (12) Barbera, M.; Mantoan F.; Bertuccio, A.; Bezzo, F.; Hydrogenation to convert CO₂ to C₁ chemicals: Technical comparison of different alternatives by process simulation. *Can J Chem Eng.*, **2020**; 98:1893–1906.
- (13) Zhang, Y.; Zhang, T.; Das, S. Catalytic Transformation of CO₂ into C₁ Chemicals Using Hydrosilanes as a Reducing Agent. *Green Chem.* **2020**, *22* (6), 1800–1820.
- (14) Jangam, A.; Das, S.; Dewangan, N.; Hongmanorom, P.; Hui, W. M.; Kawi, S. Conversion of CO₂ to C₁ Chemicals: Catalyst Design, Kinetics and Mechanism Aspects of the Reactions. *Catal. Today* **2020**, *358*, 3–29.

- (15) Li, Y.; Cui, X.; Dong, K.; Junge, K.; Beller, M. Utilization of CO₂ as a C₁ Building Block for Catalytic Methylation Reactions. *ACS Catal.* **2017**, *7* (2), 1077–1086.
- (16) Wang, Y.; Gao, X.; Wu, M.; Tsubaki, N. Thermocatalytic Hydrogenation of CO₂ into Aromatics by Tailor-Made Catalysts: Recent Advancements and Perspectives. *EcoMat* **2021**, *3* (1), e12080.
- (17) Bobadilla, L. F.; Santos, J. J.; Ivanova, S.; Odriozola, J. J.; Urakawa, A. Unravelling the Role of Oxygen Vacancies in the Mechanism of the Reverse Water–Gas Shift Reaction by Operando DRIFTS and Ultraviolet–Visible Spectroscopy. *ACS Catal.* **2018**, *8*, 8, 7455–7467.
- (18) Nelson, N.C.; Chen L.; Meira, D.; Kovarik, L.; Szanyi, J. Hydrogenation to convert CO₂ to C₁ chemicals: In Situ Dispersion of Palladium on TiO₂ During Reverse Water–Gas Shift Reaction: Formation of Atomically Dispersed Palladium. *Angew. Chem. Int. Ed.* **2020**, *59*, 17657–17663.
- (19) Pettigrew, D. J.; Trimm, D. L.; Cant, N. W. The Effects of Rare Earth Oxides on the Reverse Water-Gas Shift Reaction on Palladium/Alumina. *Catal. Lett.* **1994**, *28*, 313–319.
- (20) Kim, S. S.; Park, K. H.; Hong, S. C. Study of the Selectivity of the Reverse Water–Gas-Shift Reaction over Pt/TiO₂ Catalysts. *Fuel Process. Technol.* **2013**, 13–19.
- (21) Porosoff, M. D.; Chen, J. G. Trends in the Catalytic Reduction of CO₂ by Hydrogen over Supported Monometallic and Bimetallic Catalysts. *J. Catal.* **2013**, *301*, 30–37.
- (22) Kattel, S.; Liu, P.; Chen, J. G. Tuning Selectivity of CO₂ Hydrogenation Reactions at the Metal/Oxide Interface. *J. Am. Chem. Soc.* **2017**, *139* (29), 9739–9754.
- (23) Kattel, S.; Yan, B.; Chen, J. G.; Liu, P. CO₂ Hydrogenation on Pt, Pt/SiO₂ and Pt/TiO₂: Importance of Synergy between Pt and Oxide Support. *J. Catal.* **2016**, *343*, 115–126.
- (24) Alayoglu, S.; Beaumont, S. K.; Zheng, F.; Pushkarev, V. V.; Zheng, H.; Iablokov, V.; Liu, Z.; Guo, J.; Kruse, N.; Somorjai, G. A. CO₂ Hydrogenation Studies on Co and CoPt Bimetallic Nanoparticles Under Reaction Conditions Using TEM, XPS and NEXAFS. *Top. Catal.* **2011**, *54* (13), 778.
- (25) Yuan, H.; Zhu, X.; Han, J.; Wang, H.; Ge, Q. Rhenium-Promoted Selective CO₂ Methanation on Ni-Based Catalyst. *J. CO₂ Util.* **2018**, *26*, 8–18.
- (26) Kharaji, A. G.; Shariati, A.; Takassi, M. A. A Novel γ -Alumina Supported Fe-Mo Bimetallic Catalyst for Reverse Water Gas Shift Reaction. *Chin. J. Chem. Eng.* **2013**, *21* (9), 1007–1014.
- (27) Ye, J.; Ge, Q.; Liu, C. Effect of PdIn Bimetallic Particle Formation on CO₂ Reduction over the Pd–In/SiO₂ Catalyst. *Chem. Eng. Sci.* **2015**, *135*, 193–201.
- (28) Alekseenko, V.; Alekseenko, A. The Abundances of Chemical Elements in Urban Soils. *J. Geochem. Explor.* **2014**, *147*, 245–249.
- (29) Wang, L.; Wang, L. Meng, X, Xiao, F. New Strategies for the Preparation of Sinter-Resistant Metal-Nanoparticle-Based Catalysts. *Adv. Mater.* **2019**, *31*, 1901905.
- (30) Sengupta, S.; Jha, A.; Shende, P.; Maskara, R.; Das, A. K. Catalytic Performance of Co and Ni Doped Fe-Based Catalysts for the Hydrogenation of CO₂ to CO via Reverse Water-Gas Shift Reaction. *J. Environ. Chem. Eng.* **2019**, *7* (1).

- (31) Chen, L.; Wu, D.; Wang, C.; Ji, M.; Wu, Z. Study on Cu-Fe/CeO₂ Bimetallic Catalyst for Reverse Water Gas Shift Reaction. *J. Environ. Chem. Eng.* **2021**, *9* (3), 105183.
- (32) Li, M.; My Pham, T. H.; Ko, Y.; Zhao, K.; Zhong, L.; Luo, W.; Züttel, A. Support-Dependent Cu-In Bimetallic Catalysts for Tailoring the Activity of Reverse Water Gas Shift Reaction. *ACS Sustain. Chem. Eng.* **2022**, *10* (4), 1524–1535.
- (33) Hwang, S.-M.; Han, S. J.; Park, H.-G.; Lee, H.; An, K.; Jun, K.-W.; Kim, S. K. Atomically Alloyed Fe-Co Catalyst Derived from a N-Coordinated Co Single-Atom Structure for CO₂ Hydrogenation. *ACS Catal.* **2021**, *11* (4), 2267–2278.
- (34) Pastor-Pérez, L.; Baibars, F.; Le Sache, E.; Arellano-García, H.; Gu, S.; Reina, T. R. CO₂ Valorisation via Reverse Water-Gas Shift Reaction Using Advanced Cs Doped Fe-Cu/Al₂O₃ Catalysts. *J. CO₂ Util.* **2017**, *21*, 423–428.
- (35) Yang, L.; Pastor-Pérez, L.; Gu, S.; Sepúlveda-Escribano, A.; Reina, T. R. Highly Efficient Ni/CeO₂-Al₂O₃ Catalysts for CO₂ Upgrading via Reverse Water-Gas Shift: Effect of Selected Transition Metal Promoters. *Appl. Catal. B Environ.* **2018**, *232*, 464–471.
- (36) Tsiotsias, A. I.; Charisiou, N. D.; Yentekakis, I. V.; Goula, M. A. Bimetallic Ni-Based Catalysts for CO₂ Methanation: A Review. *Nanomaterials* **2021**, *11* (1), 28.
- (37) Hengne, A. M.; Samal, A. K.; Enakonda, L. R.; Harb, M.; Gevers, L. E.; Anjum, D. H.; Hedhili, M. N.; Saih, Y.; Huang, K.-W.; Basset, J.-M. Ni-Sn-Supported ZrO₂ Catalysts Modified by Indium for Selective CO₂ Hydrogenation to Methanol. *ACS Omega* **2018**, *3* (4), 3688–3701.
- (38) Chen, P.; Zhao, G.; Shi, X. R.; Zhu, J.; Ding, J.; Lu, Y. Nano-Intermetallic InNi₃Co_{0.5} Compound Discovered as a Superior Catalyst for CO₂ Reutilization. *iScience* **2019**, *17*, 315–324.
- (39) Frei, M. S.; Mondelli, C.; García-Muelas, R.; Morales-Vidal, J.; Philipp, M.; Safonova, O. V.; López, N.; Stewart, J. A.; Ferré, D. C.; Pérez-Ramírez, J. Nanostructure of Nickel-Promoted Indium Oxide Catalysts Drives Selectivity in CO₂ Hydrogenation. *Nat. Commun.* **2021**, *12*, 1–9.
- (40) Kresse, G.; Joubert, D. From Ultrasoft Pseudopotentials to the Projector Augmented-Wave Method. *Phys. Rev. B* **1999**, *59* (3), 1758.
- (41) Perdew, J. P.; Burke, K.; Ernzerhof, M. Generalized Gradient Approximation Made Simple. *Phys. Rev. Lett.* **1996**, *77* (18), 3865.
- (42) Kresse, G.; Hafner, J. Ab Initio Molecular-Dynamics Simulation of the Liquid-Metalamorphous- Semiconductor Transition in Germanium. *Phys. Rev. B* **1994**, *49* (20), 14251–14269.
- (43) Kresse, G.; Furthmüller, J. Efficiency of Ab-Initio Total Energy Calculations for Metals and Semiconductors Using a Plane-Wave Basis Set. *Comput. Mater. Sci.* **1996**, *6* (1), 15–50.
- (44) Grimme, S. Semiempirical GGA-Type Density Functional Constructed with a Long-Range Dispersion Correction. *J. Comput. Chem.* **2006**, *27* (15), 1787–1799.
- (45) mp-19876: InNi (hexagonal, P6/mmm, 191). <https://materialsproject.org/materials/mp-19876/> (accessed 2022-02-14).

- (46) Henkelman, G.; Uberuaga, B. P.; Jónsson, H. Climbing Image Nudged Elastic Band Method for Finding Saddle Points and Minimum Energy Paths. *J. Chem. Phys.* **2000**, *113* (22), 9901–9904.
- (47) Heidrich, D.; Quapp, W. Saddle Points of Index 2 on Potential Energy Surfaces and Their Role in Theoretical Reactivity Investigations. *Theor. Chim. Acta* **1986**, *70* (2), 89–98.
- (48) Nelson, R.; Ertural, C.; George, J.; Deringer, V. L.; Hautier, G.; Dronskowski, R. LOBSTER: Local Orbital Projections, Atomic Charges, and Chemical-Bonding Analysis from Projector-Augmented-Wave-Based Density-Functional Theory. *J. Comput. Chem.* **2020**, *41* (21), 1931–1940.
- (49) Maintz, S.; Volker, L.; Deringer, L.; Tchougr, A. L.; Dronskowski, R.; LOBSTER: A Tool to Extract Chemical Bonding from Plane-Wave Based DFT. *J. Comput. Chem.*; **2016**, *37*, 11–12.
- (50) Yu, M.; Trinkle, D. R. Accurate and Efficient Algorithm for Bader Charge Integration. *J. Chem. Phys.* **2011**, *134* (6), 064111.
- (51) Brown, P. N.; Byrne, G. D.; Hindmarsh, A. C. VODE: A Variable-Coefficient ODE Solver. *J. Sci. Stat. Comput.*, **1989**, *10*, 5, 1038-1051.
- (52) Byrne, G. D.; Hindmarsh, A. C. Stiff ODE Solvers: A Review of Current and Coming Attractions. *J. Comput. Phys.* **1987**, *70* (1), 1–62.
- (53) Byrne, G. D.; Hindmarsh, A. C. A Polyalgorithm for the Numerical Solution of Ordinary Differential Equations. *ACM Trans. Math. Softw. TOMS* **1975**, *1* (1), 71–96.
- (54) Shomate, C. H. A Method for Evaluating and Correlating Thermodynamic Data. *J. Phys. Chem.* **2002**, *58* (4), 368–372.
- (55) *NIST Chemistry WebBook*. <https://webbook.nist.gov/chemistry/> (accessed 2022-02-01).
- (56) Kozuch, S.; Shaik, S. A Combined Kinetic-Quantum Mechanical Model for Assessment of Catalytic Cycles: Application to Cross-Coupling and Heck Reactions. *J. Am. Chem. Soc.* **2006**, *128* (10), 3355–3365.
- (57) Kozuch, S.; Shaik, S. Kinetic-Quantum Chemical Model for Catalytic Cycles: The Haber-Bosch Process and the Effect of Reagent Concentration. *J. Phys. Chem. A* **2008**, *112* (26), 6032–6041.
- (58) Campbell, C. T. The Degree of Rate Control: A Powerful Tool for Catalysis Research. *ACS Catal.* **2017**, *7* (4), 2770–2779.
- (59) Filot, A. W. *Introduction to microkinetic modeling*; Technische Universiteit Eindhoven, **2022**. ISBN: 978-90-386-5573-4.
- (60) Zhang, M.; Zijlstra, B.; Filot, I. A. W.; Li, F.; Wang, H.; Li, J.; Hensen, E. J. M. A Theoretical Study of the Reverse Water-Gas Shift Reaction on Ni(111) and Ni(311) Surfaces. *Can. J. Chem. Eng.* **2020**, *98* (3), 740–748.
- (61) Wu, P.; Yang, B. Intermetallic PdIn Catalyst for CO₂ Hydrogenation to Methanol: Mechanistic Studies with a Combined DFT and Microkinetic Modeling Method. *Catal. Sci. Technol.* **2019**, *9* (21), 6102–6113.
- (62) Nakamura, J.; Campbell, J. M.; Campbell, C. T. Kinetics and Mechanism of the Water-Gas Shift Reaction Catalysed by the Clean and Cs-Promoted Cu(110) Surface: A Comparison with Cu(111). *J. Chem. Soc. Faraday Trans.* **1990**, *86* (15), 2725–2734.
- (63) Ovesen, C. V.; Stoltze, P.; Nørskov, J. K.; Campbell, C. T. A Kinetic Model of the Water Gas Shift Reaction. *J. Catal.* **1992**, *134* (2), 445–468.

- (64) Yoshihara, J.; Campbell, C. T. Methanol Synthesis and Reverse Water–Gas Shift Kinetics over Cu(110) Model Catalysts: Structural Sensitivity. *J. Catal.* **1996**, *161* (2), 776–782.
- (65) Gokhale, A. A.; Dumesic, J. A.; Mavrikakis, M. On the Mechanism of Low-Temperature Water Gas Shift Reaction on Copper. *J. Am. Chem. Soc.* **2008**, *130* (4), 1402–1414.
- (66) Mudiyansele, K.; Senanayake, S.; Ramirez, P.; Kundu, S.; Baber, A.; Yang, F.; Agnoli, S.; Axnanda, S.; Liu, Z.; Hrbek, J.; Evans, J.; Rodriguez, J.; Stacchiola, D. Intermediates Arising from the Water–Gas Shift Reaction over Cu Surfaces: From UHV to Near Atmospheric Pressures. *Top Catal* **2015**, *58*, 1–10.
- (67) Vesselli, E.; Rizzi, M.; De Rogatis, L.; Ding, X.; Baraldi, A.; Comelli, G.; Savio, L.; Vattuone, L.; Rocca, M.; Fornasiero, P.; Baldereschi, A.; Peressi, M. Hydrogen-Assisted Transformation of CO₂ on Nickel: The Role of Formate and Carbon Monoxide. *J. Phys. Chem. Lett.* **2010**, *1* (1), 402–406.
- (68) Peng, G.; Sibener, S. J.; Schatz, G. C.; Ceyer, S. T.; Mavrikakis, M. CO₂ Hydrogenation to Formic Acid on Ni(111). *J. Phys. Chem. C* **2012**, *116* (4), 3001–3006.
- (69) Filot, I. A. W.; Van Santen, R. A.; Hensen, E. J. M. Quantum Chemistry of the Fischer–Tropsch Reaction Catalysed by a Stepped Ruthenium Surface. *Catal. Sci. Technol.* **2014**, *4* (9), 3129–3140.
- (70) Filot, I. A. W.; Broos, R. J. P.; Van Rijn, J. P. M.; Van Heugten, G. J. H. A.; Van Santen, R. A.; Hensen, E. J. M. First-Principles-Based Microkinetics Simulations of Synthesis Gas Conversion on a Stepped Rhodium Surface. *ACS Catal.* **2015**, *5* (9), 5453–5467.
- (71) Wolf, A.; Jess, A.; Kern, C. Syngas Production via Reverse Water-Gas Shift Reaction over a Ni-Al₂O₃ Catalyst: Catalyst Stability, Reaction Kinetics, and Modeling. *Chem. Eng. Technol.* **2016**, *39* (6), 1040–1048.
- (72) Ashok, J.; Ang, M. L.; Terence, P. Z. L.; Kawi, S. Promotion of the Water-Gas-Shift Reaction by Nickel Hydroxyl Species in Partially Reduced Nickel-Containing Phyllosilicate Catalysts. *ChemCatChem* **2016**, *8* (7), 1308–1318.

Appendix C

C1. NiIn bulk and surface models

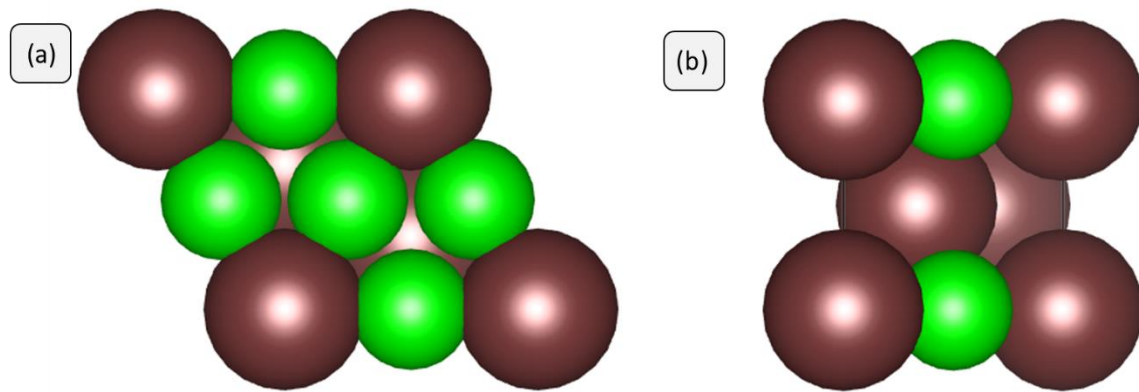
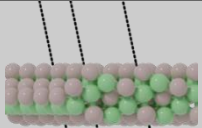
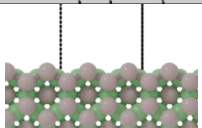
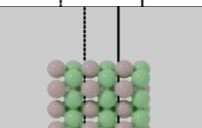
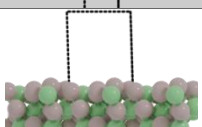
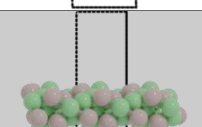
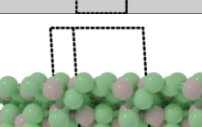


Figure C1. Unit cell bulk structure of the bimetallic NiIn phase. (a) Topview and (b) sideview of NiIn (P6/mmm). Green: Ni; brown: In.

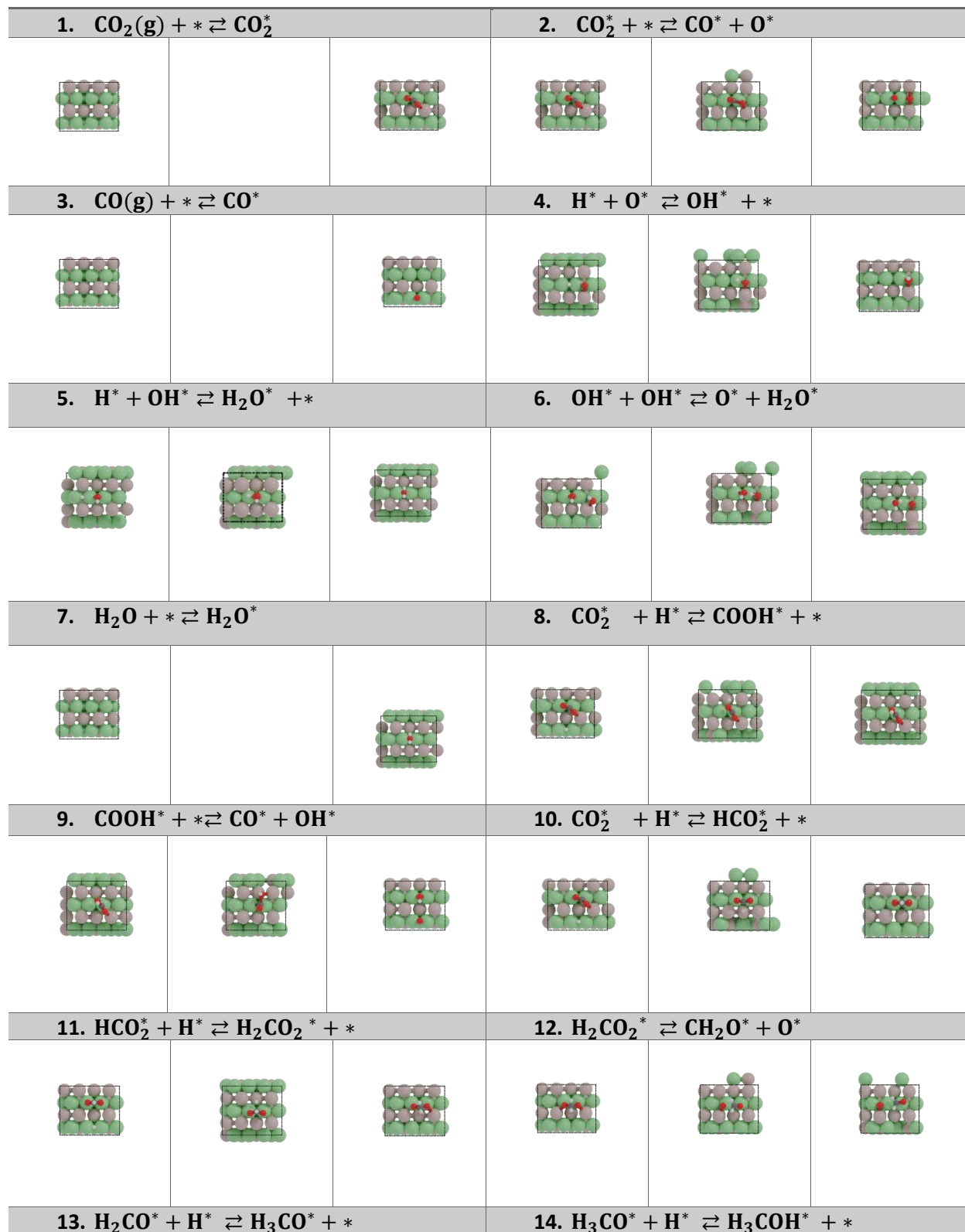
The surface energy was determined for a sampling of surface cut-offs. Crystal surface energy was calculated as stated in equation C.1

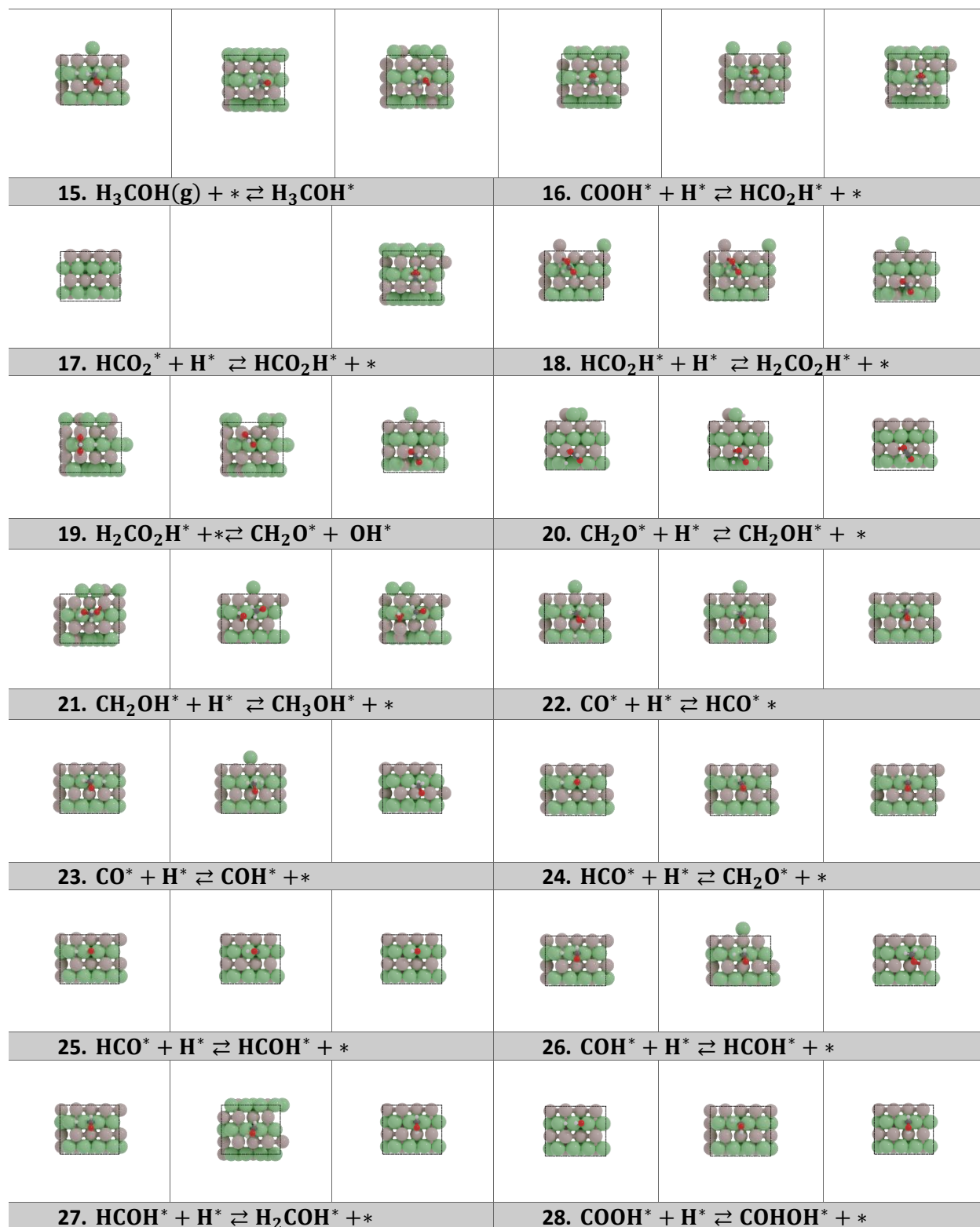
$$E_{\text{surf}} = \frac{E_{\text{slab}} - NE_{\text{bulk}}}{2A_{\text{surf}}} \quad (\text{C.1})$$

Table C1. Surface energies of three different surface termination of InNi intermetallic catalyst. Green: Ni; brown: In.

Surface termination	Side view	E_{surf} (J/m ²)
101		1.57
100		1.49
110		1.74
111		6.94
211		1.59
321		9.81

C2. Structures of reaction intermediates and transition states





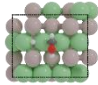
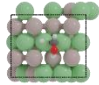
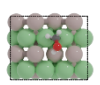
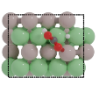
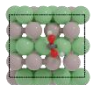
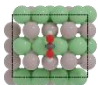
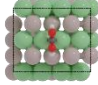
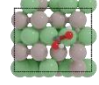
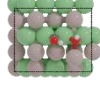
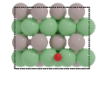
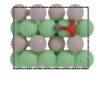
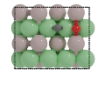
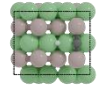

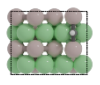
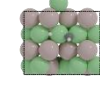
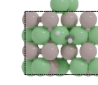
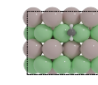
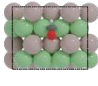
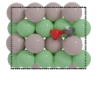
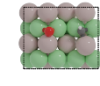
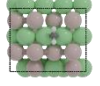
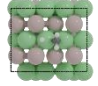
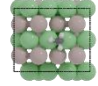
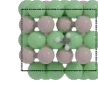
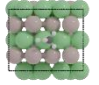
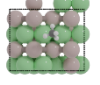
					
29. $\text{COHOH}^* + * \rightleftharpoons \text{COH}^* + \text{OH}^*$			30. $\text{CO}^* + * \rightleftharpoons \text{C}^* + \text{O}^*$		
					
31. $\text{C}^* + \text{H}^* \rightleftharpoons \text{CH}^* + *$			32. $\text{CH}^* + \text{H}^* \rightleftharpoons \text{CH}_2^* + *$		
					
33. $\text{HCO}^* + * \rightleftharpoons \text{CH}^* + \text{O}^*$			34. $\text{CH}_2^* + \text{H}^* \rightleftharpoons \text{CH}_3^* + *$		
					
35. $\text{CH}_3^* + \text{H}^* \rightleftharpoons \text{CH}_4(\text{g}) + *$					
					

Table C2: Parameters for the microkinetic model of CO₂ hydrogenation over NiIn(100). The activation and reaction energies are given in kJ/mol.

	Elementary Reaction Step	ΔE_a	ΔE_b	ΔE_R	Q_{TS}/Q_{IS}	Q_{TS}/Q_{FS}
1	$\text{CO}_2(\text{g}) + * \rightleftharpoons \text{CO}_2^*$	-	-	-32	-	-
2	$\text{CO}_2^* + * \rightleftharpoons \text{CO}^* + \text{O}^*$	127	182	-55	$1.51 \cdot 10^{-1}$	$1.51 \cdot 10^{-1}$
3	$\text{CO}(\text{g}) + * \rightleftharpoons \text{CO}^*$	-	-	-171	-	-
4	$\text{O}^* + \text{H}^* \rightleftharpoons \text{OH}^* + *$	120	102	18	$1.33 \cdot 10^0$	$7.49 \cdot 10^{-1}$
5	$\text{OH}^* + \text{H}^* \rightleftharpoons \text{H}_2\text{O}^* + *$	121	111	10	$2.65 \cdot 10^0$	$7.49 \cdot 10^{-1}$
6	$\text{OH}^* + \text{OH}^* \rightleftharpoons \text{H}_2\text{O}^* + *$	77	86	-9	$1.73 \cdot 10^0$	$3.87 \cdot 10^{-1}$
7	$\text{H}_2\text{O}(\text{g}) + * \rightleftharpoons \text{H}_2\text{O}^*$	-	-	-39	-	-
8	$\text{CO}_2^* + \text{H}^* \rightleftharpoons \text{COOH}^* + *$	168	134	34	$4.95 \cdot 10^0$	$3.73 \cdot 10^0$
9	$\text{COOH}^* + * \rightleftharpoons \text{CO}^* + \text{OH}^*$	106	132	-26	$1.75 \cdot 10^0$	$1.30 \cdot 10^0$
10	$\text{CO}_2^* + \text{H}^* \rightleftharpoons \text{HCO}_2^* + *$	162	169	-7	$1.59 \cdot 10^0$	$1.11 \cdot 10^0$
11	$\text{HCO}_2^* + \text{H}^* \rightleftharpoons \text{H}_2\text{CO}_2^* + *$	242	118	124	$1.30 \cdot 10^{-1}$	$6.07 \cdot 10^{-1}$
12	$\text{H}_2\text{CO}_2^* + * \rightleftharpoons \text{CH}_2\text{O}^* + \text{O}^*$	87	75	12	$8.69 \cdot 10^{-1}$	$1.27 \cdot 10^{-1}$
13	$\text{CH}_2\text{O}^* + \text{H}^* \rightleftharpoons \text{CH}_3\text{O}^* + *$	80	96	-16	$1.12 \cdot 10^0$	$2.51 \cdot 10^0$
14	$\text{H}_3\text{CO}^* + \text{H}^* \rightleftharpoons \text{H}_3\text{COH}^* + *$	119	97	22	$3.65 \cdot 10^{-0}$	$7.49 \cdot 10^{-1}$
15	$\text{CH}_3\text{OH}(\text{g}) + * \rightleftharpoons \text{CH}_3\text{OH}^*$	-	-	-52	-	-
16	$\text{COOH}^* + \text{H}^* \rightleftharpoons \text{HCO}_2\text{H}^* + *$	94	69	25	$5.93 \cdot 10^{-1}$	$6.22 \cdot 10^{-2}$
17	$\text{HCO}_2^* + \text{H}^* \rightleftharpoons \text{HCO}_2\text{H}^* + *$	80	27	53	$2.16 \cdot 10^0$	$2.45 \cdot 10^{-1}$
18	$\text{HCO}_2\text{H}^* + \text{H}^* \rightleftharpoons \text{H}_2\text{CO}_2\text{H}^* + *$	249	192	57	$5.84 \cdot 10^{-1}$	$2.49 \cdot 10^{-1}$
19	$\text{H}_2\text{CO}_2\text{H}^* + * \rightleftharpoons \text{CH}_2\text{O}^* + \text{OH}^*$	71	40	31	$8.65 \cdot 10^{-1}$	$1.99 \cdot 10^{-1}$
20	$\text{CH}_2\text{O}^* + \text{H}^* \rightleftharpoons \text{CH}_2\text{OH}^* + *$	103	75	28	$2.65 \cdot 10^{-1}$	$1.49 \cdot 10^0$
21	$\text{CH}_2\text{OH}^* + \text{H}^* \rightleftharpoons \text{CH}_3\text{OH}^* + *$	76	101	-25	$3.55 \cdot 10^{-1}$	$7.49 \cdot 10^{-2}$
22	$\text{CO}^* + \text{H}^* \rightleftharpoons \text{HCO}^* + *$	128	10	118	$7.62 \cdot 10^{-1}$	$3.49 \cdot 10^{-1}$
23	$\text{CO}^* + \text{H}^* \rightleftharpoons \text{COH}^* + *$	209	52	157	$2.65 \cdot 10^{-1}$	$1.49 \cdot 10^0$
24	$\text{HCO}^* + \text{H}^* \rightleftharpoons \text{CH}_2\text{O}^* + *$	77	19	58	$4.15 \cdot 10^{-1}$	$3.44 \cdot 10^{-1}$
25	$\text{HCO}^* + \text{H}^* \rightleftharpoons \text{HCOH}^* + *$	142	101	41	$1.45 \cdot 10^{-1}$	$1.19 \cdot 10^0$
26	$\text{COH}^* + \text{H}^* \rightleftharpoons \text{HCOH}^* + *$	111	102	9	$4.51 \cdot 10^{-1}$	$7.49 \cdot 10^{-1}$
27	$\text{HCOH}^* + \text{H}^* \rightleftharpoons \text{CH}_2\text{OH}^* + *$	64	18	46	$6.00 \cdot 10^{-1}$	$3.79 \cdot 10^{-1}$
28	$\text{COOH}^* + \text{H}^* \rightleftharpoons \text{COHOH}^* + *$	151	89	62	$1.14 \cdot 10^0$	$1.57 \cdot 10^0$
29	$\text{COHOH}^* + * \rightleftharpoons \text{COH}^* + \text{OH}^*$	150	125	25	$1.14 \cdot 10^{-1}$	$7.49 \cdot 10^{-1}$
30	$\text{CO}^* + * \rightleftharpoons \text{C}^* + \text{O}^*$	350	116	234	$2.65 \cdot 10^{-2}$	$7.49 \cdot 10^{-1}$
31	$\text{C}^* + \text{H}^* \rightleftharpoons \text{CH}^* + *$	74	126	-52	$2.65 \cdot 10^0$	$7.49 \cdot 10^{-1}$
32	$\text{CH}^* + \text{H}^* \rightleftharpoons \text{CH}_2^* + *$	99	105	-6	$2.65 \cdot 10^0$	$7.49 \cdot 10^{-1}$
33	$\text{CHO}^* + * \rightleftharpoons \text{CH}^* + \text{O}^*$	201	103	98	$2.75 \cdot 10^0$	$1.55 \cdot 10^0$
34	$\text{CH}_2^* + \text{H}^* \rightleftharpoons \text{CH}_3^* + *$	62	51	11	$9.14 \cdot 10^{-1}$	$4.78 \cdot 10^{-1}$
35	$\text{CH}_3^* + \text{H}^* \rightleftharpoons \text{CH}_4(\text{g}) + *$	87	124	-37	$2.65 \cdot 10^0$	$7.49 \cdot 10^{-1}$

Table C3 Activation and reaction energies (in kJ/mol) of the elementary reaction step of CO dissociation over Ni and NiIn surfaces.

Model	ΔE_a (CO \rightarrow C+O)	ΔE_R
Ni(111)	259	148
Ni(311)	144	29
NiIn(100)	350	214
NiIn(101)	315	300

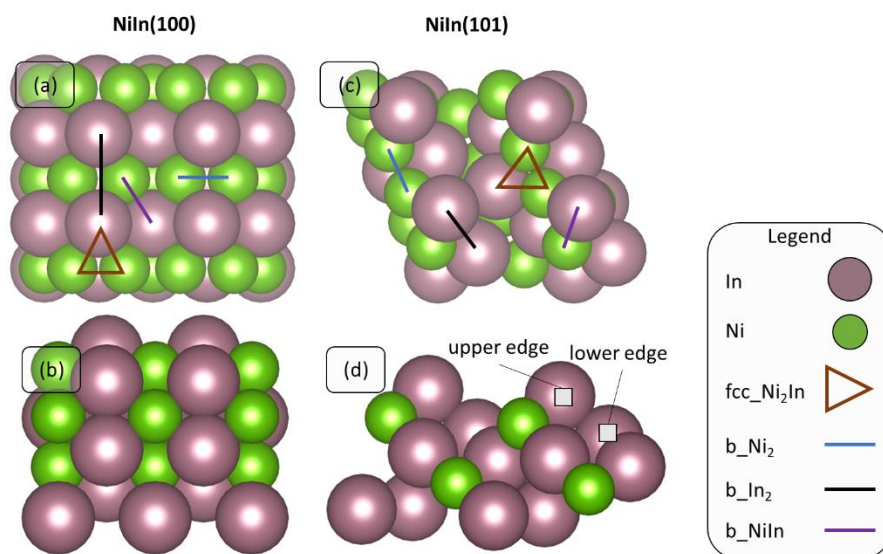


Figure C2. Schematic representation of the NiIn(100). (a) top view and (b) side view. Adsorption sites include threefold-fcc (fcc_{Ni₂In}) and bridge sites (b_{Ni₂}, b_{In₂} and b_{NiIn}).

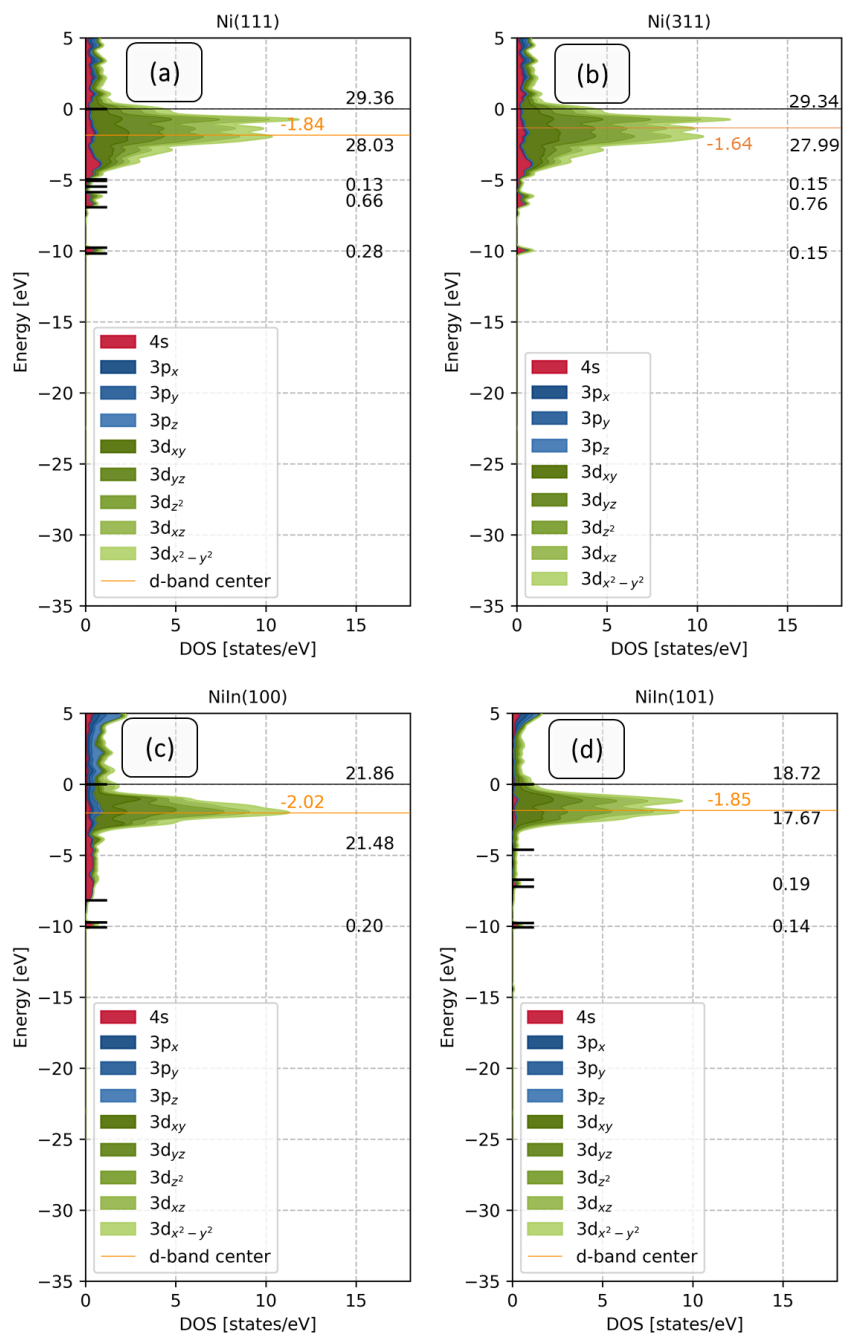


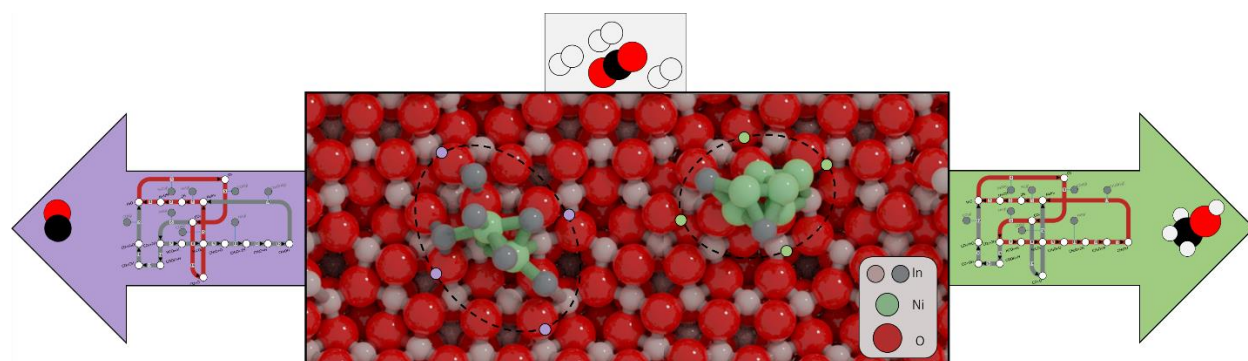
Figure C3. Partial density of states (PDOS) of Ni 4s, 3p and 3d orbitals on (a) Ni(111), (b) Ni(311), (c) NiIn(100) and (d) NiIn(101). The Fermi level is set at zero. The value of the d-band center is indicated by an orange line. The values of the single integrated peaks is also reported. In all cases, the Ni and In atoms directly binding the CO molecule are considered for the DOS analysis.

CHAPTER 6

On the role of Ni-In clusters on In_2O_3 during CO_2 hydrogenation to methanol

Abstract

Highly dispersed metal phases are known to promote the hydrogenation of CO_2 to methanol in In_2O_3 catalysts. Besides Ni clusters, also alloys of Ni and In have been implicated in this reaction. To understand the influence of the composition of NiIn alloy clusters on CO_2 hydrogenation, we employed density functional theory (DFT) and microkinetic modeling. From a database of many 8-atom NiIn clusters on the $\text{In}_2\text{O}_3(111)$ surface optimized by a combination of DFT and artificial neural networks, we selected two clusters, a Ni-rich one (Ni_6In_2) and an In-rich one (Ni_2In_6). The reaction energetics for methanol and CO formation were computed. The presence of NiIn alloy clusters increases the overall barrier of oxygen vacancy formation compared to the pristine $\text{In}_2\text{O}_3(111)$ surface. Microkinetic simulations reveal that only the supported Ni_6In_2 cluster can lead to high methanol selectivity. On this model, hydride species obtained by facile H_2 dissociation on the exposed Ni atoms are involved in the hydrogenation of adsorbed CO_2 to formate intermediates, which are subsequently converted to methanol. At higher temperatures, the decreasing hydride coverage leads to a shift in the selectivity to CO. On the Ni_2In_6 model, Ni species allow for facile CO_2 dissociation and subsequent CO desorption. Methanol formation is inhibited by high barriers for hydrogenation reactions. On both clusters, formation of methane is inhibited by high barriers for CO bond dissociation.



6.1 Introduction

Controlling anthropogenic CO₂ emissions is recognized as a crucial technological challenge to mitigate the negative effects of climate change.^{1–3} Capturing CO₂ from combustion processes or directly from air and transforming it into liquid hydrocarbons and chemicals can reduce such emissions and close the carbon cycle. Upgrading of CO₂ to hydrocarbons requires the use of hydrogen obtained from renewable energy sources such as solar and wind,^{4–6} which can contribute to the replacement of fossil transportation fuels. CO₂ can also be hydrogenated to chemicals that can serve as feedstock to various industrial chemical processes.^{7–10} In this context, methanol is particularly attractive, because it can be used as a fuel, a chemical building block and a precursor to common commodity chemicals such as olefins and aromatics.^{11–13}

Currently, large-scale methanol production is achieved by converting synthesis gas (CO/CO₂/H₂) over a Cu/ZnO/Al₂O₃ catalyst at temperatures of 473–573 K and pressures of 50–100 bar.¹⁴ Challenges arise, however, in the hydrogenation of CO₂-rich feeds to CH₃OH. Cu-based catalysts show significant activity for the reverse water-gas-shift reaction (rWGS) and suffer from deactivation by sintering of the active phase.^{15,16,17} Recently, indium oxide (In₂O₃) has emerged as a promising new catalyst for CO₂ hydrogenation to methanol.^{18–19,21,22,22–24} Advances in CO₂ hydrogenation to methanol by In₂O₃ have been reviewed recently.²⁵ Promoting In₂O₃ by metals can improve the rate of H₂ activation and CO₂ conversion. Due to the reducibility of In and the low melting temperature of In metal, the formation of alloys has been reported in metal-promoted In₂O₃ catalysts. For instance, Snider et al. combined experiments with density functional theory (DFT) calculations to show that the active sites in Pd-In catalysts are located at the interface between alloyed In–Pd particles and In₂O₃.²⁶ Modification of the In₂O₃ support has also been investigated. Frei et al. proposed that single atom (SA) Pd doped inside the In₂O₃ lattice can stabilize clusters of a few Pd atoms on the In₂O₃ surface, enhancing H₂ activation and, therefore, CH₃OH reaction rates.²⁷ Similar results have been reported for Pt-promoted In₂O₃.^{28–30} Dostagir et al. showed that Rh atoms doped in In₂O₃ can promote the formation of oxygen vacancies and methanol formation via formates.^{31,32} Given their price, it would be advantageous to replace the often used precious group metals by Earth-abundant alternatives, preferably cheap first-row transition metals. Bavykina et al. showed that alloying of Co with In can shift the selectivity from methane to methanol synthesis in CO₂ hydrogenation.³³ Jia et al. prepared highly dispersed Ni-In₂O₃ catalysts, which showed a higher activity in CO₂ hydrogenation while preserving high methanol selectivity.³⁴ In such catalysts, methane formation could be avoided by using a highly dispersed Ni phase. Recently, we showed that one of the role of Ni promoters for In₂O₃ is to facilitate H₂ dissociation on small Ni clusters.³⁵ Characterization of such Ni-In₂O₃ revealed the presence of Ni-In and Ni-Ni interactions in the used samples, suggesting the presence of small NiIn clusters. Snider et al. observed a higher activity of bimetallic Ni–In catalysts for CO₂ hydrogenation to CH₃OH compared to bare In₂O₃, which was attributed to the synergistic interactions between a Ni–In alloy and In₂O₃.²⁶ Frei et al. showed

that highly dispersed InNi₃ patches enhance methanol reaction rates on In₂O₃ by facilitating H₂ activation. This theoretical finding was contrasted with the predominant formation of CO and methane on extended surfaces of InNi₃ and Ni, respectively.³⁶ As it might be difficult to control the actual Ni/In ratio in the reduced catalysts, it is worthwhile investigating the role of this ratio on the structure and reactivity of NiIn clusters supported on In₂O₃.

In the present study, we employ DFT in combination with artificial neural networks (ANN), genetic algorithms (GA) and microkinetic modeling to systematically investigate the nature of the active sites and the mechanism of CO₂ hydrogenation to methanol and CO on NiIn clusters with different Ni/In ratios placed on the most stable In₂O₃ surface. To understand the nature of NiIn clusters on the In₂O₃(111) surface, we first explored stable structures of 8-atom NiIn cluster in the gas phase and supported on In₂O₃ using Genetic algorithms based on neural networks and DFT. Then, we selected two model systems representative of an In-rich and a Ni-rich cluster, namely Ni₂In₆ and Ni₆In₂. DFT calculations were then used to determine the energetics of the elementary reaction steps for CO₂ hydrogenation to CH₃OH, CO and H₂O. Microkinetic models based on this reaction energetics were constructed to predict the CO₂ consumption rate and the product distribution as a function of temperature. We perform a sensitivity analysis on the kinetic network to identify the elementary steps that control the rate of CO₂ consumption and CH₃OH selectivity. We herein show the factors underlying different activity and selectivity patterns on NiIn-In₂O₃ model catalysts during CH₃OH synthesis from CO₂ hydrogenation. This study highlights that NiIn clusters with exposed Ni atoms are the most active and selective to methanol, whereas clusters wherein Ni atoms are encapsulated by In atoms catalyze mainly CO formation.

6.2. Computational Methods

6.2.1 Density Functional Theory Calculations

All DFT calculations were conducted using the projector augmented wave (PAW) method³⁷ and the Perdew–Burke–Ernzerhof (PBE)³⁸ exchange–correlation functional as implemented in the Vienna Ab Initio Simulation Package (VASP) code.^{39,40} Solutions to the Kohn–Sham equations were calculated using a plane-wave basis set with a cut-off energy of 400 eV. The valence 5s and 5p states of In were treated explicitly as valence states within the scalar-relativistic PAW approach. All calculations were spin-polarized. The Brillouin zone was sampled using a 3x3x1 Monkhorst-Pack grid. Electron smearing was employed using Gaussian smearing with a smearing width (σ) of 0.1 eV. We chose the In₂O₃(111) surface termination, because it is more stable than the (110) and (100) surfaces, as shown in a previous computational study.⁴¹ The stoichiometric In₂O₃(111) surface was modelled as a two-dimensional slab with periodic boundary conditions. A vacuum region of 15.0 Å was introduced in the *c*-direction (perpendicular to the surface) to avoid spurious interactions between neighbouring supercells. It was verified that the electron density

approached zero at the edges of the periodic super cell in the c -direction. The bottom two of the four layers were frozen. The dimensions of the supercell are $14.57 \text{ \AA} \times 14.57 \text{ \AA} \times 26.01 \text{ \AA}$. The $\text{In}_2\text{O}_3(111)$ slab consisted of 96 O atoms and 64 In atoms, distributed in four atomic layers on top of which the NiIn clusters were placed. The electronic energies of gas-phase H_2 , H_2O , CO , CO_2 and CH_3OH were calculated using a cubic unit cell with lattice vector of 8 \AA . The Brillouin zone was sampled using a $1 \times 1 \times 1$ Monkhorst-Pack grid (G-point only). Gaussian smearing was employed. Electronic energies were corrected for zero-point energies of adsorbates and gas-phase molecules and finite-temperature contributions of the translational and rotational energies of gas-phase molecules.

The global minimum structure of various Ni-In compositions was obtained using artificial neural network (ANN) potentials and genetic algorithms (GA).^{42,43} These ANN potentials were used to accelerate the GA algorithm by offering a cheaper evaluation method to sample points in the phase space of cluster configurations. For constructing the ANN potential, we started with a dataset composed of In_2O_3 -supported Ni_8 clusters from an earlier study.⁴⁴ This dataset was expanded with bimetallic clusters by randomly substituting Ni with In in the clusters in the original set. Using the expanded dataset, reparameterization of the ANN potential was carried out. A GA method was then deployed to identify stable structures based on the ANN potential, which substitutes DFT calculations and, therefore, considerably speeds up the computations. DFT was still used to calculate the energies for structures that differ significantly from the training dataset. Specifically, this is done by reparametrizing the ANN potential with DFT for structures with a sample error exceeding the 2σ -range of the ANN dataset. In this way, new structures are added iteratively to the training dataset during the exploration of various Ni-In compositions. This allows the ANN to benefit from information obtained during earlier GA steps. Technical details of the ANN-GA process can be found in section D1 of the Appendix.

The influence of oxygen vacancies on the reaction energetics in the NiIn- In_2O_3 models was investigated by removing oxygen atoms from the $\text{In}_2\text{O}_3(111)$ lattice. The energy required to remove a surface oxygen to form a vacancy (ΔE_{Ov}) was calculated using either O_2 or H_2O as reference, according to the following two equations for the oxygen vacancy formation energy

$$\Delta E_{\text{Ov}} = E_{\text{defective slab}} - E_{\text{stoichiometric slab}} + E_{1/2\text{O}_2}, \quad (6.1)$$

$$\Delta E_{\text{Ov}} = E_{\text{defective slab}} - E_{\text{stoichiometric slab}} + E_{\text{H}_2\text{O}} - E_{\text{H}_2}, \quad (6.2)$$

where $E_{\text{defective slab}}$ is the electronic energy of the catalyst containing one oxygen vacancy and $E_{\text{stoichiometric slab}}$ is the reference energy of the stoichiometric slab. $E_{1/2\text{O}_2}$, $E_{\text{H}_2\text{O}}$ and E_{H_2} are the DFT-calculated energies of gas-phase O_2 , H_2O and H_2 , respectively.

The stable states were calculated using the conjugate-gradient algorithm. To find candidate transition states we employed the climbing-image nudged elastic band (CI-NEB) method.⁴⁵ A frequency analysis was performed for the stable and transition states. Specifically, it was verified that stable states have no imaginary frequencies and transition states have a single imaginary frequency in the direction of the reaction coordinate.⁴⁶ The mass-weighted Hessian matrix in this frequency analysis was constructed using a finite difference approach with a step size of 0.015 Å for displacement of individual atoms along each Cartesian coordinate. The corresponding normal mode vibrations were also used to calculate the zero-point energy (ZPE) correction and the vibrational partition functions.

Partial density of states (pDOS) analysis are conducted to analyze the electronic structure of each NiIn-In₂O₃ model catalyst using the Lobster package.^{47,48} The atomic charges of Ni atoms were calculated using the Bader charge method.⁴⁹

6.2.2 Microkinetic simulations

Microkinetic simulations were conducted based on the DFT-calculated activation barriers and reaction energies to investigate the kinetics of CO₂ hydrogenation to methanol. The chemo-kinetic network was modelled using a set of ordinary differential equations involving rate constants, surface coverages and partial pressures of gas-phase species. Time-integration of the differential equations was conducted using the linear multistep backwards differential formula method with a relative and absolute tolerance of 10⁻⁸.⁵⁰⁻
52

For the adsorption processes, the net rate of a gas-phase species i was calculated as:

$$r_i = k_{i,\text{ads}}\theta^*p_i - k_{i,\text{des}}\theta_i \quad (6.3)$$

where θ^* and θ_i are the fraction of free sites and the fraction of coverage species i , respectively. $k_{i,\text{ads/des}}$ is the rate constant for the adsorption/desorption process and p_i is the partial pressure of species i .

To derive a rate for the adsorption processes, we assumed that the adsorbate loses one translational degree of freedom in the transition state with respect to the initial state. From this assumption, the rate of adsorption derived from transition state theory can be expressed as follows:

$$k_{i,\text{ads}} = \frac{p A_{st}}{\sqrt{2\pi m_i k_B T}}, \quad (6.4)$$

where A_{st} and m_i are the effective area of an adsorption site and the molar mass of the gas species, respectively. p and T are the total pressure and temperature, respectively, and k_B is the Boltzmann constant.

The gas-phase entropy of the adsorbates was calculated using the thermochemical Shomate equation as given by

$$S^0 = A \cdot \ln(T) + B \cdot T + \frac{C \cdot T^2}{2} + \frac{D \cdot T^3}{3} - \frac{E}{2 \cdot T^2} + G, \quad (6.5)$$

where S^0 is the standard molar entropy.⁵³ The parameters A-G from equation (6.5) were obtained from the NIST Chemistry Webbook.⁵⁴ For the corresponding desorption processes, we assumed that the species gains two translational degrees of freedom and three rotational degrees of freedom in the transition state with respect to the initial state. From this assumption, the rate of desorption derived from transition state theory can be expressed as follows:

$$k_{\text{des}} = \frac{k_B \cdot T^3}{h^3} \cdot \frac{A_{\text{st}}(2\pi m k_B)}{\sigma \theta_{\text{rot}}} \cdot e^{\frac{\Delta E_{\text{des}}}{k_B T}} \quad (6.6)$$

Herein, k_{des} is the rate constant for the desorption of the adsorbate, h is the Planck constant, σ is the symmetry number and corresponds to the number of rotational operations in the point group of each molecule. θ_{rot} the rotational temperature, and ΔE_{ads} the desorption energy. The value of A_{st} is equal to $9 \cdot 10^{-19} \text{ m}^2$.

Finally, the rate constant (k) of an elementary reaction step is given by

$$k = \frac{k_B T}{h} \frac{Q^\ddagger}{Q} e^{\left(\frac{-\Delta E_{\text{act}}}{k_B T}\right)}, \quad (6.7)$$

where Q^\ddagger and Q are the partition functions of the activated complex and its corresponding initial state, respectively, and ΔE_{act} is the ZPE-corrected activation energy.

To identify the steps that control the CO₂ consumption rate and the product distribution, we employed the concepts of the degree of rate control (DRC) developed by Kozuch and Shaik⁵⁵⁻⁵⁶ and popularized by Campbell⁵⁷ as well as the degree of selectivity control (DSC).⁵⁷⁻⁵⁹

Herein, the degree of rate control coefficient is defined as

$$X_{\text{RC},i} = \left(\frac{\partial \ln r_i}{\partial \ln k_i} \right)_{k_{j \neq i}, K_i} \quad (6.8)$$

A positive DRC coefficient indicates that the elementary reaction step is rate-controlling, whereas a negative coefficient suggests that the step is rate-inhibiting. When a single elementary reaction step has a DRC coefficient of 1, this step is identified as the rate-determining step. Under zero extent of reaction, the sum of the DRC coefficients is conserved at one.⁶⁰

The DSC quantifies the extent to which a particular elementary reaction step influences the selectivity to certain products for which methanol is of our primary interest. The DSC of a particular key component is expressed as

$$X_{SC,i,c} = \left(\frac{\partial \eta_c}{\partial \ln k_i} \right)_{k_{j \neq i}, K_i}, \quad (6.9)$$

where $X_{SC,i,c}$ is the DSC of product C due to a change in the kinetics of elementary reaction step i , and η_c is the selectivity towards a key product (methanol in this work). Note that the relationship between DRC and DSC coefficient is given by

$$X_{SC,i,c} = \eta_c (X_{c,i} - X_{\text{reactant},i}). \quad (6.10)$$

Note that the sum of the DSC values of all elementary reaction steps for a single product equals zero.⁵⁸

6.3 Results and discussion

6.3.1 NiIn-In₂O₃ models

The ANN-GA method was used to identify stable structures for 8-atoms clusters, exploring the whole range of Ni/In ratios. The 10 most stable structures for each cluster composition are displayed in the Appendix D (Tables D3-5). We focus in this work on clusters with the following compositions, i.e. Ni₈, In₈, Ni₂In₆, and Ni₆In₂. For comparison, we also determined the most stable structures of the clusters in the gas phase (Figure 6.1). the free In₈-cluster adopts a cubic structure (Figure 6.1a). Bulk metallic In exists in tetragonal and cubic forms.³¹ On the In₂O₃(111) surface, the most stable In₈-cluster adopts a flat shape in which the number of In-In bonds is lowered compared to the gas-phase cluster due to the formation of In-O bonds (Figure 6.1b). The change in the morphology is driven by the stronger In-O (320 kJ/mol) compared to the In-In bond (100 kJ/mol) based on formation enthalpies of In₂O₃ and In metal.⁶¹ In accordance with this, the 10 most stable ANN-GA structures for In₈-In₂O₃ reported in Table D5 show that less stable clusters contain more In-In bonds. In the most stable gas-phase Ni₂In₆ cluster, the two Ni atoms form a Ni-Ni bond at the center of the cluster, whilst each Ni atom is coordinated by 4 In atoms (Figure 6.1c). This configuration can be explained by the stronger Ni-Ni bond in bulk Ni (262 kJ/mol) than the In-In bond in bulk In (100 kJ/mol).⁶¹ The Ni-Ni distance in the cluster is 2.31 Å, which is significantly shorter than the Ni-Ni distance in bulk Ni. The supported Ni₂In₆ cluster is shown in Figure 1d. The two Ni atoms bind directly to the In₂O₃(111) surface. Two In atoms adsorb on top of the two Ni atoms forming Ni-In bonds pointing away from the surface, while the other 4 In atoms adsorb around the Ni atoms binding to surface O atoms in different configurations. One of the In atoms has detached from the cluster. On average, each Ni atom is now coordinated by 1 O atoms of the support and 3 In atoms. The Ni-Ni distance in this configuration is 2.42 Å, which is slightly longer than the Ni-Ni distance in the gas-phase Ni₂In₆ cluster. The In atoms in the

Ni_2In_6 cluster carries a partial positive charge, while the Ni neighbors carry a slightly negative charge (Figure D2). The positive polarization of the In atoms is due to the different electronegativity between Ni and In (1.91 vs 1.78 on the Pauling scale, respectively), in line with an earlier theoretical work on PdIn alloys.⁶² The most stable Ni_6In_2 cluster in the gas phase contains a core of 6 Ni atoms with the two In atoms being three-fold coordinated on this core. The most stable Ni_6In_2 cluster placed on the In_2O_3 support adopts a bilayer structure, in line with previous work on a $\text{Ni}_8\text{-In}_2\text{O}_3$ cluster.⁴⁴ The bottom layer directly interacting with the support O atoms is formed by 4 Ni atoms with the other two Ni atoms being located in three-fold sites in the second layer (Figure 6.1f). The two In atoms occupy bridge and four-fold Ni sites. The In and Ni atoms in the Ni_6In_2 -cluster carry a partial positive charge, in line with a Ni_8 -cluster (Figure D2). Higher energy structures of the Ni_6In_2 clusters feature different adsorption positions for the In atoms and are more flat compared to the energy-minimum structure (Table D4). For completeness, we also show the most stable forms of the Ni_8 cluster in the gas phase (Figure 1g) and on the $\text{In}_2\text{O}_3(111)$ support (Figure 6.1h) taken from earlier work. The free Ni_8 -cluster has a square bipyramidal shape in line with an earlier computational study.⁶³ On the support the Ni_8 -cluster adopts a bilayer structure where 6 Ni atoms form the bottom layer with the other two Ni atoms placed on three-fold sites of the first Ni layer.

To determine the occurrence of configurations different from the minimum energy structure, we determined the Boltzmann probability distribution for the structures (section D2.2 of the Appendix). This analysis demonstrates that the most stable structure will be predominant (occurrence >90%) at a temperature at 400 K (Figure D3). Higher energy structures are thus not likely to occur at relevant temperatures. Accordingly, we focused only on the minimum energy structures of the clusters in our investigation of the kinetic mechanism. We noted that the Ni atoms the most stable Ni_2In_6 -clusters are surrounded by either In atoms from the cluster (in the gas phase, Figure 6.1c) or by atoms of the support and In atoms from the cluster (in the supported case, Figure 1d). Visual inspection of less stable structures shows that the Ni atoms are then also exposed (Table D5), suggesting that the low-energy structures expose more of the less reactive In metal atoms. To quantitatively understand these differences, we employed a statistical analysis. We first calculate the O or In atom with the smallest sum of squared distances with respect to the atoms in the cluster. We denote these atoms as O' and In'. We then determine the average distance of Ni and In atoms in the cluster with respect to O' and In'. The analysis reported in Figure D4 shows that both the In-O' and In-In' distances are on average always larger than the Ni-O' and Ni-In' ones. This indicates that, on average, Ni atoms are closer to the support, whereas In atoms are farther away from it. For the 50 most stable clusters, there are only six clusters for which the Ni-O' distance is larger than the In-O' distance (Figure D5a). These clusters have clearly exposed Ni atoms and are higher in energy (less stable) in comparison to the minimum energy structure (Table D6).

To gauge the stability of the supported clusters, we also calculated the energetics of removing one of the Ni or In atoms from the perimeter of the cluster. The results of these calculations are reported in Table D7-10. Removing a Ni atom from the clusters (Tables D7-8) is associated with high barriers ($\Delta E_{a, Ni_2In_6} = 201$ kJ/mol and $\Delta E_{a, Ni_2In_6} = 251$ kJ/mol) and is strongly endothermic ($\Delta E_{R, Ni_2In_6} = 219$ kJ/mol and $\Delta E_{R, Ni_2In_6} = 231$ kJ/mol). This is in line with the energy needed to remove a Ni atom from the Ni₈ cluster reported in an earlier study ($\Delta E_{a, Ni_8} = 232$ kJ/mol and $\Delta E_{R, Ni_8} = 192$ kJ/mol).⁴⁴ On the contrary, removing an In atom is much easier with activation energies of 64, 59 and 51 kJ/mol for Ni₂In₆, Ni₆In₂ and In₈, respectively (Table D9-10). The reactions are endothermic for Ni₂In₆ ($\Delta E_{R, Ni_2In_6} = 32$ kJ/mol) and Ni₆In₂ ($\Delta E_{R, Ni_6In_2} = 59$ kJ/mol) and nearly energy neutral for the In₈ cluster ($\Delta E_{R, In_8} = -1$ kJ/mol). The low barriers for migration of In is in line with the low In-O binding energy ref and the experimental observation of high mobility of reduced In species under CO₂ hydrogenation conditions.⁶⁴

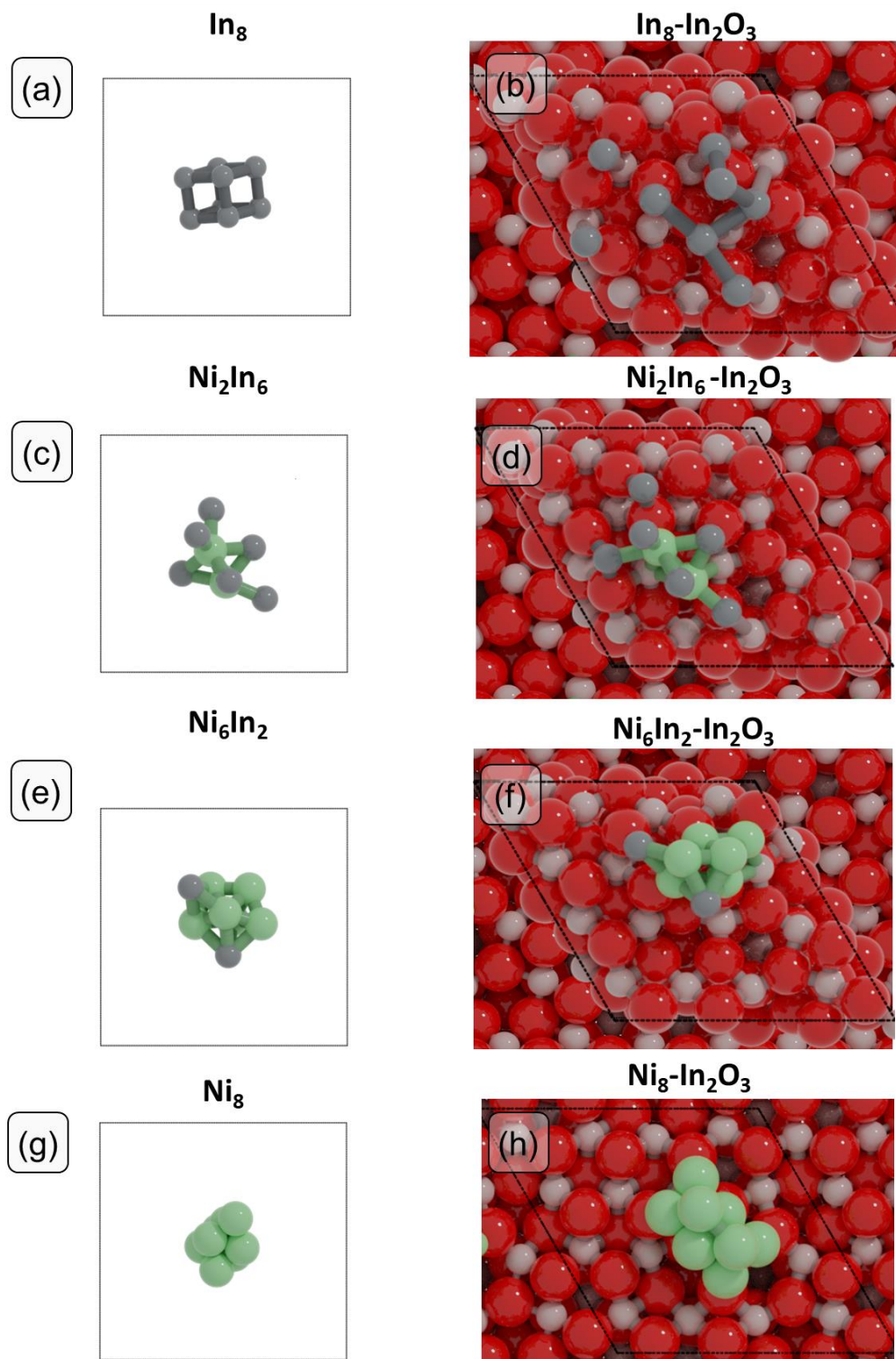


Figure 6.1. Energy minima structures obtained by the ANN-GA for gas-phase (a, c, e) and supported (b, d, f) In_8 , Ni_2In_6 and Ni_6In_2 clusters, respectively. Red: O; light grey: In atoms in In_2O_3 ; dark grey: In atoms in the cluster; green: Ni.

6.3.2 Oxygen vacancy formation

Previous experimental and theoretical works have clearly shown the important role of oxygen vacancies (Ov) in the In₂O₃ surface for CO₂ hydrogenation.^{18,20,21} The oxygen vacancy (Ov) formation energies (E_{Ov} , in eV) were calculated for the NiIn-In₂O₃ surfaces and compared with values for the In₂O₃(111) surface (Figure 6.2). As the oxygen vacancies in In₂O₃ are mainly obtained by reduction in H₂ leading to water formation, we report the E_{Ov} values with respect to gas-phase water. On the bare In₂O₃(111) surface (Figure 6.2a), the energy needed to remove an oxygen atom ranges between -0.65 and 0.99 eV.⁴¹ For the In₈ cluster on In₂O₃, the E_{Ov} values are significantly higher, namely between 0.36 and 1.29 eV (Figure 6.2b). The same holds for the Ni₂In₆ cluster on In₂O₃ with values between 0.18 and 1.04 eV (Figure 6.2c). For the Ni-rich Ni₆In₂ cluster, oxygen vacancy formation becomes easier with values ranging between -0.59 and 1.01 eV (Figure 6.2d). For comparison, we mention that the corresponding range for Ni₈-In₂O₃ is -0.22-0.99 eV.⁴⁴

Overall, the presence of the Ni₂In₆ and Ni₆In₂ clusters on the In₂O₃(111) surface results in changes in the oxygen vacancy formation energy. The oxygen vacancy formation process is endothermic referenced to water formation for the In₈ and Ni₂In₆ clusters, whereas it is exothermic for the Ni₆In₂ and Ni₈ clusters. Despite these differences, the energetics are not unfavorable with respect to oxygen vacancy formation under typical CO₂ hydrogenation conditions as discussed before.⁴⁴ To understand the role of these oxygen vacancies during CO₂ hydrogenation, we studied the elementary reaction steps leading to oxygen vacancy formation as part of the CO₂ hydrogenation mechanism to various products by DFT. The reaction energetics

will then be used in microkinetic simulations for the most stable Ni_2In_6 and Ni_6In_2 clusters placed on the In_2O_3 support.

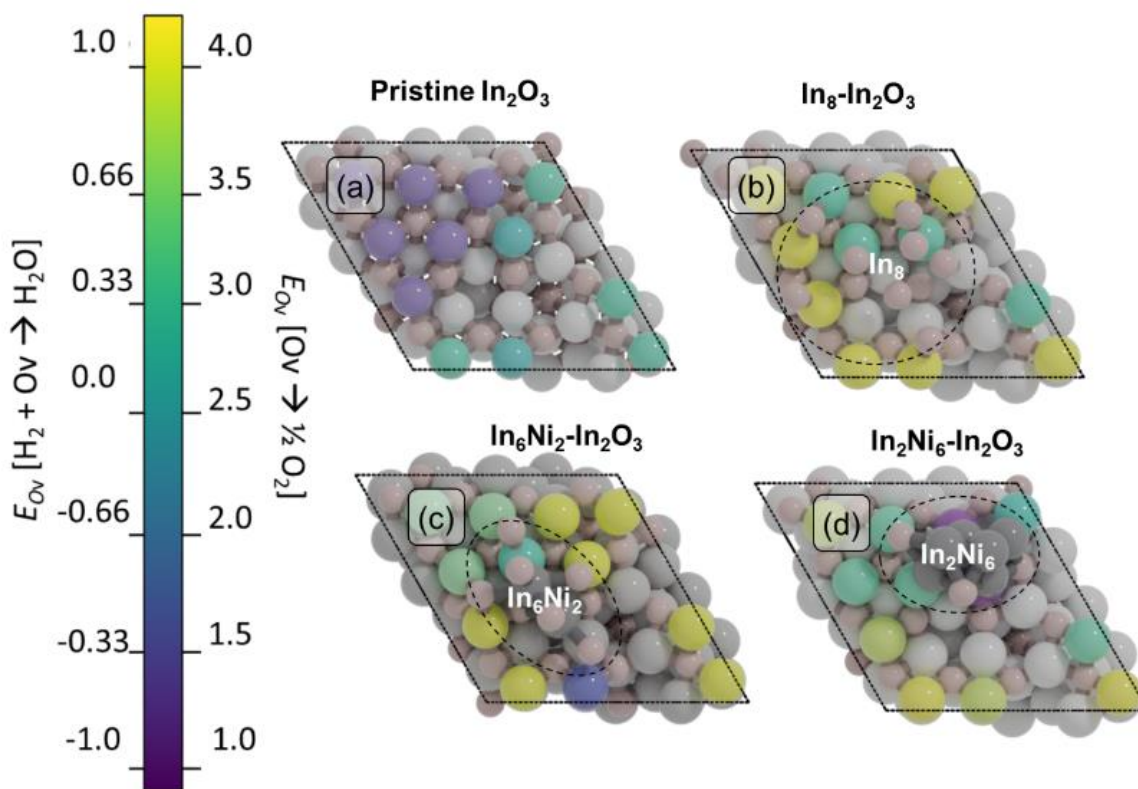


Figure 6.2: Oxygen vacancy formation energies (E_{Ov}) for the 12 surface oxygens on (a) bare In_2O_3 , (b) $\text{In}_8\text{-In}_2\text{O}_3$ (c) $\text{Ni}_6\text{In}_2\text{-In}_2\text{O}_3$ (d) $\text{Ni}_2\text{In}_6\text{-In}_2\text{O}_3$. The computed energies are referenced to gaseous O_2 and H_2O . The coloring of the 12 surface oxygen atoms represents their E_{Ov} . Ni atoms are colored in dark grey, while all other atoms are colored in light grey. The Ni species are highlighted inside dashed circles.

6.3.3 Reaction mechanism

We performed DFT calculations to elucidate the reaction mechanism of CO_2 hydrogenation to methanol (CH_3OH), carbon monoxide (CO) and water (H_2O). As methane was not observed in experiments for catalysts containing small Ni clusters placed on In_2O_3 ^{32,34} and, moreover, the use of NiIn alloys blocks methane formation pathways as compared to Ni,⁶⁶ we did not explore the full reaction pathways towards methane. In a previous theoretical study, we could explain the absence of methane formation for small Ni clusters to the very high barriers associated with C-O bond scission in adsorbed CO .⁴⁴ To verify that CO_2 methanation on small NiIn clusters is also difficult, we included direct CO dissociation as the most likely rate-limiting step in CO_2 methanation in the present study. The reaction network explored in this study is depicted in Figure 3. Based on previous computational studies, we investigated specific pathways for the

formation of oxygen vacancies via H₂O formation, the formation of CH₃OH via formate, and the reverse water-gas shift (rWGS) reaction leading to CO.⁶⁷⁻⁶⁹ The latter can take place either via direct C-O bond cleavage in CO₂ (redox pathway) or via an H-assisted pathway involving the COOH intermediate (carboxyl pathway). We discuss these steps for the Ni₂In₆ and Ni₆In₂ models to compare a Ni-lean and a Ni-rich cluster. We do not study the mechanism on the In₈-cluster as it does not contain Ni atoms. We highlight the main trends in activation energies and transition state structures and compare key elementary reaction steps with those found for the In₂O₃-supported Ni₈-cluster.⁴⁴ The structures corresponding to initial, transition and final states for all elementary reaction steps are shown in Appendix D (Section D5-6).

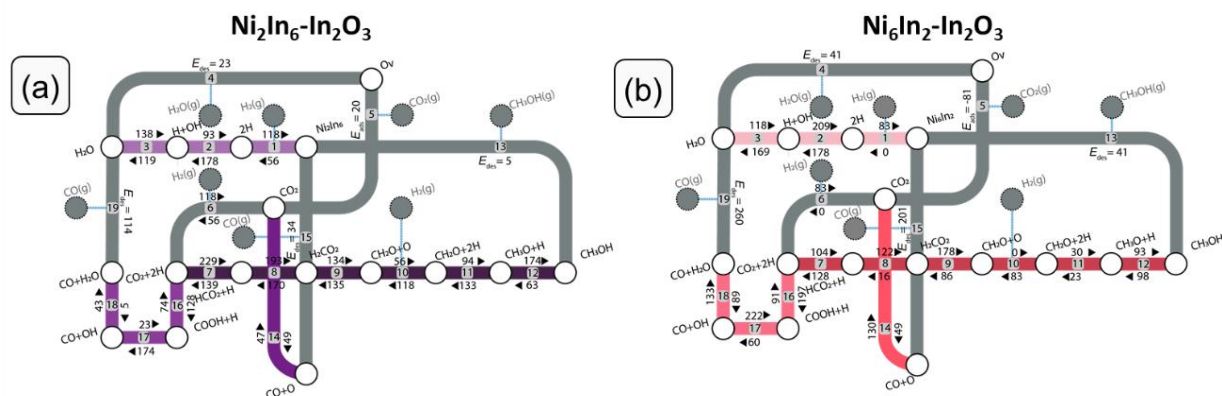


Figure 6.3. Full kinetic networks for CO₂ hydrogenation to CO and CH₃OH for (a) Ni₆In₂-In₂O₃ and (b) Ni₂In₆-In₂O₃ models. The numbers correspond to the elementary reaction steps as listed in Tables S11a-c.

6.3.3.1 Oxygen vacancy formation

We first discuss formation of an oxygen vacancy via formation of H₂O (steps 1-3). For each of the considered NiIn-In₂O₃ surfaces, we removed the oxygen with the lowest E_{Ov} (Figure 6.2). On Ni₂In₆-In₂O₃, dissociative adsorption of H₂ to form 2 Ni-H groups (step 1) has an activation energy of $\Delta E_a = 56$ kJ/mol and a reaction energy of $\Delta E_R = -62$ kJ/mol. In the final state (FS), one H atom occupies a bridge site between two Ni atoms, while the other H atom is at a bridge site between Ni and In. H₂ dissociation on In sites is associated with a high barrier (112 kJ/mol). This is expected as metallic indium is hardly capable of activating H₂ as reported in an earlier theoretical study.⁷⁰

H₂ activation on Ni₆In₂-In₂O₃ is spontaneous and results in two Ni-H moieties ($\Delta E_R = -83$ kJ/mol). This is in line with an earlier work on Ni clusters on In₂O₃ that highlighted how facile H₂ activation is a key factor in promoting methanol synthesis.⁴⁴ In the FS, both H atoms occupy threefold Ni sites. As a next step, we studied hydrogenation of the oxygen atom of the support with the lowest E_{Ov} to yield OH (step 2). The barrier for OH formation is 178 kJ/mol for both clusters. On Ni₂In₆, this step is endothermic ($\Delta E_R = 85$ kJ/mol) and results in a OH group bonded in bridge configuration between Ni and In. This step is

exothermic on Ni₆In₂ ($\Delta E_R = -32$ kJ/mol), which can be explained by the stronger binding of the OH group to only a Ni atom. The subsequent H₂O formation step (step 3) has a barrier of 119 kJ/mol ($\Delta E_R = -19$ kJ/mol) on Ni₂In₆, while this step has a high barrier of 169 kJ/mol ($\Delta E_R = 51$ kJ/mol) on Ni₆In₂. Water desorption from the surface (step 4) costs 23 and 41 kJ/mol on Ni₂In₆ and Ni₆In₂, respectively. The overall barriers for oxygen formation with respect to gas-phase H₂ are 122 kJ/mol for Ni₆In₂ and 123 kJ/mol for Ni₂In₆. The corresponding overall reaction energies are -13 kJ/mol for Ni₆In₂ and +28 kJ/mol for Ni₂In₆. The corresponding values for the Ni₈-cluster on In₂O₃(111) are $\Delta E_a = 57$ kJ/mol ($\Delta E_R = -22$ kJ/mol) and for the unpromoted In₂O₃(111) surface an overall barrier of $\Delta E_a = 57$ kJ/mol ($\Delta E_R = -64$ kJ/mol) is found.^{44,67}

6.3.3.2 Methanol formation

We start to explore methanol formation from the surfaces with an oxygen vacancy by adsorbing CO₂ (step 5). The potential energy diagram is shown in Figure 6.4. On Ni₂In₆, CO₂ adsorbs at the oxygen vacancy with the carbon atom coordinating to a lattice oxygen and the oxygen atoms bonding to In atoms of the cluster. On Ni₆In₂, CO₂ also adsorbs with its C atom in the oxygen vacancy and the oxygen atoms in CO₂ binding to In atoms of the cluster. Adsorbed CO₂ on the Ni₂In₆-cluster also occupies the oxygen vacancy but the O atoms in CO₂ bind to Ni atoms of the cluster. The CO₂ adsorption energy are -20 kJ/mol for Ni₂In₆ and -81 kJ/mol for Ni₆In₂. This is in line with the notion that the Ni–O bond (396 kJ/mol) is stronger than the In–O bond (320 kJ/mol) in the bulk oxides.⁷¹ On both clusters, another H₂ molecule dissociatively adsorbs on Ni next to adsorbed CO₂ (steps 6) similar to step 1. Next, CO₂ can be hydrogenated to formate, which is a precursor to methanol (steps 7-12). On Ni₂In₆, the HCOO intermediate is obtained by proton migration via the In atom (step 7). This step has a high barrier of 229 kJ/mol and is endothermic by 90 kJ/mol. The HCOO intermediate binds only to In atoms of the cluster. On Ni₆In₂, CO₂ is hydrogenated by Ni-H, resulting in a lower barrier of 104 kJ/mol ($\Delta E_R = 24$ kJ/mol). The resulting HCOO intermediate binds to Ni atoms. Next, HCOO is hydrogenated to H₂COO (step 8). On Ni₂In₆, hydrogenation by an In-H has a barrier of 193 kJ/mol ($\Delta E_R = 23$ kJ/mol). On the Ni₆In₂-cluster, hydrogenation by a Ni-H results again in a lower barrier of 122 kJ/mol ($\Delta E_R = 106$ kJ/mol). Next, cleavage of a C-O bond in the H₂CO₂ intermediate yields CH₂O with the O atom healing the oxygen vacancy (step 9). On Ni₂In₆, this step has a barrier of 134 kJ/mol and is energy neutral. The barrier is higher on Ni₆In₂ ($\Delta E_a = 178$ kJ/mol and $\Delta E_R = 92$ kJ/mol). Dissociative adsorption of another H₂ molecule on the cluster (step 10) leads to the CH₂O+2H state from which methanol is obtained via two consecutive hydrogenation steps. CH₃O formation on Ni₆In₂ (step 11) has an activation energy of 30 kJ/mol and is endothermic by $\Delta E_R = 7$ kJ/mol. On Ni₂In₆, this step is associated with a higher barrier of $\Delta E_a = 94$ kJ/mol and exothermic by $\Delta E_R = -39$ kJ/mol. The last hydrogenation event to adsorbed CH₃OH (step 12) features barriers of 174 and 93 kJ/mol on Ni₂In₆ and Ni₆In₂, respectively, with respective reaction energies of $\Delta E_R = 111$ kJ/mol and $\Delta E_R = -5$ kJ/mol. An important corollary of the findings so far is that hydrogenation involving Ni-H for the Ni₆In₂ cluster results

in lower barriers for hydrogenation as compared to In-H species for the Ni₂In₆ cluster. Desorption of methanol (step 13) closes the catalytic cycle of methanol synthesis with desorption energies of 5 and 41 kJ/mol on Ni₂In₆ and Ni₆In₂, respectively.

To verify that CO₂ methanation on small In₂O₃-supported Ni clusters does not occur, we computed the barriers for direct CO dissociation. This step is anticipated to be the key rate-limiting step in CO₂ methanation.⁷² The results are reported in Table D12. The structures of the IS, TS and FS can be found in Table D13. We can compare these results to data for CO dissociation pathways on In₂O₃-supported Ni clusters and extended surfaces of Ni by Sterk et al.⁷² The barriers for direct CO dissociation on Ni₂In₆ and Ni₆In₂ are close to 300 kJ/mol, close to the value of 312 kJ/mol for the Ni₈-cluster on In₂O₃(111).⁴⁴ In contrast, a significantly lower value is found on a Ni(110) surface ($\Delta E_a = 150$ kJ/mol) by Sterk et al.⁷²

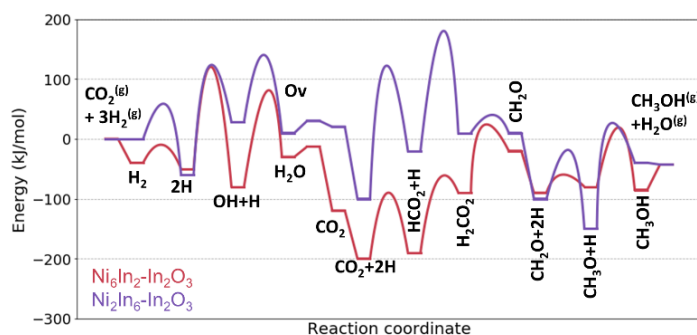


Figure 6.4. Potential energy diagrams of the conversion of CO₂ and H₂ to CH₃OH, and H₂O.

6.3.3.3 CO formation

Two pathways were considered for CO formation via the rWGS reaction namely the redox (PED in Figure 6.5a) and carboxyl (PED in Figure 6.5b) mechanism. The redox pathway involves the formation of an oxygen vacancy via H₂O formation (steps 1-4), adsorption of CO₂ (step 5) and subsequent dissociation of CO₂ and desorption of CO (steps 14 and 15, respectively). On both models, CO₂ dissociation takes place on the cluster. CO₂ adsorbs weaker on the clusters than on the Ov sites. CO₂ adsorption energies are -11 and -39 kJ/mol for Ni₂In₆ and Ni₆In₂, respectively, compared to typical values of -81 and -20 kJ/mol for adsorption in the Ov sites. Attempts to identify transition states for C-O dissociation in CO₂ adsorbed on an oxygen vacancy were not successful. Direct C-O bond scission in CO₂ is associated with a forward barrier of 49 kJ/mol on both clusters. On Ni₂In₆, this step is energy neutral with the CO finally binding to two Ni atoms. However, on Ni₆In₂ this step is exothermic by $\Delta E_R = -81$ kJ/mol, which relates to the stronger adsorption of CO in a three-fold site. CO desorption is endothermic by 34 and 201 kJ/mol on Ni₂In₆- and Ni₆In₂-In₂O₃, respectively.

Alternatively, CO can be obtained via the carboxyl mechanism involving a COOH intermediate, which occurs on the clusters, in line with an earlier work on In_2O_3 -supported Ni clusters.⁴⁴ No TS could be found for the redox pathway starting from CO_2 adsorbed on the oxygen vacancy site. First, one of the oxygen atoms of the adsorbed CO_2 molecule is protonated to form COOH (step 16). This step has an activation energy of 128 and 197 kJ/mol for Ni_2In_6 and Ni_6In_2 , respectively. Furthermore, this step is endothermic for both systems ($\Delta E_{\text{R, Ni}_2\text{In}_6} = +53$ kJ/mol and $\Delta E_{\text{R, Ni}_6\text{In}_2} = +106$ kJ/mol). Next, the COOH intermediate dissociates into CO and OH (step 17). On Ni_2In_6 , this step is associated with a barrier of 174 kJ/mol and is endothermic ($\Delta E_{\text{R}} = +152$ kJ/mol). In the FS, CO and OH occupy bridge Ni-Ni and bridge In-In sites, respectively. This step is exothermic on Ni_6In_2 by $\Delta E_{\text{R}} = -162$ kJ/mol with an activation energy of $\Delta E_{\text{act}} = 60$ kJ/mol. Both CO and OH moieties end up binding to Ni atoms of the cluster. The formation of Ni-O bonds results in a more stable FS compared to the Ni_2In_6 cluster where In-O bonds are formed. Hydrogenation of OH originating from COOH scission leads to the formation of H_2O (step 18). On Ni_2In_6 , this step has an activation energy of 43 kJ/mol and is endothermic by $\Delta E_{\text{R}} = +44$ kJ/mol. On Ni_6In_2 , this step has a higher barrier of 133 kJ/mol and a reaction energy of $\Delta E_{\text{R, Ni}_6\text{In}_2} = +44$ kJ/mol. Finally, CO desorbs (step 19) with a desorption barrier of 114 and 260 kJ/mol on Ni_2In_6 and Ni_6In_2 , respectively.

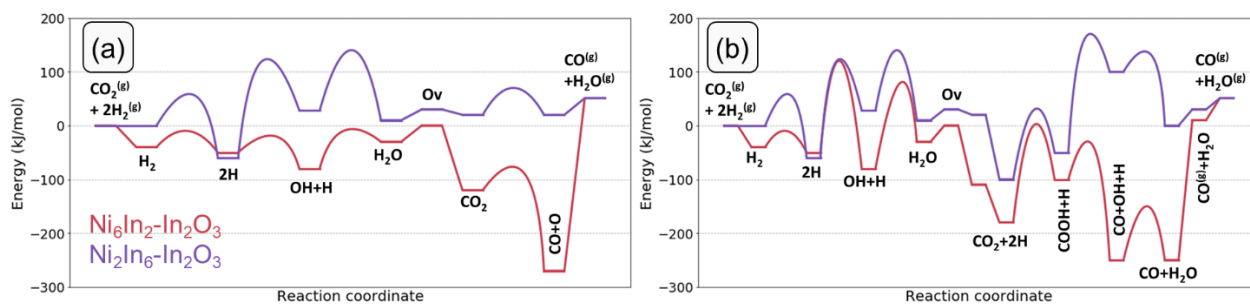


Figure 6.5. Potential energy diagrams of the conversion of CO_2 and H_2 to CO and H_2O . (a) redox pathway and (b) carboxyl pathway.

6.3.4 Microkinetic simulations

6.3.4.1 Overall kinetics

To compare the catalytic performance of the different NiIn- In_2O_3 models, we compute the CO_2 hydrogenation reaction rate employing microkinetic simulations based on the DFT-computed reaction energetics. The active sites in our model consist of clusters placed on the In_2O_3 support. We do not take migration of intermediates between the active sites into account. Co-adsorbed species are modelled as distinct varieties of a single active site. In this approximation, all elementary reaction steps are unimolecular, with exception of the adsorption and desorption steps. A detailed list of the elementary reaction steps is provided in Appendix D.

The CO₂ consumption rate and the CH₃OH selectivity as a function of temperature are shown in Figure 5. Herein, we also compare the current reaction kinetics to those obtained for bare In₂O₃ based on published DFT data by Frei et al.⁶⁷ and for a Ni₈-cluster on In₂O₃ based on our previous data.⁴⁴ Furthermore, the turnover frequencies (TOF) towards CH₃OH and CO are given in Figure D6. For $T < 300$ °C, the CO₂ conversion rate decreases in the order Ni₈ > Ni₆In₂ = In₂O₃ > Ni₂In₆ (Figure 6.5a). Concerning methanol selectivity (Figure 6.5b), In₂O₃ is the most selective (100% methanol selectivity at $T = 200$ °C) followed by the Ni₈- and Ni₆In₂-cluster (methanol selectivity of 95% and 92% at $T = 200$ °C, respectively). Notably, these results are qualitatively in line with the experimental results published by Jia et al for Ni-In₂O₃ catalysts.³⁴

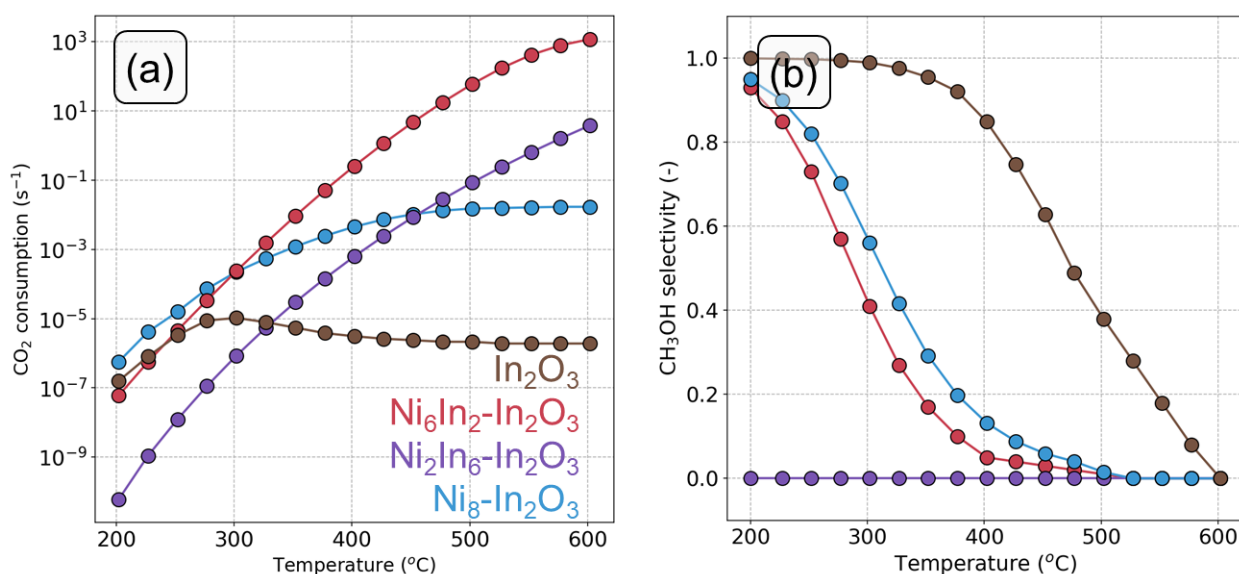


Figure 6.5. (a) CO₂ consumption rate (s⁻¹) and (b) CH₃OH selectivity as a function of temperature on different models ($p = 50$ bar, H_2/CO_2 ratio =5). The data for In₂O₃-bare are taken from reference [73] while the data for Ni₈-In₂O₃ is taken from reference.⁴⁴

The results in terms of coverage, apparent activation energy (E_{app}) and reaction orders as a function of temperature are given in Figure 6.6. The dominant state on the Ni₂In₆-cluster for $T < 500$ °C features two adsorbed H species (Figure 6.6a). This is because the two subsequent steps of hydrogenation of a lattice oxygen to form H₂O in the oxygen vacancy formation pathway (steps 2-3) are associated with high barriers (178 and 119 kJ/mol, respectively). These steps are the most difficult ones in the oxygen vacancy pathway (Figure 3a). At $T > 500$ °C, formation of H₂O is easier, leading to more oxygen vacancies. This results in a decrease in the coverage of 2H in favor of the Ov state (Figure 6.6a). At low temperature, the reaction orders in both CO₂ and H₂ are close to zero (Figure 6c). Under these conditions, the reaction is limited by the rate of OH hydrogenation (step 2) which is not affected by the partial pressures of H₂ and CO₂.

Furthermore, sufficient H is available on the surface, as follows from Figure 6.6a. At higher temperature ($T > 500$ °C), a positive reaction order in CO_2 is observed. As under these conditions adsorption of CO_2 on the surface becomes more difficult, a higher partial pressure of CO_2 would increase the overall rate. On the Ni_2In_6 -cluster, the apparent activation energy (E_{app}) is constant at 178 kJ/mol for temperatures below 500 °C (Figure 6.6c). This value corresponds to the activation energy of OH hydrogenation (178 kJ/mol). As the temperature increases this step becomes more kinetically accessible and, as a result, E_{app} decreases.

The Ni_6In_2 cluster predominantly resides in the HCO_2+H state at $T < 400$ °C (Figure 6.6b). The reason for this is that hydrogenation of HCO_2 to H_2CO_2 has a high barrier ($\Delta E_a = 122$ kJ/mol). Furthermore, the subsequent step of H_2CO_2 dissociation into $\text{CH}_2\text{O}+\text{O}$ is associated with a high barrier ($\Delta E_a = 178$ kJ/mol). This results in an overall barrier associated with converting the HCO_2+H state to the $\text{CH}_2\text{O}+\text{O}$ state of 201 kJ/mol, limiting the progress of the overall reaction. For $T > 400$ °C, the coverage of HCO_2+H decreases in favor of the CO_2 and Ov states. The latter becomes dominant for $T > 575$ °C. At low temperature, the reaction order in both H_2 and CO_2 is close to zero because the surface is mainly covered by HCO_2+H , originating from CO_2 hydrogenation (Figure 6.6d). Thus, further increasing the partial pressure of the reactants will not affect the reaction rate. With increasing temperature, the reaction order in H_2 becomes negative indicating that an increase in the partial pressure of this reactant would push the reaction away from the dominant product. At high temperature ($T > 500$ °C), the reaction order in CO_2 becomes positive. Under these conditions, a higher partial pressure of CO_2 results in a higher coverage of reaction intermediates derived from CO_2 , increasing the CO_2 turnover rate. This behavior is also reflected in the E_{app} trend (Figure 6.6d). The E_{app} is approximately constant below 400 °C and decreases at higher temperature. By comparing Figure 6.6b and 6.6d, it can be seen that the decrease in the E_{app} goes together with an increase of the oxygen vacancies, resulting in a higher coverage of CO_2 . The exothermic energy of CO_2 adsorption ($\Delta E_{\text{ads}} = -81$ kJ/mol) lowers the apparent activation energy of the overall reaction.

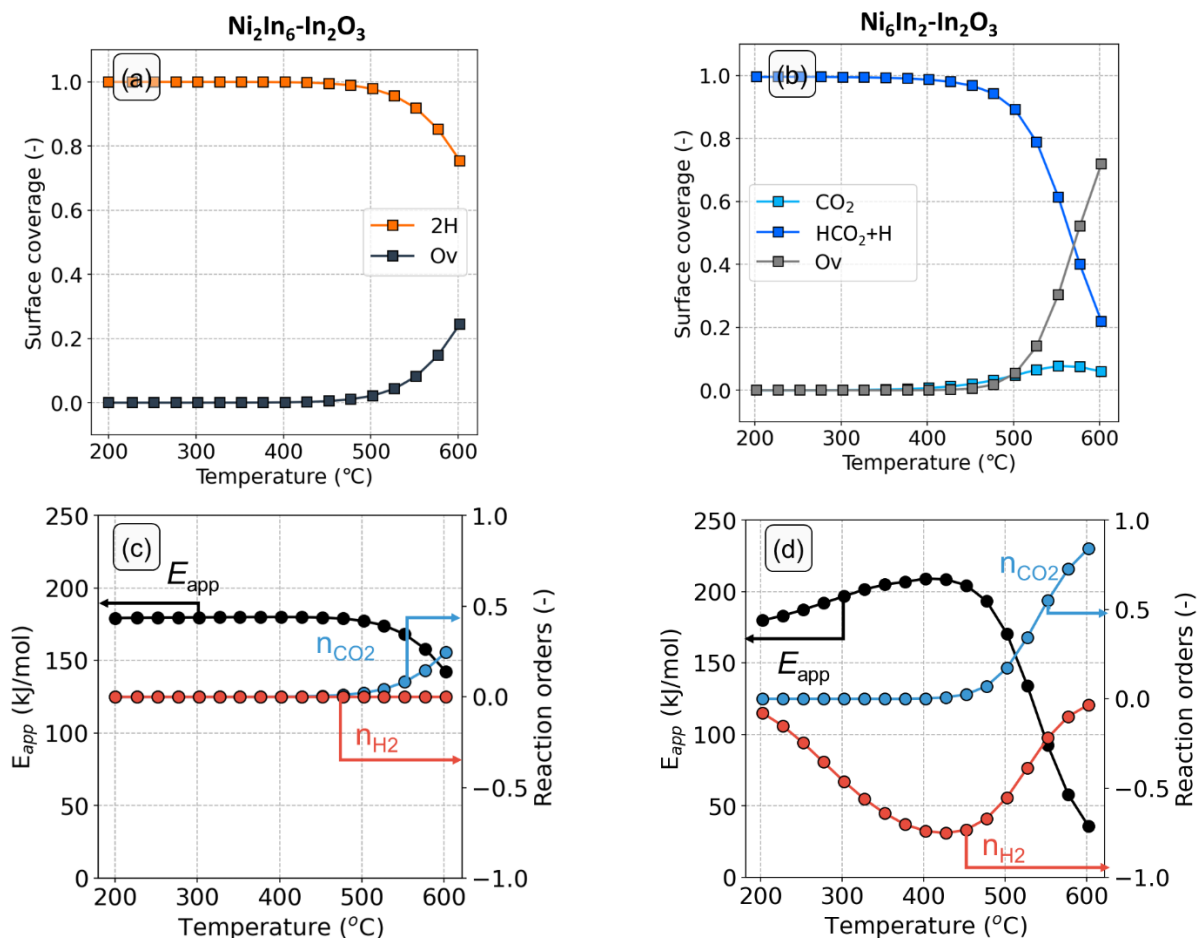


Figure 6.6. Surface state of different model catalysts (a-b) and reaction orders and apparent activation energies (c-d) with CO_2 as key component as a function of temperature.

6.3.4.2 Rate and selectivity control of the reaction network

In this section, we discuss in detail the reaction network that leads to CH_3OH and CO formation from CO_2 hydrogenation on the two $\text{NiIn-In}_2\text{O}_3$ models. We identify the elementary steps that control the overall CO_2 consumption rate and the CH_3OH selectivity and investigate how these steps change with reaction temperature. For this purpose, we conduct a sensitivity analysis based on Campbell's degree of rate control (DRC)⁵⁷ and selectivity control (DSC).^{59,74}

6.3.4.2.1 Ni_2In_6 -cluster

The DRC analysis and reaction flux analysis for the Ni_2In_6 -cluster model are shown in Figure 6.7a and 6.7b, respectively. At $T < 500$ °C, the CO_2 consumption rate is mostly controlled by the rate of OH hydrogenation (step 2), because this elementary step has the highest barrier in the oxygen vacancy formation pathway ($\Delta E_a = 178$ kJ/mol). This result is consistent with the surface state of the catalyst featuring mostly adsorbed hydrogen species (2H, Figure 6.6b). At higher temperature ($T > 500$ °C), formation of oxygen vacancies

and subsequent adsorption of CO_2 result in a decrease in the DRC coefficient of OH hydrogenation (step 2) in favor of CO_2 dissociation (step 14, $\Delta E_a = 49$ kJ/mol). The dominant pathway (Figure 6.7b, right) proceeds via a redox pathway involving formation of an oxygen vacancy (steps 1-3), direct dissociation of CO_2 and subsequent CO desorption (steps 14 and 19, respectively). The redox pathway is preferred over the carboxyl pathway for CO formation because CO_2 hydrogenation to COOH is associated with a higher barrier compared to CO_2 direct dissociation (128 and 49 kJ/mol, respectively). Compared to the dominant pathway to CO, the formate pathway to methanol has very low fluxes. This pathway is not taken because the hydrogenation of CO_2 to HCO_2 (step 7) is associated with a high barrier ($\Delta E_a = 229$ kJ/mol) inhibiting methanol formation. The preference of the redox pathway to CO over the formate pathway to methanol results in a negligibly low methanol selectivity as shown in Figure 6.5b.

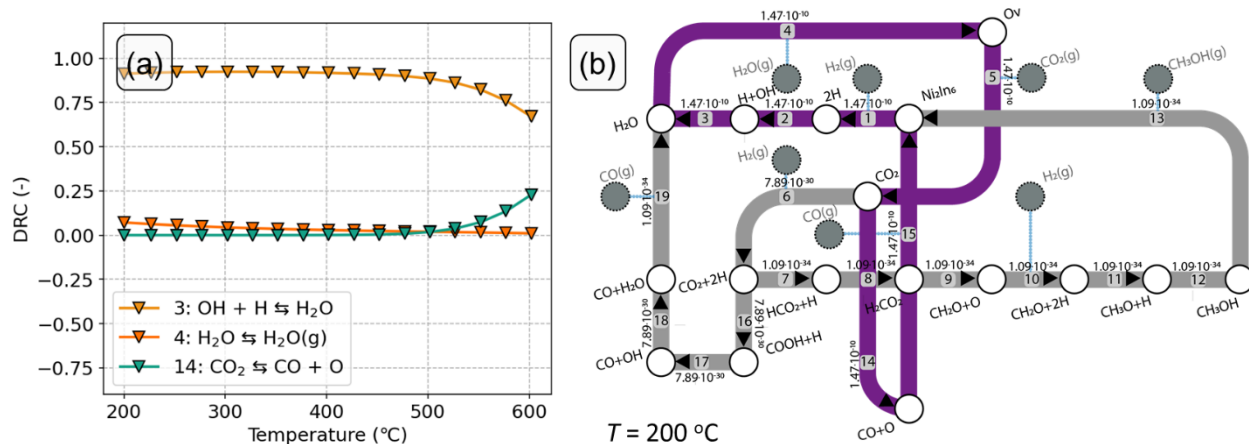


Figure 6.7. (a) Degree of rate control analysis with CO_2 as key component as a function of temperature for the $\text{Ni}_2\text{In}_6\text{-In}_2\text{O}_3$ model. (b) Reaction network analysis for CO_2 hydrogenation to CH_3OH , CO and H_2O at $T = 200$ °C. Herein, the dominant pathway is highlighted in purple, whereas the other paths are in grey. The numbers in the arrows are molar reaction rates (s^{-1}) and are normalized with respect to the amount of adsorbed CO_2 .

6.3.4.2.2 Ni_6In_2 -cluster

The DRC and DSC analyses for the Ni_6In_2 -cluster model are reported in Figures 8a and 8b, respectively. At low temperature (200 °C $< T < 300$ °C), the rate of CO_2 consumption is mainly controlled by the rate of H_2CO_2 dissociation into $\text{CH}_2\text{O} + \text{O}$ (step 9, Figure 6.8a). This step has the highest activation energy in the dominant pathway as seen from Figure 8b ($\Delta E_a = 178$ kJ/mol). With respect to the dominant state ($\text{HCO}_2 + \text{H}$, Figure 6b), the overall barrier of the main rate-limiting step to methanol formation amounts to 201 kJ/mol. The step of CO_2 dissociation (step 14, $\Delta E_a = 49$ kJ/mol) controls the overall rate to a smaller extent as can be seen by its lower DRC coefficient. This result is in line with the reaction order in H_2 and CO_2 of zero

predicted by the model (Figure 6.6d). An increase in the partial pressure of the reactants would not affect this elementary step and thus the overall rate. The DSC analysis (Figure 6.8c) shows that the same elementary steps that are controlling the rate are also controlling methanol selectivity. An increased rate of H₂CO₂ dissociation would result in a higher flux in the route towards methanol, benefiting its formation at the expense of CO formation. With increasing temperature, a change in the selectivity from methanol to CO is observed (Figure 6.5b), which is reflected by the DRC analysis. Herein, the DRC coefficient of H₂CO₂ dissociation decreases, whereas the DRC coefficient of CO₂ dissociation (step 14, $\Delta E_a = 49$ kJ/mol) increases. This last step pertains to the rWGS branch in the kinetic network and thus inhibits the selectivity towards methanol. The selectivity shift towards CO at high temperature can be explained on the basis of the surface state of the Ni₆In₂-In₂O₃ model. At high temperature, Ni-H species are less abundant, as we previously observed (Figure 6.6a). This suggests that steps requiring less surface hydrogen, like the ones pertaining to the rWGS pathway are preferred over steps of the formate pathway. To confirm the effect of H₂ partial pressure on CH₃OH selectivity, we performed a simulation with a H₂:CO₂ ratio of 1:5 (instead of 5:1) and observed that the selectivity to CH₃OH decreases to 45% at 250 °C (Figure D7). Thus, the selectivity shift to CO observed at high temperature can be explained by the lower availability of Ni-H species at such temperatures. This is in line with our earlier work on Ni clusters on In₂O₃.⁴⁴

Figures 6.8b and 6.8d show the flux analysis at low and high temperature, respectively. At low temperature (Figure 6.8b), the dominant pathway features the formation of an oxygen vacancy (steps 1-4), followed by CO₂ adsorption (step 5) and hydrogenation to methanol via formate (steps 6-13). At high temperature (Figure 8d), the dominant pathway features the formation of an oxygen vacancy, followed by adsorption and dissociation of CO₂ (steps 5 and 14, respectively) and subsequent CO desorption (step 15). The redox pathway is preferred over the carboxyl pathway for the formation of CO because hydrogenation of CO₂ to COOH is associated with a higher barrier compared to direct CO₂ dissociation (197 and 49 kJ/mol, respectively).

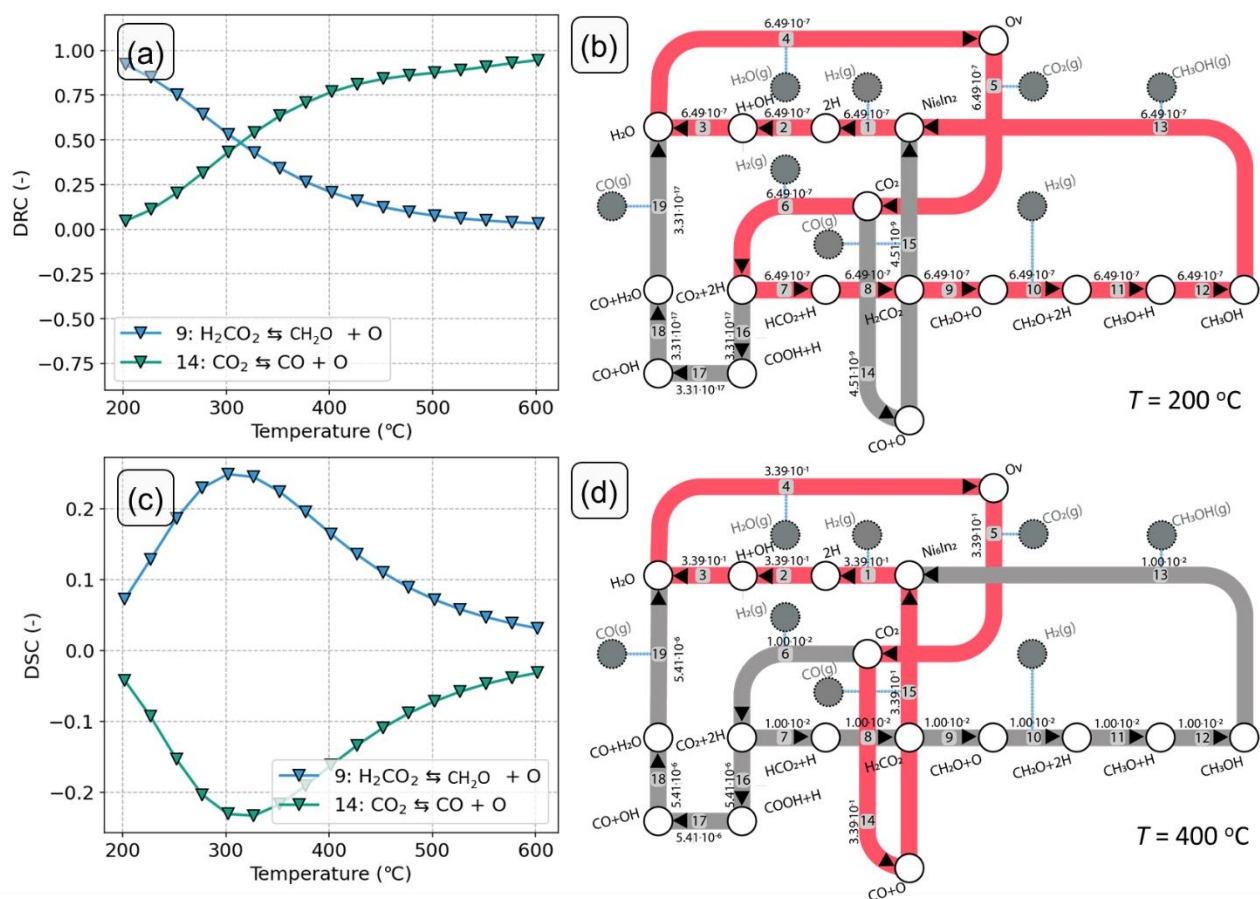


Figure 6.8. (a) DRC and (b) DSC analysis with CO₂ as key component as a function of temperature for the Ni₆In₂-In₂O₃ model. Reaction network analysis for CO₂ hydrogenation to CH₃OH, CO and H₂O at (a) $T = 200$ °C and (b) $T = 400$ °C. Herein, the dominant pathway is highlighted in pink, whereas the other paths are in grey. The numbers in the arrows are molar reaction rates (s⁻¹) and are normalized with respect to the amount of adsorbed CO₂.

6.3.4.3 General Discussion

The present study provides new insights into the role of Ni-In clusters in the In₂O₃-catalyzed hydrogenation of CO₂ to methanol. The explored reaction mechanism includes a direct route for CO₂ hydrogenation to methanol (formate pathway) and the competing reverse water-gas shift (rWGS) reaction. The latter can take place either via direct C-O bond cleavage in CO₂ (redox pathway) or via an H-assisted pathway involving the COOH intermediate (carboxyl pathway). A key result of this study is that an In₂O₃-supported Ni₆In₂ cluster (representing Ni-rich clusters) mainly catalyzes methanol formation, whereas a Ni₂In₆ cluster (representing In-rich clusters) mainly catalyze CO formation.

Methanol formation involves oxygen vacancies in the In₂O₃ support. Frei et al. reported oxygen vacancy formation on an In₂O₃(111) surface via homolytic dissociation of molecular hydrogen forming two surface OH groups, followed by water formation and desorption.⁷³ Oxygen vacancy formation has an overall barrier of 67 kJ/mol with respect to gas-phase H₂.⁴¹ Heterolytic H₂ dissociation on this surface was found to have a similar overall barrier.⁷⁵ The presence of Ni₂In₆ or Ni₆In₂ clusters increases the overall barrier to 122 and 123 kJ/mol, respectively. Notably, these values are also higher than the ones found for a In₂O₃-supported Ni₈ cluster (57 kJ/mol) in an earlier work.⁴⁴

On the Ni₆In₂ cluster, at relatively low temperature, the formate pathway to methanol is preferred over the rWGS reaction, resulting in high methanol selectivity. We compare the results in terms of TOF_{CH₃OH} of the Ni₆In₂ cluster with the supported Ni₈ cluster reported in an earlier work.⁴⁴ Although methanol is the main product at low temperature for both cases, the Ni₆In₂ cluster exhibits a lower TOF_{CH₃OH} at low temperature (Figure D6). This can be explained by differences in the overall barrier of the rate-determining step for methanol formation with respect to the dominant state, which is in both cases the HCO₂+H state. The overall barrier is higher for the Ni₆In₂ cluster (201 kJ/mol) compared to the Ni₈-cluster (177 kJ/mol). With increasing temperature, the selectivity shifts to CO (Figure 6.5b) in line with experimental observations for typical Ni-In₂O₃ catalysts.^{34,35} The dependence of the selectivity on the temperature relates to the presence of hydride species on exposed Ni sites (NiH^δ). At relatively low temperature, there are sufficient hydrides present, which are involved in hydrogenation reactions. With increasing temperature, the H coverage decreases. As the rWGS reaction requires less H atoms than methanol formation, the selectivity shifts to CO when the H coverage decreases. We find that small Ni and (Ni-rich) NiIn clusters on In₂O₃ catalyze methanol formation via the same mechanism.

On the Ni₂In₆ cluster model, oxygen vacancy formation is endothermic and is furthermore kinetically limited by OH hydrogenation. The presence of Ni sites surrounded by inactive In atoms results in a lower coverage with H. The dominant pathway is a redox mechanism involving formation of oxygen vacancies, direct CO₂ dissociation and CO desorption. Compared to this, the formate pathway to methanol has very high barriers, resulting in a very low methanol selectivity. We explain the higher barrier for the formate pathway on Ni₂In₆ in comparison to Ni₆In₂ using Bader charges (BC) for the atoms involved in the elementary step of CO₂ hydrogenation to HCOO (step 6 in Figure 6.3). The results are shown in Figure D8. As previously discussed, the In atoms in the Ni₂In₆ cluster carry a slightly positive charge due to the electronegativity difference between Ni and In. In the initial state of step 6, the C atoms the CO₂ and the neighboring In atom ($d(\text{C-In}) = 2.8 \text{ \AA}$) carry the charges +2.1 |e| and +0.6 |e|, respectively (Figure D8a). This leads to electrostatic repulsion between the adsorbate and the neighboring In atom, which destabilizes the TS, resulting in a high barrier ($\Delta E_{a,\text{Ni}_2\text{In}_6} = 229 \text{ kJ/mol}$). On top of this electrostatic repulsion, the In

atoms in the cluster weaken adsorption of CO₂ due to the absence of *d*-orbitals in their valence shell. In contrast, on the Ni₆In₂ cluster, adsorbed CO₂ (BC(C) = +2.1 |e|) neighbors a Ni atom (d(C-Ni) = 2.7 Å) which has a lower charge (BC(Ni) = +0.3 |e|, Figure D8b) compared to the charge on the In atom in the Ni₂In₆ cluster. This results in a lower destabilization effect on the TS and, thus, in a lower barrier compared to the Ni₂In₆ cluster ($\Delta E_{a, Ni_6In_2} = 104$ kJ/mol). Similar considerations can explain the different barriers of other steps of the formate pathway (steps 8, 11-13) for the two models.

We also discuss here our results in comparison to those recently reported in the literature. Large Ni particles mainly catalyze methane formation in CO₂ hydrogenation due to the presence of step-edge sites, which can catalyze C-O bond scission with relatively low barriers.⁷⁶ With decreasing Ni particle size, the number of step-edge sites decreases, resulting in a lower methane selectivity.⁷² In earlier works, we reported that small Ni clusters promote H₂ dissociation, resulting in enhanced methanol formation compared to the unpromoted oxide.^{44,65} Such clusters are inactive for CO bond dissociation and thus do not lead to methane product. Thanks to the reducibility of In and its mobility due to the low melting point of In, it is likely that Ni-In alloys are formed, which has been experimentally confirmed.^{36,65} Frei et al. reported that InNi₃ patches on the In₂O₃(111) surface supply neutral hydrides to the In₂O₃, thereby boosting methanol formation at the expense of CO formation. This is in line with our findings that an interface between Ni-rich bimetallic phases (Ni₆In₂) and In₂O₃ would mainly lead to methanol. In contrast, the presence of Ni sites surrounded by In atoms (Ni₂In₆) results in CO as the main reaction product.

6.4. Conclusions

The role of NiIn clusters on In₂O₃ for CO₂ hydrogenation to methanol was investigated using DFT and microkinetic simulations. We explored the structure of a range of 8-atom clusters containing Ni and In placed on the most stable In₂O₃ termination using artificial neural networks and genetic algorithms. We selected two clusters, one rich in In, Ni₂In₆, and one rich in Ni, Ni₆In₂. The presence of such clusters increases the overall barrier of oxygen vacancy formation compared to the pristine In₂O₃(111) surface. Microkinetic simulations reveal that the Ni-rich Ni₆In₂ cluster is conducive to the formation of methanol, while the In-rich one only leads to CO formation. The mechanism involves oxygen vacancy formation in the support, CO₂ adsorption and hydrogenation to formates that further react to methanol. The decreasing H coverage at higher temperature leads to a shift in the product distribution to CO. CO formation involves direct CO₂ dissociation on oxygen vacancies. The lower stability of H species on the Ni₂In₆ cluster precludes formation of methanol and, henceforth, CO is the dominant product.

6.5 References

- (1) González-Garay, A.; Frei, M. S.; Al-Qahtani, A.; Mondelli, C.; Guillén-Gosálbez, G.; Pérez-Ramírez, J. Plant-to-Planet Analysis of CO₂-Based Methanol Processes. *Energy Environ. Sci.* **2019**, *12*, 3425–3436.
- (2) Kondratenko, E. V.; Mul, G.; Baltrusaitis, J.; Larrazábal, G. O.; Pérez-Ramírez, J. Status and Perspectives of CO₂ Conversion into Fuels and Chemicals by Catalytic, Photocatalytic and Electrocatalytic Processes. *Energy Environ. Sci.* **2013**, *6*, 3112.
- (3) Dias, V.; Pochet, M.; Contino, F.; Jeanmart, H. Energy and Economic Costs of Chemical Storage. *Front. Mech. Eng.* **2020**, *6*, 21.
- (4) Álvarez, A.; Bansode, A.; Urakawa, A.; Bavykina, A. V.; Wezendonk, T. A.; Makkee, M.; Gascon, J.; Kapteijn, F. Challenges in the Greener Production of Formates/Formic Acid, Methanol, and DME by Heterogeneously Catalyzed CO₂ Hydrogenation Processes. *Chem. Rev.* **2017**, *117*, 9804–9838.
- (5) Zhong, J.; Yang, X.; Wu, Z.; Liang, B.; Huang, Y.; Zhang, T. State of the Art and Perspectives in Heterogeneous Catalysis of CO₂ Hydrogenation to Methanol. *Chem. Soc. Rev.* **2020**, *49*, 1385–1413.
- (6) Jiang, X.; Nie, X.; Guo, X.; Song, C.; Chen, J. G. Recent Advances in Carbon Dioxide Hydrogenation to Methanol via Heterogeneous Catalysis. *Chem. Rev.* **2020**, *120*, 7984–8034.
- (7) Wang, J.; Zhang, G.; Zhu, J.; Zhang, X.; Ding, F.; Zhang, A.; Guo, X.; Song, C. CO₂ Hydrogenation to Methanol over In₂O₃-Based Catalysts: From Mechanism to Catalyst Development. *ACS Catal.* **2021**, *2020*, 1406–1423.
- (8) Daza, Y. A.; Kuhn, J. N. CO₂ Conversion by Reverse Water Gas Shift Catalysis: Comparison of Catalysts, Mechanisms and Their Consequences for CO₂ Conversion to Liquid Fuels. *RSC Adv.* **2016**, *6*, 49675–49691.
- (9) Saeidi, S.; Amin, N. A. S.; Rahimpour, M. R. Hydrogenation of CO₂ to Value-Added Products - A Review and Potential Future Developments. *J. CO₂ Util.* **2014**, *5*, 66–81.
- (10) Li, W.; Wang, H.; Jiang, X.; Zhu, J.; Liu, Z.; Guo, X.; Song, C. A Short Review of Recent Advances in CO₂ Hydrogenation to Hydrocarbons over Heterogeneous Catalysts. *RSC Advances*. Royal Society of Chemistry February 16, 2018, pp 7651–7669.
- (11) Gumber, S.; Gurumoorthy, A. V. P. Methanol Economy Versus Hydrogen Economy. *Methanol Sci. Eng.* **2018**, 661–674.
- (12) Olah, G. A. Beyond Oil and Gas: The Methanol Economy. *Angew. Chemie - Int. Ed.* **2005**, *44*, 2636–2639.
- (13) Goepfert, A.; Czaun, M.; Jones, J. P.; Surya Prakash, G. K.; Olah, G. A. Recycling of Carbon Dioxide to Methanol and Derived Products – Closing the Loop. *Chem. Soc. Rev.* **2014**, *43*, 7995–8048.
- (14) Baltes, C.; Vukojević, S.; Schüth, F. Correlations between Synthesis, Precursor, and Catalyst Structure and Activity of a Large Set of CuO/ZnO/Al₂O₃ Catalysts for Methanol Synthesis. *J. Catal.* **2008**, *258*, 334–344.
- (15) Behrens, M. Promoting the Synthesis of Methanol: Understanding the Requirements for an Industrial Catalyst for the Conversion of CO₂. *Angew. Chemie Int. Ed.* **2016**, *55*, 14906–14908.
- (16) Nakamura, J.; Choi, Y.; Fujitani, T. On the Issue of the Active Site and the Role of ZnO in Cu/ZnO Methanol Synthesis Catalysts. *Top. Catal.* **2003**, *22*, 277–285.
- (17) Fichtl, M. B.; Schlereth, D.; Jacobsen, N.; Kasatkin, I.; Schumann, J.; Behrens, M.; Schlögl, R.; Hinrichsen,

- O. Kinetics of Deactivation on Cu/ZnO/Al₂O₃ Methanol Synthesis Catalysts. *Appl. Catal. A Gen.* **2015**, *502*, 262–270.
- (18) Ye, J.; Liu, C.; Ge, Q. DFT Study of CO₂ Adsorption and Hydrogenation on the In₂O₃ Surface. *J. Phys. Chem. C* **2012**, *116*, 7817–7825.
- (19) Frei, M. S.; Mondelli, C.; Cesarini, A.; Krumeich, F.; Hauert, R.; Stewart, J. A.; Curulla Ferré, D.; Pérez-Ramírez, J. Role of Zirconia in Indium Oxide-Catalyzed CO₂ Hydrogenation to Methanol. *ACS Catal.* **2020**, *10*, 1133–1145.
- (20) Sun, Q.; Ye, J.; Liu, C.; Ge, Q. In₂O₃ as a Promising Catalyst for CO₂ Utilization: A Case Study with Reverse Water Gas Shift over In₂O₃. *Greenh. Gases Sci. Technol.* **2014**, *4*, 140–144.
- (21) Ye, J.; Liu, C.; Mei, D.; Ge, Q. Active Oxygen Vacancy Site for Methanol Synthesis from CO₂ Hydrogenation on In₂O₃ (110): A DFT Study. *ACS Catal.* **2013**, *3*, 1296–1306.
- (22) Cao, A.; Wang, Z.; Li, H.; Nørskov, J. K. Relations between Surface Oxygen Vacancies and Activity of Methanol Formation from CO₂ Hydrogenation over In₂O₃ Surfaces. *ACS Catal.* **2021**, *11*, 1780–1786.
- (23) Wang, J.; Zhang, G.; Zhu, J.; Zhang, X.; Ding, F.; Zhang, A.; Guo, X.; Song, C. CO₂ Hydrogenation to Methanol over In₂O₃-Based Catalysts: From Mechanism to Catalyst Development. *ACS Catal.* **2021**, *11*, 1406–1423.
- (24) Posada-Borbón, A.; Grönbeck, H. A First-Principles-Based Microkinetic Study of CO₂ Reduction to CH₃OH over In₂O₃(110). *ACS Catal.* **2021**, *11*, 9996–10006.
- (25) Wang, J.; Zhang, G.; Zhu, J.; Zhang, X.; Ding, F.; Zhang, A.; Guo, X.; Song, C. CO₂ Hydrogenation to Methanol over In₂O₃-Based Catalysts: From Mechanism to Catalyst Development. *ACS Catal.* **2021**, *11*, 1406–1423.
- (26) Snider, J. L.; Streibel, V.; Hubert, M. A.; Choksi, T. S.; Valle, E.; Upham, D. C.; Schumann, J.; Duyar, M. S.; Gallo, A.; Abild-Pedersen, F.; Jaramillo, T. F. Revealing the Synergy between Oxide and Alloy Phases on the Performance of Bimetallic In-Pd Catalysts for CO₂ Hydrogenation to Methanol. *ACS Catal.* **2019**, *9*, 3399–3412.
- (27) Frei, M. S.; Mondelli, C.; García-Muelas, R.; Kley, K. S.; Puértolas, B.; López, N.; Safonova, O. V.; Stewart, J. A.; Curulla Ferré, D.; Pérez-Ramírez, J. Atomic-Scale Engineering of Indium Oxide Promotion by Palladium for Methanol Production via CO₂ Hydrogenation. *Nat. Commun.* **2019**, *10*, 1–11.
- (28) Sun, K.; Rui, N.; Zhang, Z.; Sun, Z.; Ge, Q.; Liu, C. J. A Highly Active Pt/In₂O₃ Catalyst for CO₂ Hydrogenation to Methanol with Enhanced Stability. *Green Chem.* **2020**, *22*, 5059–5066.
- (29) Sun, K.; Rui, N.; Shen, C.; Liu, C. J. Theoretical Study of Selective Hydrogenation of CO₂ to Methanol over Pt₄/In₂O₃ Model Catalyst. *J. Phys. Chem. C* **2021**, *125*, 10926–10936.
- (30) Han, Z.; Tang, C.; Wang, J.; Li, L.; Li, C. Atomically Dispersed Ptⁿ⁺ Species as Highly Active Sites in Pt/In₂O₃ Catalysts for Methanol Synthesis from CO₂ Hydrogenation. *J. Catal.* **2020**, *394*, 236–244.
- (31) Dostagir, N. H. M.; Thompson, C.; Kobayashi, H.; Karim, A. M.; Fukuoka, A.; Shrotri, A. Rh Promoted In₂O₃ as a Highly Active Catalyst for CO₂ Hydrogenation to Methanol. *Catal. Sci. Technol.* **2020**, *10*, 8196–8202.

- (32) Wang, J.; Sun, K.; Jia, X.; Liu, C. jun. CO₂ Hydrogenation to Methanol over Rh/In₂O₃ Catalyst. *Catal. Today* **2021**, *365*, 341–347.
- (33) Bavykina, A.; Yarulina, I.; Al Abdulghani, A. J.; Gevers, L.; Hedhili, M. N.; Miao, X.; Galilea, A. R.; Pustovarenko, A.; Dikhtiarenko, A.; Cadiou, A.; Aguilar-Tapia, A.; Hazemann, J.-L.; Kozlov, S. M.; Oud-Chikh, S.; Cavallo, L.; Gascon, J. Turning a Methanation Co Catalyst into an In–Co Methanol Producer. *ACS Catal.* **2019**, *9*, 6910–6918.
- (34) Jia, X.; Sun, K.; Wang, J.; Shen, C.; Liu, C. jun. Selective Hydrogenation of CO₂ to Methanol over Ni/In₂O₃ Catalyst. *J. Energy Chem.* **2020**, *50*, 409–415.
- (35) Zhu, J.; Cannizzaro, F.; Liu, L.; Zhang, H.; Kosinov, N.; Filot, I. A. W.; Rabeah, J.; Brückner, A.; Hensen, E. J. M. Ni-In Synergy in CO₂ Hydrogenation to Methanol. *ACS Catal.* **2021**, *11*, 11371–11384.
- (36) Frei, M. S.; Mondelli, C.; García-Muelas, R.; Morales-Vidal, J.; Philipp, M.; Safonova, O. V.; López, N.; Stewart, J. A.; Ferré, D. C.; Pérez-Ramírez, J. Nanostructure of Nickel-Promoted Indium Oxide Catalysts Drives Selectivity in CO₂ Hydrogenation. *Nat. Commun.* **2021**, *12*, 1–9.
- (37) Kresse, G.; Joubert, D. From Ultrasoft Pseudopotentials to the Projector Augmented-Wave Method. *Phys. Rev. B* **1999**, *59*, 1758.
- (38) Perdew, J. P.; Burke, K.; Ernzerhof, M. Generalized Gradient Approximation Made Simple. *Phys. Rev. Lett.* **1996**, *77*, 3865.
- (39) Kresse, G.; Hafner, J. Ab Initio Molecular-Dynamics Simulation of the Liquid-Metallamorphous-Semiconductor Transition in Germanium. *Phys. Rev. B* **1994**, *49*, 14251–14269.
- (40) Kresse, G.; Furthmüller, J. Efficiency of Ab-Initio Total Energy Calculations for Metals and Semiconductors Using a Plane-Wave Basis Set. *Comput. Mater. Sci.* **1996**, *6*, 15–50.
- (41) Albani, D.; Capdevila-Cortada, M.; Vilé, G.; Mitchell, S.; Martin, O.; López, N.; Pérez-Ramírez, J. Semihydrogenation of Acetylene on Indium Oxide: Proposed Single-Ensemble Catalysis. *Angew. Chemie Int. Ed.* **2017**, *56*, 10755–10760.
- (42) Behler, J.; Parrinello, M. Generalized Neural-Network Representation of High-Dimensional Potential-Energy Surfaces. *Phys. Rev. Lett.* **2007**, *98*, 146401.
- (43) Klumpers, B.; Hensen, E. J. M.; Filot, I. A. W. Lateral Interactions of Dynamic Adlayer Structures from Artificial Neural Networks. *J. Phys. Chem. C* **2022**, *126*, 5529–5540.
- (44) Cannizzaro, F.; Hensen, E. J. M.; Filot, I. A. W. The Promoting Role of Ni on In₂O₃ for CO₂ Hydrogenation to Methanol. *ACS Catal.* **2023**, *13*, 1875–1892.
- (45) Henkelman, G.; Jónsson, H. Improved Tangent Estimate in the Nudged Elastic Band Method for Finding Minimum Energy Paths and Saddle Points. *J. Chem. Phys.* **2000**, *113*, 9978–9985.
- (46) Heidrich, D.; Quapp, W. Saddle Points of Index 2 on Potential Energy Surfaces and Their Role in Theoretical Reactivity Investigations. *Theor. Chim. Acta* **1986**, *70*, 89–98.
- (47) Nelson, R.; Ertural, C.; George, J.; Deringer, V. L.; Hautier, G.; Dronskowski, R. LOBSTER: Local Orbital Projections, Atomic Charges, and Chemical-Bonding Analysis from Projector-Augmented-Wave-Based Density-Functional Theory. *J. Comput. Chem.* **2020**, *41*, 1931–1940.

- (48) Maintz, S.; Volker, L.; Deringer, L.; Tchougr, A. L.; Dronskowski, R. ; LOBSTER: A Tool to Extract Chemical Bonding from Plane-Wave Based DFT. *J. Comput. Chem.*; **2016**, *37*, 11–12.
- (49) Yu, M.; Trinkle, D. R. Accurate and Efficient Algorithm for Bader Charge Integration. *J. Chem. Phys.* **2011**, *134*, 064111.
- (50) Brown, P. N.; Byrne, G. D.; Hindmarsh, A. C. VODE: A Variable-Coefficient ODE Solver. *J. Sci. Stat. Comput.*, 1989, *10*, 5, 1038-1051
- (51) Byrne, G. D.; Hindmarsh, A. C. Stiff ODE Solvers: A Review of Current and Coming Attractions. *J. Comput. Phys.* **1987**, *70*, 1–62.
- (52) Byrne, G. D.; Hindmarsh, A. C. A Polyalgorithm for the Numerical Solution of Ordinary Differential Equations. *ACM Trans. Math. Softw.* **1975**, *1*, 71–96.
- (53) Shomate, C. H. A Method for Evaluating and Correlating Thermodynamic Data. *J. Phys. Chem.* **2002**, *58*, 368–372.
- (54) NIST Chemistry WebBook <https://webbook.nist.gov/chemistry/> (accessed Feb 1, 2022).
- (55) Kozuch, S.; Shaik, S. A Combined Kinetic-Quantum Mechanical Model for Assessment of Catalytic Cycles: Application to Cross-Coupling and Heck Reactions. *J. Am. Chem. Soc.* **2006**, *128*, 3355–3365.
- (56) Kozuch, S.; Shaik, S. Kinetic-Quantum Chemical Model for Catalytic Cycles: The Haber-Bosch Process and the Effect of Reagent Concentration. *J. Phys. Chem. A* **2008**, *112*, 6032–6041.
- (57) Campbell, C. T. The Degree of Rate Control: A Powerful Tool for Catalysis Research. *ACS Catalysis*. American Chemical Society April 7, 2017, pp 2770–2779.
- (58) Filot, A. W. *Introduction to microkinetic modeling*; Technische Universiteit Eindhoven, **2022**. ISBN: 978-90-386-5573-4.
- (59) Stegelmann, C.; Schiødt, N. C.; Campbell, C. T.; Stoltze, P. Microkinetic Modeling of Ethylene Oxidation over Silver. *J. Catal.* **2004**, *221*, 630–649.
- (60) Filot, A. W. *Introduction to microkinetic modeling*; Technische Universiteit Eindhoven, **2022**. ISBN: 978-90-386-5573-4.
- (61) Benson, S. W. III - Bond Energies. *J. Chem. Educ.* **1965**, *42*, 502–515.
- (62) Pavesi, D.; Dattila, F.; Van de Poll, R. C. J.; Anastasiadou, D.; García-Muelas, R.; Figueiredo, M.; Gruter, G. J. M.; López, N.; Koper, M. T. M.; Schouten, K. J. P. Modulation of the Selectivity of CO₂ to CO Electroreduction in Palladium Rich Palladium-Indium Nanoparticles. *J. Catal.* **2021**, *402*, 229–237.
- (63) de Amorim, R. V.; Batista, K. E. A.; Nagurniak, G. R.; Orenha, R. P.; Parreira, R. L. T.; Piotrowski, M. J. CO, NO, and SO Adsorption on Ni Nanoclusters: A DFT Investigation. *Dalt. Trans.* **2020**, *49*, 6407–6417.
- (64) Wang, Y.; Wang, G.; Van Der Wal, L. I.; Cheng, K.; Zhang, Q.; De Jong, K. P.; Wang, Y. Visualizing Element Migration over Bifunctional Metal-Zeolite Catalysts and Its Impact on Catalysis. *Angew.Chem.Int.Ed.*, **2021**, *60*, 17735–17743.
- (65) Zhu, J.; Cannizzaro, F.; Liu, L.; Zhang, H.; Kosinov, N.; Filot, I. A. W.; Rabeah, J.; Brückner, A.; Hensen, E. J. M. Ni-In Synergy in CO₂Hydrogenation to Methanol. *ACS Catal.* **2021**, *11*, 11371–11384.
- (66) Chen, P.; Zhao, G.; Shi, X. R.; Zhu, J.; Ding, J.; Lu, Y. Nano-Intermetallic InNi₃C_{0.5} Compound Discovered

- as a Superior Catalyst for CO₂ Reutilization. *iScience* **2019**, *17*, 315–324.
- (67) Frei, M. S.; Capdevila-Cortada, M.; García-Muelas, R.; Mondelli, C.; López, N.; Stewart, J. A.; Curulla Ferré, D.; Pérez-Ramírez, J. Mechanism and Microkinetics of Methanol Synthesis via CO₂ Hydrogenation on Indium Oxide. *J. Catal.* **2018**, *361*, 313–321.
- (68) Ye, J.; Liu, C.; Mei, D.; Ge, Q. Active Oxygen Vacancy Site for Methanol Synthesis from CO₂ Hydrogenation on In₂O₃(110): A DFT Study. *ACS Catal.* **2013**, *3*, 1296–1306.
- (69) Ye, J.; Liu, C.; Ge, Q. DFT Study of CO₂ Adsorption and Hydrogenation on the In₂O₃ Surface. *J. Phys. Chem. C* **2012**, *116*, 7817–7825.
- (70) Guo, S.; Heck, K.; Kasiraju, S.; Qian, H.; Zhao, Z.; Grabow, L. C.; Miller, J. T.; Wong, M. S. Insights into Nitrate Reduction over Indium-Decorated Palladium Nanoparticle Catalysts. *ACS Catal.* **2018**, *8*, 503–515.
- (71) Li, Y.; Xu, W.; Liu, W.; Han, S.; Cao, P.; Fang, M.; Zhu, D.; Lu, Y. High-Performance Thin-Film Transistors with Aqueous Solution-Processed NiInO Channel Layer. *ACS Appl. Electron. Mater.* **2019**, *1*, 1842–1851.
- (72) Sterk, E. B.; Nieuwelink, A. E.; Monai, M.; Louwen, J. N.; Vogt, E. T. C.; Filot, I. A. W.; Weckhuysen, B. M. Structure Sensitivity of CO₂ Conversion over Nickel Metal Nanoparticles Explained by Micro-Kinetics Simulations. *J. Am. Chem. Soc.* **2022**.
- (73) Frei, M. S.; Capdevila-Cortada, M.; García-Muelas, R.; Mondelli, C.; López, N.; Stewart, J. A.; Curulla Ferré, D.; Pérez-Ramírez, J. Mechanism and Microkinetics of Methanol Synthesis via CO₂ Hydrogenation on Indium Oxide. *J. Catal.* **2018**, *361*, 313–321.
- (74) Stegelmann, C.; Andreasen, A.; Campbell, C. T. Degree of Rate Control: How Much the Energies of Intermediates and Transition States Control Rates. *J. Am. Chem. Soc.* **2009**, *131*, 8077–8082.
- (75) Qin, B.; Li, S. First Principles Investigation of Dissociative Adsorption of H₂ during CO₂ Hydrogenation over Cubic and Hexagonal In₂O₃ Catalysts. *Phys. Chem. Chem. Phys.* **2020**, *22*, 3390–3399.
- (76) Schmider, D.; Maier, L.; Deutschmann, O. Reaction Kinetics of CO and CO₂ Methanation over Nickel. *Ind. Eng. Chem. Res.* **2021**, *60*, 5792–5805.

Appendix D**D1. Details of the ANN-GA**

The workflow for generating structures using the transfer dataset ANN/GA method is presented in Figure D1. The initial dataset of structure geometries comprised 200 Ni_8 structures obtained during a DFT-GA study performed in earlier work.¹ These structures were used to generate clusters for Ni_6In_2 , Ni_2In_6 and In_8 through random substitution of In and Ni atoms. 500 clusters were generated initially. Single-point calculations are performed on these clusters. The DFT energies are then used to train an ANN. The training process is described in an earlier publication.² Training statistics are provided in Table S1.

Table D1: RMSE and bias for the prediction of energies within the training subsets for the ANN of clusters supported on $\text{In}_2\text{O}_3(111)$. Values are provided in meV/atom.

System	Training		Validation		Test	
	Error	Bias	Error	Bias	Error	Bias
Ni_6In_2	1.321	0.031	1.352	-0.021	1.422	0.033
Ni_2In_6	1.350	0.029	1.374	-0.025	1.423	-0.018
In_8	1.193	0.025	1.216	0.030	1.278	0.027

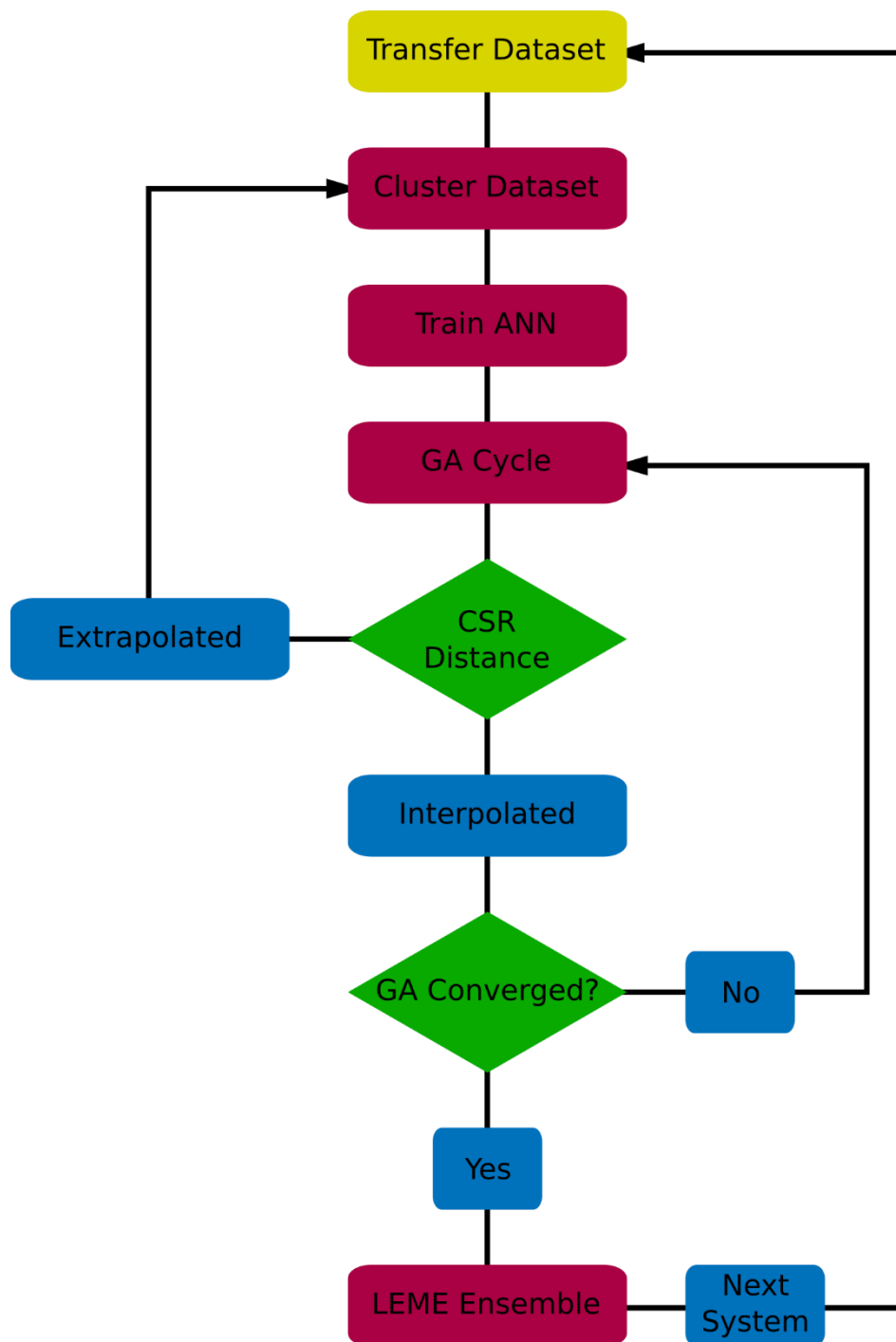


Figure D1. Flow chart of the ANN-GA algorithm used to generate In_2O_3 -supported NiIn clusters.

The ANN is used to perform the energy calculations for the GA. The GA is configured to generate 40 structures per cycle. The GA runs until at least 1000 clusters are generated. Once this target has been achieved, the GA is set to converge when the global energy minimum remains unchanged for 10 cycles.

During the GA cycles, if structures are encountered that differ significantly from the dataset, the energy of these samples is verified using DFT. Structures are compared based on their CSR distance:

$$D_a = \min_b \sum_i^N \left| \frac{G_i^a - G_i^b}{N \cdot G_i^b} \right| \quad (\text{D.1})$$

Where G the ANN input-vector, a denoting the candidate and b the dataset samples. This metric finds the sample with the closest-matching fingerprint in the known dataset. Structures with a minimum distance exceeding 20% are verified using DFT. If the sample-error is found to exceed the 2σ -range of the ANN, it is added to the dataset and the ANN is re-parametrised. By this process, the geometric dataset is iteratively compiled. This improves the quality of the 1st ANN parametrisation for each system, thereby reducing the number of (slow) DFT stages. The final dataset contained 800 samples. The GA generated 10^3 - 10^5 samples per system. Once the GA had converged, the LEME set is made to comprise the 100 clusters with the lowest energy (for each composition). These structures are optimised with DFT to eliminate any residual bias and to validate the ANN predictions.

For the proceeding Boltzmann analysis of the LEME set, a 0.2 eV search-window contains 99.7% of the accessible structures at 400 K. During convergence testing, no new structures were identified within this operating window during the final 10 cycles. As such, the LEME distributions can be considered converged to within the limits of the GA. The results of the ANN/GA conducted in the presence of a surface oxygen vacancy are presented in Table D2.

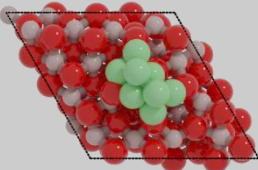
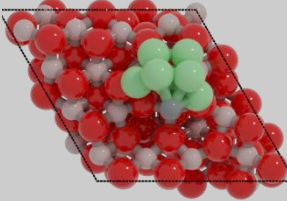
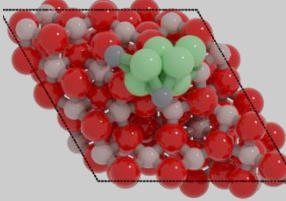
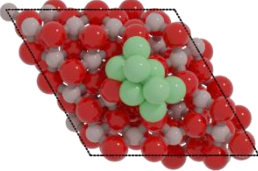
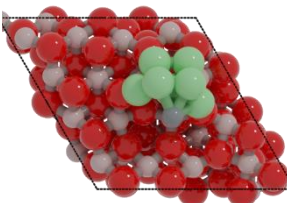
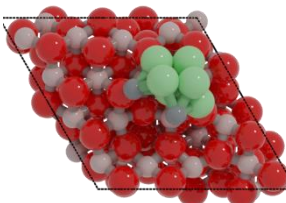
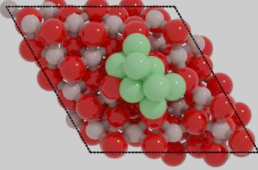
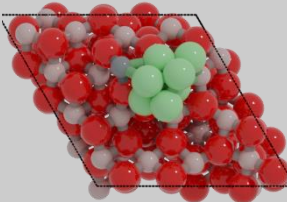
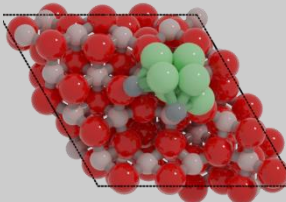
Table D2: RMSE and bias for the prediction of energies within the training subsets for the ANN of clusters supported on $\text{In}_2\text{O}_3(111)$ in the presence of an oxygen vacancy. Values are provided in meV/atom.

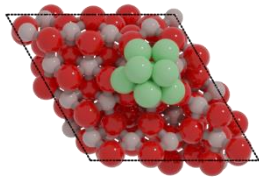
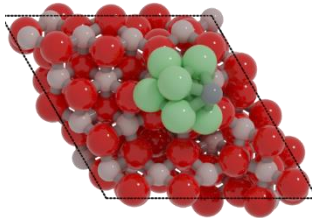
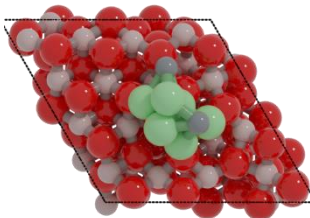
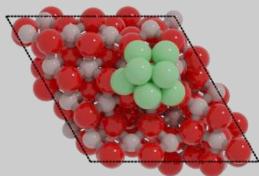
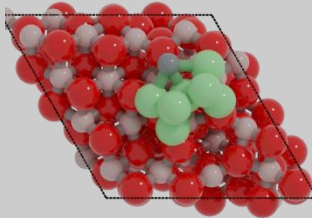
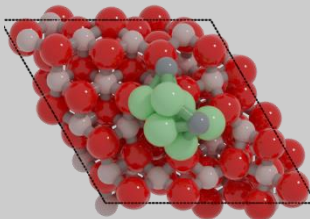
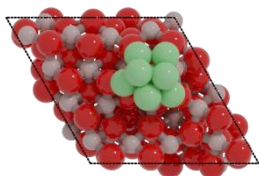
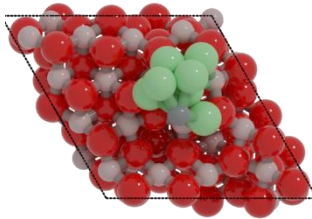
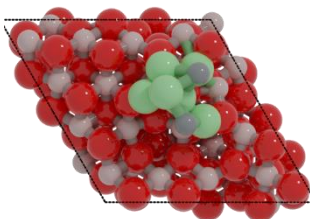
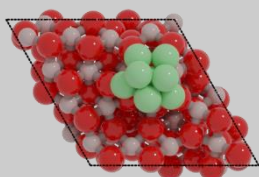
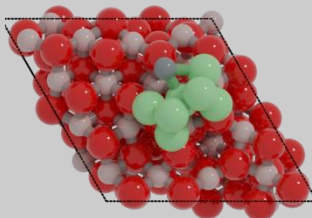
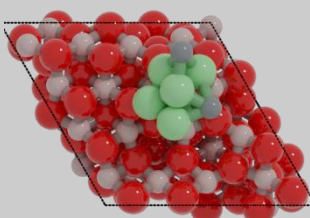
System	Training		Validation		Test	
	Error	Bias	Error	Bias	Error	Bias
Ni₆In₂	1.311	0.033	1.322	0.041	1.374	0.022
Ni₂In₆	1.334	0.031	1.316	0.035	1.363	-0.018
In₈	1.188	0.022	1.221	0.040	1.233	0.017

D2. Structure analysis of ANN-GA-obtained NiIn-In₂O₃ clusters

D2.1 ANN-GA obtained NiIn-In₂O₃ clusters

Table D3. Most stable candidate structures and their energy relative to the minimum energy structure (kJ/mol) for the Ni₈- Ni₇In₁- and Ni₆In₂-In₂O₃ models.

ID	Ni ₈	Ni ₇ In ₁	Ni ₆ In ₂
1	 $\Delta E = 0$	 $\Delta E = 0$	 $\Delta E = 0$
2	 $\Delta E = 7$	 $\Delta E = 49$	 $\Delta E = 21$
3	 $\Delta E = 9$	 $\Delta E = 50$	 $\Delta E = 36$

4	 $\Delta E = 11$	 $\Delta E = 55$	 $\Delta E = 46$
5	 $\Delta E = 17$	 $\Delta E = 57$	 $\Delta E = 61$
6	 $\Delta E = 21$	 $\Delta E = 79$	 $\Delta E = 64$
7	 $\Delta E = 23$	 $\Delta E = 82$	 $\Delta E = 67$

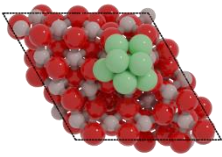
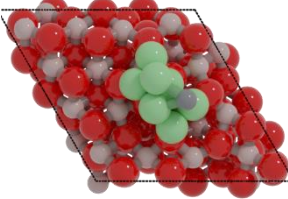
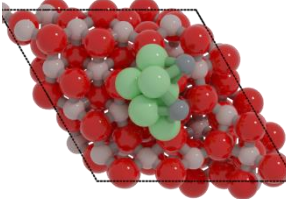
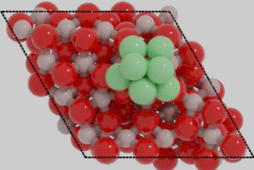
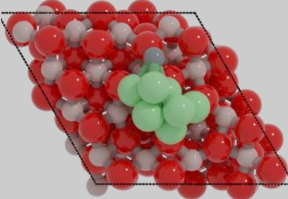
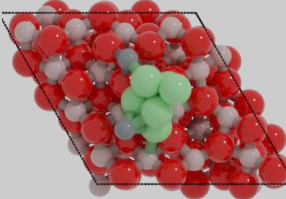
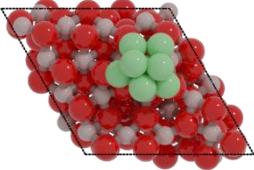
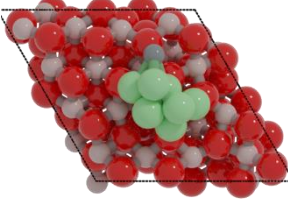
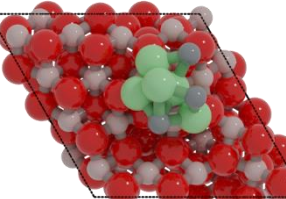
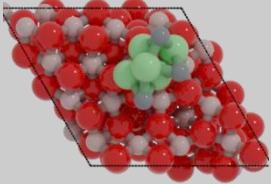
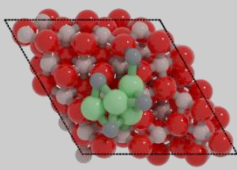
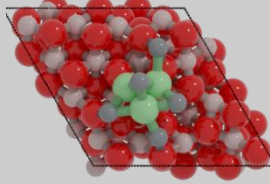
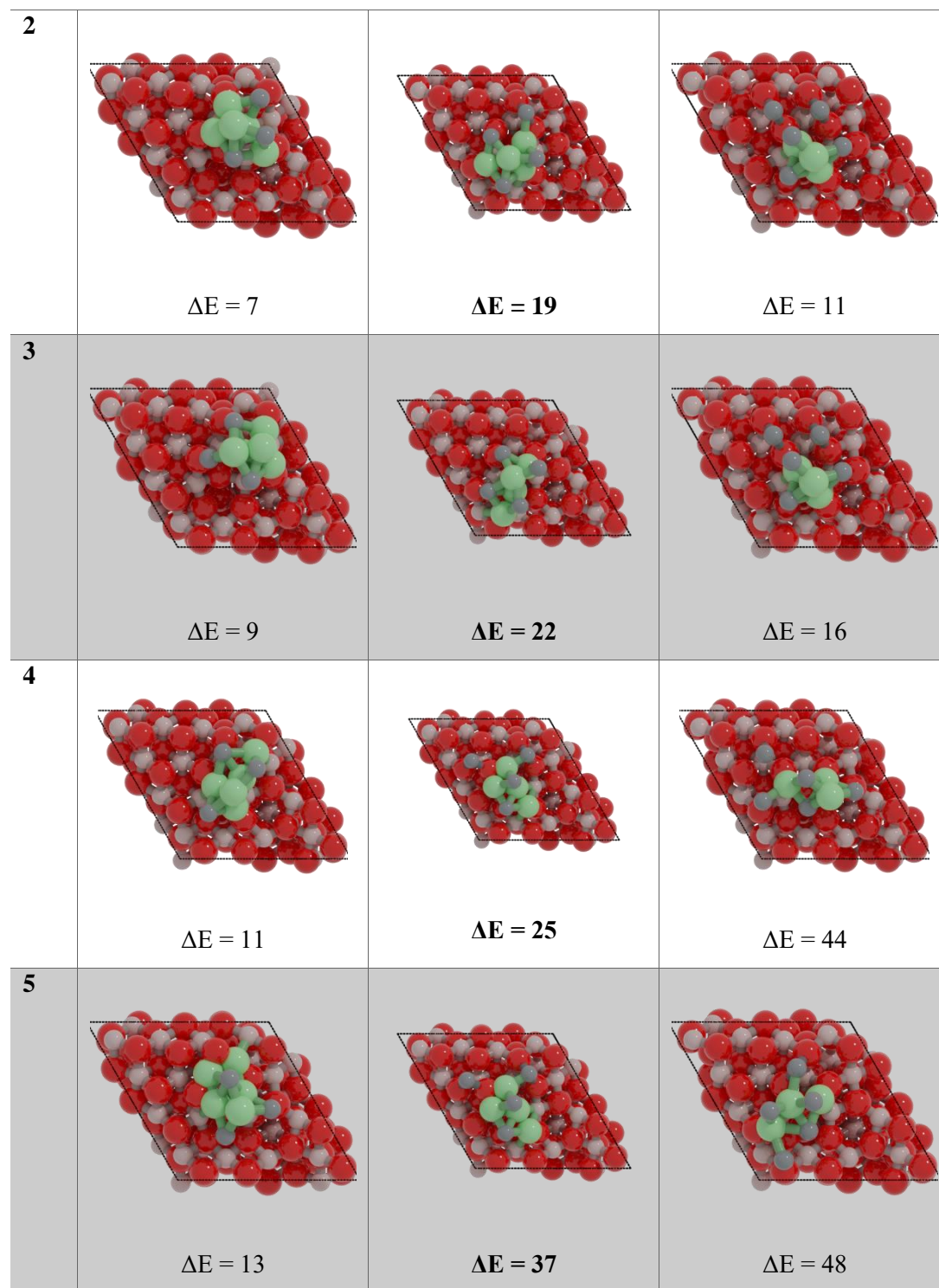
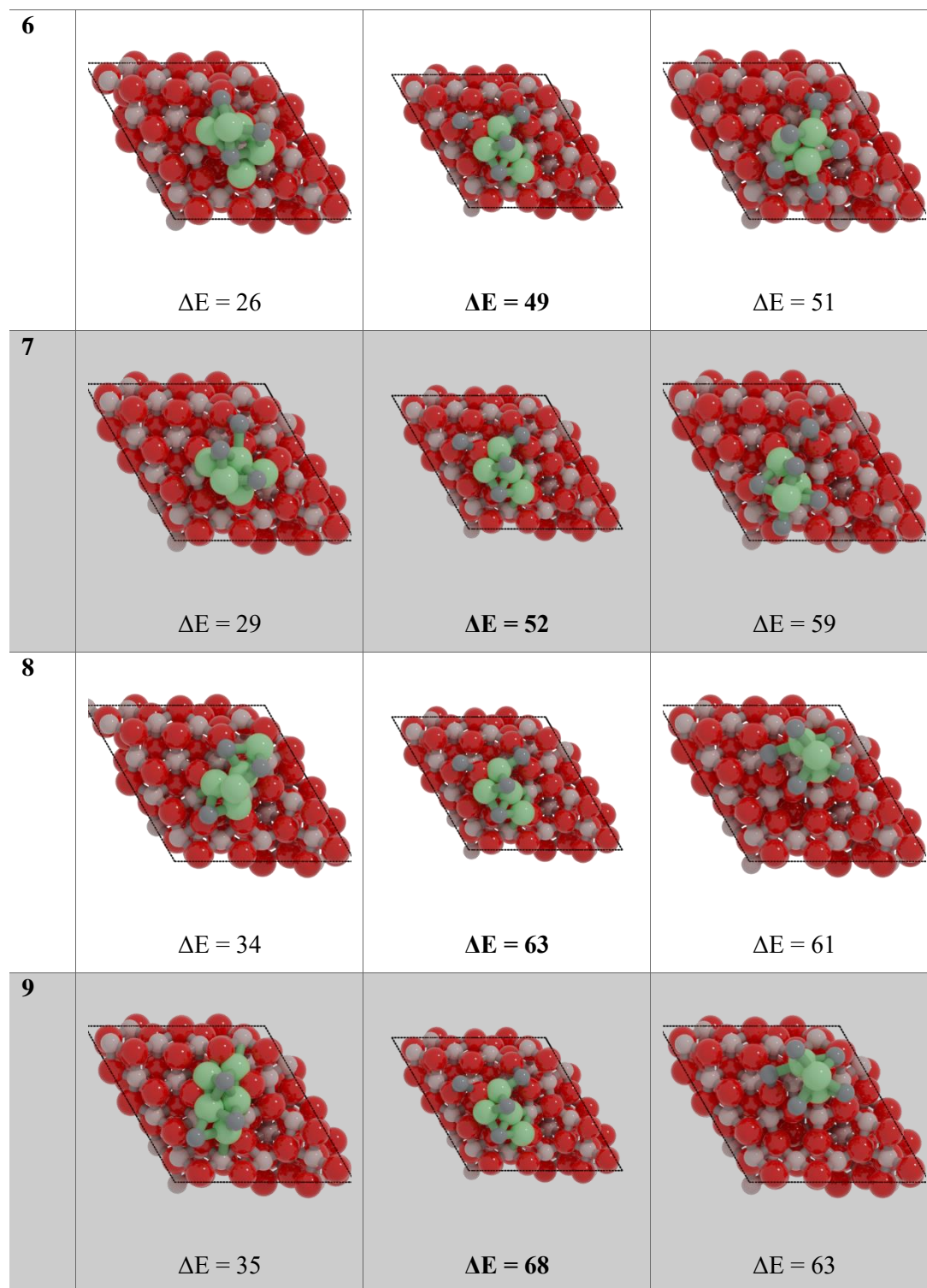
8	 <p>$\Delta E = 26$</p>	 <p>$\Delta E = 83$</p>	 <p>$\Delta E = 68$</p>
9	 <p>$\Delta E = 27$</p>	 <p>$\Delta E = 88$</p>	 <p>$\Delta E = 69$</p>
10	 <p>$\Delta E = 28$</p>	 <p>$\Delta E = 88$</p>	 <p>$\Delta E = 70$</p>

Table D4. Most stable candidate structures and their energy relative to the minimum energy structure (kJ/mol) for the Ni₅In₃-, Ni₄In₄- and Ni₃In₅-In₂O₃ models.

ID	Ni ₅ In ₃	Ni ₄ In ₄	Ni ₃ In ₅
1	 <p>$\Delta E = 0$</p>	 <p>$\Delta E = 0$</p>	 <p>$\Delta E = 0$</p>





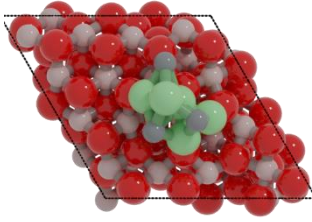
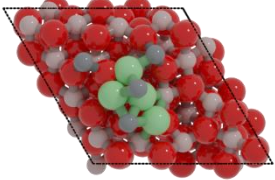
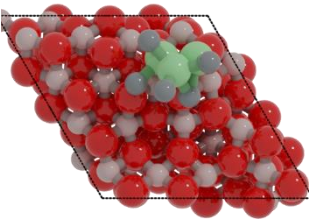
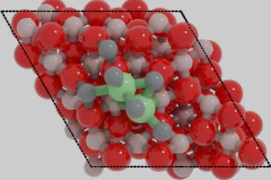
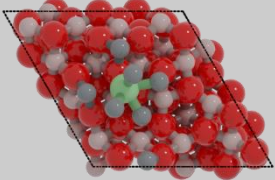
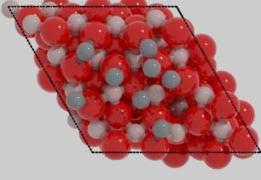
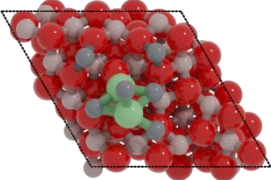
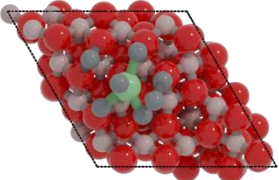
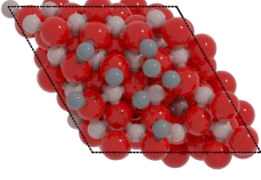
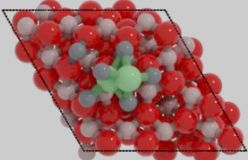
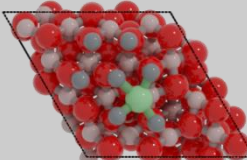
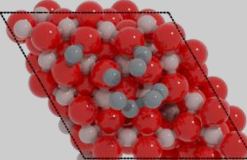
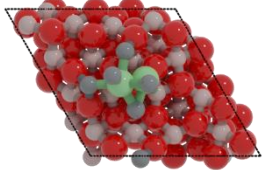
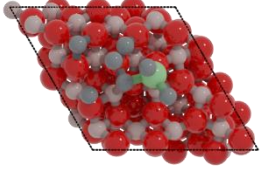
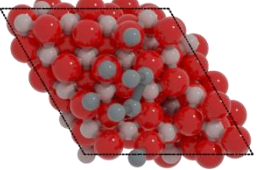
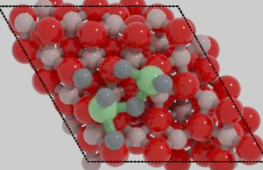
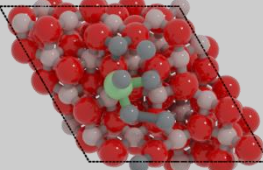
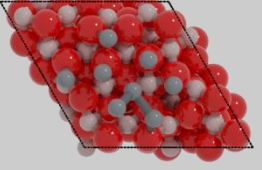
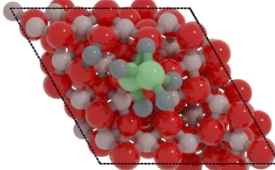
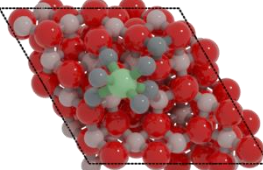
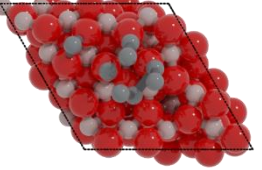
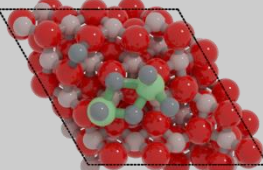
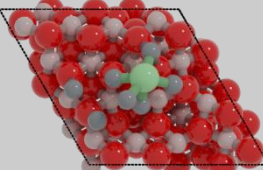
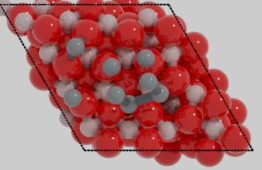
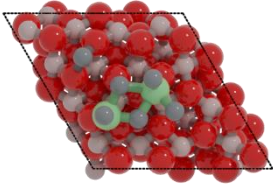
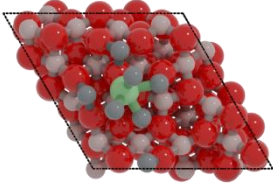
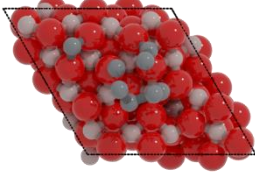
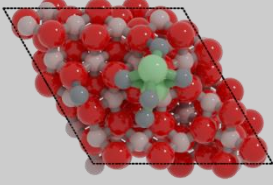
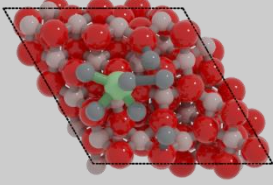
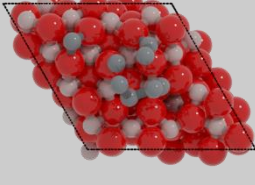
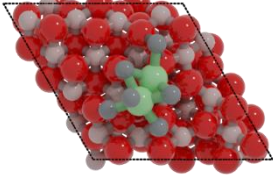
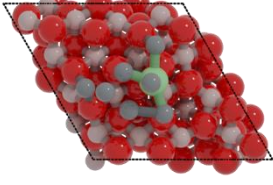
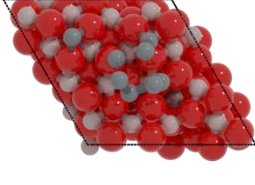
10			
	$\Delta E = 40$	$\Delta E = 88$	$\Delta E = 64$

Table D5. Most stable candidate structures and their energy relative to the minimum energy structure (kJ/mol) for the Ni_2In_6 -, Ni_1In_7 - and In_8 - In_2O_3 model.

ID	Ni_2In_6	Ni_1In_7	In_8
1			
	$\Delta E = 0$	$\Delta E = 0$	$\Delta E = 0$
2			
	$\Delta E = 15$	$\Delta E = 52$	$\Delta E = 27$
3			

On the role of Ni-In clusters on In_2O_3 during CO_2 hydrogenation to methanol

	$\Delta E = 17$	$\Delta E = 57$	$\Delta E = 28$
4	 $\Delta E = 18$	 $\Delta E = 61$	 $\Delta E = 37$
5	 $\Delta E = 41$	 $\Delta E = 62$	 $\Delta E = 41$
6	 $\Delta E = 45$	 $\Delta E = 64$	 $\Delta E = 42$
7	 $\Delta E = 45$	 $\Delta E = 64$	 $\Delta E = 42$

	$\Delta E = 47$	$\Delta E = 77$	$\Delta E = 43$
8	 $\Delta E = 50$	 $\Delta E = 88$	 $\Delta E = 46$
9	 $\Delta E = 51$	 $\Delta E = 91$	 $\Delta E = 47$
10	 $\Delta E = 52$	 $\Delta E = 92$	 $\Delta E = 55$

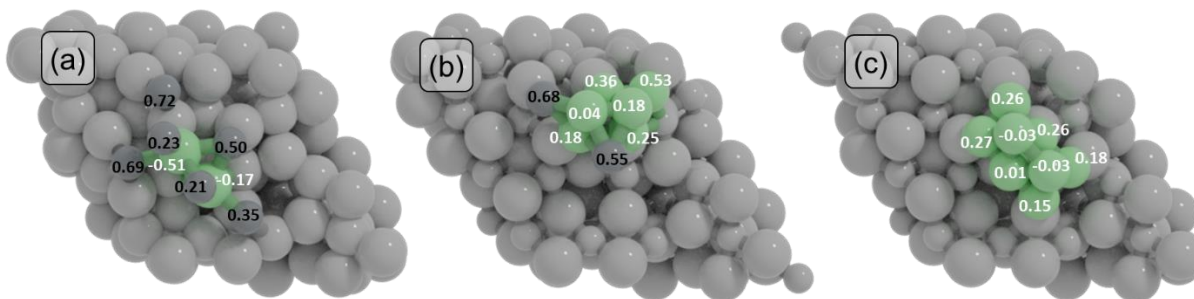


Figure D2. Bader charge analysis of different models. (a) Ni₂In₆⁻, (b) Ni₆In₂⁻ and (c) Ni₈-cluster.

D2.2. Statistical Analysis of NiIn-In₂O₃ clusters

To assess the probability to find a structure different than the energy minimum one, we performed an analysis based on the Boltzmann probability distribution as given by:

$$\frac{p_i}{p_j} = e^{\frac{\epsilon_j - \epsilon_i}{kT}} \quad (\text{D.2})$$

where p_i is the probability of the system being in state i , ϵ_i is the energy of that state, ϵ_j the energy of the energy minimum structure, and kT is the product of Boltzmann's constant k and temperature T . This function gives the probability that the system will be in a certain state (e.g., a given cluster configuration) as a function of the energy of that state and the temperature.

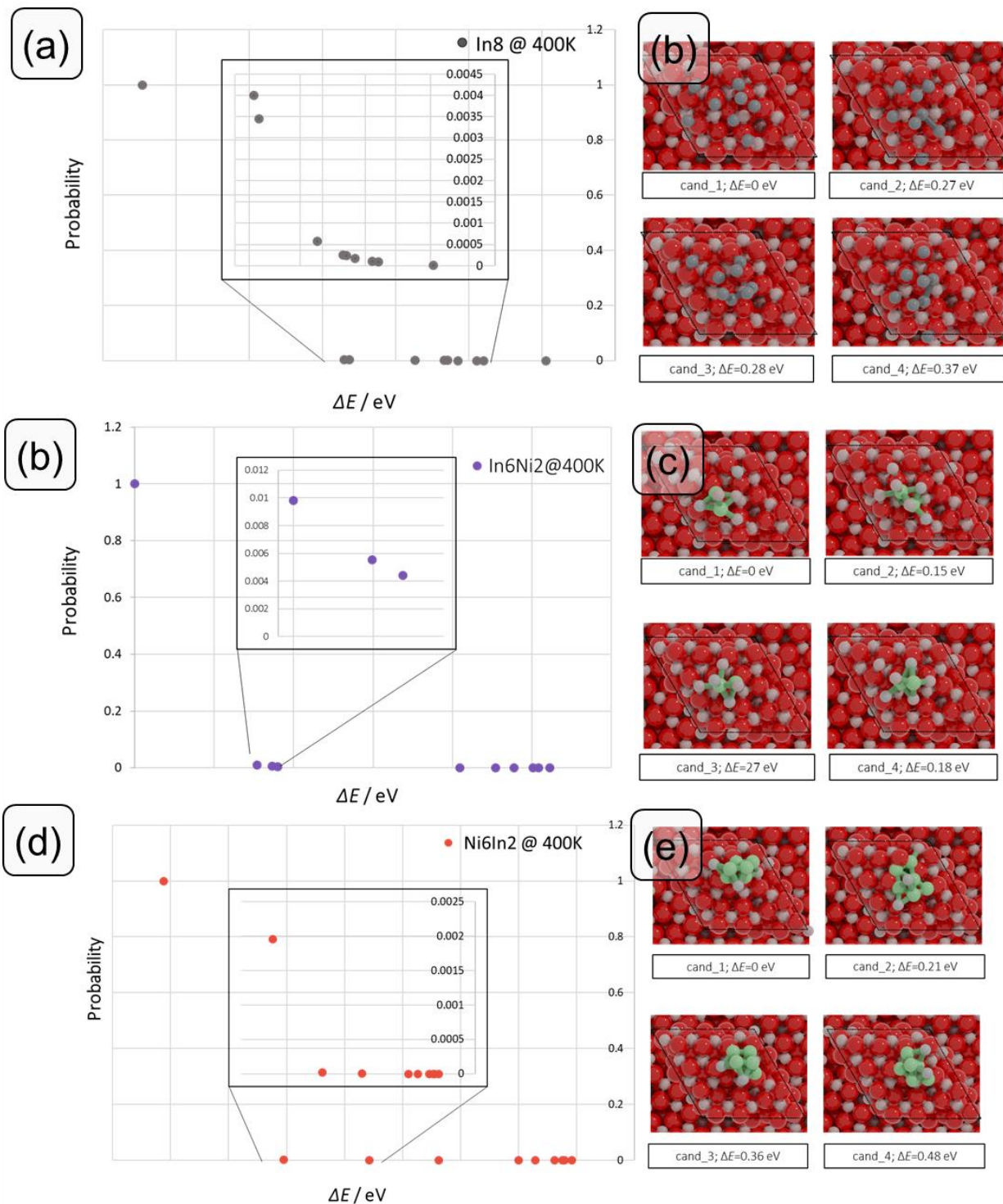


Figure D3. Analysis of GA-computed candidate structures. (a) Boltzmann probability distribution of the candidate structures; the inset shows more in detail the structures closest to the energy minimum ($\Delta E < 0.2$ eV). (b) top-view of the candidate structures with at least 10% probability and their energy relative to the energy minimum (cand_1).

To find the quadratically closest O (O') we evaluate the following for each O atom in the lattice (96 atoms):

$$\text{dist}_O = \sum_{j=1}^8 (X_{O,i} - X_{clus,j})^2 \quad (\text{D.3})$$

Where $X_{O,i}$ is the coordinate of an oxygen atom in the lattice and $X_{clus,j}$ is the coordinate of an atom in the cluster. By finding the minimum of the resulting 1x96 array, the closest oxygen atom to the cluster is found.

Similarly, to find the quadratically closest In (In') we evaluate the following distance for each In atom in the lattice (64 atoms):

$$\text{dist}_{In} = \sum_{j=1}^8 (X_{In,i} - X_{clus,j})^2 \quad (\text{D.4})$$

Where $X_{In,i}$ is the coordinate of an indium atom in the lattice. By performing a minimization, we obtain the closest oxygen atom to the cluster.

Next, we determine the average distance of Ni or In atoms in the cluster with the closest oxygen or indium atom that are plotted in Figure D4 for the energy-minimum Ni₂In₆ cluster and in Figure D4 for a set of 50 clusters.

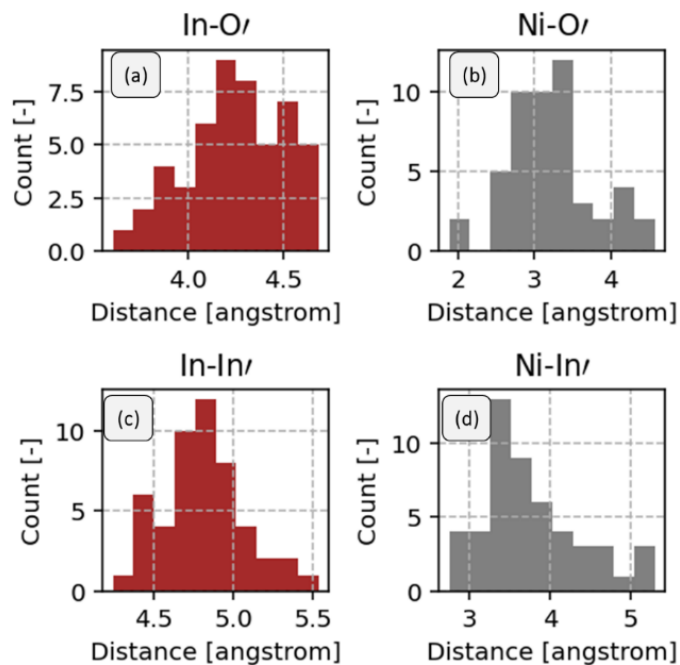


Figure D4. Distance between an In (a) and Ni (b) atom in the cluster and quadratically closest O atom on the support. Distance between an In (c) and Ni (d) atom in the cluster and quadratically closest In atom on the support

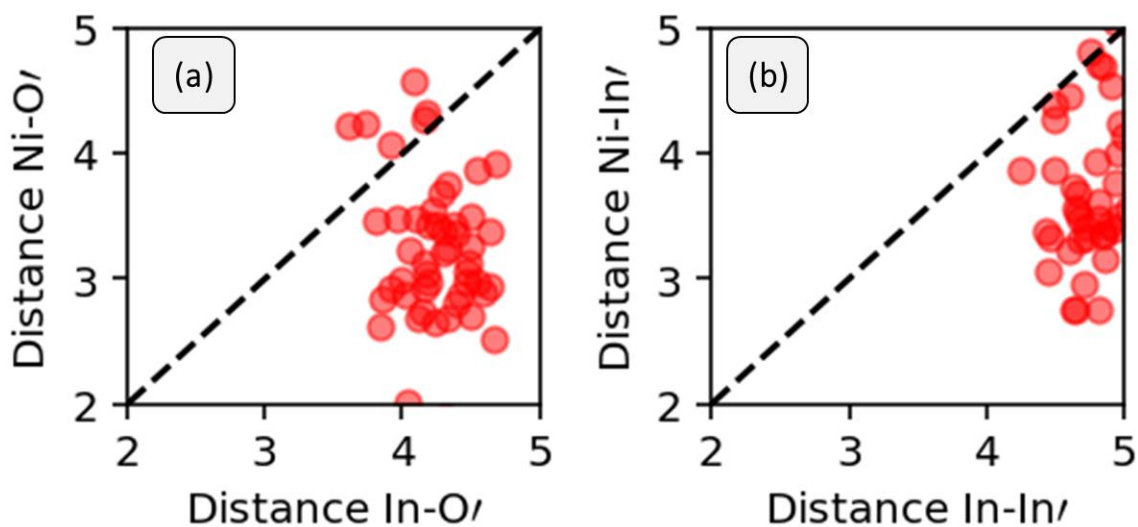
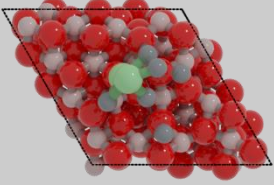
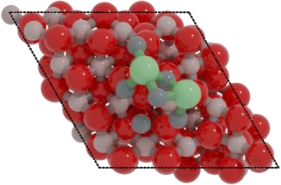
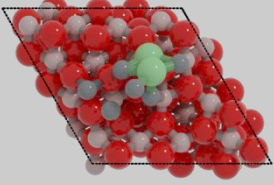
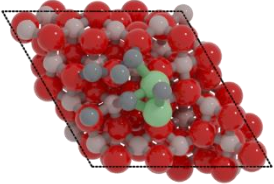
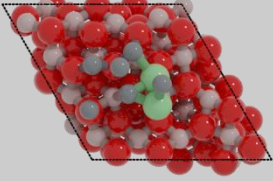
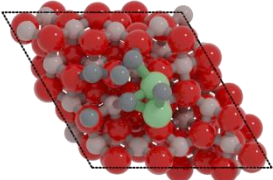


Figure D5. Relation between (a) the Ni-O' and In-O' distance and (b) Ni-In' distance and In-In' distance.

Table D6. Ni₂In₆ structures with exposed Ni phases and their energy relative to the energy minimum structure.

ID	Structure	E – Emin [kJ/mol]
1		48
2		96
3		120
4		128

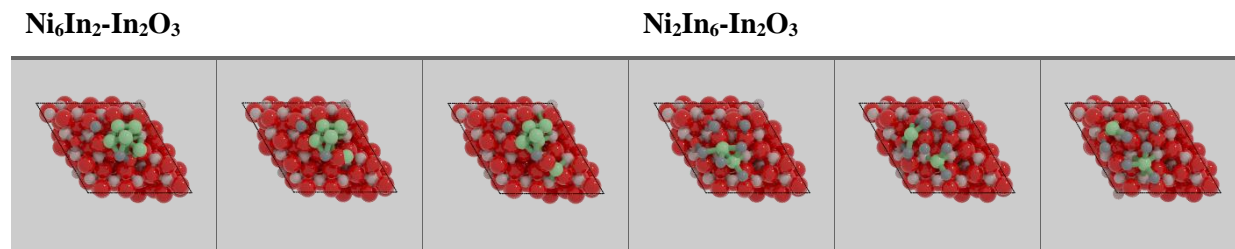
5		138
6		201

D2.2 Stability of NiIn-In₂O₃ clusters

Table D7. Activation and reaction energies (in kJ/mol) for the removal of a single Ni atom from the perimeter of the cluster on Ni₆In₂ and Ni₂In₆.

Model	E_a [kJ/mol]	E_R [kJ/mol]
Ni ₆ In ₂	201	219
Ni ₂ In ₆	251	231

Table D8. Initial, transition and final states the calculations as reported in Table D7.

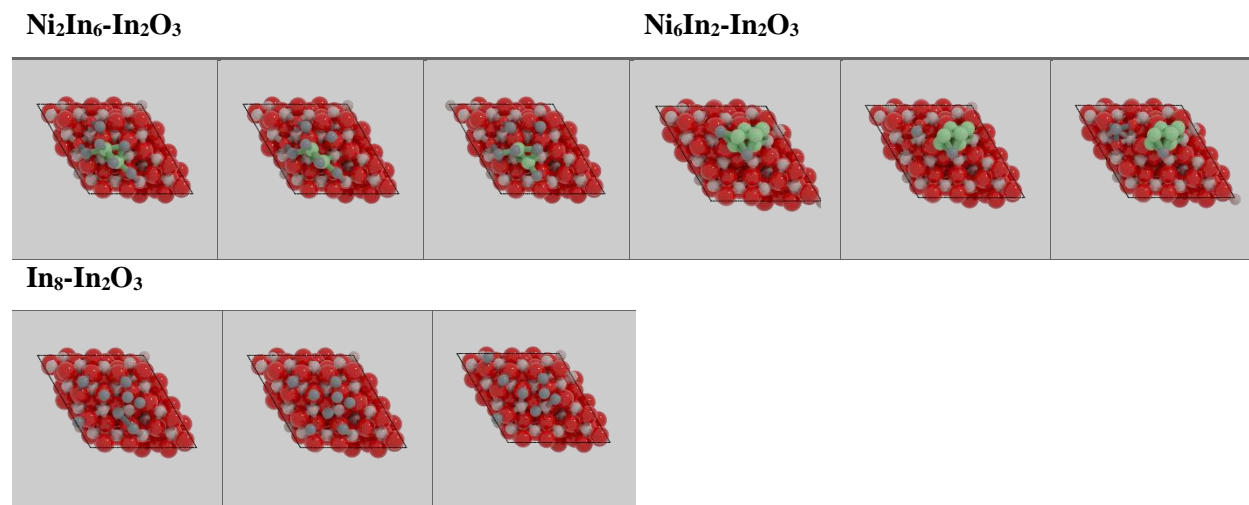


On the role of Ni-In clusters on In_2O_3 during CO_2 hydrogenation to methanol

Table D9. Activation and reaction energies (in kJ/mol) for the removal of a single In atom on different models.

Model	E_a [kJ/mol]	E_R [kJ/mol]
$\text{Ni}_2\text{In}_6\text{-In}_2\text{O}_3$	64	32
$\text{Ni}_6\text{In}_2\text{-In}_2\text{O}_3$	59	59
$\text{In}_8\text{-In}_2\text{O}_3$	51	-1

Table D10. Initial, transition and final states the calculations as reported in Table D9.



D4. DFT data

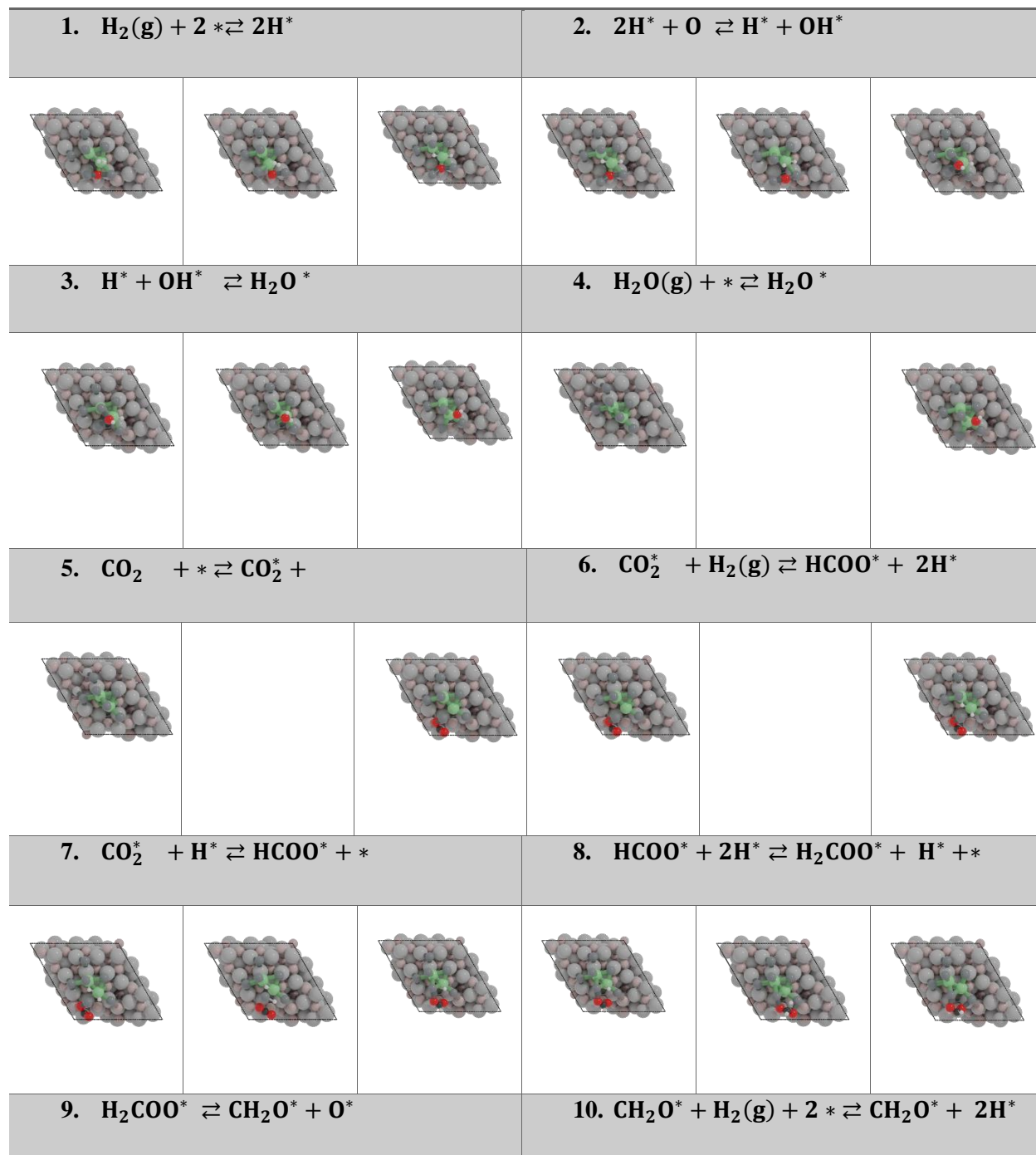
Table D11a. Kinetic parameters for CO₂ hydrogenation to CH₃OH, CO and H₂O over Ni₂In₆-In₂O₃ model.

	Elementary steps	Q _{TS} /Q _{IS}	Q _{TS} /Q _{FS}	E _r (kJ/mol)	E _b (kJ/mol)	E _r (kJ/mol)
ID	Oxygen vacancy formation pathway					
1	H ₂ (g) + 2 * ⇌ 2H*	1.00	1.00	56	118	-62
2	2H* + O ⇌ H* + OH*	1.45	0.065	178	93	85
3	H* + OH* ⇌ H ₂ O* + *	0.26	0.11	119	138	-19
4	H ₂ O* ⇌ H ₂ O(g) + *	1.00	1.00	-	-	41
	Formate pathway					
5	CO ₂ (g) * ⇌ CO ₂ *	1.00	1.00	-	-	-20
6	CO ₂ * + H ₂ (g) + 2 * ⇌ CO ₂ * + 2H*	1.00	1.00	56	118	-62
7	CO ₂ * + 2H* ⇌ HCO ₂ * + H* + *	2.26	0.05	229	139	90
8	HCO ₂ * + H* ⇌ H ₂ CO ₂ *	0.09	0.32	193	170	23
9	H ₂ CO ₂ * + * ⇌ CH ₂ O* + O*	3.41	3.41	134	135	-1
10	CH ₂ O* + H ₂ (g) + 2 * ⇌ CH ₂ O* + 2H*	1.00	1.00	56	118	-62
11	CH ₂ O* + 2H* ⇌ CH ₃ O* + H* + *	0.06	0.1	94	133	-39
12	CH ₃ O* + H* ⇌ CH ₃ OH* + *	0.28	0.02	174	63	111
13	CH ₃ OH* ⇌ CH ₃ OH(g) + *	1.00	1.00	-	-	5
	rWGS pathway					
14	CO* ₂ + * ⇌ CO* + O*	0.87	4.79	49	47	2
15	CO* ⇌ CO(g) + Ov	1.00	1.00	-	-	114
16	CO* ₂ + 2H* ⇌ COOH* + H* + *	0.82	0.03	128	74	53
17	COOH* + * ⇌ CO* + OH*	0.36	0.03	174	23	152
18	CO* + OH* + H* ⇌ H ₂ O* + CO* + *	0.03	0.67	43	-5	48
19	CO* ⇌ CO(g) + *	1.00	1.00	-	-	34
	Activation energies were directly obtained from DFT calculations. Pre-exponential factors were estimated by transition state theory at T = 550 K. Elementary steps ID correspond to Figure 6.3a					

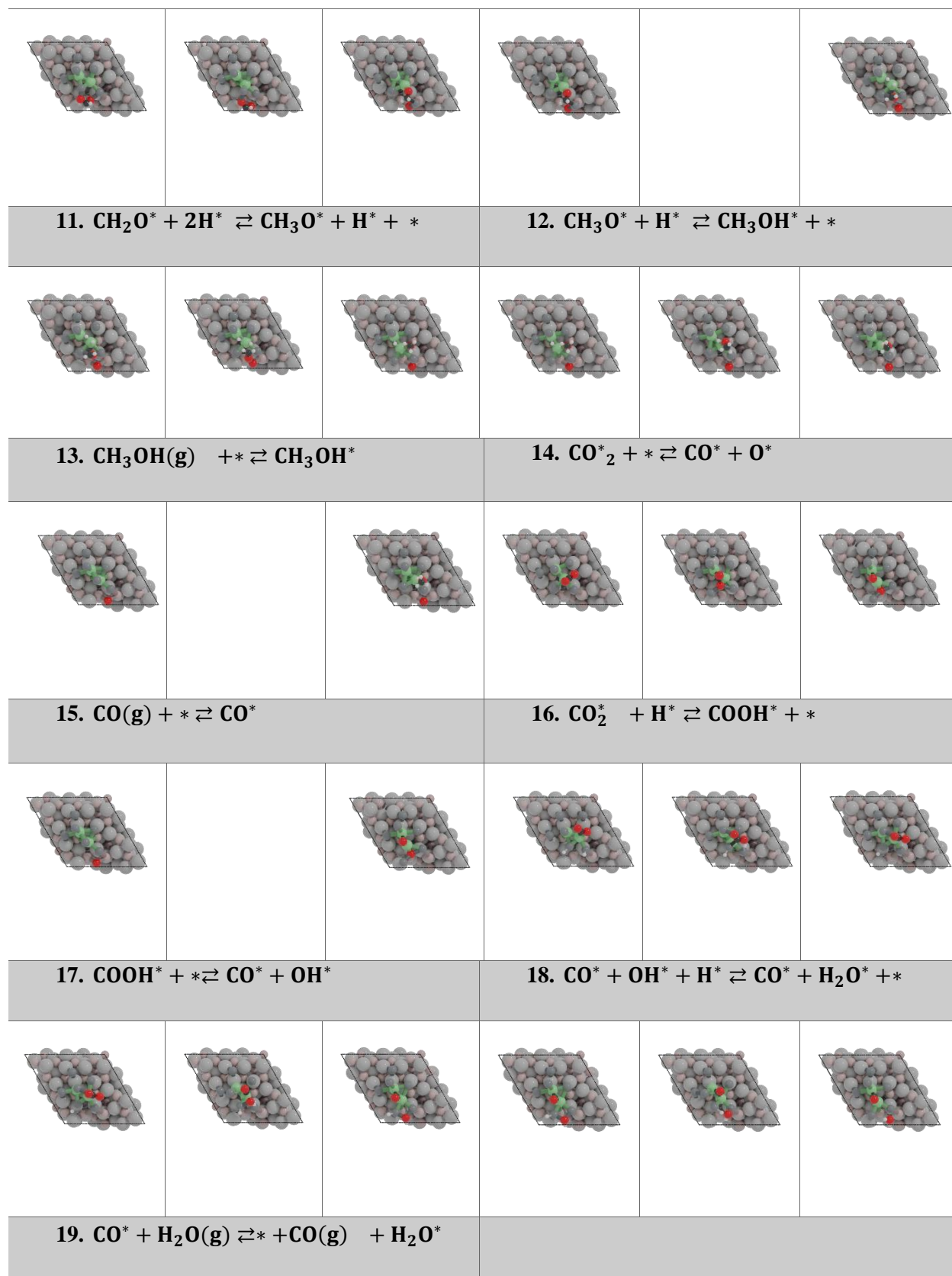
On the role of Ni-In clusters on In₂O₃ during CO₂ hydrogenation to methanol

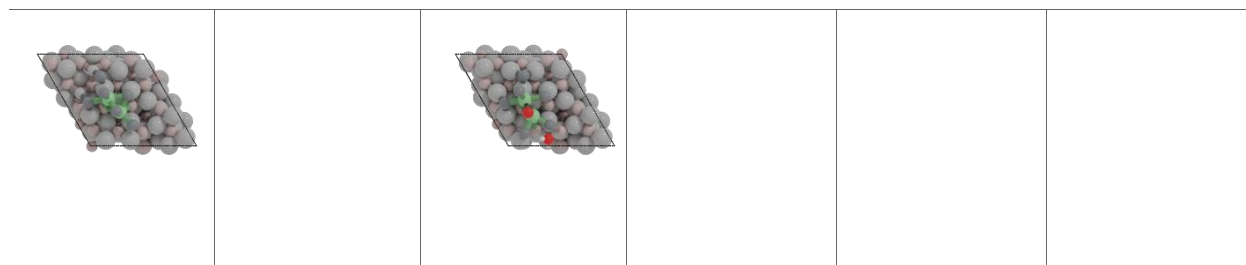
Table D11b. Kinetic parameters for CO₂ hydrogenation to CH₃OH, CO and H₂O over Ni₆In-In₂O₃ model.

	Elementary steps	Q _{TS} /Q _{IS}	Q _{TS} /Q _{FS}	E _r (kJ/mol)	E _b (kJ/mol)	E _r (kJ/mol)
	Oxygen vacancy formation pathway					
1	H ₂ (g) + 2 * ⇌ 2H*	1.00	1.00	-	-	-83
2	2H* + O ⇌ H* + OH*	10.36	1.00	178	209	-32
3	H* + OH* ⇌ H ₂ O* + *	0.75	0.25	169	118	51
4	H ₂ O* ⇌ H ₂ O(g) + *	1.00	1.00	-	-	41
	Formate pathway					
5	CO ₂ (g) * ⇌ CO ₂ *	1.00	1.00	-	-	-81
6	CO ₂ * + H ₂ (g) + 2 * ⇌ CO ₂ * + 2H*	1.00	1.00	-	-	89
7	CO ₂ * + 2H* ⇌ HCO ₂ * + H* + *	1.74	0.03	104	128	-24
8	HCO ₂ * + H* ⇌ H ₂ CO ₂ *	0.22	1.25	122	16	106
9	H ₂ CO ₂ * + * ⇌ CH ₂ O* + O*	4.71	0.09	178	86	92
10	CH ₂ O* + H ₂ (g) + 2 * ⇌ CH ₂ O* + 2H*	1.00	1.00	-	-	89
11	CH ₂ O* + 2H* ⇌ CH ₃ O* + H* + *	0.01	0.01	30	23	7
12	CH ₃ O* + H* ⇌ CH ₃ OH* + *	0.16	1.54	93	98	-5
13	CH ₃ OH* ⇌ CH ₃ OH(g) + *	1.00	1.00	-	-	41
	rWGS pathway					
14	CO* + * ⇌ CO* + O*	0.44	0.07	49	130	-81
15	CO* ⇌ CO(g) + O _v	1.00	1.00	-	-	265
16	CO* + 2H* ⇌ COOH* + H* + *	0.67	0.01	197	91	106
17	COOH* + * ⇌ CO* + OH*	0.01	0.04	60	222	-161
18	CO* + OH* + H* ⇌ H ₂ O* + CO* + *	0.04	0.03	133	89	44
19	CO* ⇌ CO(g) + *	1.00	1.00	-	-	201
<p>Activation energies were directly obtained from DFT calculations. Pre-exponential factors were estimated by transition state theory at T = 550 K. Elementary steps ID correspond to Figure 6.3b</p>						

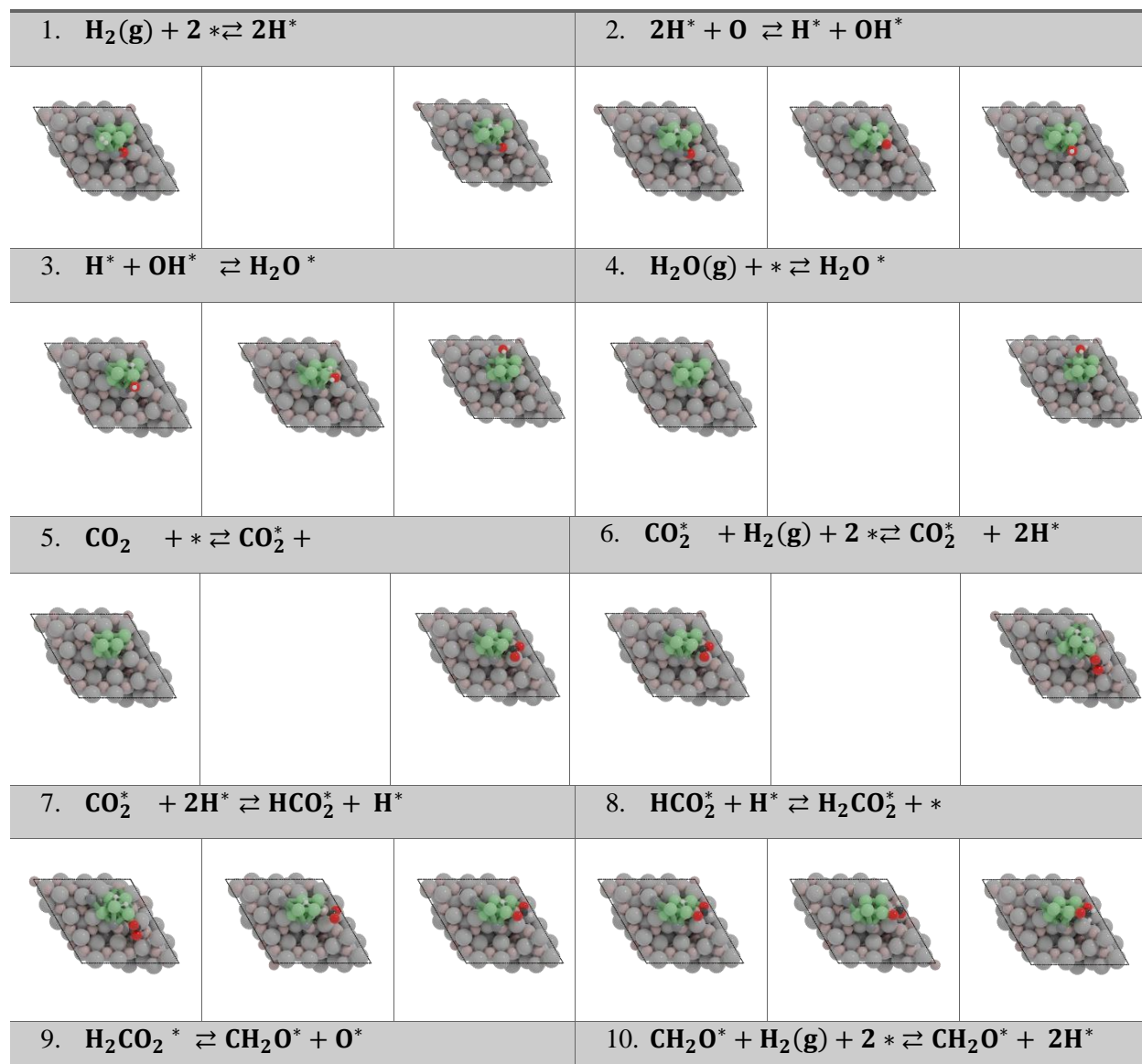
D5. Ni₂In₆-In₂O₃

On the role of Ni-In clusters on In₂O₃ during CO₂ hydrogenation to methanol





D6. Ni₆In₂-In₂O₃



On the role of Ni-In clusters on In₂O₃ during CO₂ hydrogenation to methanol

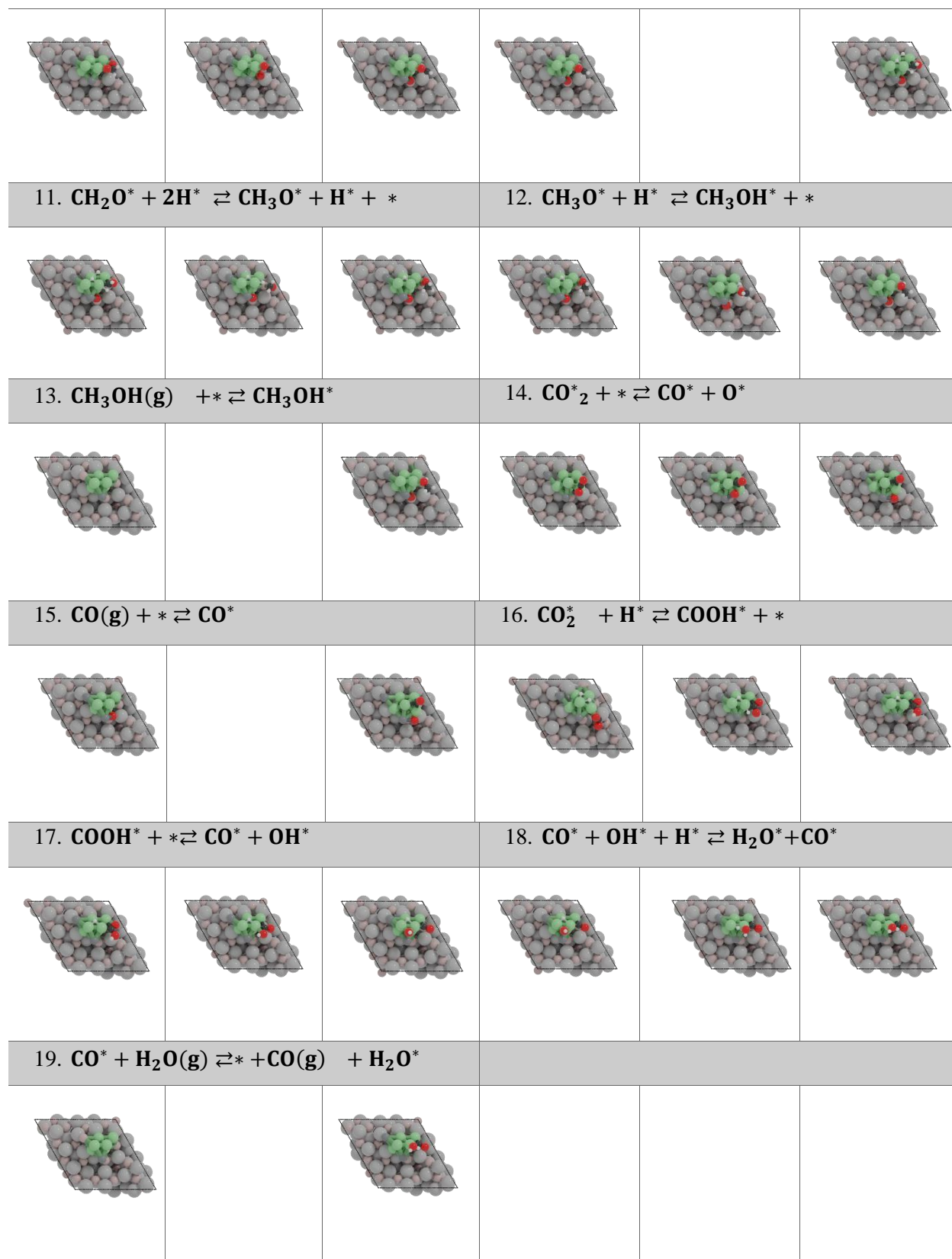
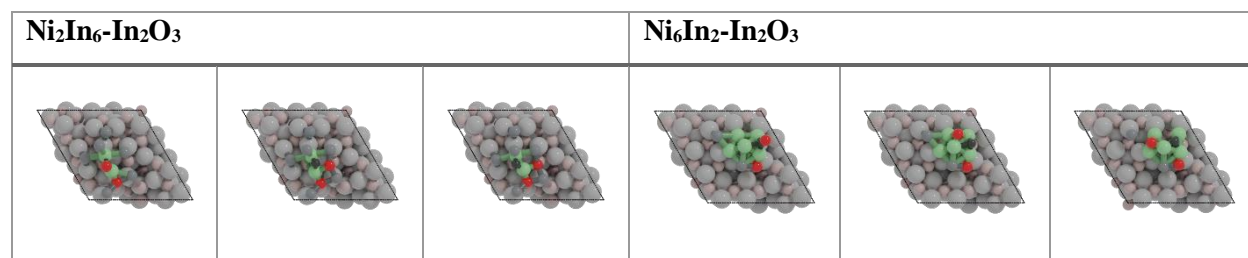


Table D12. Forward and backward activation energies (in kJ/mol) for direct CO dissociation for different models.

Elementary Reaction Step	E_a	E_b
$\text{Ni}_2\text{In}_6\text{-In}_2\text{O}_3$	302	165
$\text{Ni}_6\text{In}_2\text{-In}_2\text{O}_3$	298	178

Table D13. Structures of IS, TS and FS for the CO dissociation elementary reaction steps from Table S10.



D7. Microkinetic simulations

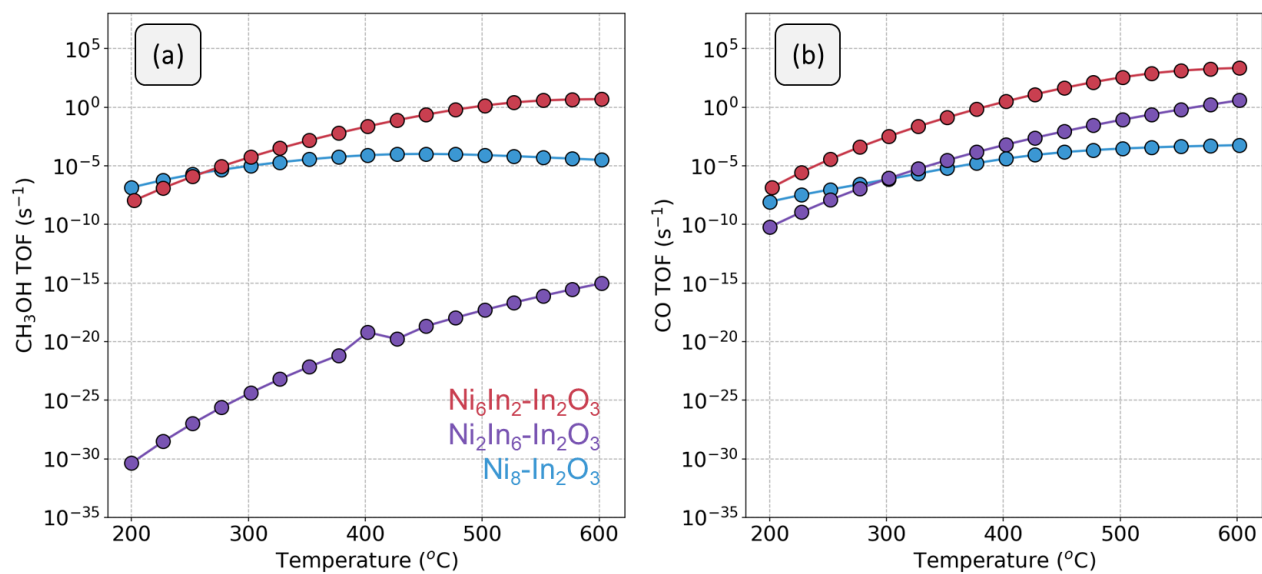


Figure D6. (a) $\text{TOF}_{\text{CH}_3\text{OH}}$ and (b) TOF_{CO} (s $^{-1}$) as a function of temperature on different models ($p = 50$ bar, $\text{H}_2\text{:CO}_2$ ratio = 5). The data for the data for $\text{Ni}_8\text{-In}_2\text{O}_3$ is taken from reference.¹

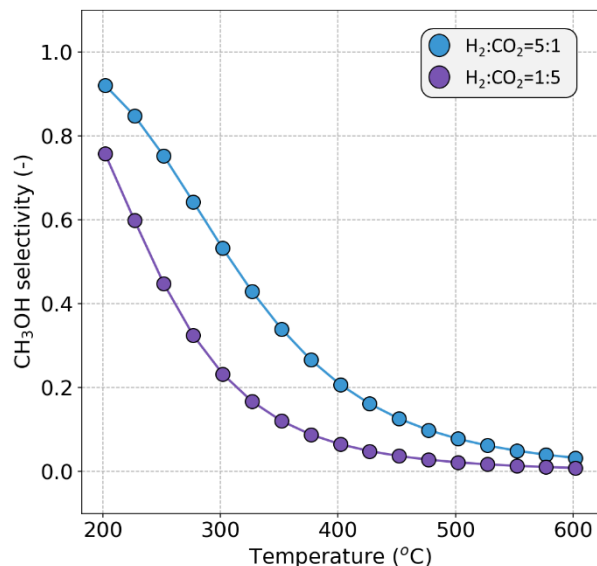


Figure D7. Methanol selectivity on the Ni₆In₂-In₂O₃ model at different H₂:CO₂ ratios.

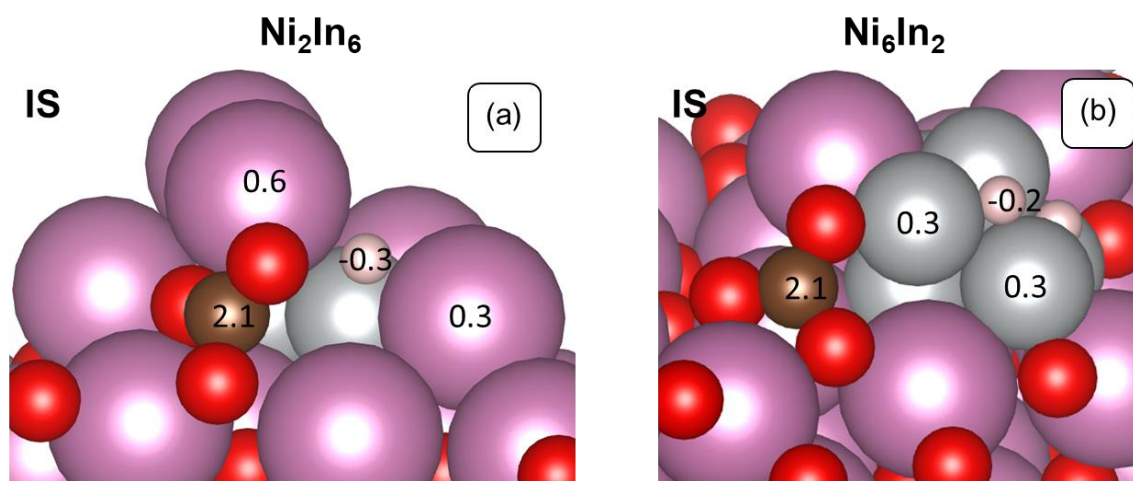


Figure D8. Bader charge analysis of the IS of the elementary step of CO₂ hydrogenation to HCOO on (a) Ni₂In₆ and (b) Ni₆In₂. Pink: In, grey: Ni, black: C, red: O, white: H.

References:

- (1) Cannizzaro, F.; Hensen, E. J. M.; Filot, I. A. W. The Promoting Role of Ni on In₂O₃ for CO₂ Hydrogenation to Methanol. *ACS Catal.* **2023**, *13*, 1875–1892.
- (2) Klumpers, B.; Hensen, E. J. M.; Filot, I. A. W. Lateral Interactions of Dynamic Adlayer Structures from Artificial Neural Networks. *J. Phys. Chem. C* **2022**, *126* (12), 5529–5540.
- (3) Frei, M. S.; Capdevila-Cortada, M.; García-Muelas, R.; Mondelli, C.; López, N.; Stewart, J. A.; Curulla Ferré, D.; Pérez-Ramírez, J. Mechanism and Microkinetics of Methanol Synthesis via CO₂ Hydrogenation on Indium Oxide. *J. Catal.* **2018**, *361*, 313–321.

Summary and Outlook

Summary

Due to the depletion of fossil fuels and environmental concerns related to CO₂ emissions, converting CO₂ with hydrogen to methanol is considered as a key technology for the sustainable energy transition. Methanol produced from CO₂ with H₂ derived from renewable energy sources could act as a sustainable energy carrier and green chemical intermediate for the manufacture of chemicals that modern society heavily depends on.

Heterogeneous catalysts play a key role in current commercial methanol production. Recently, indium oxide (In₂O₃) has emerged as a highly selective catalyst for CO₂ hydrogenation to methanol. Oxygen vacancies on the surface of In₂O₃ play a critical role in determining the high selectivity and activity toward CH₃OH. Furthermore, adding metal promoters to In₂O₃ can significantly enhance methanol production. However, the kinetic mechanism of this process and the nature of the active site remain still poorly understood.

The rapid increase in computing power allows for studying of comprehensive chemical networks such as that of CO₂ hydrogenation to methanol and CO on metal-promoted In₂O₃ catalysts. This can be done by constructing microkinetic simulations based on computed molecular reactivity data. Based on these simulations, the dominant mechanism, critical active site configurations and the most important elementary reactions steps can be elucidated. In conjunction with detailed electronic structure analysis, important insights can be derived that not only offer new insights into existing processes, but also aids in future catalyst design.

In this thesis, the focus has mainly been on Ni to promote In₂O₃. In contrast to expensive noble-metal promoting agents, Ni is earth-abundant and therefore significantly less expensive. In Chapter 3 we studied single atoms (SA) catalysts supported on a In₂O₃(111) surface. We herein compared the CO₂ hydrogenation activity and selectivity of Ni in comparison to three commonly used Pt-group metals, i.e. Pd, Pt and Rh. The explored reaction mechanism includes a direct route for CO₂ hydrogenation to methanol (formate pathway), a pathway to methanol via CO hydrogenation and the competing reverse water-gas shift (rWGS) reaction. Microkinetic simulations reveal that CO is the main product on all models and is obtained via a redox mechanism involving formation of oxygen vacancies followed by CO₂ adsorption and dissociation. The carboxyl pathway is not taken because removing of OH resulting from COOH dissociation is associated with high barriers. Furthermore, all SA-In₂O₃ models show a negligibly low methanol selectivity because hydrogenation of formates is associated with high barriers compared to the dominant pathway.

In Chapter 4, we investigated the promotional effect of sub-nanometer Ni catalysts on In₂O₃ catalyst with a combination of computational methods. The model catalysts included in our investigations are: (i) a single-atom Ni doped inside the In₂O₃ lattice, (ii) a Ni single atom adsorbed on top of the In₂O₃ and (iii) a cluster of 8 Ni atom on top of In₂O₃. Genetic algorithms are used to identify optimum structure of the Ni

clusters on the In₂O₃ surface. Microkinetic models reveal that small Ni clusters mainly catalyze methanol formation via hydrogenation of a formate intermediate. At higher temperatures, the lack of Ni-H species at the surface results in a shift of the selectivity to CO via a mechanism involving a COOH intermediate. Single atoms of Ni either doped in or adsorbed on the In₂O₃ surface mainly catalyze CO formation via a redox mechanism.

In Chapter 5, we explored the effect of alloying Ni with In on catalyzing CO₂ hydrogenation. DFT-based microkinetics showed that the formation of isolated Ni sites results in facile CO₂ dissociation and high activity for the rWGS reaction. The activity to methane is severely hampered by high barriers associated with CO activation. The results of Chapter 5 are further expanded in Chapter 6 where we provided insights into the role of bimetallic Ni-In clusters in In₂O₃ during CO₂ hydrogenation to methanol. We studied two representative 8-atoms cluster models supported on the In₂O₃(111) surface: (i) a Ni₂In₆ and (ii) a Ni₆In₂ cluster. Genetic algorithms based on density functional theory and artificial neural networks are used to identify optimum structures of the supported clusters with different Ni/In ratio. Microkinetic simulations revealed that significant methanol formation occurs only for the Ni₆In₂-cluster model. Exposed Ni atoms of the Ni₆In₂-cluster catalyze methanol synthesis at intermediate temperatures via a mechanism involving oxygen vacancies and hydrogenation of CO₂ via formates. These results are in line with the Ni₈-cluster reported in Chapter 4. On the Ni₂In₆-cluster, lack of hydride species and facile CO₂ dissociation on isolated Ni sites result in the rWGS pathway being preferred leading to negligibly low methanol selectivity.

Outlook

Investigating catalytic phenomena requires the combination of different methods on different time and length scales, i.e. a multiscale approach. The combination of density functional theory calculations and microkinetic simulations is such a multiscale approach. It provides an essential tool to develop an atomistic understanding of catalytic performance. In a multiscale approach, the molecular properties such as electronic energies are bridged with macroscale properties such as reaction kinetics. In this thesis, we show applications of this approach in studying the active phase and reaction mechanism of Ni-In₂O₃ catalysts. However, any kind of multiscale method is inherently bound to assumptions as the very reason why we construct such models is because a single method is incapable of describing larger length- and time-scales. Such assumptions may influence the overall results.

Our microkinetic simulations rely on the assumption of a static catalytic surface. In reality, the formation of surface alloys between In and the metal promoters and the catalyst deactivation due to excessive reduction could lead to a surface restructuring process. To better understand these mechanisms, computational models that describe the dynamic evolutions of atomic systems over time are required. Ideally, molecular dynamics (MD) would be used for these simulations. However, when the phenomena of interest occur over relatively long time-scales, MD simulations become intractable. This limitation could

be overcome by kinetic Monte Carlo (kMC) schemes by exploiting the fact that long-time dynamics typically consist of different jumps between states. Nevertheless, to ensure an accurate chemical description of the catalytic phenomenon on large scales, quantum chemical calculations will be required. This comes at a high computational cost that limits quantum chemical calculations to relatively small system sizes and time scales.

Future research should focus on better understanding the effect of oxygen vacancies and interfacial sites on the catalytic mechanism. These sites can offer different kinetic pathways towards chemical conversion and are thus important to investigate, yet poorly understood. Furthermore, even if these sites are not active in the catalytic mechanism, they can change the electron density of neighboring active sites resulting in different activation energies. This modulating effect on the electron density of neighbor sites might be a very attractive design tool to enhance catalytic conversion. However, fundamental knowledge on this topic is still lacking. To unravel the effect of defects and interfacial sites on the mechanism detailed analysis of the electronic structure such as partial density of states or crystal orbital Hamiltonian population, is necessary.

Another ambitious point for future development involves the creation of algorithms for automatic generation of reaction mechanisms. By using pattern recognition algorithms, possible active sites can be found on which adsorbates can be placed to study the elementary reaction steps. Machine learning could support this, however sufficiently large databases with reaction and activation energies are still lacking. Recent advance in this direction include the ReaxPro project,¹ an automatic reaction pathway exploration methods with an interface to kinetic Monte Carlo implemented in the Amsterdam Modeling Suite.² However, for the time-being, chemical intuition remains crucial in studying reaction mechanism on catalytic surfaces.

References

- (1) ReaxPro: Multiscale Modeling Software for Reactive Materials & Processes Software for Chemistry & Materials <https://www.scm.com/about-us/eu-projects/reaxpro-multiscalereactormodeling/> (accessed Feb 23, 2023).
- (2) Amsterdam Modeling Suite Making Computational Chemistry Work For You Software for Chemistry & Materials <https://www.scm.com/> (accessed Feb 23, 2023).

Curriculum Vitae



Francesco Cannizzaro was born in Palermo, Italy, in 1994. After finishing high school in 2012, he studied Chemical Engineering at the University of Palermo, Italy. After completing his Bachelor degree, between April and August 2016, he joined the Biofluid, Tissue and Solid Mechanics for Medical Applications group chaired by Prof. Patrick Segers for a research internship, focusing on computational fluid dynamics-based design of catheters for drug delivery in oncology therapy at the University of Ghent, Belgium. In 2016 he started his MSc in Chemical engineering at Politecnico di Milano within the “Alta Scuola Politecnica” excellence program. As part of his graduation project, he spent a two-months period between March and May 2018 at the group of Theoretical Chemistry chaired by Prof. Karsten Reuter at the Technical

University of Munich where he developed density functional theory models of CO₂ hydrogenation on Rh catalysts. Later the same year he obtained his dual Master’s degree at Politecnico di Milano and Politecnico di Torino graduating with a thesis on the first-principle assessment of the UBI-QEP semi-empirical method for predicting catalytic mechanisms applied to CO₂ activation via the reverse water-gas shift reaction carried out at the Laboratory of Catalysis and Catalytic Processes of the Politecnico di Milano chaired by Prof. Matteo Maestri. In March 2019 he started a Ph.D. project at the Eindhoven University of Technology in the Inorganic Materials and Catalysis group chaired by prof. Emiel Hensen, focusing his research on microkinetic modeling of CO₂ hydrogenation to methanol on metal-promoted In₂O₃ catalysts. The main results of this research are presented in this dissertation.

List of publications

1. Jiadong Zhu, **Francesco Cannizzaro**, Liang Liu, Hao Zhang, Nikolay Kosinov, Ivo. A. W. Filot, Jabor Rabeah, Angelika Brückner, and Emiel J. M. Hensen, Ni-In Synergy in CO₂ Hydrogenation to Methanol, *ACS Catal.* **2021**, 11, 18, 11371–11384
2. **Francesco Cannizzaro**, Emiel J. M. Hensen and Ivo A. W. Filot, The promoting role of Ni on In₂O₃ for Co₂ hydrogenation to methanol, *ACS Catal.* **2023**, 13, 3, 1875–1892
3. **Francesco Cannizzaro**, Sjoerd Kurstjens, Tom van den Berg, Emiel J. M. Hensen and Ivo A. W. Filot, A computational study of CO₂ hydrogenation on single atoms of Pt, Pd, Ni and Rh on In₂O₃(111), **submitted**
4. **Francesco Cannizzaro**, C. Suurmond, Ivo A. W. Filot and Emiel J. M. Hensen, Isolated Ni sites as the active phase of the rWGS reaction on InNi catalysts, **in preparation**
5. **Francesco Cannizzaro**, Bart Klumpers, Ivo A. W. Filot and Emiel J. M. Hensen, The role of In_xNi_y clusters on In₂O₃ during CO₂ hydrogenation to methanol, **in preparation**

Conference Contributions

1. **Francesco Cannizzaro**, Ivo. A. W. Filot, Emiel J. M. Hensen, The promoting role of Ni on In₂O₃ for CO₂ hydrogenation to methanol, NWO CHAINS, September 19-23, 2022, Veldhoven, The Netherlands (**oral presentation**).
2. **Francesco Cannizzaro**, Ivo. A. W. Filot, Emiel J. M. Hensen, Microkinetic modeling of CO₂ hydrogenation on InNi intermetallic catalysts, Catalysis Connected, September 15-16, 2022, Veldhoven, The Netherlands. (**poster**).
3. **Francesco Cannizzaro**, Ivo. A. W. Filot, Emiel J. M. Hensen, Proof that single atoms drive selectivity to CO on In₂O₃ catalysts, Seminars of the KNCV Division Computational & Theoretical Chemistry, July 05, 2022, online, The Netherlands. (**oral presentation**).
4. **Francesco Cannizzaro**, Ivo. A. W. Filot, Emiel J. M. Hensen, The promoting role of Ni on In₂O₃ for CO₂ hydrogenation to methanol, The 27th North American Catalysis Society Meeting, May 25-29, 2021, New York, United States. (**oral presentation**).
5. **Francesco Cannizzaro**, Ivo. A. W. Filot, Emiel J. M. Hensen, Applications of Genetic Algorithms in molecular catalysis, Han-sur-Lesse School of Theoretical Chemistry and Spectroscopy, December 01-05, 2021, Han-sur-Lesse, Belgium. (**oral presentation**).
6. **Francesco Cannizzaro**, Ivo. A. W. Filot, Emiel J. M. Hensen, Computational insights into the Ni-In₂O₃ synergy during CO₂ hydrogenation to methanol, The Netherlands' Catalysis and Chemistry Conference, March 01-05, 2021, online. (**oral presentation**).
7. **Francesco Cannizzaro**, Ivo. A. W. Filot, Emiel J. M. Hensen, Computational insights into the Ni-In₂O₃ synergy during CO₂ hydrogenation to methanol, 13th European Congress of Chemical Engineering and 6th European Congress of Applied Biotechnology, May 01-05, 2021, online. (**poster**).
8. **Francesco Cannizzaro**, Ivo. A. W. Filot, Emiel J. M. Hensen, Quantum chemical and microkinetic modeling of the methane-to-ethylene reaction on Mo/ZSM5 catalysts, Han-sur-Lesse School of Theoretical Chemistry and Spectroscopy, December 01-05, 2019, Han-sur-Lesse, Belgium. (**oral presentation**).

Acknowledgments

Undertaking and completing a PhD project is no walk in the park. This is way there are people along the way helping you carry it out and they deserve proper acknowledgment.

First, starting by my supervisors. Emiel, thank you for accepting me as a PhD candidate in the Inorganic Materials and Catalysis (IMC) group. The first time I met you, I immediately felt how passionate and knowledgeable you are about catalysis. Later, I discovered your passion for seeking excellence in the details and I believe that has been a key factor in boosting the quality of this book. Ivo, your contribution as daily supervisor has been essential for the success of this work. Together with you, I have learned a lot about foundations of quantum chemistry, kinetics of catalytic reactions, microkinetic modeling, programming and rendering of computer images. Your motto “*to understand something you got to build it*” resonates in this book and will accompany me for the rest of my career.

I am grateful to prof.dr. Matteo Maestri, prof.dr. Nuria Lopes, prof.dr.ir. John van der Schaaf and prof.dr.ir. Martin van Sintannaland for taking part in my reading committee and attending my defense ceremony. Matteo, it is especially gratifying that you decided to join the doctoral committee already having been the supervisor of my MSc thesis in Milano together with Zhaobin. That is where my passion for computational catalysis started. Angelina and Gianluca, thank you for being my paranymphs. You have supported me during my PhD studies and helped me a lot during the ceremony and for the preparation of it.

The IMC group is a fantastic collection of nerds of all kinds that makes the group strong and special. Jiadong, our discussions on In_2O_3 together with Nikolay have been key to the start of my research and lead to an excellent publication and part of Chapter 4 of this thesis. Michel, you welcomed me so warmly in the group and it has been a pleasure to be your office mate. Together with you, Rim, Bianca and Michelle we shared unforgettable times at the F.O.R.T. followed by eating pizza at the Happy Italy and crowning it up with even more unforgettable singing performances at the karaoke bar. Xianxuan, you succeeded Michel as my office mate. It has been a pleasure to share the office with you, talking about our workouts, sharing delicious snacks and solving scientific problems together. The IMC Theory group in particular, is a supporting network of scientists that has a special place in my heart. We have learned a lot together. Bart Zijlstra and Robin, you helped me a lot understanding microkinetic modeling at the beginning of my PhD. Ming-Wen, your help with the genetic algorithms (GA) has been key to start my research of supported Ni clusters collected in Chapter 4 and I am very grateful for that. Bart Klumpers, your work on improving the GA thanks to artificial neural networks has lead to the structures used in Chapter 6 of this thesis and I am very happy of that. Roos, you helped me better understand DOS and pCOHP plots. I also enjoyed our deep conversations, walks and coffee breaks. Working directly with all of you guys has been great. You are attentive to detail, professional and deliver on your promises. Lulu, it has been a great pleasure to share scientific discussions and delicious Chinese food with you. I hope you will continue the “*hotpot tradition*” in the future. Zhaochun, I will never forget your amazing singing and dancing skills. Many other colleagues made life at IMC special. Ferdy, thank you very much for reminding us that “*it is almost weekend*”. We really need that sometimes. You do have very poor taste in music, but I still like you. Floriane, Anna and Tim, dancing Zumba and going on bike rides with you has been so much fun. Having lunch together with Dimitra, Laura and Rim and delighting you with my nerdy jokes has been a great pleasure. Bianca and Jerome, I enjoyed climbing mount Etna with you and sharing drinks and food in Palermo, you guys are great. Laura, thank you so much for taking care of the illustration of the cover page of the thesis. Working with you has been fun and I hope you enjoyed too. Also, partying with you is an experience that I would recommend to everyone. Hao, we spent lots of time together in New York together with Jerome and Rim. I enjoyed this time a lot and you have been very helpful to get out and about in the Big Apple, thanks for

that. Marta, thank you so much for helping me prepare for job interviews. I learned a lot and I always enjoy having a drink with you. Nikolay, thank you for critical discussions about the Ni-In systems and for your sharp irony. Also, to all of you who had to suffer my snoring during conferences: thank you for the patience and for not strangling me.

I feel very lucky that I have the chance to thank two secretaries. Emma, you welcomed me to the IMC group warmly. Your strong positive attitude has been at the heart of the IMC group and we do our best to follow your example. I wish you to enjoy your pension and grandkids. Sue, you helped me a lot during the procedure to obtain the doctoral degree. I have learned good life lessons from you and I am very grateful for your support. I wish you to enjoy working at IMC.

Having a supporting network is key in life. In these 4 years in the Netherlands, I have learned good lessons about friendship and love. Angie, thank you (again) for all the love and support, you are a great friend. Ruud, making fun of you is one of the finest pleasures in life especially when you activate the “*question-Ruud-mode*”. Gianluca and Alice, you supported me a lot in times where I needed the most and I am very grateful for that. Francesco, I love spending time with you. It was so much fun to go to the gay pride in Antwerp and celebrate a Christmas party with Victor and our friends. Sebas and Ursha, I loved our time in Valencia with Seba’s family and *gato loco*. You are good friends and I hope to go to another trip soon. Eelkje, Gozde and Atinç, thank you for the good times and parties, hope to spend even more time together soon. Çagla, I enjoy so much my time with you, being at a party or deep conversation about relationships and life. Antonio, Erdi, Atul, Jesus, Mohammed and Ved, you guys are so much fun and make Eindhoven’s nightlife sparkling. Especially thanks to Atul for so many interesting conversations and career advice. Lara and Leo, it is so nice to have you as neighbors, drinking coffee together and sharing stories. Anna and Stasja, I always enjoy my time with you, being drinking tea or going for a walk or to Natlab. Thank you for making the time in Eindhoven so special. Mitch, thank you for the years together that I will never forget. You always inspired me to not work too much and this has helped me keeping a good balance. Elena, from Milan to the Netherlands, I am happy that we kept our friendship. I enjoyed celebrating new year’s eve with you and your friends in Palermo. Emanuela and Giulia, “*pinguini*”, thank you for always being there for me already for a long time. Condi and Deborah, I always enjoy spending time with you. Mike, thank you for carrying me around South America for 3 weeks. You know a lot about this continent and helped me enjoying my time there, even if you are very “*strurusu*” and sometimes “*t’ammazzassi*”. To all the volunteers I have met around South America, thank you for sharing your stories and life lessons.

Mamma, Emanuele e Nonna, in questi anni il vostro supporto non e’ mai mancato, specialmente nei momenti piu’ difficili. Grazie per aver creduto in me e per impegnarvi a mantenere un rapporto solido nonostante la distanza. Lo stesso vale per Stefania, Giuseppe e Gabriele e per gli zii Mario e Adelaide. Mi auguro che rimarremo sempre uniti. Mimma, grazie per i bei momenti a Macari, ormai sei come parte della nostra famiglia. Un ringraziamento anche a *Ucchio* e *Attarune* che mi hanno ricordato, a modo loro, di non lavorare troppo e prendermi una pausa ogni tanto.